Study of the Mechanical Behavior of Lead-free Solder Joints and Its Individual Phases under Various Harsh Environments

by

Abdullah Fahim

A dissertation submitted to the Graduate Faculty of
Auburn University
in partial fulfillment of the
requirements for the Degree of
Doctor of Philosophy

Auburn, Alabama
May 1, 2021

Keywords: microelectronics reliability, lead-free solder, harsh environment applications, high temperature aging, nanoindentation, microstructural evolution

Approved by

Jeffrey C. Suhling, Chair, Quina Distinguished Professor of Mechanical Engineering
Hareesh V. Tippur, McWane Professor of Mechanical Engineering
Michael J. Bozack, Professor Emeritus of Physics
James S. Davidson, Gottlieb Professor of Civil Engineering

Abstract

Solder joints provide mechanical support, electrical and thermal interconnection between packaging levels in microelectronics assembly systems. Proper functioning of these interconnections and the reliability of the electronic packages depend largely on the mechanical properties of the solder joints. Lead free solders are common as interconnects in electronic packaging due to their relatively high melting point, attractive mechanical properties, thermal cycling reliability, and environment friendly chemical properties. However, environmental conditions, such as, operating temperature, aging temperature, and aging time significantly affect these properties due to the microstructural evolution of the solder that occurs during aging. Moreover, electronic devices, sometimes experience harsh environment applications including well drilling, geothermal energy, automotive power electronics, and aerospace engines, where solders are exposed to very high temperatures from T = 100 -200 °C. Also, solder joints in many electronic packages are exposed to temperature cycling environments. During high temperature dwell, solder joints go under isothermal aging phenomena. However, additional aging can occur during the ramp time. In real scenario, CTE mismatch occurs between die and PCB causes shear fatigue on solder joints and affects the reliability of the entire package. Mechanical properties of lead-free solders at elevated temperatures are limited. This research involves several projects to create a database of mechanical properties of bulk and real solder joints, its individual phases and the associated mechanical and microstructural changes of them under the exposure of harsh environments.

In the first project, several SAC and SAC+X lead free solder alloys, recommended for high reliability applications have been chemically analyzed and then mechanically tested in order to determine the temperature dependent mechanical properties of these alloys. The alloys include SAC405, Cyclomax (SAC_Q), and Innolot. The mechanical behavior of these alloys have been explored at several extreme high temperatures from 100 to 200 °C. For each of 5 elevated temperatures (T = 100, 125, 150, 175, and 200 °C), creep tests were performed at two different stress level (σ = 10, and 15 MPa). For each alloy and testing temperature, secondary creep strain rate was measured and compared.

In the second project, mechanical behavior of individual phases of solder joints (Intermetallics and β-Sn phase) was nano-mechanically characterized as a function of operating temperature condition using nanoindentation technique. At first phase, mechanical behaviors of IMC particles and layers, as well as β-Sn in SAC solder joints have been characterized using nanoindentation at room temperature. Solder joints were extracted from 14 x 14 mm PBGA assemblies (0.8 mm ball pitch, 0.46 mm ball diameter). Then, SAC BGA solder joints were aged for 6 months at T = 125 ^{o} C. Intermetallics formed in the bulk solder region, copper pad and SAC solder interface, and ENIG plating finish and SAC solder interface were then indented to measure their room temperature mechanical properties including the elastic modulus, hardness, and creep strain rate. At the second phase, same intermetallics were indented to measure their mechanical properties which includes the elastic modulus and hardness at elevated temperatures (50, 75, 100 and 125 ^{o} C) using a heating stage. A special high temperature stage and test protocol was used within the nanoindentation system to carefully control the testing temperature, and make the measurements insensitive to thermal drift problems. Time dependent deformation

(creep) behaviors were also evaluated at 100 ^{o} C and then compared to room temperature results to see the effect of high temperature on the creep rate of IMCs.

In third project, the aging induced variations of the mechanical properties of the β-Sn phase, and of Sn-Ag-Cu IMC particles in SAC solder joints have been explored using nanoindentation. SAC solder joints extracted from SuperBGA (SBGA) packages were aged for different time intervals (0, 1, 5, 10 and 30 days) at T = 125 °C. Nanoindentation test samples were prepared by cross sectioning the solder joints, and then molding them in epoxy and polishing them to prepare the joint surfaces for nanoindentation. Multiple β-Sn grains were identified in joints using optical polarized microscopy and IMCs were also observed. Individual β-Sn grains and IMC particles were then indented at room temperature to measure their mechanical properties (elastic modulus and hardness) and time dependent creep deformations. Properties measured at different aging time were then compared to explore aging induced degradations of the individual phases.

In the fourth project, nanoindentation technique was used to understand the evolution of mechanical properties (modulus, hardness and creep behavior) of SAC305 BGA solder joints subjected to thermal cycling loading for various durations. In addition, microstructural changes in those joints that occur during thermal cycling were observed using both SEM and optical microscopy. BGA solder joint strip specimens were first prepared by cross sectioning BGA assemblies followed by surface polishing to facilitate SEM imaging and nanoindentation testing. The strip specimens were chosen to contain several single grain solder joints. This enabled large regions of solder material with equivalent mechanical behavior, which could then be indented several times after various durations of cycling. After preparation, the solder joint strip samples were thermally cycled

from T = -40 to 125 ^{o} C in an environmental chamber. At various points in the cycling (e.g., after 0, 50, 100, 250, 500, 750, 1000 cycles), the package was taken out from the chamber, and nanoindentation was performed on each single grain joint to obtain the modulus, hardness, and creep behavior at 25 ^{o}C. This allowed the evolution of the mechanical properties with the duration of thermal cycling to be determined. Moreover, microstructural changes were also observed after various durations of cycling using optical microscopy.

In the final project, evolution of mechanical behavior of the various materials within PBGA package assembly which includes die attachment adhesive, silicon die, and solder mask material for various durations of thermal cycling. Test specimens were first prepared by cross sectioning a PBGA package to reveal the different materials, followed by surface polishing to facilitate SEM imaging and nanoindentation testing. After preparation, the package samples were thermally cycled from T = −40 to 125 °C in an environmental chamber. At various points in the cycling (e.g., after 0, 50, 100, 250, 500, 750 and 1000 cycles), the package was taken out from the chamber, and nanoindentation was performed on above mentioned materials to observe evolution of mechanical behavior (modulus, hardness and creep) at room temperature (25 °C).

Acknowledgments

I would like to express my deepest appreciation to my advisor Dr. Jeffrey C. Suhling for his continuous supervision and untiring support throughout my PhD study at Auburn University. I am grateful for getting the opportunity to work with a mentor like him. He is one of my role models and a source of inspiration. He continuously and convincingly conveys a spirit of pursuit of excellence and perfection in research. I am really grateful that I had the opportunity to work with an exceptional mentor who taught me beyond what is expected in academia. I am also grateful to my advisory committee members including Dr. Hareesh V. Tippur, Dr. Michael J. Bozack, and Dr. James Davidson for their insightful discussion about this research work. Special thanks are extended to my friends and co-workers Dr. Munshi Basit, Dr. Md. Hasnine, Dr. Nianjun Fu, Dr. Quang Nguyen, Dr. Sudan Ahmed, Dr. ChienChih Chen, Dr. Promod Chowdhury, Dr. Md Mahmudur Rahman Chowdhury, KM Rafidh Hasan, Jing Wu, Jun Chen, Mohd Aminul Hoque, Kamrul Hasan, Mohammad Ashraful Haq, Al Ahsan, Debabrata Mondal, Rakib Mojumder, Jason Smith, and John Marcell for their support.

I am heartily grateful to my parents and all of my family members for their support to my study and life in the United States. Finally, I solemnly dedicate this dissertation and all achievements in pursuit of doctoral degree to my wife, Nasima Akhter, for her perseverance and support, and her understanding during my busy time at graduate school have been priceless to me.

Table of Contents

Abstract ……..……ii

Acknowledgments…..... vi

Table of Contents….. vii

List of Figures…… xv

List of Tables…… xx

CHAPTER 1……. 1

INTRODUCTION…. 1

1.1 Overview of Solders in Microelectronics 1

1.2 Lead Free Solders Choices.....3

1.3 Candidates for Alternative Lead-Free Solders.....5

1.3.1 Tin 6

1.3.2 Chromium (Cr)..... 7

1.3.3 Nickel (Ni) 8

1.3.4 Zinc (Zn) 8

1.3.5 Cobalt (Co)..... 9

1.3.6 Bismuth (Bi)..... 9

1.3.7 Antimony (Sb) 9

1.3.8 Germanium (Ge) 10

1.3.9 Sn-Ag-Cu System 10

1.3.10 Sn-Ag-Cu + X System 13

1.4 Characteristics and Applications of Sn-Ag-Cu Solder Material.....14

1.5 Mechanical Properties of Lead Free Solders 14
1.5.1 Tensile Properties (Stress-Strain Behavior) 15
1.5.2 Creep Properties 18
1.5.3 Mechanisms of Creep Deformation 21
1.6 Nanoindentation 23
1.7 Harsh Environment applications of Electronics 24
1.8 Objectives of This Research 26
1.9 Organization of the Dissertation 27
CHAPTER 2…….. 29
LITERATURE REVIEW 29
2.1 Introduction 29
2.2 Aging Effects on Tensile Properties 30
2.2.1 Aging Effects on Bulk Solders 31
2.2.2 Aging Effects on Solders Joints 32
2.3 Aging Effects on Creep Properties 36
2.4 Effects of Thermal Cycling on Solder Joints 37
2.5 Constitutive Modeling for Stress-Strain Tests 38
2.6 Constitutive Modeling for Creep 39
2.7 Reduction of Aging and Thermal Cycling Effect by Dopant 42
2.8 Role of Intermetallic in Solder Interconnects 47
2.9 Study of Individual Phases of SAC Solder Joint 48
2.10 Nanoindentation on SAC Solder Joints 49
2.11 PBGA Package Materials and their Mechanical Behavior 51

2.12 Summary 53

CHAPTER 3……. 55

EXPERIMENTAL PROCEDURE 55

3.1 Introduction 55

3.2 Uniaxial Test Sample Preparation 56

3.3 Uniaxial Tensile Testing System 60

3.4 Typical Testing Data and Data Processing 61

3.4.1 Typical Test Data 61

3.4.2 Stress-Strain and Creep Data Processing 62

3.5 Microstructure Study 64

3.6 Nanoindentation Method for Mechanical Behavior and Creep Tests on Solder Joints 66

3.6.1 Sample Preparation for Nanoindentation 66

3.6.2 Nanoindentation Machine and Test Procedures 68

3.6.3 Measurement of Elastic Modulus and Hardness 71

3.7 Summary and Discussion 74

CHAPTER 4…… 76

HIGH TEMPERATURE MECHANICAL BEHAVIOR OF SAC AND SAC+X LEAD FREE SOLDERS…… 76

4.1 Introduction 76

4.2 Chemical Composition of the Solder Alloys 77

4.3 Creep Strain vs. Time Data for Various Temperature and Stress Levels 78

4.4 Comparison of Creep Behavior of Solder Alloys at Various Temperature and Stress level 82
4.5 Creep Strain Rate as a Function of Temperature and Stress Level....87
4.6 Summary and Discussion....90
CHAPTER 5……. 92
INVESTIGATION ON MECHANICAL PROPERTIES OF.... 92
INTERMETALLIC COMPOUNDS (IMCS) IN SAC SOLDER JOINTS AT ROOM TEMPERATURE AND ELEVATED TEMPERATURES 92
5.1 Introduction....92
5.2 Mechanical and Creep Behavior of Intermetallic Compounds....93
5.3 Room Temperature Nanoindentation System and Test Procedures: 95
5.4 Formation of Intermetallic Compounds....96
5.4.1 Cu_6Sn_5 Intermetallic Layers.... 96
5.4.2 $(Cu_{1-x}Ni_x)_6$-Sn_5 Intermetallic Layers.... 97
5.4.3 Ag_3Sn Intermetallic Layers.... 97
5.5 Chemical Composition Analysis....99
5.6 Nanoindentation Results 100
5.6.1 Modulus and Hardness Values.... 100
5.6.2 Creep Behavior of Intermetallics 106
5.7 High Temperature Nanoindentation Tests of Intermetallics....113
5.8 Sample Preparation for High Temperature Nanoindentation 113
5.9 High Temperature Nanoindentation System and Test Procedures 113
5.10 Measurement of High Temperature Creep Behavior....115

5.11 High Temperature Nanoindentation Test Results (25-125 °C).....116
5.11.1 Elastic Modulus and Hardness Measurements 116
5.11.2 Explore Substrate Effect for Nanoindentation..... 122
5.11.3 High Temperature Creep Results..... 123
5.12 Summary and Discussion.....126
CHAPTER 6…….. 128
MECHANICAL CHARACTERIZATION OF INDIVIDUAL PHASES..... 128
(IMC AND β-SN PHASE) IN PB-FREE SOLDER JOINTS DURING ISOTHERMAL
AGING……..... 128
6.1 Individual Phases of SAC Solder Joint.....128
6.2 Aging Effect on Individual Phases of SAC Solder Joint 129
6.3 Super BGA Solder Joints.....130
6.4 Identification of Individual Phases 134
6.5 Factors Influence in Nanoindentation Test Results 134
6.5.1 Influence of Holding Time on Modulus and Hardness..... 135
6.5.2 Influence of Surface Effect on Modulus and Hardness 139
6.6 Modulus and Hardness Measurements on Individual Phases 140
6.7 Evolution of Mechanical Properties of Individual Phases with Aging.....145
6.8 Creep Analysis of Individual Phases 147
6.9 Evolution of Creep Behavior with Aging 149
6.10 Summary and Discussion.....151
CHAPTER 7…….. 153

MECHANICAL BEHAVIOR OF SAC305 SOLDER JOINTS UNDER THERMAL CYCLING LOADING…… 153

7.1 Introduction.....153

7.2 Sample Preparation for Thermal Cycling Study.....154

7.3 Thermal Cycling Chamber.....155

7.4 Nanoindentation Test Procedure for Thermal Cycling.....158

7.5 Nanoindentation Test Results for Thermal Cycling 159

7.5.1 Optical Microscopic and SEM Images 159

7.5.2 Microstructure in As-Reflowed Condition 163

7.5.3 Modulus and Hardness Measurements 164

7.5.4 Microstructure Evolution during Thermal Cycling 169

7.5.5 Measurement of Creep Behavior 170

7.6 Summary and Discussion.....176

CHAPTER 8……. 178

NANOINDENTATION CHARACTERIZATION OF VARIOUS MATERIALS IN PBGA PACKAGES UNDER THE EXPOSURE OF THERMAL CYCLING LOADING..... 178

8.1 Introduction.....178

8.2 PBGA Package Materials 179

8.3 Experimental Procedure.....182

8.4 Solder Mask Materials 183

8.4.1 As Reflowed Condition Mechanical Properties..... 183

8.4.2 Evolution of Mechanical Behavior with Thermal Cycling..... 185

8.4.3 Evolution of Creep Behavior for Solder Mask Material..... 187

8.5 Die Attach Materials 189
8.5.1 As-Reflowed Condition Mechanical Properties 189
8.5.2 Evolution of Mechanical Behavior with Thermal Cycling 190
8.5.3 Evolution of Creep Behavior for Die Attach Material 192
8.6 Silicon Die Materials 194
8.6.1 As-Reflowed Condition Mechanical Properties 194
8.6.2 Evolution of Mechanical Behavior for Die Material 195
8.6.3 Creep Behavior of Die Material 196
8.7 Summary 197
CHAPTER 9……. 198
SUMMARY AND CONCLUSIONS 198
9.1 Literature Review 198
9.2 Experimental Procedures 199
9.3 High Temperature Creep Behavior of SAC and Doped Lead Free Solders 200
9.4 Mechanical Behavior of IMC Compounds at Room Temperature 200
9.5 Nanoindentation Characterization of IMCs and β-Sn Phase at High Temperatures 201
9.6 Mechanical Behavior of Individual Phases of SAC Solder Joints as a Function of Aging Using Nanoindentation 202
9.7 Mechanical Behavior of SAC Solder Joints under Thermal Cycling Loading 203
9.8 Mechanical Behavior of PBGA Package Materials under Thermal Cycling 203
9.9 Summary 204
9.10 Future Work 205

REFERENCES……. 207

List of Figures

Figure 1.1 Lead Free Solder Market Share 5

Figure 1.2 Elastic Modulus and Coefficient of Thermal Expansion (CTE) of Tin as a Function of Crystal Orientation [1] 7

Figure 1.3 Typical 3-D Ternary Phase Diagram 11

Figure 1.4 Sn-Ag-Cu Ternary Phase Diagram 11

Figure 1.5 Schematic Overview of Mechanical Behavior of a) Ceramics, Polymers below their Glass Transition Temperature (Tg) and Non Ductile Material b) Ductile Materials c) Polymers above Tg 16

Figure 1.6 Typical Stress-Strain Curve 18

Figure 1.7 Typical Creep Curve 20

Figure 1.8 A Typical Creep Deformation Map. 22

Figure 1.9 Berkovich Tip. 24

Figure 1.10 Temperature Cycling of Electronic Packages 25

Figure 3.1 Equipment used for Specimen Preparation 57

Figure 3.2 Water Quenched (WQ) Cooling Profiles 58

Figure 3.3 Heller 1800EXL Reflow Oven 58

Figure 3.4 Reflow (RF) Cooling Profiles 58

Figure 3.5 Solder Uniaxial Test Specimens 60

Figure 3.6 X-Ray Inspection of Solder Test Specimens (Good and Bad Samples) 60

Figure 3.7 Mechanical Test System with Uniaxial Sample 61

Figure 3.8 SAC Stress-Strain Curve and Material Properties 62

Figure 3.9 Empirical Model Fit to Solder Stress-Strain Curves 63

Figure 3.10 Grinding and Polishing Machine 64

Figure 3.11 OLYMPUS BX60 Optical Microscope 65

Figure 3.12 Zeiss Polarized Light Microscope 65

Figure 3.13 JEOL JSM-7000F Field Emission SEM 66

Figure 3.14 iNEMI Test Board and BGA Package 67

Figure 3.15 IsoMet 1000 Precision Cutter 67

Figure 3.16 Sample Preparation Procedure for High Temperature Nanoindentation 68

Figure 3.17 Hysitron TI950 TriboIndenter 69

Figure 3.18 SAC305 Solder Joint after Nanoindentation Testing 70

Figure 3.19 An Example of The Loading Profile Used During Nanoindentation Testing 70

Figure 3.20 An Example of Load-Displacement Curve Obtained 71

Figure 4.1 Creep strain vs. Time Curves for SAC405 at Temperatures (100-200 ^{o}C) 79

Figure 4.2 Comparison of secondary creep strain rate as a function of temperature at 10 and 15 MPa for SAC405, SAC_Q and Innolot 89

Figure 5.1 Nanoindentation System for Room Temperature testing 96

Figure 5.2 SEM Image of a) Solder Joints b) Single Solder Joint with Different IMC Layers and Particles 98

Figure 5.3 EDX Analysis Results of IMCs 100

Figure 5.4 Load-Displacement Curve for a) Cu_6Sn_5 b) $(Cu_{1-x}Ni_x)_6Sn_5$ & c) Ag_3Sn IMCs (d) Combined curve showing all phases 104

Figure 5.5 Indents on Ag3Sn Particles (a) 3000X and (b) 5000X 106

Figure 5.6 Creep Displacement vs. Time Curve of Various Phases 108

Figure 5.7 (a) Hardness vs. Time and (b) Stress vs. Time Curve 109

Figure 5.8 Creep Strain Rate vs. Applied Stress Curve of Various Phases 110

Figure 5.9 Creep Strain Rate vs. Applied Stress Curve of Various Phases 111

Figure 5.10 SPM Images of Indents after Nanoindentation Test 112

Figure 5.11 High Temperature Nanoindentation System 114

Figure 5.12 Solder Joint Sample in the High Temperature Stage 114

Figure 5.13 Modulus and Hardness Measurement in Nanoindentation 115

Figure 5.14 Creep Measurement in Nanoindentation 116

Figure 5.15 Load- Displacement Curve for (a) Cu_6Sn_5 (b) $(Cu_{1-x}Ni_x)_6Sn_5$ & c) Ag_3Sn IMCs from 25-125 °C 119

Figure 5.16 Modulus and Hardness as a Function of Temperature (25-125 °C) 121

Figure 5.17 Explore Substrate Effect in IMCs during Nanoindentation 122

Figure 5.18 Modulus and Hardness as a Function of Temperature (25-125 °C) 125

Figure 6.1 (a) (c) (e) Optical Microscopy and (b) (d) (f) Polarized Microscopy of Super BGA Solder Joints 133

Figure 6.2 Identification of Different Phases in Solder Joints 134

Figure 6.3 Load –Displacement Curve (A) Standard Polycarbonate 136

Figure 6.4 Load –Displacement Curve (A) Standard Quartz 137

Figure 6.5 Variation of (A) Modulus and (B) Hardness with Different Holding Time. 138

Figure 6.6 Multiple Load-unload Load Function 139

Figure 6.7 Variation of Modulus and Hardness of (a) IMC and (b) β-Sn 140

Figure 6.8 (a) Nanoindentation load-displacement curve for β-Sn (grain 1); (b) SPM imaging showing indents on grain 1 142

Figure 6.9 (a) Nanoindentation load-displacement curve for β-Sn (grain 2); (b) SPM imaging showing indents on grain 2 143

Figure 6.10 (a) Nanoindentation load-displacement curve for IMCs; (b) SPM imaging showing indents on IMCs 144

Figure 6.11 (a) Variations of (a) Modulus and (b) Hardness for β-Sn 146

Figure 6.12 (a) Nanoindentation Creep Displacement vs. Time Curve for (a) β-Sn Phase (Grain 1 and 2) and (b) IMC Phase..... 148

Figure 6.13 (a) Nanoindentation Creep Displacement vs. Time Curve for (a) β-Sn Phase (Grain 1 and 2) and (b) IMC Phase as a Function of Aging Time (0-30 Days) 151

Figure 7.1 Sample preparation of PBGA packages by cross sectioning and polishing. 156

Figure 7.2 (a) Thermal cycling chamber (b) Thermal cycling profile 157

Figure 7.3 (a) Optical and (b) polarized microscopy of joint A, ... 161

Figure 7.4 (a) Optical and (b) polarized microscopy of joint C,..... 163

Figure 7.5 SAC305 dendritic microstructure in as-reflowed condition..... 164

Figure 7.6 Indentation regions (0, 50, 100, 250, 500, 750, 1000 cycles) 165

Figure 7.7 Permanent Indentation after Testing 165

Figure 7.8 Representative Nanoindentation Load-Displacement 167

Figure 7.9 Mechanical Property Variation with Thermal Cycling 169

Figure 7.10 (a) Microstructure and (b) Grain Morphology 170

Figure 7.11 Creep Indentation regions (0, 50, 100, 250, 500, 750, 1000 cycles)..... 171

Figure 7.12 Nanoindentation Creep Displacement on SAC305 Joints..... 173

Figure 7.13 Creep Strain Rate vs. Applied Stress Plot 175

Figure 7.14 Extended creep strain rate vs. time curves using exponential creep model 176

Figure 8.1 Various Materials within PBGA Packages..... 180

Figure 8.2 Nanoindentation for PBGA Package Materials..... 183

Figure 8.3 (a) Indentation Marks and on Solder Mask Materials 184

Figure 8.4 Evolution of (a) Modulus and (b) Hardness of Solder Mask Material as a Function of Thermal Cycling..... 186

Figure 8.5 Creep Deformation of Solder Mask as a Function of Thermal Cycling..... 188

Figure 8.6 Creep Strain Rate vs. Stress of Solder Mask as a Function of Thermal Cycling 188

Figure 8.7 Representative Load-Displacement Curve for Die Attach..... 189

Figure 8.8 Evolution of (a) Modulus and (b) Hardness of Die Attach Material as a Function of Thermal Cycling..... 191

Figure 8.9 Creep Deformation of Die Attach as a Function of Thermal Cycling 193

Figure 8.10 Creep Strain Rate vs. Stress of Die Attach as a Function of Thermal Cycling 193

Figure 8.11 Representative Load-Displacement Curve for Die Attach..... 194

Figure 8.12 Evolution of (a) Modulus and (b) Hardness of Si Die Material as a Function of Thermal Cycling 196

Figure 8.13 Creep Deformation of Die Material as a Function of Thermal Cycling..... 197

List of Tables

Table 4.1 Chemical Compositions of the Solder Alloys 77

Table 4.2 Comparison of Creep Strain Rate 88

Table 5.1 EDX results of Cu_6Sn_5 IMC Layer 99

Table 5.2 EDX results of $(Cu_{1-x}Ni_x)_6Sn_5$ IMC Layer 100

Table 5.3 EDX results of Ag_3Sn IMC Layer 100

Table 4.4 Modulus of IMCs as a Function of Temperature 120

Table 4.5 Hardness of IMCs as a Function of Temperature 120

Table 6.1 Properties of β-Sn and IMC Phase 145

Table 7.1 Thermal Cycling Profile 158

Table 7.2 Mechanical Properties of Joint 1 and Joint 2 167

Table 8.1 Modulus and Hardness of Solder Mask Material at No Cycling 185

Table 8.2 Modulus and Hardness of Die Attach Material at No Cycling 190

Table 8.3 Modulus and Hardness of Die at No Cycling 195

CHAPTER 1

INTRODUCTION

1.1 Overview of Solders in Microelectronics

Lead free solders provide excellent thermo-mechanical properties and commonly used as interconnections in electronic packages. As a joining material, in electronic assemblies, Solder joints provide mechanical support, electrical and thermal interconnection between packaging levels in microelectronics assembly systems. It also helps to dissipate the heat generated from the Si-chip [1].

With the emergence of the modern electronic packaging technology over the last few decades, solder alloys have been the primary interconnect material used in electronic packaging. In the past, eutectic 63Sn-37Pb has been the most extensively used soldering alloy in the packaging industries. The eutectic Sn-Pb solders were very attractive due to their relatively low melting temperature (183 °C) and excellent ductility and good reliability and for their superior wettability and compatibility with most substrates and devices [2].

There is a general trend towards products that minimize harmful effects on the environment and human health. This trend is further reinforced by the RoHS ban on harmful substances and WEEE regulations on recycling and minimizing of electronic wastes. In June 2000, the EU adopted two directives, the Waste of Electrical and Electronic

Equipment (WEEE) and the Directive of the Restriction of the Use of Certain Hazardous Substances (RoHS) [3]. The WEEE directive requires that lead has to be removed from any end-of-life electrical or electronic components. The RoHS specifically bans lead from electrical and electronic components manufactured after July 1, 2006. As a result of the enforcement of the directives, all electrical or electronic equipment and devices produced in or imported to E.U. member states must comply with these lead-free standards except those items that are exempted from the bans. In addition to legislation enforcement there are emerging detection technologies to enforce compliance. So due to the general push towards the eco-efficiency and green electronics, manufacturers are motivated for the adoption of lead free electronics. Therefore, the conversion to lead free solders in the global electronic market appears imminent [4].

In the United States, as soon as lead-free solder legislation was proposed, the lead-free solder project headed by the NCMS initiated research and development of lead-free solder in a program lasting 4 years [5]. The results of the project have been made available in a database and offer information on such matters as modifying equipment and processes for selecting alternative materials. The project initially selected for study 79 types of alloys considered at the time to be potential candidates for use in lead-free solder. Basic attributes considered included toxicity, resource availability, economic feasibility, and wetting characteristics. The selection process narrowed the field down to the final seven alloys, and these received secondary evaluation for reliability and ease of mounting manufacturing. Evaluation of the individual alloys did not result in the final selection of a single candidate, but three alloys, Sn–58Bi, Sn–3.5Ag–4.8Bi, and Sn–3.5Ag, were recommended as candidates. Screening comments indicated that the Sn–58Bi eutectic alloy

was not suitable for use as standard solder due to the scarcity of Bi resources. However, since this material can be used for mounting at less than 200 °C, and has chalked up a 20-year plus record of use in mainframe computers, this solder was deemed suitable for special applications. These results were used to construct a database on lead-free solder that includes the information in these tables along with other items such as (1) recommended applications for lead-free solder, (2) alloy composition guidelines reflecting price and availability, (3) database of the 7 selected alloys and comparison with Sn–Pb eutectic alloy, (4) data on the characteristics of the other 70 eliminated alloys, (5) optimal process conditions using various test PWBs, (6) strength evaluation and metallurgical reaction analysis for the selected alloys and various surface mounting process reactions, (7) predicted life (using NCMS Project proprietary life prediction software) and thermal fatigue evaluation for 4 of the selected alloys, and (8) assessment of nontoxicity and alloy composition.

1.2 Lead Free Solders Choices

In selecting suitable alternative of Sn-Pb soldering materials, it is important to take into consideration that the properties of the alternative solders are comparable or superior to Sn-Pb solders. Compatible candidates of the Sn-Pb solders must have the following behaviors [6]:

- melting temperature similar to eutectic Sn-Pb for a similar reflow profile
- sufficient wettability for good metallization process
- good electrical properties for transmitting electrical signals
- strong mechanical properties for good fatigue resistance and reliability

- inexpensive and easier manufacturability

Among various alloy systems that are considered as lead-free solder candidates, Sn-Ag-Cu alloys have been recognized as the most promising because of their relatively low melting temperature (compared with the Sn-Ag binary eutectic lead free solder), superior mechanical properties, and good compatibility with other components [7-9]. Sn-Ag-Cu alloys are widely used as lead-free solutions for ball-grid-array (BGA) interconnection in the microelectronic packaging industry as solder balls and pastes. Although no "drop in" replacement has been identified that is suitable for all applications, Sn-Ag, Sn-Ag-Cu (SAC), and other alloys involving elements such as Sn, Ag, Cu, Bi, In, and Zn have been identified as promising replacements for standard 63Sn-37Pb eutectic solder. Industries have proposed several SAC alloys which include 96.5Sn-3.0Ag-0.5Cu (SAC 305) in Japan, 95.5Sn-3.8Ag-0.7Cu (SAC 387) in the EU, and 95.5Sn-3.9Ag-0.6Cu (SAC 396) in the USA. The International Printed Circuit Association has suggested that 96.5Sn-3.0Ag-0.5Cu (SAC305) and Sn-3.9Ag- 0.6Cu (two near-eutectic alloys) will be the most widely used alloys in the future [10]. This prediction is attributed to their good mechanical properties, acceptable wetting properties, and suitable melting points [8, 11, 12].

A relatively large number of lead-free solder alloys have been proposed so far, including binary, ternary and even quaternary alloys. More than 70 alloys have been identified in the literature. Among them, the majority of the alloys are Sn-based alloys, that is, Sn is the preferred major constituent. In fact, Sn-rich lead-free alloys have occupied more than 80% in the wave solder market share and more than 90% in the reflow solder market share (Figure 1.1). The main benefits of the various SAC alloy systems are their

relatively low melting temperatures compared with the 96.5Sn–3.5Ag binary eutectic alloy, as well as their superior mechanical and solderability properties when compared to other lead-free solders. There are some major challenges for the current series of lead-free solders. SAC series alloys have a higher melting temperature, around 217 °C, compared to 183 °C for the eutectic Sn-Pb solders. They thus require higher reflow temperature during the manufacturing process, which can lead to reliability problems. The excessive buildup of intermetallic formed at the interface between the solder joints and the copper pad can also cause reliability problems. High costs are another issue for lead-free solders.

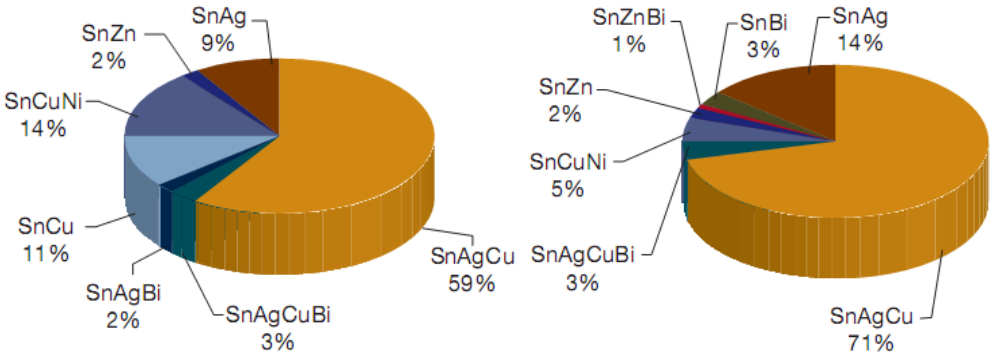

(a) Wave Solders (b) Reflow Solders

Figure 1.1 Lead Free Solder Market Share

1.3 Candidates for Alternative Lead-Free Solders

About 70 different alloys were proposed as an alternative to the Sn-Pb solder. Most of these are Sn based solder where Sn is the main constituent along with one, two or even three other minor elements. These minor elements are added mainly to 1) decrease the melting temperature and 2) improve wetting and reliability of the solder [1]. The properties

of Sn and the effects of different alloying elements on the Sn based solder alloys are described below:

1.3.1 Tin

The melting temperature of elemental Sn is 231 °C. One of the main reasons of choosing Sn as the principle component in the lead free solder for electronic applications is its ability to spread and wet a number of various different substrates. In the solid state, tin can have two different phases or crystal structures 1) white or β-Sn with tetragonal crystal structure and 2) gray or α-Sn with diamond cubic crystal structure. At the room temperature the thermodynamically stable phase is β-Sn. Upon cooling, when the temperature goes below 13 °C (allotropic transformation temperature), α-Sn becomes the thermodynamically stable phase. The allotropic transformation of β-Sn to α-Sn, results a significant volume change (around 27%) causing blistering of the tin surface, cracking or disintegration. This phenomenon is mainly a surface event and often referred as 'tin pest'. The low ductility of α-Sn is another reason of causing blistering and cracking of the tin after the transformation [1, 13, 14]. Although the equilibrium temperature for β-Sn to α-Sn is 13 °C, the transformation occurs only after a significant undercooling and an extensive incubation period as long as several years. For example, no 'tin pest' was found on a SAC387 bulk sample after storing at -40 °C for 5 years [14]. Presence of heterogeneous nuclei, also known as seeding, can considerably accelerate the kinetics of the transformation. The possibility of β → α transformation in a actual solder joint is even limited due to the constraints (component and substrate) on the both side of the joint [13, 14].

Addition of other elements, as an impurity, can affect the allotropic transformation. For example, the presence of Pb, Bi, Sb, Cu, Ge and Si inhibit β → α transformation while the presence of As, Zn, Al and Mg promote the transformation [13, 14].

Sn has a body centered tetragonal crystal structure (β-Sn), at room temperature, which is anisotropic. Hence, tin shows an anisotropic thermal (e.g., CTE) and mechanical (e.g. elastic modulus) properties as shown in Figure 1.2. As a result, during thermal cycling experiment, cracking occurs along the grain boundaries [1].

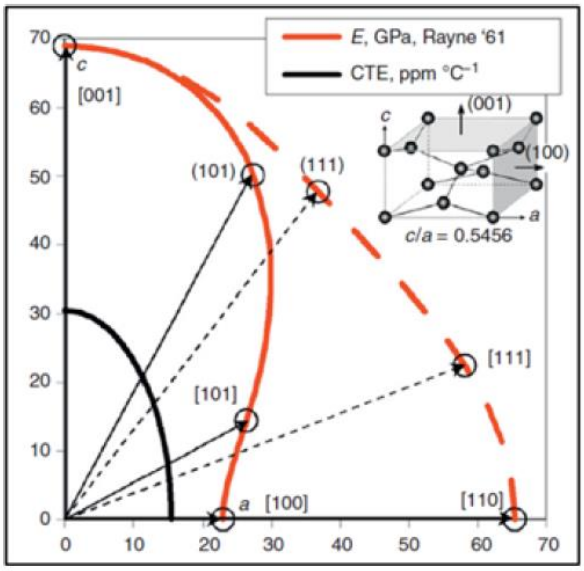

Figure 1.2 Elastic Modulus and Coefficient of Thermal Expansion (CTE) of Tin as a Function of Crystal Orientation [1]

1.3.2 Chromium (Cr)

Cr helps to improve shear ductility after long term aging. Besides, it also suppress kirkendall void formation in the solder joints [15].

1.3.3 Nickel (Ni)

Among all the micro-alloy additives, Ni is one of the most common elements. Addition of Ni improves fluidity of SAC solders. Ni also improves the high strain rate properties of solder joints. For example, the drop strength of SAC alloys can be significantly improved by Ni addition. Although Ni does not have any significant influence on the creep properties of the solder, it inhibits Cu diffusion and thus reduce the thickness of Cu_3Sn intermetallic compound (IMC). The Ni addition greater than 0.01 wt% could suppress the growth of Cu_3Sn IMC even after long term (2000 hours) aging. Since Cu_3Sn IMC is very brittle, the growth of Cu_3Sn layer is very critical for the brittle failure of the solder joints. Addition of Ni on SAC solder causes to form more stable $(Cu, Ni)_6Sn_5$ IMC which act as a barrier layer and suppress the growth of Cu_3Sn layer. Therefore, by reducing the thickness of brittle Cu_3Sn layer, Ni helps to improve strength of the solder joints. Ni also helps to improve strength by refining solder microstructure [16].

1.3.4 Zinc (Zn)

While Ni reduces only the formation Cu_3Sn, Zn doping can retard both Cu_3Sn and Cu6Sn5 IMC's in SAC solders. Zn also helps to improve the interface quality after multiple reflow and high temperature aging. Addition of 1.5% Zn in SAC207 solder could refine Ag_3Sn and Cu6Sn5 IMC's and hence increase strength by dispersion strengthening [15].

1.3.5 Cobalt (Co)

Co helps to reduce the growth of Cu_3Sn layer during high temperature aging. Addition of small amount of Co (<0.1 wt.%) can improve the properties of SAC solders. Co increases the number of nucleation sites and hence significantly refine the grains of SAC305 solder. Thus it helps to improve shear strength of the solder joints [15].

1.3.6 Bismuth (Bi)

If added in small amount, Bi can improve the wetting ability and reduce melting temperature of lead free solder alloys. It also increases strength of the bulk solder and inhibit the large Ag_3Sn formation in the bulk solder. It is recommended to avoid Pb contamination in the solder before using Bi as an additive. Because Bi can react with Pb to form a brittle IMC at the grain boundary and reduce strength significantly. If present in excess amount, Bi can cause solidification crack due to the increase in the gap between solidus and liquidus temperature [15].

1.3.7 Antimony (Sb)

Sb improves mechanical properties of lead-free solders but it is toxic in nature. A small percentage (0.5 wt%) of Sb can improve drop test reliability of SAC solder joints [16]. Besides, Sb also helps to enhance strength of the solder by solid solution strengthening [17].

1.3.8 Germanium (Ge)

Ge doped solders shows low Cu dissolution from the Cu pad and hence suitable for the wave soldering process. Ge significantly improve wetting properties of the lead free solders and refine the solder microstructure. As a result, Ge addition improves the strength and ductility of the lead free solder [16].

1.3.9 Sn-Ag-Cu System

As shown in Figure 1.1, Sn-Ag-Cu (SAC) has been the most popular, widely used lead free solder in today's market. Although they are still not identified as the "drop in" replacement for all applications, a variety of SAC alloys with different chemical compositions have been the proposed by various user groups and industry experts. These include: SAC105 (98.5Sn-1.0Ag-0.5Cu), SAC205 (97.5Sn-2.0Ag-0.5Cu), SAC305 (96.5Sn-3.0Ag-0.5Cu), and SAC405 (95.5Sn-4.0Ag-0.5Cu), known as the SACN05 series; SAC387 (95.5Sn-3.8Ag-0.7Cu), SAC396 (95.5Sn-3.9Ag-0.6Cu), and SAC357 (95.2Sn-3.5Ag-0.7Cu), identified as near eutectic SAC choices; SAC3810 (95.2Sn-3.8Ag-1.0Cu), SAC3595 (95.55Sn-3.5Ag-0.95Cu), SAC0307 (9Sn-0.3Ag-0.7Cu), and SAC107 (98.3Sn-1.0Ag-0.7Cu), designed for special needs such as high temperature application, drop and shock optimization, etc. The main benefits of the various SAC alloy systems are their relatively low melting temperatures compared with the 96.5Sn-3.5Ag binary eutectic alloy, as well as their superior mechanical and manufacturability properties when compared to other lead free solders [18].

Figure 1.3 shows a typical 3-D ternary phase diagram. The contours on the top surfaces of the figure represent the isothermal lines. Each of the 3 sectors represents the

binary phase diagram of two of the three elements. The center of the diagram, where the isothermal lines reach the common, lowest point, is the eutectic point of the ternary system. Figure 1.4 is the top view (2-D) of the ternary phase diagram of Sn-Ag-Cu.

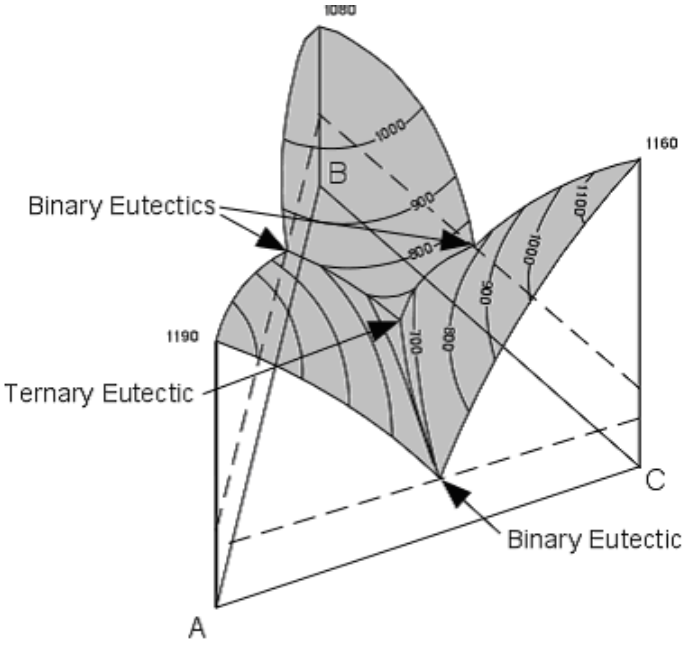

Figure 1.3 Typical 3-D Ternary Phase Diagram

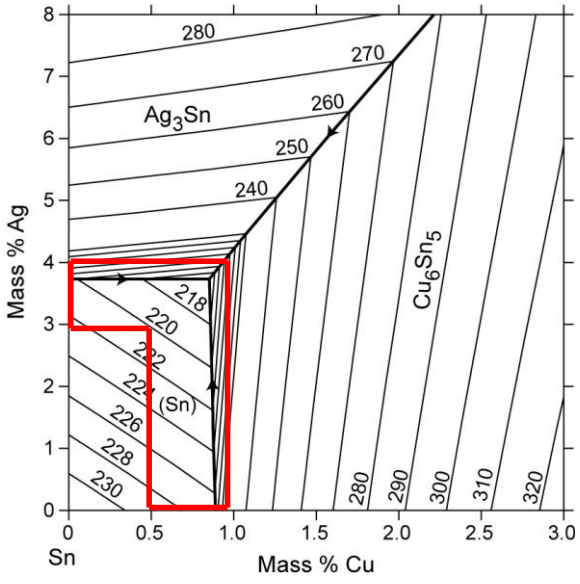

Figure 1.4 Sn-Ag-Cu Ternary Phase Diagram

The area indicated in the red box is the near eutectic region. Most of the SAC alloy compositions currently on the market are within this region. The eutectic and near eutectic melting temperature has been determined to be 217 °C, although the precise eutectic point is not known [19].

In SAC alloys, the formation of intermetallic compounds between the primary elements Sn and Ag, and Cu affect all the properties of the alloys. There are three possible intermetallic compounds that may be formed: Ag_3Sn forms due to the reaction between Sn and Ag (Figure 1.5) and Cu6Sn5 forms due to the Sn and Cu reaction. The compound Cu_3Sn will not form at the eutectic point unless the Cu content is high enough for the formation of Cu_3Sn at higher temperatures, so in bulk specimens Cu_3Sn is not presented. There is no reaction between Ag and Cu to form any kind of intermetallic compounds. The particles of intermetallic compounds possess much higher strength than the bulk material. Fine intermetallic particles in the Sn matrix can therefore strengthen the alloys. The intermetallic compounds can also improve the fatigue life of the solders, as SAC alloys are reported to be 3-4 times better fatigue properties than the Sn-Pb eutectic solders. The higher fatigue resistance is believed to be contributed by the interspersed Ag_3Sn and Cu6Sn5 particles, which pin and block the movement of dislocations. The many patents that have been granted for SAC systems have limited their use and hindered research on several of the SAC alloys. However, many familiar alloy such as SAC305 and SAC405 are not patented to avoid excessive licensing and fees [18].

Despite the benefits mentioned above, SAC family solders sometimes are still questionable as complete substitutes for eutectic Sn-Pb because of costs, some patent issues

(particularly outside Europe), aesthetic consideration (dross problem of SAC solders), and relatively high melting temperature (217 °C vs. 183 °C).

1.3.10 Sn-Ag-Cu + X System

Sn-Ag-Cu alloys have shown potential to be successful substitutes for eutectic Sn-Pb, however, the industry is still looking for a "perfect" solution. According to the results of many recent studies, performance characteristics of solder alloys are able to be optimized by doping, that is, by adding a small amount of other alloying elements into the SAC solder alloys.

The proposed doping element candidates include Bi, Ni, Co, Ge, Zn, La, Mg, Mn, Ce, Ti, Fe, In, B, etc. For example, adding 0.05% (wt.) Ni can successfully stabilize the microstructure, inhibit the excessive consumption of metal base and thus increase the reliability of the solder joints [20-22]. In addition, doping rear earth (RE) elements can significantly enhance wettability, refine microstructure and improve ductility of SAC alloys [23-26].

Even though dopants can greatly alter the mechanical, electrical and physical behavior of SAC solders, the effect on melting temperature, however, is found to be negligible. This is another advantage for doped solder alloys because manufacturers can still use the same processing conditions as conventional SAC alloys.

Meanwhile, the known issues for SAC-X solders are also apparent. For instance, the material properties and interfacial behavior of solder alloys have been demonstrated to be very sensitive to the quantity of the X-additive. As a result, it takes much more time and cost to figure out the optimal composition levels for the dopants.

1.4 Characteristics and Applications of Sn-Ag-Cu Solder Material

The advantages of SAC series over other Pb-free systems include relatively low melting temperatures, superior mechanical and solderability properties, and good tolerance for Pb contamination. These characteristics give SAC alloys good compatibility with existing electronics packaging infrastructure. In fact, there is a long history of using 95.5Sn–4.0Ag–0.5Cu (SAC405) to form solder joints for BGA packages. The high market share (≈ 70%) by SAC series alloys on a global scale provides strong evidence of its world-wide acceptance. Also, nanoscale lead-free solders ("nano-solders") have been proposed and investigated in the development of nano-soldering technique for nanoscale assembly and integration. Tin (Sn)-based and indium (In)-based lead-free nano-solders have been synthesized directly onto multisegmented nanowires using electro deposition method in nanoporous templates. Furthermore, high temperature lead free solders are being used in medical industries today where a variety of intrusive procedures used requiring tools, instruments, sensors and components in materials that are inert with respect to reactions with the body [27]. Also, new surgical techniques have been developed to improve the quality of operations, reduce the risk to patients and reduce the pain experienced by patients. Environmental concerns and the concern about toxicity and health hazards indicate that there is a drive to develop and use lead-free solders.

1.5 Mechanical Properties of Lead Free Solders

In an electronic device, a number of different types of engineering materials exists in a close proximity. For example, a printed circuit board (PCB) is typically a glass fiber

reinforced polymer (composite material), a die is a semiconductor material which is often encapsulated in a plastic or a ceramic, and the tracking and the solder joints are metallic materials. Solder joints are used to create an electrical circuit by mounting chips and components on the PCB. Hence an ideal solder joint should have a good conductivity to transmit electrical signals and at the same time, adequate strength to provide mechanical support and connection. Hence, mechanical properties of solder joints are critically important to ensure reliability of the electronic products. Among all the mechanical properties, tensile, fatigue, and creep performance of the solder are critically important. Thus an accurate measurement of mechanical properties and development of constitutive equations for solder materials are required in mechanical design, process optimization and reliability assessment.

1.5.1 Tensile Properties (Stress-Strain Behavior)

Under the action of an increasing stress, metals usually exhibit elasticity, plasticity, and a maximum in stress is followed by necking and fracture. The slope of the linear elastic portion of the stress vs. strain plot is the modulus, and the stress at termination of elastic behavior is the yield stress. The extent of deformation prior to fracture is known as ductility. Ceramics display only elastic behavior until fracture, which is associated with cracking and very limited deformation (brittleness). Polymers may exhibit both characteristics above according to the temperature. Above the glass transition temperature, T_g, extensive deformation due to mechanisms quite unlike those in metals may follow a small degree of elasticity. Below this temperature, polymers exhibit ceramic-like behavior. In all material categories, the maximum stress attained is the tensile/compressive/shear

strength according to the mode of stressing employed. Composites are physical mixtures and exhibit the average properties of their components, taking into account the proportions of each. These characteristic features of monotonic behavior are summarized in Figure 1.5. The fracture strains of brittle materials and the yield strains of metals are generally less than 1% (the yield strain of solders is around 0.1–0.2%). The amount of deformation prior to the attainment of maximum strength is between about 3% and 7% for common solder alloys.

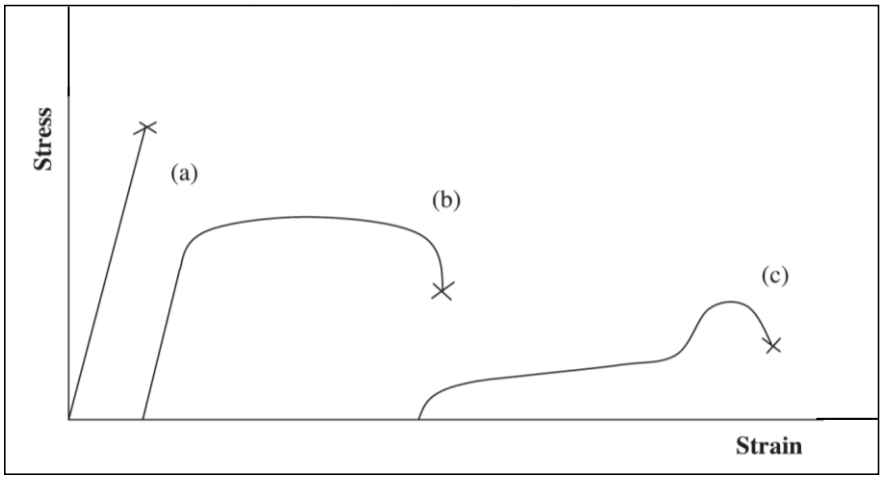

Figure 1.5 Schematic Overview of Mechanical Behavior of a) Ceramics, Polymers below their Glass Transition Temperature (Tg) and Non Ductile Material b) Ductile Materials c) Polymers above Tg

Tensile properties indicate how the material will react to forces being applied in tension. Although solder joints are rarely under pure tensile/compressive loading, tensile properties are still crucial indicators for design purposes. Through tensile tests, several material properties can be determined, such as effective modulus, yield stress (YS),

ultimate tensile strength (UTS), elongation, etc. In most of the cases that engineering stress-strain curves are employed by neglecting the change in cross sectional area.

Tensile properties are generally described by stress-strain curves. Figure 1.6 shows a typical engineering stress strain curve. A typical engineering stress-strain curve for solder alloys consists of an elastic region and a plastic region. In the elastic region, when the stress is reduced, the material will return to its original shape. In this linear region, the material obeys the relationship defined by Hooke's Law. However, since the effective modulus includes small inelastic deformations or time-dependent deformations such as creep, it is usually smaller than the dynamic modulus measured by the acoustic or ultrasonic wave method, which largely eliminates the inelastic deformation due to rapid wave propagation [28-30]. Also, Ralls, et al. showed that the elastic modulus of metal will decrease with increasing temperature [31]. The underlying reason for this is because the distance between adjacent atoms increases at higher temperatures which in turns decrease the elastic modulus.

When the load is high enough to exceed the elastic limits the material will experience plastic deformation, which is permanent. At this stage the material is undergoing a rearrangement of its internal molecular or microscopic structure, in which atoms are being moved to new equilibrium positions. Specimens subject to plastic deformation will simultaneously elongate and decrease in diameter. The Yield Stress (YS) is defined as just enough stress to cause the onset of plastic deformation. However, YS is difficult to determine. In engineering practice, a specified small amount of plastic deformation is used, with 0.2% being the widely accepted value [32]. This is determined by a parallel line drawn at 0.2% of the strain to the elastic slope (Figure 1.6). When the

load is removed at a point above the yield stress, the stress-strain curve will be approximately parallel to the initial modulus.

The ultimate tensile strength (UTS) is the maximum engineering stress level reached in a stress-strain test. In ductile materials similar to solders, the UTS are usually well outside of the elastic portion and the elastic strain is very small comparing to the plastic strain. When necking occurs, the engineering stress decreases and the specimen eventually fail.

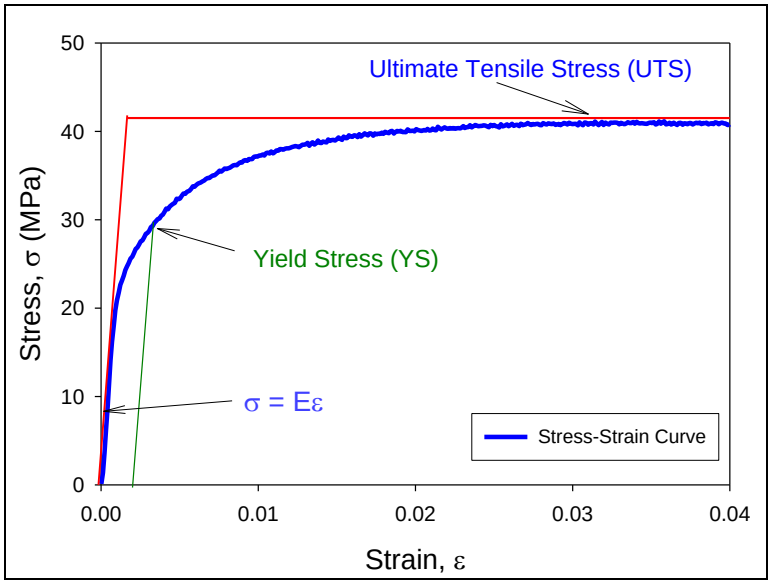

Figure 1.6 Typical Stress-Strain Curve.

1.5.2 Creep Properties

Creep deformation refers to the time dependent plastic flow or deformation of a material that occurs when the material is exposed to a constant load, typically below yield stress, for a long period of time. Creep deformation becomes significant when the material

operates at a high homologous temperature (T_h), which is defined by the ratio of operating temperature (T) and the melting temperature (T_m) of the material.

$$T_h = \frac{T}{T_m} \tag{1.4}$$

Creep deformation becomes the dominant failure mode in a metallic material if T_h is greater than $0.5T_m$ [33]. The melting temperature of lead free SAC solder is around 217 °C (490 K) causing T_h for the alloys, for room temperature (298 K) operating conditions, is $0.61T_m$. As a result, lead free SAC solder alloys display creep deformation even in room temperature operating condition. Due to the mismatches of the coefficient of thermal expansion (CTE) of silicon chip and other assembly materials used in an electronic package, solder joints are remain under mechanical stress. These mechanical stresses can cause time dependent creep deformation of solder materials. In microelectronic packaging, creep deformation is regarded as one of the major failure mechanisms of solder joints [34].

Creep test is typically conducted by applying a constant uniaxial load on the test specimen at a particular temperature. During the test, deformation of the test specimen is recorded as a function of test time and the result of the creep test is presented as a 'creep strain' vs. 'time' plot. The extent of creep deformation significantly depends on the applied stress level and the test temperature. Figure 1.7 represents a typical creep curve which consists of three distinct regions, after the initial jump, namely, primary, secondary, and tertiary regions.

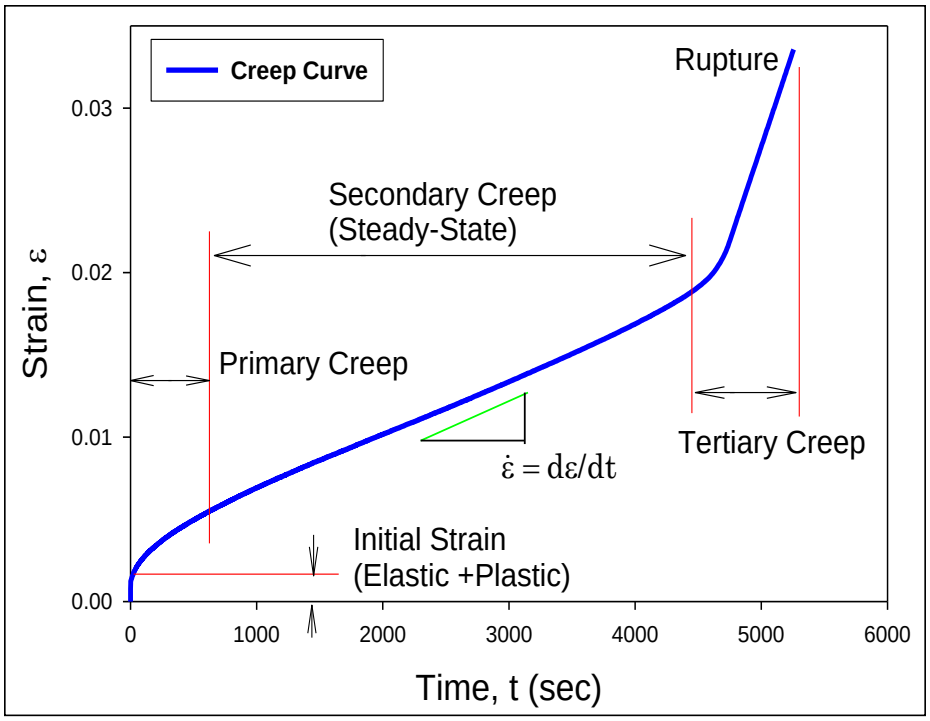

Figure 1.7 Typical Creep Curve.

Every creep test begins with an initial strain which corresponds to the instantaneous response (mostly elastic) of the material due to the applied force/load. In the primary creep stage, the material starts to deform with at a high strain rate (high slope at the beginning of the primary region) and then the strain rate decrease gradually with increasing time. This is due to the work hardening of the material which resists deformation. Eventually, with increasing test time, the creep strain rate reaches to a steady state stage which is known as steady state creep or secondary creep region. The constant creep rate, in the secondary stage, is due to the dynamic balance between strain hardening and recrystallization [32]. The strain rate in the secondary stage is very important since very often researchers use this parameter in the finite element simulations to predict reliability of the solder joints under different test conditions. After secondary creep, the material enter into the tertiary

creep region followed by an immediate rupture. Tertiary region begins when the strain rate start increasing abruptly from the constant value.

1.5.3 Mechanisms of Creep Deformation

Several creep mechanisms have been proposed such as dislocation glide, dislocation creep, grain boundary diffusion, and lattice diffusion which can be summarized in a creep deformation map, as shown in Figure 1.8 [35, 36]. The deformation diagram was first introduced by Ashby in 1972 [36], and has been widely accepted and studied by other researchers in the area. In the deformation map show in Figure 1.8, the abscissa is the homologous temperature and the ordinate is normalized tensile or shear stress. The top of the map is bounded to the theoretical or ideal stress, below which is the onset of dislocation glide. *Dislocation glide* occurs at high stress levels over the entire homologous temperature range. In this case, the dislocation moves along the slip planes [37]. Dislocation creep is characterized by a high-temperature deformation mechanism with homologous temperatures greater than $0.5T_m$ and requiring intermediate high stress. The deformation results from diffusion controlled dislocation movement, with dislocations climbing away from barriers.

Coble proposed a *grain boundary based diffusion* mechanism, which involves the atomic or ionic diffusion along the grain boundaries [38]. The deformation occurs at intermediate low stress levels over an intermediate to low temperature range. Nabarro-Herring Creep or *lattice or bulk diffusion* occurs at low stress level and high temperature. In this case, interstitial atoms and lattice vacancies along the gradient of a grain boundary migrate in reversed directions in the presence of tension or compression pressure. Lattice

or bulk diffusion becomes the primary deformation mechanism under this circumstance [39]. If there is no pressure, interstitial atoms and lattice vacancies will migrate in proportion to the gradient of their concentrations. Under pressure, the lattice defects tend to move in directions to relieve the imbalance of pressure. The movement will eventually cause creep deformation.

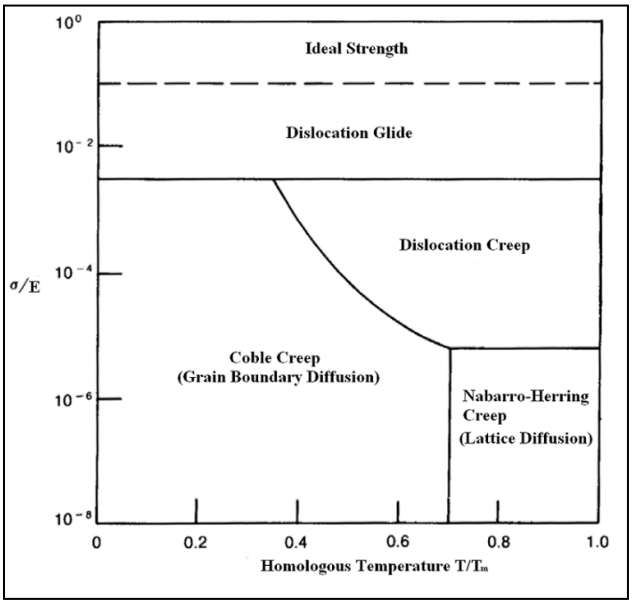

Figure 1.8 A Typical Creep Deformation Map.

Grain-boundary sliding may also be involved in the creep deformation at high temperatures [30] where the displacement of grains can be induced by stress at high temperatures. However, this is not an independent deformation mechanism, but may accompany one or more of the above deformation mechanisms.

Due to the high homologous temperature ($> 0.5T_m$) of most solder alloys under normal operating conditions, the stress level determines the creep deformation mechanism. At low stress levels, the controlling mechanism is lattice diffusion and grain-boundary

diffusion. As the stress rises to intermediate levels, dislocation creep takes over, and at high stress level, dislocation gliding becomes dominant. Additionally, the contribution of grain boundary gliding to creep deformation should be taken in account at all stress levels.

1.6 Nanoindentation

Indentation testing is a technique where a hard tip, with known mechanical properties, is pressed into the surface of a test sample to extract the test sample's properties. The load applied on the indenter tip caused it to penetrate into the test sample surface. When the applied load reaches to the user specified value, it can be held for a certain period of time (for creep properties) or remove instantaneously (for hardness and elastic modulus). Removal of the applied load leaves an impression or indent on the sample surface.

Nanoindentation (NI) is a kind of indentation testing where the penetration length is measured in nanometer. The development of the NI technique has been motivated by the miniaturization of the engineering materials as well as the development of the nanostructured materials. Since the area of the indenter tip is well defined (known geometry), the indent area can be easily determined from the tip penetration depth from the sample surface. Elastic modulus, hardness and creep properties of a material can be obtained from indentation load displacement data [40].

Because of having very high hardness and elastic modulus, diamond is typically used to make indenter tip. Indenter tips are available in different shape and the choice of indenter tip shape depends on the type of required information from a NI test. Berkovich tip is used in this study (Figure 1.9).

This is the most common indenter tip and used to measure mechanical properties using a NI technique. The shape of a Berkovich tip is similar to a three-sided pyramid where the faces meet at a single point (Figure 1.5). The tip can maintain its self-similar geometry to a significantly small scale. The center to face angle of the tip is 65.3^{o}.

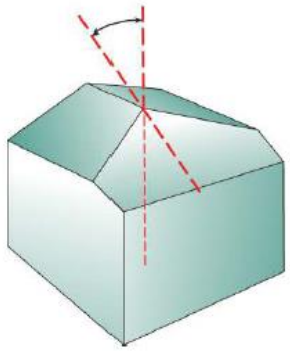

Figure 1.9 Berkovich Tip.

1.7 Harsh Environment applications of Electronics

The reliability of electronics used in various devices depends on the environmental conditions experienced during field use. In oil and gas exploration, avionics, automotive, and defense applications, electronics typically experience very harsh environments compared to consumer electronics [41, 42]. The electronic systems used in under-the-hood automotive applications can be operated at temperatures over 150 °C [43, 44]. For example, engine control modules mounted directly onto the engine experiences high-temperature excursions while in operation. In vehicles, when the engine is turned on, it continues to ramp up to the maximum operating temperature from the ambient temperature while the engine continues to be in operational state. Electronics experience extremely

high temperatures during this period, and there can be fluctuation in the temperature conditions.

The electronic systems used in daily applications, also experiences ambient temperatures above 100 °C, and temperature changes [45]. During this application, specifically in winter countries, the temperature fluctuates from negative to high temperature up to 125 °C. The reliability of electronics is an important concern here since temperature changes causes CTE mismatch happens between various components in electronic packages. CTE mismatch between die and PCB causes shear fatigue on solder joints and causes crack initiation, propagation and failure of the components.

Electronics used in commercial and defense aircrafts and ground military vehicles also experience high temperatures and thermal cycling environment.

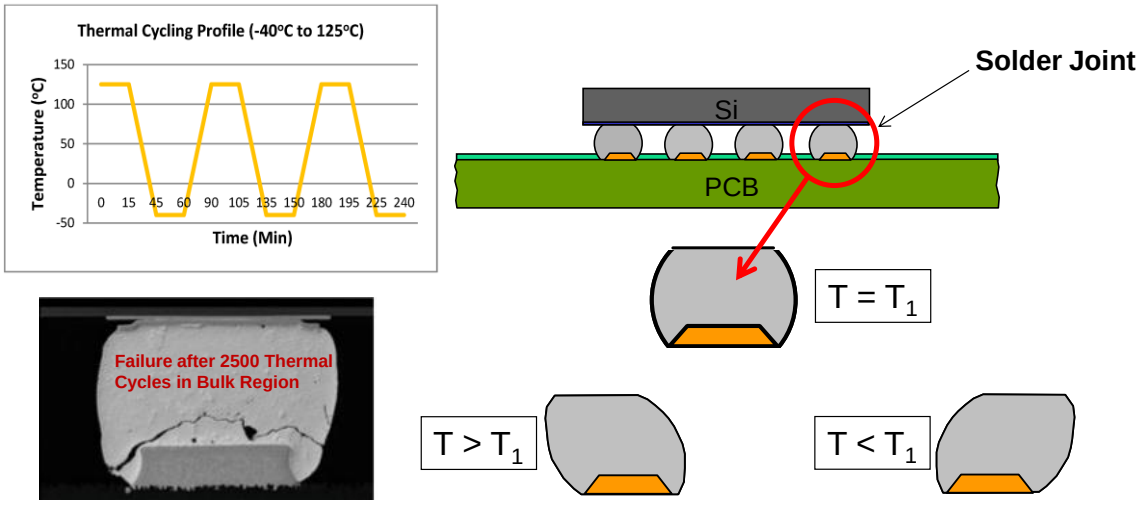

Figure 1.10 Temperature Cycling of Electronic Packages

1.8 Objectives of This Research

The motivation of this research is to explore the high temperature mechanical behavior of lead-free solder alloys and its's individual phases for harsh environment applications like aging and thermal cycling to predict solder joint reliability in microelectronic packaging. The Primary objectives of this research involve:

(1) Investigate the uniaxial creep properties of SAC405 and doped SAC solders at very high temperatures (up to 200 °C).

(2) Understand mechanical behavior of IMC compounds at room temperature operating conditions using nanoindentation.

(3) Perform nanomechanical characterization of IMC phases at elevated temperature conditions.

(4) Understand aging induced evolution of mechanical and creep behavior of individual phases of SAC solder joints

(5) Perform nanomechanical characterization of SAC305 solder joints under the exposure of thermal cycling.

(6) Understand evolution of creep behavior of SAC305 solder joints when exposed to thermal cycling environment.

(7) Perform nanomechanical characterization of various materials within PBGA packages under the exposure of thermal cycling

(8) Understand evolution of creep behavior of various materials within PBGA packages when exposed to thermal cycling environment.

1.9 Organization of the Dissertation

This dissertation mainly focuses on investigating the aging dependent Mechanical behavior and microstructural evolution of lead-free Solder alloys and is presented in the following chapters:

Chapter 1: Introduction to lead free solders alloys and mechanical properties of solder materials.

Chapter 2: Literature review on isothermal aging effects, mechanical properties, nanoindentation on SAC solder joints, nanoindentation at elevated temperature, microstructural evolution during aging of SAC alloys, life prediction and reliability models of electronic packages that consist of lead free solder materials based on coarsening of IMC particles.

Chapter 3: Description of experimental procedure, sample preparation, uniaxial creep tests, nanoindentation modulus and hardness test, nanoindentation creep tests, data processing.

Chapter 4: Characterization of uniaxial creep properties of different lead free solder alloys and comparison of the properties to examine the effect of the dopants.

Chapter 5: Investigation of Mechanical Properties of Intermetallic Compounds (IMCs) in SAC Solder Joints at Room Temperature and Elevated Temperatures.

Chapter 6: Mechanical characterization of Individual Phases (IMC and β-Sn Phase) in Pb-Free Solder Joints during Isothermal Aging.

Chapter 7: Mechanical Behavior of SAC Solder Joints Under Thermal Cycling Loading.

Chapter 8: Creep Behavior of Various Materials Within PBGA Packages Subjected to Thermal Cycling Loading

Chapter 9: Summary and conclusions of the dissertation

CHAPTER 2

LITERATURE REVIEW

2.1 Introduction

As the electronic industries transition to lead free soldering by the motivation of environmental concerns, legislative mandates, and market differentiation, great efforts have been undertaken to develop desirable lead free solders and establish a corresponding database of material properties. Many researchers have attempted to measure the key mechanical properties of lead free solders. However, large discrepancies have been found in the published data from various groups. There are several reasons for these discrepancies. Firstly, the differences in specimen preparation methods among the researchers cause different microstructures in the specimens that directly affect the experimental results significantly. Secondly, the testing methods and the test conditions may also be different which will again affect the results. Thirdly, mechanical properties obtained from the bulk solders might be different from the measured properties of solder joints. Finally, the lack of standardization in the data acquisition and processing of mechanical properties makes it difficult to obtain good laboratory-to-laboratory comparisons.

Apart from the above-mentioned reasons for the discrepancies in solder material properties, another critical factor is aging effects. Aging is mostly neglected in the majority

of prior studies, which will further exacerbate these problems. It has been observed from recent studies that isothermal aging leads to large reductions (up to 50%) in several key material properties for lead free solders including stiffness (modulus), yield stress, ultimate strength, and strain to failure [33]. Even more dramatic evolution has been observed in the creep response of aged lead free solders, where up to 100X increases were found in the steady state (secondary) creep strain rate (creep compliance) of SAC solders that were simply aged at room temperature [46, 47]. For elevated temperature aging at 125 °C [48], the creep strain rate was observed to change even more dramatically (up to 10,000X increase for SAC105).

In real applications, solder joints are continuously exposed to aging/thermal cycling during service. It has been well documented that the microstructure, mechanical response, and failure behavior of solder materials are constantly evolving under such circumstances [49-84]. It has also been demonstrated that aging effects are universally detrimental to reliability and cause reductions in stiffness, yield stress, ultimate strength, and strain to failure, as well as highly accelerated creep. Solder joints with highly degraded microstructure and material properties are so vulnerable that the service life of the package is often severely shortened.

2.2 Aging Effects on Tensile Properties

Studies on the effects of aging on solder material properties are primarily divided into two groups, which are aging effects on bulk solders and aging effects on solder joints. These are described in subsequent sub-sections.

2.2.1 Aging Effects on Bulk Solders

Evolution of mechanical properties with aging in both Sn-Pb and lead free solders has been reported in recent years. Researchers have done numerous studies on the effects of aging on bulk solder properties as well as some studies on solder joints in actual components. Most studies show aging has significant effects on the mechanical properties of solder materials. In 1956, Medvedev [62] reported a 30% loss of tensile strength for bulk Sn-Pb solder after 450 days of room temperature (RT) aging, and a 23% loss in tensile strength for solder joints under a similar exposure. Room temperature aging effects on solder alloys has been presented by Lampe [60]. He showed that after 30 days of room temperature aging, the shear strength and the hardness of Sn-Pb and Sn-Pb-Sb solders reduced by approximately 20%. Miyazawa [77] reported reduction of hardness and microstructural coarsening for Sn-Pb solders aged at 25 and 100 °C for 1000 hours.

Xiao, et al. [66] investigated the stress-strain behavior of SAC396 solder alloy which were subjected to aging at 25 and 180 °C for various amount of time. They have shown that the strength reduces by 25% for aging at room temperature for 35 days and a 33% reduction for aging at 180 C for 9 days. Ding, et al. investigated the influence of aging on fracture behavior of Sn-Ag solder in tensile tests [56]. They have shown that the solder samples tensile strength reduce very quickly for isothermal aging at 180 °C for 120 hours. Ma, et al. [85] studied the evolution of Young's modulus, yield stress, and ultimate tensile strength of SAC305 and SAC405 solder alloys under various aging conditions. A linear-exponential model was developed to describe the material property evolution. They have shown that the material properties decreased dramatically in the first 20 days for both

room temperature aging as well as elevated temperature aging. After 20 days of aging, the properties change slowly and linearly and it continues for longer aging time.

Zhang, et al. [86] also studied the aging effects on tensile properties of SACN05 (N = 1%, 2%, 3% and 4% silver) series solders for different amount of aging at temperatures 25-125 °C. They have demonstrated that the mechanical properties degraded more dramatically when the aging temperature was increased. The data also shows that the degradation becomes linear with longer aging time. Cai, et al. [51] have also shown that the aging effects are significant for lead free solders (SAC105, SAC205, SAC305 and SAC405) for room temperature aging as well as elevated temperature aging. They have also shown that the aging effects can be reduced by using certain dopants to (e.g. Bi, In, Ni, La, Mg, Mn, Ce, Co, Ti, Zn, etc.) SAC solder alloys to enhance the reliability of lead free solders. Finally, Mustafa, et al. [78] have demonstrated that the hysteresis loop area in cyclic (tension/compression) loading of various SAC solder alloys changes significantly with aging. For strain controlled tests, the hysteresis loop area deceases and for the stress controlled tests, the loop area increases with aging time.

2.2.2 Aging Effects on Solders Joints

Isothermal aging effects have also been reported to lower the strength and to reduce reliability of solder joints. The mechanical response of solder joints to external loading can be different from the bulk solders due to fine microstructure, grain orientation (single grain/ multigrain), and the presence of intermetallic compounds at joint boundaries.

Coyle, et al. [87] reported 20% shearing strength reduction of BGA solder joints after 240 hours of aging at room temperature. A 10% shearing strength reduction has been

reported by Lee, et al. [88] for the BGA packages just after 3 days room temperature aging. Chilton, et al. [89] reported a 15% fatigue strength reduction of Sn-Pb solder joints of a SMD test package which were aged for 60 days at room temperature. Li, et al. [90] studied the elevated temperature aging effects on flip-chip packages with SAC solders. They have shown that the shear strength of solder bumps subjected to aging at 80 °C decreased gradually with aging. Also for the aging temperatures 150 and 175 °C, the degradation of shear strength of the bumps were much faster. They also reported that the fracture of the solder bumps occurred at the bulk solder. Koo, et al. [91] found that 63Sn-37Pb solder joint strength on electroplated Ni/Au BGA substrate was significantly affected by aging at 170 °C for up to 21 days, while the deterioration of shear properties of Sn-3.5Ag was much smaller. Darveaux [92] indicated that after 24 hours of aging at 125 °C, all alloys showed a 10% to 30% reduction in solder joint strength. All of the solder joints failed within the bulk solder and exhibited high ductility. In addition, the ductility of all of the Pb-free solder joints decreased with increased aging [66]. Oliver et al. [93] reported that the joint strength of Sn-3.5Ag and SAC325 solder on both Ni/Au and Sn/Pb pad metallizations were unchanged after aging at room temperature as well as elevated temperature for 1000 hours. However they found reduction in shear strength of solder joint in Sn-Pb solders.

Pang, et al. [94] studied the aging effects on the mechanical properties and fatigue life of Sn-Pb solder joint specimens that were subjected to thermal cycling conditions from -40 to 125 °C. They have shown that the shear strength reduces significantly for specimens that were subjected to 1000 thermal cycles. They have also shown that the fatigue life of the specimens dropped by 6 times compared to non-cycled specimens. Zhou, et al. compared the joint strengths of SAC387 on both Cu and Ag substrates at an aging

temperature of 170 °C, and concluded that aging had little effect on the SAC/Ag interface, but dramatically softened the SAC/Cu joint. The softening difference was said to be due to lower residual stresses at the SAC/Ag joint interface. Chen, et al. [73] studied the effects of aging on the solder bump shear strength for both Sn-Pb and Sn-3.5Ag solders. They reported that shear strength for both solder materials decreases after aging at 150 °C for 1500 hours, 8.9% for Sn-Pb solder bumps and 5.3% for Sn-3.5Ag. Kim, et al. [59] also reported similar results in which they reported an average 5% decrease in joint strength in stud bump samples for aging at 150 °C for 300 hours.

The degradations of the stiffness, strength, and creep compliance with aging are expected to be universally detrimental to reliability of solder joints in lead free assemblies. This has been demonstrated explicitly in the recent investigation of Lee and coworkers [88], where aging has been shown to degrade the Thermal Cycling Reliability (TCR) of lead free Plastic Ball Grid Array (PBGA) assemblies subjected to Accelerated Life Testing (ALT). They have shown dramatic degradation in fatigue life of BGA components with SAC 305 solders, which were subjected to thermal cycling from 0 to 100 °C with prior aging at either 100 or 150 °C. The amount of life degradation was found to be dependent on the surface finish of the PCB substrates, with 44% degradation observed for ENIG surface finish and 20% degradation observed for OSP surface finish under the most severe aging conditions (1000 hours at 150 °C) prior to thermal cycling accelerated life testing.

In a similar study, Lee, et al. [95] showed that the lifetime of wafer-level chip scale packages with SAC305 solder interconnects was reduced by 29% for 500 hours of aging at 150 °C. Zhang, et al. [81] have investigated the correlation between the effects of isothermal aging on the reliability of PBGA components. They have shown that for 6

months aging at 125 °C that the reliability of SAC105 components dropped by 53%. Smetana, et al. [96] have performed an extensive study on the effects of prior isothermal preconditioning (aging) on the thermal cycling lifetime for a variety of components. Similar to the investigations discussed above, it was observed that prior aging reduced the thermal cycling characteristic life of SAC BGA assemblies subjected to 0 to 100 °C cycling. It was also found that changes occurred in the Weibull slope, suggesting other failure modes were created by aging. They also found that prior aging increased the thermal cycling reliability of certain components (e.g. 2512 chip resistors and certain QFNs). Similar results of improved reliability with aging were found for components subjected to a smaller thermal cycling range of 20 to 80 °C. This led them to conclude that aging does not universally reduce solder joint fatigue life.

The effects of aging on the degradation of the thermal cycling reliability of lead free BGA assemblies have been studied recently by Zhang, et al. [81]. In their studies, PBGA daisy chain test assemblies were subjected to up to 2 years of aging (25, 55, 85, and 125 °C), followed by thermal cycling from -40 to 125 °C or -40 to 85 °C to failure. They have shown that for all component sizes and lead free solder alloys, the solder joint thermal cycling reliabilities of the BGA components were severely reduced by prior aging. For up to 12 months prior aging for the components with Im-Ag PCB surface finish and thermal cycling from -40 to 125 °C, they have observed clear degradation in life for aged components relative to non-aged components and the amount of degradation was exacerbated with higher aging temperatures. Using the 63.2% Weibull characteristic life (η) as a failure metric, the reliability was observed to decrease by 37% (6 months aging)

and 53% (12 months aging) for the 19 mm BGA components subjected to aging at 125 °C prior to thermal cycling.

Gradual aging also occurs during thermal cycling tests due to the high temperature dwells at the top of each thermal cycle. Several recent studies [97-101] have demonstrated that there is a strong dwell time effect on thermal cycling reliability for lead free electronics; with longer dwell times leading to reductions in the thermal cycling life.

2.3 Aging Effects on Creep Properties

It has been found in the literature that aging at room temperature as well as elevated temperatures have significant effects on creep deformation of lead free solder alloys. Darveaux, et al. [92] reported a faster creep rate for aged solder specimens than non-aged specimens. For both SAC305 and SAC405 solders and for aging at 125 °C for 1 day, they found 20 times increase in the creep rate for aged specimens. Xiao, et al. [66] found that SAC396 showed much lower absolute creep rates compared with eutectic Sn-Pb and ascribed this increase in creep resistance to the finely dispersed intermetallic compound (IMC) precipitates in the Sn matrix. Wiese, et al. [65, 102] investigated the creep behavior of SAC 387 solder with short (1 day at 125 °C) and long (49 days at 125 °C) thermal storage times. They found that the creep rate of solder increase significantly for short time aging at 125 C but relatively smaller changes occurred for longer aging times.

Ma, et al. [103] studied the evolution of secondary creep rate with aging for SAC305 and SAC405 solders. They showed that the secondary creep rates for SAC solders increase with aging at either room temperature or elevated temperature. Also, for both SAC solders exposed to elevated temperature aging, the effects were much higher than

those for room temperature aging. A more detailed investigation was conducted by Zhang, et al. [86] on aging effects on the creep behavior of lead free solders. They reported that for 6 months aging at 125 °C, the secondary or steady state creep rate of SAC105 solder increased by about 10000 times. Also, for other aging temperatures (25 to 125 °C), they found that the both the primary and secondary creep rates increase with 6 months aging. Finally, Cai, et al. [51] demonstrated that by using certain types of dopants in SAC solders, the aging effects on steady state creep rate can be reduced. They showed that for no aging the creep rates of doped solders were higher than SAC105 and SAC205 due to lower silver contents of the doped solders compared to SAC105. However, with 6 months aging at temperatures 25 to 125 °C, the secondary creep rates of the doped solders were smaller than the creep rates of SAC105.

2.4 Effects of Thermal Cycling on Solder Joints

In microelectronics packaging, complex stresses and strains are usually generated in the components due to the CTE mismatch of different materials. Coefficient of Thermal Expansion (CTE) mismatch between the package and the board during the cycles was considered as the dominant factor that affects the reliability of board-level solder interconnections [54, 55]. Due to the miniaturization of electronic devices along with the adoption of lead-free solder alloys [57], solder interconnection reliability has received an increasing attention during the recent years. Numerous studies have been carried out to find out the root causes of failures in electronic devices under various operation conditions. Researchers have found that the CTE mismatch between the Printed Circuit Board (PCB) which is composed of FR4 material and polymer; and the package, which is composed of

substrate, die, and mold compound, results in a thermomechanical fatigue damage of solder joints when the board- level package subjected to thermal cycling. In many cases, failure occurs due to thermomechanical shear fatigue where cracks initiate and then propagate through the bulk solder joint [61, 64-65].

2.5 Constitutive Modeling for Stress-Strain Tests

The linear elastic region in a uniaxial stress-strain curve can be modeled by Hooke's law where stress and strain are related by an elastic modulus (E). The plastic strain hardening region can be modeled by a time-independent non-linear stress-strain relationship based on either isotropic or kinematic strain hardening. Isotropic hardening assumes that the origin of the von Mises yield surface remains stationary in the stress space and the size of its yield surface expands resulting from strain hardening. In kinematic hardening, the von Mises yield surface does not change in size, but the origin of the yield surface is allowed to translate in the stress space to model strain hardening effects of increasing plastic flow stress. For solder materials, the tensile stress and strain curves are dependent on the test temperature and strain rate. The elastic modulus (E), yield stress (YS) and the tensile strength (UTS) properties vary with temperature and strain rate.

For a typical thermal cycling temperature range from -40 to 125 ^{o}C, these mechanical properties reduce with the increase in temperature. The solder material has a homologous temperature from 0.5 to 0.8 for this temperature range. Also, the creep deformation in a solder material is highly dependent on the stress and temperature state. Thus, a time-dependent elastic-plastic-creep constitutive model, or viscoplastic constitutive model, is needed to facilitate finite element modeling for simulation of solder

joint reliability during thermal cycling tests. High temperatures induce transitions in macroscopic fracture, and these transitions parallel the changes in the strength and ductility of materials [104]. Materials lose strength at higher temperatures. Hertzberg stated that the material strength increases with the testing strain rate, following a form similar to Holloman's Equation [104], where stress is related to strain rate through some strain hardening exponent.

Solder alloys possess very high homologous temperatures. The properties of solder alloys are strongly dependent on both the temperature and strain rate. Jones, et al. [105, 106] have observed an approximately linear relationship between the strength and temperature. Pang, Shi and co-workers [107] have observed similar experimental results, with a near linear relationship with temperature and a power law relation with the strain rate. Several other studies have also observed similar material behavior for both Sn-Pb eutectic and lead-free solder alloys [108-123].

The Ramberg-Osgood model describes the elastic-plastic behavior of materials, and can be used to describe to describe the stress-strain curve of solder materials [112]. In prior work, the Ramberg-Osgood model hardening exponent n and the stress coefficient σ_o were modified to be temperature and strain rate dependent. The temperature and strain-rate dependent modified Ramberg-Osgood model was also applied by Pang, et al. [112].

2.6 Constitutive Modeling for Creep

In general, the creep behavior of materials consists of three different stages: primary creep, secondary creep, and tertiary creep. In the primary creep regime, the material undergoes strain hardening, resulting in a decreasing strain rate with time. In the secondary

stage, also known as steady-state creep regime, the creep strain rate is essentially constant, showing a very slow decrease. In tertiary stage, strain rate increases with time and ultimately results in failure of the material. Solder alloys are often subjected to steady-state creep regime under typical thermo-mechanical loading conditions. Constitutive modeling of creep deformation is needed to predict the end-of-life of electronic components by using finite element analysis. A constitutive creep model is established by conducting creep tests at different temperatures and stress levels. The materials constants are important in determining the accuracy of end-of–life predictions for solder joints using finite element analysis. Large discrepancies between the creep model and experimental data would degrade the accuracy of these predictions.

The minimum creep rate may be linked with the applied stress, σ, by a series of equations according to the dominant creep mode. There are mainly three types of creep modes, namely, power law creep, exponential creep, and combination creep. Creep is highly sensitive to both applied stress level and to test temperature. As a thermally activated process, the creep rates increase exponentially with temperature. The effect of stress is dependent upon the controlling creep mechanism. The two widely used creep models are the Dorn power law model [113], and the Garofalo hyperbolic sine model [114]. In logarithmic coordinates, the Dorn power law model yields a linear relationship between the creep strain rate and applied stress for a specified temperature. Nonlinear experimental curves for creep, however, have been found over the entire stress range. The high stress regime exhibits the largest stress exponent n, and the low stress regime exhibits the smallest n value for any given temperature. This phenomenon is referred to as “power law break

down" and indicates that the Dorn model is not suitable for fitting data obtained over large stress ranges.

The Garofalo model was established for matching creep behavior at both low and high stresses. At low and medium stresses, the creep strain rate depends on stress to the power n. At high stresses, the creep strain rate is an exponential function of stress. The model is able to predict the creep deformation over intermediate temperature regimes for the entire stress range, but it underestimates the creep deformation at both low (-40 °C) and high (125 and 150 °C) temperatures.

Ma and Suhling [33] have evaluated the creep parameters in the two models for various Pb-containing and Pb-free solder alloys and found large discrepancies in the creep data for solder alloys of the same chemical composition. There are several reasons that could explain the differences, including the specimen design, variations in testing method and test conditions used by different researchers, and storage time and temperature before the creep test. Moreover, it is important to recognize that the creep behavior of bulk solder significantly differs from solder in a joint due to the effects of microstructure evolution, intermetallic compound formation, and constraint due to different methods of assembly. Since creep modeling is often to be incorporated in finite element analysis to predict the end-of-life of electronic package, the discrepancies in material constants will directly affect the accuracy of prediction.

A third widely used creep constitutive model was proposed by Weise, et al. [102], and is often referred to as the double power law. They identified two mechanisms for steady state creep deformation for the bulk and PCB samples. They attributed them to climb controlled (low stress process) and combined gliding/climbing (high stress process)

behavior and represented steady state creep behavior using two power law terms. In electronic packages, thermal mismatch induced stresses can result in extensive plastic deformation at solder joints, which is responsible for the low cycle thermal fatigue failure of solder materials. An expression for the strain was proposed by Yang, et al. [100] where total strain was divided into elastic, plastic, and creep strains.

Apart from these models, several other creep constitutive models have been proposed by researchers. Shi, et al. [101] established a unified dislocation-controlled creep constitutive model that described the creep deformation of solder alloy over a wide temperature range (-40 to 150 °C) and explained the temperature dependencies of the stress exponent n and activation energy Q. For creep strain rates at very low stress levels, they further developed a unified diffusion-controlled creep constitutive model to describe low temperature Coble creep and high temperature Nabarro-Herring creep. Clech [99] established obstacle-controlled creep models for both Pb-containing and Pb-free solder alloys. Creep deformation is impeded by discrete obstacles (phases, precipitates, grain boundaries, and other defects) distributed throughout the Sn-matrix in Sn-based solders. By taking these impeding elements into consideration, the rate-dependent obstacle-controlled creep models are able to resolve the anomalies observed in the classical analysis of creep data including stress and/or temperature dependences of activation energies and stress exponents in the Power Law or Hyperbolic Sine models.

2.7 Reduction of Aging and Thermal Cycling Effect by Dopant

Addition of 4th element in the SAC solder is known as doped SAC alloy. Dopants play an important role to control microstructure and mechanical properties of the alloy.

Dopants have been found to strongly influence the properties and behaviors of lead free solders. For example, addition of Bismuth (Bi) as a dopant has been demonstrated to have several beneficial effects. Bi helps to reduce solidification temperature, increases strength by means of precipitation hardening, and also helps to reduce IMC (Intermetallic Compound) layer thickness in lead free solder materials [123]. The Effect of Bi on the mechanical properties of a SAC (Sn3.5Ag0.9Cu) alloy was investigated by Matahir and coworkers [124]. They reported that the shear strength increased with increasing Bi addition up to 2 wt%. Beyond that point, the shear strength decreased with increasing Bi%. Improved shear strength might attribute to the role of Bi on the morphology of microstructure and distribution of dominant IMC (Ag_3Sn). Reduction of strength at higher Bi content was due to the evolution of Bi rich phase and fragmentation of the IMC. Pandher, et al. [125] also reported that addition of 2% Bi in SAC alloys improves wetting and alloy spreading.

Zhao, et al. [126] found that addition of 0.02% Ni to SAC105 increased the formation of NiCuSn IMC and reduced the localized grain size at solder/NiAu pad interface. In addition, the effects using various doped elements (i.e. Co, Fe, In, Ni, Zn and Cu) in SAC305 BGA solder joints on Cu pads were studied by Sousa, et al. [127]. They concluded that addition of low levels of Zn had a significant beneficial effect on the interfacial IMC. Lee and coworkers [128] found that micro-alloying SAC alloys with Ni and Bi improved thermal fatigue life and drop impact resistance. Yeung, et al. [129] studied a novel lead-free solder SAC_Q. Based on drop test, thermal cycling, and finite element simulation, they conclude that the doped alloy has improved board level reliability

when compared to SAC105. Additional literature publications on the effects of dopants have been reviewed in reference [51].

Sun et al. [130] reviewed the effects of different alloying elements (Mn, Fe, Bi, Ni, In, Zn, Ga, Sb, Mg), Rear Earth (RE) Elements (Ce, La, Y, Er, Pr, Nd, Yb), and nanoparticles (Al_2O_3, Al, TiO_2, ZnO, ZrO_2, CNT, Graphene, CeO_2, TiB_2, Ni-Coated CNT, Mo, SiC, $SrTiO_3$, Co) on melting temperature, wettability, mechanical properties, microstructure, interfacial reaction and Sn whiskers.

For SAC305 solder, average width of eutectic region was found as 6.8±2.8 μm and grain size of β-Sn was 24.8±5.9 μm. Indium (In), helps to refine IMC and Sn-rich phase as well as makes the microstructure more uniform. Titanium (Ti) can significantly reduce Sn grain size and width of eutectic region by heterogeneous nucleation of IMC's. Iron (Fe) forms large $FeSn_2$ IMC which has a weak interface with β-Sn matrix. Magnesium (Mg) helps to coarsen eutectic region. Addition of Al in SAC105 refines β-Sn dendrites and enlarge eutectic regions. Besides, it also prevent Ag_3Sn and Cu6Sn5 and forms two new IMC Ag_3Al and Al_2Cu. Zn also helps to refine β-Sn dendrites significantly. Ni was found to reduce the size of Sn-rich phase and refine the microstructure. Since Antimony (Sb) has higher affinity towards Sn, presence of Sb reduces the driving force to form Cu-Sn IMC's resulting a narrow IMC layer in the solder joint. Sb also helps to refine IMC grain size.

RE elements can significantly refine the microstructure of SAC solders. Er can reduces the particle size of Ag_3Sn and Cu6Sn5 whereas Pr and Nd refine β-Sn dendrites and IMC particle size by forming uniformly dispersed fine $RESn_3$. These fine particles act as heterogeneous nucleation sites during solidification. However, excessive amount of RE

elements will cause to form bulk $RESn_3$ phase which has a negative effect on mechanical properties. La, Ce, and Y also have a similar effect on solder microstructure.

Al and Ni nanoparticle was found to reduce IMC particle size, spacing and IMC layer thickness by forming very fine and uniformly dispersed Sn-Ni-Cu and Sn-Sg-Al IMCs. Addition of small amount of Fe nanoparticles refine the microstructure and forms $FeSn_2$ phase. Al_2O_3 nanoparticles increase the size of eutectic region and reduce Ag_3Sn particle size. TiO_2 and SiC nanoparticle reduces the size and spacing between Ag_3Sn particles. $SrTiO_3$ nanoparticle reduces the size of Ag_3Sn and Cu6Sn5 particles by promoting the rate of nucleation during solidification. ZnO suppresses Ag_3Sn and Cu6Sn5 IMC formation and reduces β-Sn grain size by 22%.

The effect of dopants on the aging induced changes in microstructure was also studies by a number of scientists. Sadiq et al. [131] worked with different Lanthanum (La) doped SAC305 alloys and recorded the changes in microstructure and mechanical properties during isothermal aging at 150 °C for 6 different aging conditions (i.e. 0 , 10, 25, 50, 100 and 200 hours). They reported that La drastically reduces the IMC particle size and also significantly inhibit the growth of IMC particles during isothermal aging. Based on polarized light image they found that in as cast condition, grain size of SAC305 was ~8 mm and was significantly reduced (~1 mm) after La addition. From the graph presented in that paper, it is also clear that aging doesn't have any significant influence in average grain size.

In another study, Lee et al. [132] studied the effect of Lanthanum (La) addition and high temperature storage on the microstructure and microhardness of Sn-3.5Ag solder joints. Their experimental results confirms that addition of La refine the solder

microstructure. They explained that during solidification of the solder, $LaSn_3$ compounds form at the beginning and provide extra nucleation sites for Ag_3Sn IMC to grow resulting a refine microstructure. Addition of La was also found to reduce the thickness of IMC layer after soldering as well as isothermal aging. They also reported that La addition helps to improve microhardness and thermal resistance of solder joints.

Hao et al. [133] studied the effects rare earth element Er addition on the evolution of microstructure of lead free eutectic SAC (Sn-3.8Ag-0.7Cu) solder joints during isothermal aging. Aging was conducted at 170 °C for 4 different holding periods (i.e. 0, 200, 500 and 1000 hours). The authors measured the thickness of IMC layer of Sn-3.8Ag-0.7Cu and Sn-3.8Ag-0.7Cu-0.15Er alloy after different aging duration. They found that Er addition reduces the thickness of IMC layer in as reflowed condition and also significantly reduces the growth during aging. They argued that Er combines with Sn to form $ErSn_3$ IMC and reduces the activity of Sn which subsequently suppress the formation of Cu6Sn5 IMC layer. They also observed that $ErSn_3$ IMCs formed during solidification of solder act as a heterogeneous nucleation site for Ag_3Sn and Cu6Sn5 precipitates. The increase in nucleation sites results a refinement of Ag_3Sn and Cu6Sn5 particles. Addition of Er also found to make the microstructure more uniform and reduce the coarsening rate of the IMCs during isothermal aging.

Witkin [134] and Delhaise et al. [135] studied the effect of aging of Bi doped SAC alloys. In both study, the authors reported an elimination or at least reduction of aging induced degradation in SAC-Bi alloys.

2.8 Role of Intermetallic in Solder Interconnects

Intermetallic compounds (IMCs), which form at the interface between the solder and its bonding pad (Cu), play significant role in the integrity of the solder joint, especially when suffering high strain rate deformation and hence affect the reliability of electronic packages. For instance, portable electronic devices that are popular these days could undergo accidental shock loading, and the fracturing of solder joints subjected to drop impact generally occurs at IMCs which are very brittle in nature [136]. Deng [137] suggested that the damage criteria in the solder joints is regulated by competing mechanisms of solder-controlled plastic deformation at low strain rates, to the brittle failure (fracturing) of interfacial IMCs at high strain rates. Based on researches into the mechanical drop behavior of different solder and metallization combinations, Gao, et al. [138] proposed that the main failure mechanism under mechanical shock loading may be related to the high deformation rates and strain-rate hardening of the solder alloys which actually forces cracks to propagate in the IMC layers instead of the bulk solder. Hence, fracture through the brittle intermetallic layers is often identified as a common mechanism for early failure of microelectronic solder joints. Formation of IMC layers occur at solder/metal interface due to diffusion of different materials (i.e. Sn, Ag, Cu, Ni, Zn etc.) during the soldering reflow process [139-142]. Most IMCs at metal pad interfaces are found to be tin-based binary or ternary compounds of which most common are Cu6Sn5 or CuNi-Sn intermetallics. Due to the isothermal aging, these IMC layers grow in thickness which adversely affect the overall life of SAC solder joints [138]. Additionally, usage of lead-free solders has been shown to produce intermetallic particle formations in the solder joint bulk. Several morphologies not commonly observed in Pb-Sn soldering can be

present, including Ag_3Sn needles and particles that may span an entire solder joint. These particles coalesce and also become larger over time during exposure of the solder joint to isothermal aging [143-145]. Dopants are now added in solder materials [141] which are found effective to reduce the IMC growth and results in improved reliability of solder materials. Understanding the mechanical properties of IMCs and increased knowledge about their behavior in different operating conditions becomes desirable since the microelectronics industry has been facing significant challenges with these IMCs. The size of devices and solder joints are continuously decreasing, and, hence, the IMCs are occupying a key volume fraction of the entire package. Besides, electronic packages are now subjected to harsh operating conditions (i.e. extreme temperature). Understanding of the mechanical properties of these individual phases at various operating conditions makes predictions of the mechanical behavior of an overall joint more straightforward. Efforts are also being made to perform reliability analysis from finite element modeling of solder joints at the microstructural level [143-145]. These investigations provide the necessary input data for mechanical properties while performing finite element analysis. It gives the potential to simulate the influence of microstructure (which includes the IMCs) on the strength and reliability of solder joints.

2.9 Study of Individual Phases of SAC Solder Joint

Single solder joint consists of various phases i.e. (β-Sn,eutectic phase, IMC particle/layer). Most of the studies deal with the overall/global property of the solder alloy [138], which were found to decrease with aging [19-142]. The primary reason was considered as the coarsening of the IMC particles in the bulk solder region. However, very

few studies were performed to measure properties of small individual phases (β-Sn, Eutectic phase, IMC particle/layer) [138-139]. Moreover, systematic study to measure properties of these small phases due to isothermal aging were not studied much. In addition, it was not understood whether these phases could possibly degrade with aging and contributes to the overall degradation of the solder joint. Measurement of the mechanical properties of individual phases in a solder joint is now possible using an instrumented indentation technique commonly known as nanoindentation. This nanoindentation technique has now received a great attention to researchers as valuable method for obtaining the mechanical behavior of materials at very small scales by probing, i.e. it has capability to measure the properties of materials in very thin films and coatings [140-142]. This technique is well suited to investigate mechanical properties of solder joints and IMC particles that exist in bulk solder region [140-145]. Testing with this tool can be done to probe small volumes by utilizing a diamond indenter tip attached to a sensitive capacitive transducer, which is operated at ultralow load (e.g., 0.1–10 mN). Throughout the testing load and displacement of the tip are measured which allows the user to determine elastic modulus from the unloading curve. It also gives measurement of hardness by calculating depth at the maximum load point.

2.10 Nanoindentation on SAC Solder Joints

Most prior work on solder mechanical behavior and aging effects has involved tension, compression, and shear testing of miniature bulk solder specimens. Sample geometries have included traditional uniaxial tensile specimens, small cylinders in compression, lap shear specimens, and Iosipescu shear specimens. A more limited number

of researchers have examined aging effects by mechanical loading of solder joints [57, 64, 65, 92]. These studies have involved shearing of custom fabricated solder ball arrays [64, 65, 92], as well as impression creep experiments [57].

Nanoindentation techniques [40] have recently become popular for measuring mechanical properties and creep deformation behavior of extremely small material samples, and several investigators [75, 136-148] have applied them to lead free solders. Early solder nanoindentation studies included room temperature measurements of the elastic modulus E and hardness H of β-Sn dendrites, eutectic phases, and individual Ag_3Sn and Cu6Sn5 intermetallic compounds [136, 137, 146, 148]. Hasnine et al. [75, 140-142], have examined aging effects in SAC solder joints extracted from PBGA assemblies using nanoindentation. Their results showed that the aging induced degradations of the room temperature mechanical properties (modulus, hardness) of single grain SAC joints were of similar magnitudes to those seen previously by testing of larger "bulk" solder specimens with hundreds of grains. However, the degradation of the creep response, while still significant (15-100X increase), was less in the solder joints relative to larger uniaxial tensile specimens (200-7500X increase). This was due to the single grain nature of the joints considered, and the lack of the grain boundary sliding creep mechanism. They also tested very small tensile specimens (10 mm long) with 10-20 grains, and the creep degradation results were similar to the single joint specimens.

Knowledge of elevated temperature behavior, especially creep behavior, is critical to understanding solder joint reliability in thermal cycling and accelerated life testing. Elevated temperature nanoindentation measurements of modulus and hardness of bulk SAC305 and SAC357 solder samples were performed by Gao, et al. [138], and Han and

coworkers [139]. In addition, the latter authors also examined the sensitivity of the creep response of lead free solder to temperature. Sadiq, et al. [147]have investigated the nanoindentation elastic modulus and hardness of β-Sn and eutectic phases within a SAC305 solder joint at temperatures ranging from 45-85 °C. Another solder nanoindentation study over a larger temperature range (25-150 °C) was performed by Lotfian, et al. [143], where they reported the mechanical properties of the constituent phases of SAC397 solder joints. Marques, et al. [144, 145] used nanoindentation to study mechanical properties and creep behavior of SAC305 solder joints over a wide temperature range (25-175 °C). Based on finite element simulations, they also developed a method to correlate nanoindentation creep results with uniaxial creep data.

2.11 PBGA Package Materials and their Mechanical Behavior

One of the mostly used electronics packages is PBGA package technology in semiconductor industry. This PBGA technology has been proven as one of the most popular packaging solutions which have many advantages in thermoelectro-mechanical reliability, performance, and cost effectiveness. A typical PBGA package consists of different component materials, e.g. solder interconnect, silicon die, die attachment adhesive, mold compound, and solder mask. All these package materials play an important role in the reliability of the BGA assembly. Many researchers have studied these materials and their behaviors in the PBGA package. However, the packages studied by researchers mostly were based on their as prepared condition. During operation, the materials might change their mechanical behavior, which could significantly impact the reliability and if not taken into consideration cause the failure of the electronic package in the long run.

Hence, it is important to understand the evolution of the mechanical behavior of these individual PBGA component materials during operation. Solder interconnects have been considered as one of the most important component in PBGA packages in recent years which we have described earlier [149-160]. A solder mask is typically a thin polymer layer in the package which is often is seen as the green colored outer layer on the printed circuit board. It prevents forming oxidation and helps in resisting solder bridges between copper pads. This solder mask layer covers a significant area, and hence finding the mechanical properties of solder masks is very important for getting high interconnect reliability during operation. Zhu et al. worked on different solder mask materials and showed their mechanical properties and creep response [161]. Chowdhury et al. [162] studied solder mask material mechanical property under different temperatures and various durations of UV exposure. Their study showed elastic modulus and ultimate tensile strength drops with temperature and increases with UV exposure. Die attachment materials are used to attach silicon die to as substrate beneath. Die attach materials have two key functions 1) conducting heat away from the die, and 2) mechanical fixation of the die onto the substrate. Researchers have been studying different die attach materials specially suitable at high temperature applications and sustainable in harsh environments. Siow and Chua [163] studied silver sintered joints as die attach materials, and measured their shear strengths under thermal cycling conditions. They found out that the shear strength of the sintered die attach material drops with the number of thermal cycles. Researchers have also studied die attach and silicon die mechanical behavior during environmental harsh exposures. Chen and coworkers [164] measured die stress during exposure of a PBGA package to various

moisture conditions. They found out that die stress increases with moisture exposure time and severe moisture exposure causes higher die stress.

2.12 Summary

In this chapter, the existing literature on the effects of aging and thermal cycling on the mechanical properties and the microstructure of lead free solder and various materials in PBGA packages was extensively discussed. The mechanical properties of a solder are strongly influenced by its microstructure, which is controlled by its thermal history including its solidification rate and thermal exposures after solidification. Aging and thermal cycling of lead free solders leads to degradations in their mechanical and failure behaviors. For example, research in the literature has shown that aging and thermal cycling leads to large reductions in solder material properties including shear strength, elastic modulus, nanoindentation joint modulus and hardness, high strain rate mechanical behavior, creep response. Other studies have shown that aging causes severe degradations in uniaxial cyclic stress-strain curves and fatigue life, shear cyclic stress-strain curves and fatigue life, fracture behavior, drop reliability, and thermal cycling reliability.

Dopants have been found to strongly influence the properties and behaviors of lead free solders. For example, Bi helps to reduce solidification temperature, increases strength by means of precipitation hardening, helps to reduce IMC (Intermetallic Compound) layer thickness, and also reduce aging induced degradation of mechanical properties in lead free solder materials. Ni helps to improve thermal fatigue life and drop test performance by refining Sn grain size and reducing the IMC layer formation near the Cu pad. The effects

of rear earth (RE) elements and nanoparticle addition on the properties of lead free solder was also discussed in this chapter.

Nanoindentation methods have shown great potential for characterizing solder materials and its individual phases to observe temperature, aging and temperature cycling effects at the joint scale. Nanoindentation is mainly used to extract elastic modulus and hardness of solder joints. Many of the prior works have also used nanoindentation technique to characterize the creep properties although most of the nanoindentation experiments, on solder joints, were conducted at room temperature.

The changes in solder mechanical behavior are a result of the evolution of the SAC solder microstructure that occurs during aging. The most well-known and widely observed changes are coarsening of the Ag_3Sn and Cu_6Sn_5 intermetallic compounds (IMCs) present in the eutectic regions between beta-Sn dendrites. Several researchers have proposed empirical models to describe the growth of these secondary phase particles as a function of aging temperature and aging time, and related this growth to mechanical property changes.

CHAPTER 3

EXPERIMENTAL PROCEDURE

3.1 Introduction

The specimen preparation and testing techniques are presented in this chapter. Micro-scale uniaxial tensile specimens were prepared in a rectangular shaped hollow glass tube using a vacuum suction method. The test specimens were then cooled either by a water quenched profile or an industry standard reflow profile. Typical dimension of the uniaxial tensile specimens were 80 (length) X 3 (width) X 0.5 (height) mm. Uniaxial tensile tests were performed using a micro tension torsion testing system.

Solder joints were typically extracted from 14 x 14 mm PBGA assemblies (0.8 mm ball pitch, 0.46 mm ball diameter) that are part of the iNEMI Characterization of Pb-Free Alloy Alternatives Project. For solder joint individual phase and thermal cycling study, samples were extracted from package boards obtained from department of defense. SuperBGA solder joint was used for individual phase study with following specifications: 31 x 31mm package, 304 balls, 0.8 mm ball diameter, and 1.27 mm ball pitch. For thermal cycling study, lead-free solder joints were obtained from plastic ball grid array (PBGA) assemblies (Amkor CABGA) with following specifications: 17 x 17 mm, 256 balls, 0.5 mm ball diameter, and 1 mm ball pitch. Solder alloy considered was SAC305 (97.5Sn-3.0Ag-0.5Cu).

After extraction, a typical sample mounting and polishing procedure was followed to make the solder joints suitable for nanoindentation tests. Since the properties of SAC solder joints are highly dependent on crystal orientation, polarized light microscopy techniques was utilized to determine the orientation of the tested joints. For all the experiments, only single grain solder joints were used to avoid introducing any unintentional variation from changes in the crystal orientation across the joint cross-section.

3.2 Uniaxial Test Sample Preparation

Initially, bulk solder material is melted in a quartz crucible using circular heating elements (see Figure 3.1). The heater in the melting process is excited using a digital controller, which uses feedback from a thermocouple attached on the crucible. The solder is drawn into the glass tube by inserting one end into the molten solder in the crucible, and then applying suction to the other end using a rubber tube connected to a vacuum source. The amount of solder drawn into the tube is controlled using a regulator on the vacuum line. After the desired amount of solder fills the tube, it is solidified by quenching in a room temperature water bath.

Tensile specimens were prepared using two different solidification profiles.

1) Water quenched (WQ) solidification profile, leading to fine microstructures and the upper limits of the mechanical properties for each alloy.

Reflowed (RF) solidification profile, leading to a coarse microstructure very similar to an actual solder joints. The solder test specimens were passed through a controlled heating and cooling chamber using a SMT (surface mount technology) reflow oven. The

temperature vs. time variations for the WQ profile is shown in Figure 3.2. For the samples with reflowed profile, test specimens were initially prepared using WQ profile and then the samples within the glass tubes were sent through a 9 zone Heller 1800EXL reflow oven (Figure 3.3).

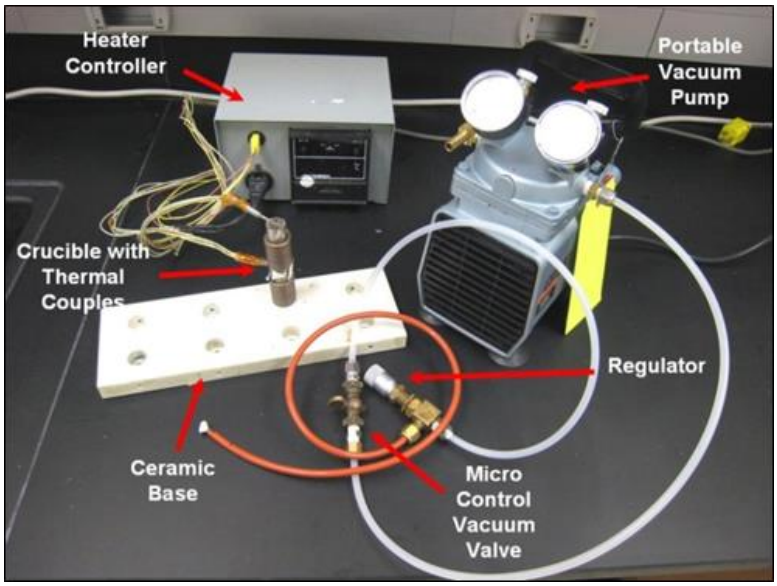

Figure 3.1 Equipment used for Specimen Preparation

2)

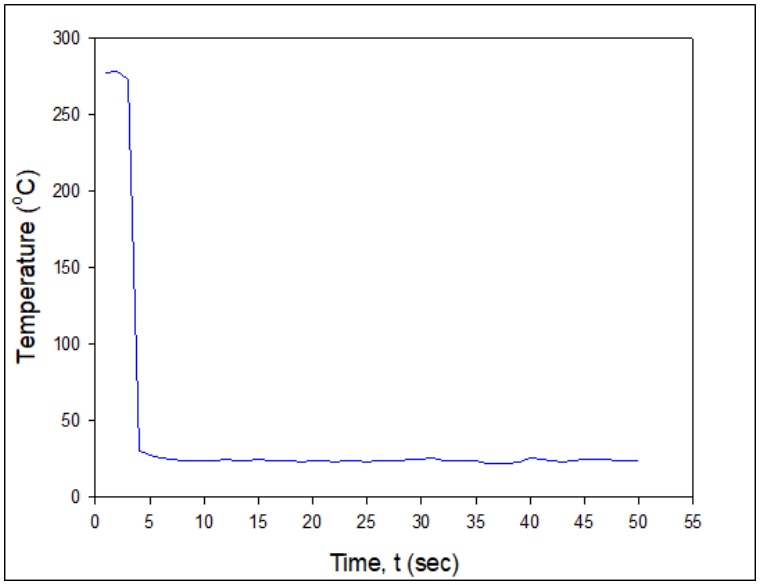

Figure 3.2 Water Quenched (WQ) Cooling Profiles

Figure 3.3 Heller 1800EXL Reflow Oven

Inside the oven, solder samples were re-melted and experienced to a pre-set temperature profile which is very similar to that used for the actual solder joints. The reflow temperature profile used in this study is presented in Figure 3.4.

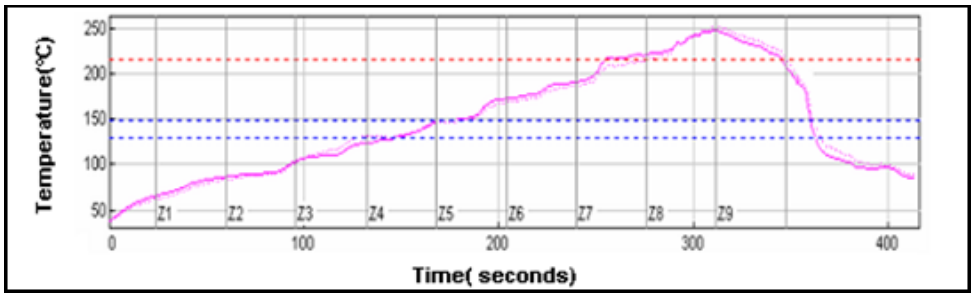

Figure 3.4 Reflow (RF) Cooling Profiles

A typical glass tubes filled with solder and final solder samples after extraction from the glass tubes are shown in Figure 3.5. Glass has lower coefficient of thermal expansion (CTE) compared to solder. As a result, for some solder alloy and cooling rate

combinations, solidified solder samples were easily pulled out from the glass tube due to the difference is the CTE of glass and solder. Another way followed to extract the solder sample from the glass tube is by carefully breaking the glass. The tubes in this work had a length of 120 mm, and a cross-sectional area of 3.0 x 0.5 mm. A thickness of 0.5 mm was chosen since it matches the height of typical BGA solder joints. The nominal dimensions of the final test samples were 80 x 3 x 0.5 mm. The specimens were stored in a low temperature freezer after the water quenched/reflow process to minimize any aging effects. The solder microstructure has been verified to be consistent throughout a specimen volume, and from specimen to specimen by cross-sectioning. A micro-focus x-ray system was used to inspect the samples for the presence of flaws (e.g. notches and external indentations) and/or internal voids (non-visible). Specimens with no flaws and voids were generated using proper experimental techniques, and Figure 3.6 illustrates x-rays scans for good and poor specimens.

(a) Within Glass Tubes

(b) After Extraction

(c) Cross-Section

Figure 3.5 Solder Uniaxial Test Specimens

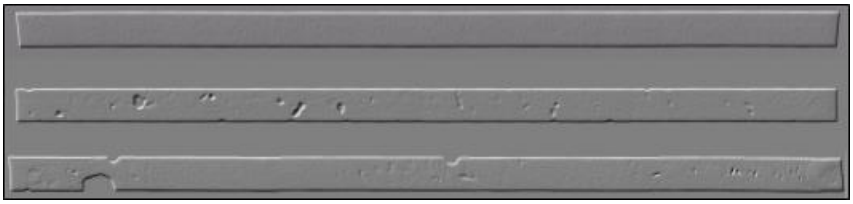

Figure 3.6 X-Ray Inspection of Solder Test Specimens (Good and Bad Samples)

3.3 Uniaxial Tensile Testing System

The tension/torsion thermo-mechanical test system (Wisdom Technology MT-200) used to perform the stress-strain tests in this study is presented in Figure 3.7. This instrument is optimized for loading small specimens such as thin films, solder joints, gold wire, fibers, etc. It provides an axial displacement resolution of 0.1 micron. Samples can be tested over a temperature range of -185 to +300 °C using supplemental environmental chambers added to the system. However, the high temperature system has been calibrated to accurately control the specimen temperature. Appendix A.1 represents the variation in set temperatures and specimen temperatures. The calibrated temperature table has also been included in Appendix A.1.

(a)

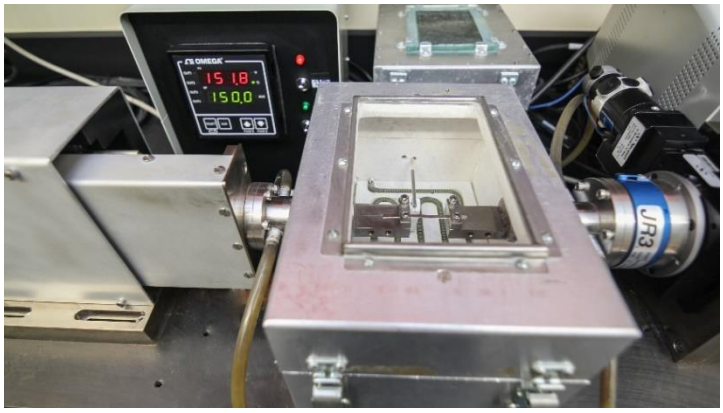

(b)

Figure 3.7 Mechanical Test System with Uniaxial Sample

Forces and displacements were measured in the uniaxial tests, and the axial stress and axial strain were calculated using

$$\sigma = \frac{F}{A} \qquad \varepsilon = \frac{\Delta L}{L} = \frac{\delta}{L} \tag{3.1}$$

Where, F is the measured uniaxial force, δ is the measured crosshead displacement, σ is the uniaxial stress, ε is the uniaxial strain, A is the original cross-sectional area, and L is the chosen specimen gage length (initial length between the grips). The gage length of the specimen was kept as 60 mm (thus the length to width ratio was 20 to 1).

3.4 Typical Testing Data and Data Processing

3.4.1 Typical Test Data

A typical SAC solder tensile stress strain curve is illustrated in Figure 3.8. The standard material properties are labelled on the graph including the effective elastic modulus E (initial slope of the stress-strain curve). This effective modulus is rate dependent since solder behavior is viscoplastic. The value of the effective modulus will

become the true elastic modulus as the testing speed is increased to the limit of infinite strain rate. The yield stress σ_Y (YS) is defined using the typical definition of the stress level that results in a permanent strain of $\varepsilon = .002 = 0.2\%$ upon unloading. The maximum (saturation) stress on the stress-strain curve is the ultimate tensile strength σ_u (UTS). As shown the figure, the stress-strain curve for the solder material has an elastic region at the beginning, a small transition region followed by a plastic region. As the strain becomes significantly high, localized deformation takes place which is also known as necking. Necking causes a visible reduction in cross-sectional area and a drop in the applied load, near the end of the stress strain curve, leading towards a rupture.

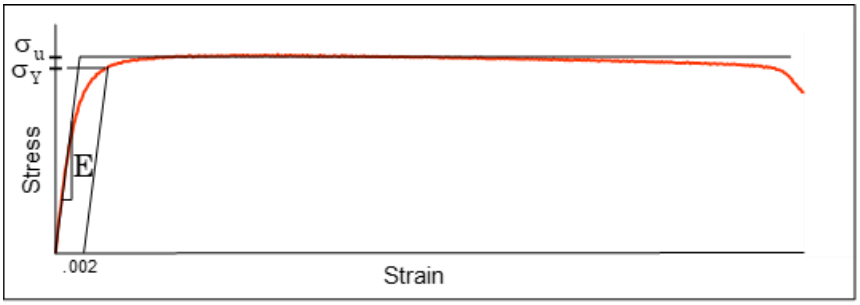

Figure 3.8 SAC Stress-Strain Curve and Material Properties

3.4.2 Stress-Strain and Creep Data Processing

Figure 3.9 illustrates a typical set of 5 solder stress strain curves measured for the same alloy under similar environmental and aging conditions. In this work, a four parameter hyperbolic tangent empirical model

$$\sigma = C_1 \tanh(C_2\varepsilon) + C_3 \tanh(C_4\varepsilon) \tag{3.2}$$

has been used to represent the "average" stress-strain curve through a set of experimental data (red curve in Figure 3.9). Material constants C_1, C_2, C_3, and C_4 are determined through regression fitting of the model to experimental data. The effective elastic modulus E at zero strain is calculated from the model constants using

$$E = \sigma'(0) = C_1 C_2 + C_3 C_4 \tag{3.3}$$

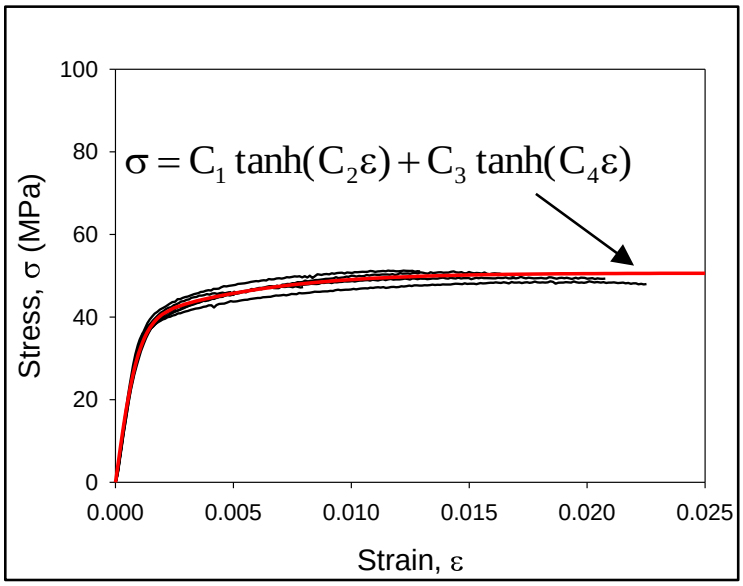

Figure 3.9 Empirical Model Fit to Solder Stress-Strain Curves

For the creep testing, 5 constant load/stress tests were performed for each leg of the test matrix. The four parameter Burger's (spring-dashpot) model given by

$$\varepsilon = C_0 + C_1 t + C_2 (1 - e^{-C_3 t}) \tag{3.4}$$

was used to fit the average raw experimental data, where C_0, C_1, C_2, and C_3 are fitting constants. Constant C_1 represents the "steady state" creep strain rate.

3.5 Microstructure Study

For microstructure analysis, the fabricated solder samples were cut into small pieces and potted in epoxy. Details of the preparation process included mechanical grinding with several SiC papers (#320 to #400, #600, #800 and #1200) in a rotating metallographic disc as shown in Figure 3.10. The final polishing was conducted with 0.02 μm colloidal silica suspensions (BUEHLER MasterMet 2) and BUEHLER ChemoMet polishing cloth. This procedure resulted in mirror finish samples suitable for optical microscopy, Scanning Electron Microscopy (SEM), as well as nanoindentation. Microstructure analysis of the solder alloys was performed on the mounted and polished testing coupons by using an OLYMPUS BX60 Optical Microscope (Figure 3.11), Zeiss Polarized Light Microscope (Figure 3.12), and a JEOL JSM 7000F Field Emission SEM (Figure 3.13). In addition, EDS (Energy-Dispersive X-ray Spectroscopy) was employed to explore the chemical composition of different phases in the microstructure.

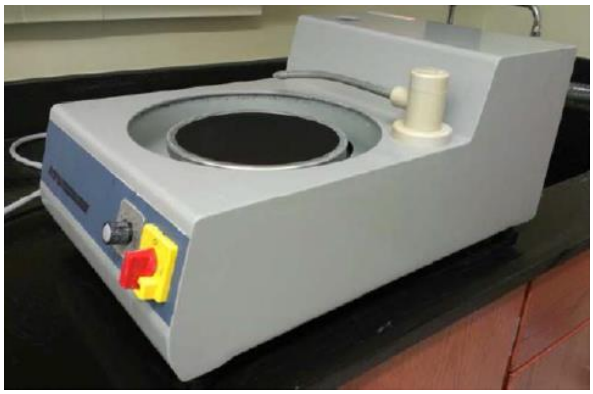

Figure 3.10 Grinding and Polishing Machine

Figure 3.11 OLYMPUS BX60 Optical Microscope

Figure 3.12 Zeiss Polarized Light Microscope

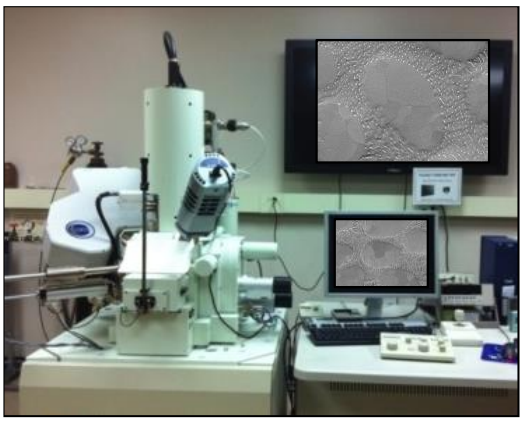

Figure 3.13 JEOL JSM-7000F Field Emission SEM

3.6 Nanoindentation Method for Mechanical Behavior and Creep Tests on Solder Joints

3.6.1 Sample Preparation for Nanoindentation

SAC305 (96.5Sn-3.0Ag-0.5Cu) lead free solder joints were extracted from PBGA assemblies (Amkor CABGA, 14 x 14 mm, 192 balls, 0.8 mm ball pitch, 0.46 mm ball diameter) that were assembled for the iNEMI Characterization of Pb-Free Alloy Alternatives Project (Figure 3.14). Prior to cross sectioning, the PBGA test assemblies were stored in a freezer at T = -10 °C to minimize any aging effects after board assembly. The assembled PBGA components were cut out from the test boards and then cross-sectioned using BUEHLER IsoMet 1000 Precision Cutter (Figure 3.15). The maximum allowable sample height is around 3 mm, which impose a restriction of using an epoxy mounted sample inside the high temperature stage. As a result, an alternative approach was developed to polish solder joint samples without any epoxy encapsulate. As shown in Figure 3.16, cross-sectional samples were mounted on a cylindrical epoxy preform by double-sided tape to facilitate polishing. The polished solder joint array cross-sections were then carefully extracted from the preform.

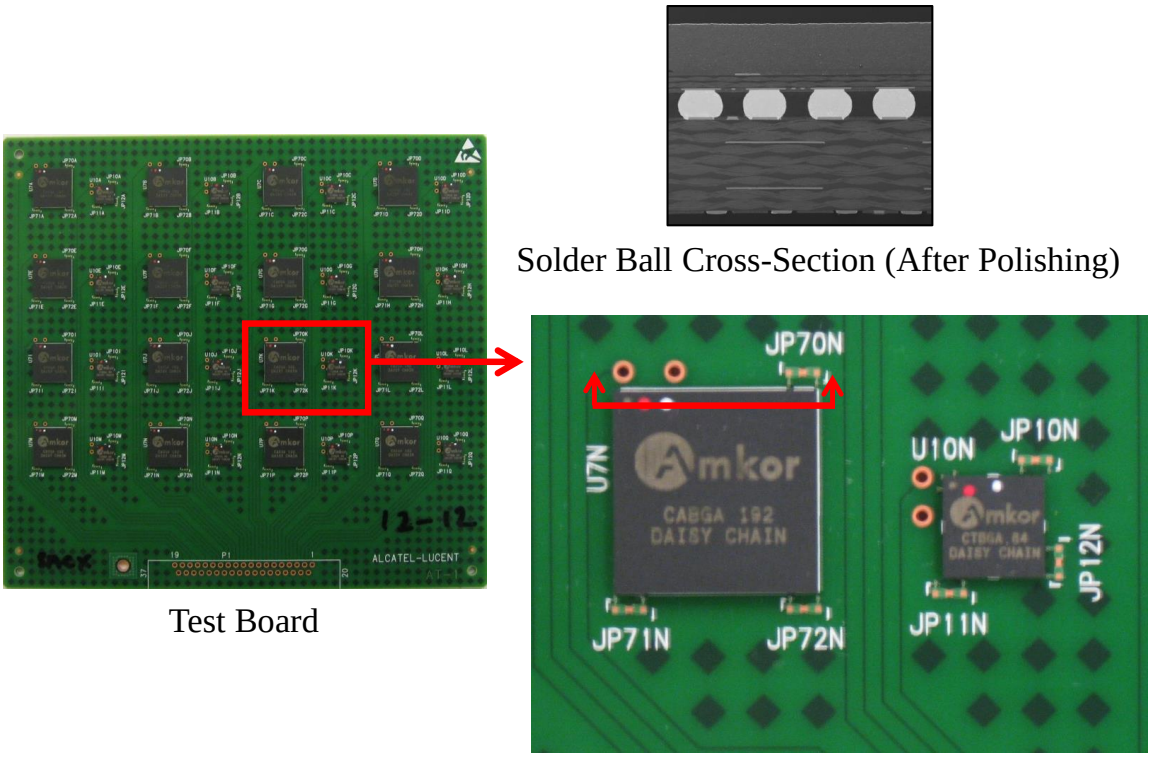

Figure 3.14 iNEMI Test Board and BGA Package

Figure 3.15 IsoMet 1000 Precision Cutter

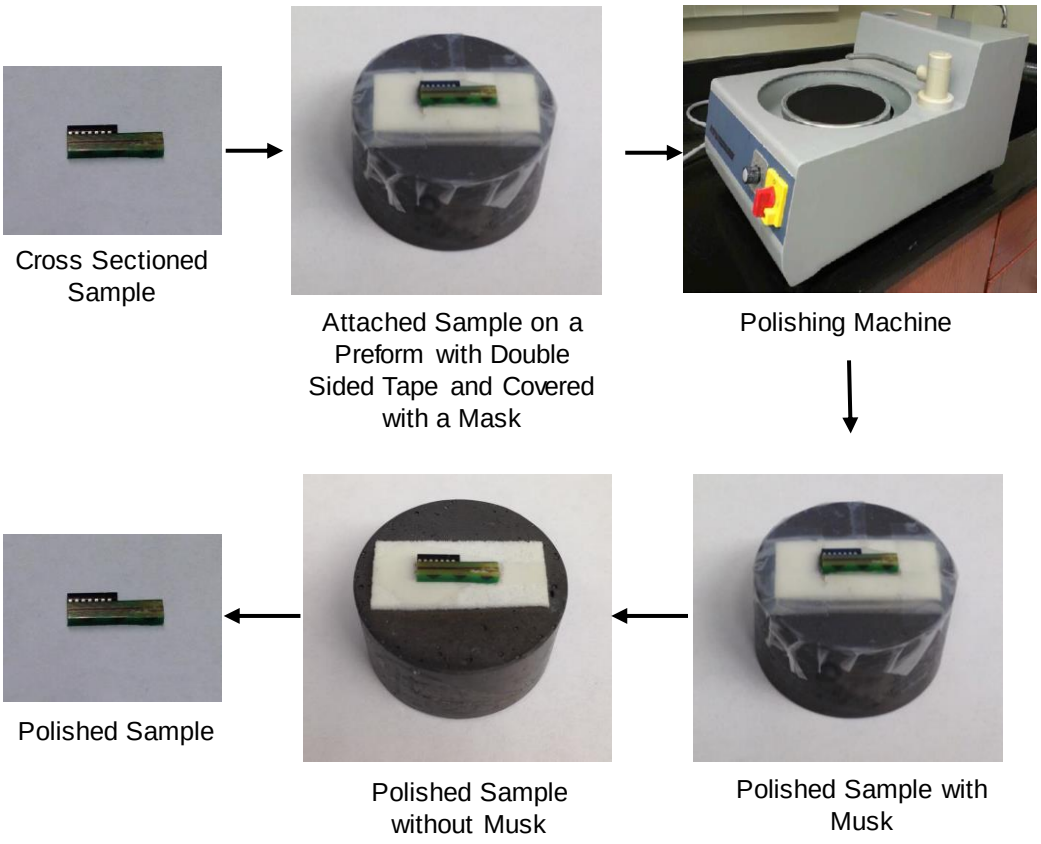

Figure 3.16 Sample Preparation Procedure for High Temperature Nanoindentation

3.6.2 Nanoindentation Machine and Test Procedures

The nanoindentation tests in this work were performed using an instrumented Hysitron TI 950 nanoindentation system (Figure 3.17) and a Berkovich indenter tip. During each indentation experiment, load versus indentation displacement response of the test samples in the direction normal to the cross-sectional surface was measured.

Figure 3.17 Hysitron TI950 TriboIndenter

Figure 3.18 shows a typical cross-sectioned SAC305 lead free solder joint sample after nanoindentation testing. A set of indents were made, and the measured test data were averaged to obtain statistically relevant results and consistency of inspection. The indents in a set were positioned at least 3b apart, where b is the width of a single indent, to avoid interactions between the plastic zones created by the indentations. Figure 3.19 shows a typical example of loading profile used during nanoindentation, for hardness and modulus testing. The loading profile has three segments 1) loading from 0 mN to peak force, 2) holding at peak force, and 3) unloading from peak force to 0 mN. Depending on the type of the test material, the different parameters in the loading profile was adjusted to get an accurate measurement.

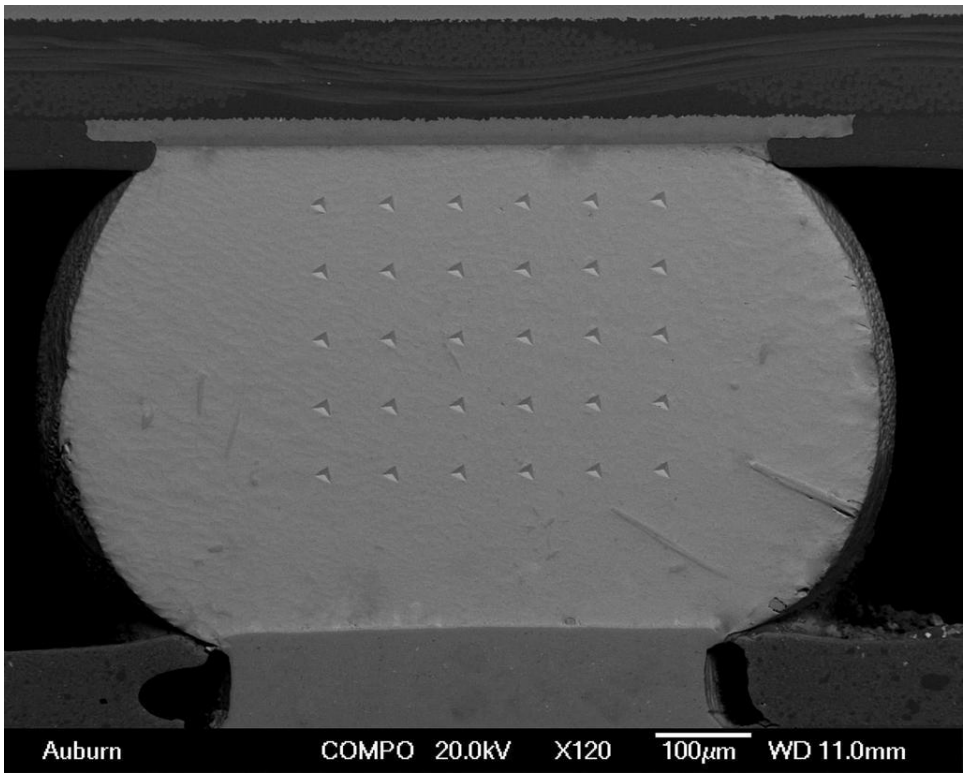

Figure 3.18 SAC305 Solder Joint after Nanoindentation Testing

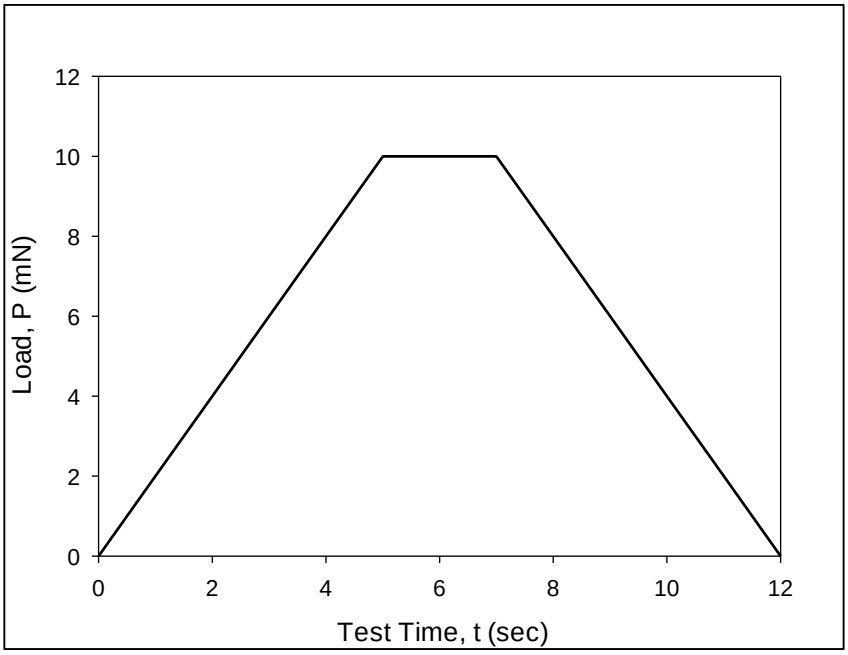

Figure 3.19 An Example of The Loading Profile Used During Nanoindentation Testing

3.6.3 Measurement of Elastic Modulus and Hardness

A typical load (P) versus displacement (h) curve, obtained after a nanoindentation test, is presented in Figure 3.20. This curve has three different segments where the first, second, and third segments represent the displacements during the loading, holding and unloading period, respectively.

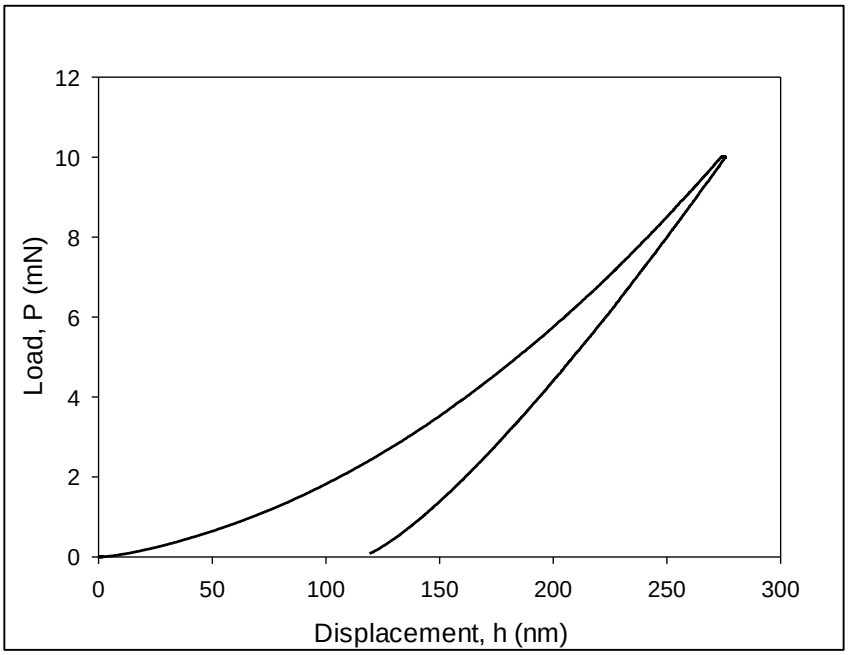

Figure 3.20 An Example of Load-Displacement Curve Obtained After Nanoindentation Test

During a nanoindentation experiment, the effects of the non-rigidity of an indenter, during a nanoindentation experiment, can be addressed by introducing a term called reduced modulus (E_r) through the following equation:

$$\frac{1}{E_r} = \frac{(1- \nu^2)}{E} + \frac{(1- \nu_i^2)}{E_i} \tag{3.5}$$

where E is the elastic modulus of the test specimen, E_i is the known elastic modulus of the indenter tip material, ν and ν_i are the Poisson's ratio of the test specimen and the indenter tip, respectively. Typically reduced modulus was measured from an indentation experiment using the following equation

$$E_r = \frac{\sqrt{\Pi}}{2} \cdot \frac{S}{\sqrt{A}} \tag{3.6}$$

Where S is the stiffness of the test specimen at the maximum load and A is the projected contact area at the maximum load. Stiffness was determined from the initial slope $(\frac{dP}{dh})$ of the unloading segment of a load displacement curve. The contact area A was measured following the technique proposed by Oliver and Pharr [165] where they assumed the contact area to be a function of contact depth. For an ideal Berkovich tip, it can be expressed as

$$A(h_c) = 24.5h_c^2 \tag{3.7}$$

In order to address any deviation from the ideal Berkovich geometry due to tip blunting, a modified version of Equation 3.7 was utilized.

$$A(h_c) = 24.5h_c^2 + C_1h_c^1 + C_2h_c^{1/2} + C_3h_c^{1/4} + C_4h_c^{1/8} + C_5h_c^{1/16} \tag{3.8}$$

Where C_1, C_2, C_3, C_4, and C_5 are fitting constants. In order to determine the values of these constants, multiple indents were made at multiple depths on a quartz sample with known elastic modulus (69.6 GPa). The contact areas at the different known depths were determined from Equation 3.7 and these values were plotted to get a A versus h_c plot. The values of constants C_1 to C_5 were determined by fitting the plot by Equation 3.8. Once the values of the constants are known for a particular tip geometry, Equation 3.6 was used to

determine the value of reduced modulus (E_r) for any unknown material and Equation 3.5 was used to convert E_r to elastic modulus E.

Hardness is a material property that defines the resistance of the surface against plastic deformation. During a nanoindentation experiment, hardness H was determined by dividing the maximum load by the projected contact area.

$$H = \frac{P_{max}}{A} \tag{3.9}$$

Tabor [166] developed an approximate relationship between hardness and yield stress of which is true for many metals.

$$H \approx 3\sigma_Y \qquad \text{or} \qquad \sigma_Y \approx \frac{H}{3} \tag{3.10}$$

The above equation was used to determine stress during nanoindentation experiments.

Nanoindentation creep testing was performed during the hold/dwell at the constant peak load. The total indentation displacements were measured continuously, from which the creep displacement during the constant load period were extracted. The creep displacement experimental data can be fit well with various empirical models. In this work, the following log hyperbolic tangent model was chosen for fitting the raw data:

$$h = C_1 \ln(1 + t) + C_2 \tanh(C_3 t) + C_4 t + C_5 \tag{3.11}$$

Where C_1, C_2, C_3, C_4 and C_5 are fitting constants, h is the indentation displacement and t is dwell time.

The creep deformation rate (creep rate) can be determined by taking the derivative of the creep displacement vs. time response. The creep deformation rate can be found from following:

$$\dot{h} = \frac{dh}{dt} \tag{3.12}$$

Using the fitting curve from Eq. (3.12), this deformation rate can be easily evaluated as a function of time. Mayo and Nix [167-168] developed the concept of indentation creep strain rate and defined it by dividing the creep deformation rate (found from eq. (3.12)) by the instantaneous creep deformation at each time

$$\dot{\varepsilon} = \frac{1}{h}\frac{dh}{dt} \tag{3.13}$$

Yield stress can be found from hardness value by the Tabor Relationship.

$$\sigma_Y \approx \frac{H}{3} \tag{3.14}$$

3.7 Summary and Discussion

All the experimental procedures and the data processing steps were presented in this chapter. Micro-scale uniaxial tensile specimens were prepared in a rectangular shaped hollow glass tube using a vacuum suction method. Typical dimension of the uniaxial tensile specimens were 80 (length) × 3 (width) × 0.5 (height) mm. Uniaxial tensile tests were performed using a micro tension torsion testing system. Nanoindentation experiments were conducted on actual solder joints which were typically extracted from 14 x 14 mm PBGA assemblies (0.8 mm ball pitch, 0.46 mm ball diameter). Nanoindentation experiments were performed using Hysitron TI950 TriboIndenter.

Nanoindenter can be used to indent vary small volume element to extract various mechanical properties like elastic modulus and hardness.

CHAPTER 4

HIGH TEMPERATURE MECHANICAL BEHAVIOR OF SAC AND SAC+X LEAD FREE SOLDERS

4.1 Introduction

Prolonged exposures of lead free solders at high temperatures will cause aging effects, which involve evolution (coarsening) of the intermetallic compound (IMC) particles in microstructure resulting in further degradations of their mechanical properties [169]. Most prior researches on lead free solder have been restricted to testing at or below T = 100 °C. Extreme high temperatures properties up to T = 200 °C are relatively unexplored. Mechanical behaviors of lead free solder alloys at such extreme high temperatures are necessary to support several harsh environment electronics applications. In this chapter, we have characterized the high temperature creep behavior of SAC405 (95.5Sn4.0Ag0.5Cu) lead free solder, which is the most creep resistant of the standard SACN05 alloys. In addition, we have studied the creep behaviors of two doped SAC solders, SAC_Q and Innolot, which have been previously shown to out-perform SAC405 in simple mechanical stress-strain tests at room temperature. Tensile specimens were formed in rectangular cross-section glass tubes using a vacuum suction process, and a water quenched (WQ) solidification profile was utilized to yield fine microstructures and the upper limits of the mechanical properties for each alloy. The samples were then aged for

10 days at room temperature to stabilize their microstructures. After aging, creep testing was performed at two different stress levels (10, 15 MPa) and several different extreme/high testing temperatures (T = 100, 125, 150, 175, and 200 ^{o}C). For each set of conditions, the creep performances of the three alloys were compared. Five specimens were tested f or each combination of solder alloy, temperature, and stress level. Using the measured creep strain vs. time data, the secondary creep rates were obtained for both the standard and doped SAC alloys.

4.2 Chemical Composition of the Solder Alloys

Chemical compositions of the SAC405 and doped solder alloys (SAC+X) are presented in Table 4.1. SAC405 is consisted of tin, silver and copper with 96.5 %, 4% and 3.50%, respectively. Innolot is an engineering alloy with 6-element target composition having additional bismuth, nickel, and antimony. The compositions of SAC_Q (also known as Cyclomax) are unpublished. Energy Dispersive X-Ray Spectroscopy (EDX) was used to explore the compositions of these doped alloys. All three alloys were found to employ Bismuth (Bi) as the primary X-additive. The silver contents of SAC_Q and Innolot are similar to SAC305, with 3.41% and 3.80%, respectively. Nickel (0.15%) and antimony (1.4%) are present in Innolot.

Table 4.1 Chemical Compositions of the Solder Alloys

Alloy	Sn	Ag	Cu	Bi	Ni	Sb
SAC 405	95.50	4.00	0.50	0.00	0.00	0.00
SAC_Q	92.77	3.41	0.52	3.30	0.00	0.00
Innolot	90.95	3.80	0.70	3.00	0.15	1.40

4.3 Creep Strain vs. Time Data for Various Temperature and Stress Levels

The measured high temperature creep strain vs. time curves for SAC405, SAC_Q, and Innolot alloys are shown in Figures 4.1-4.3. Figures 4.1 (a), 4.2 (a), and 4.3 (a) illustrate typical recorded creep curves at the fixed stress level of 10 MPa for the SAC405, SAC_Q, and Innolot solder materials, respectively. Analogous results for the stress level of 15 MPa are presented in Figures 4.1 (b), 4.2 (b), and 4.3 (b). The five colored curves in each plot are for the five different testing temperatures (T = 100, 125,150, 175, and 200 ^{o}C). Each colored curve is the "average" experimental curve for a particular temperature and stress level. They were determined by performing nonlinear regression fits of the empirical Burger's model in Equation 3.4 (chapter 3) to the experimental data (five recorded curves for each alloy and set of conditions). The colors of the curves represent the testing temperature with red = 100 °C, light green = 125 °C, dark green = 150 °C, pink= 175 °C and blue= 200 °C.

It can be seen from the graphs that, as the temperature increases creep deformation at the same time also increases. At 200 °C, the creep deformation is the highest for all the alloys. Also, we can see that, if the stress level is increased from 10 MPa to 15 MPa, creep deformation also goes up. This phenomenon can be found at all the alloys that are mentioned above. At high temperature and the higher stress level, dislocation movement due to creep became more significant, which resulted in higher creep deformation for all of the alloys. At higher temperatures, the movement of dislocations is enhanced resulting more creep deformation.

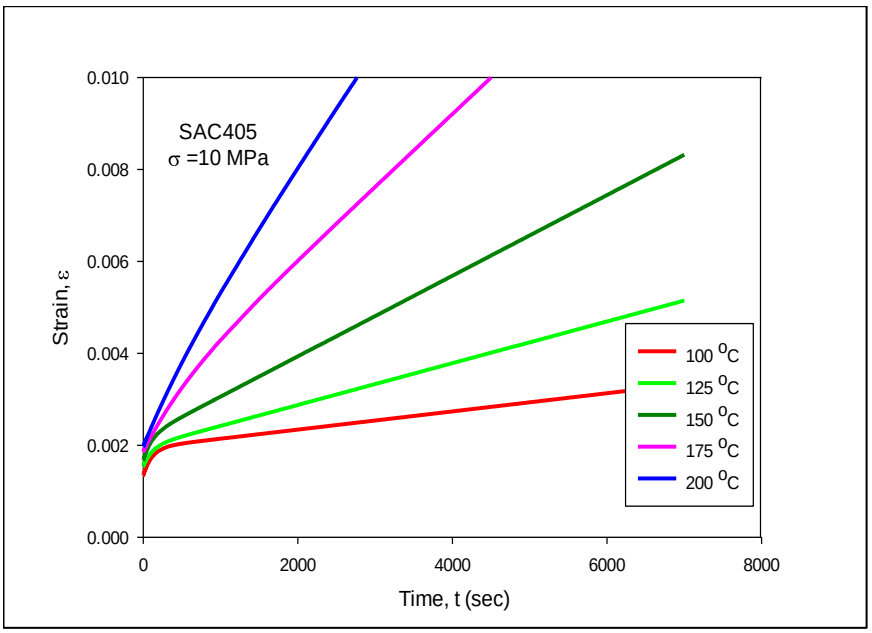

(a)

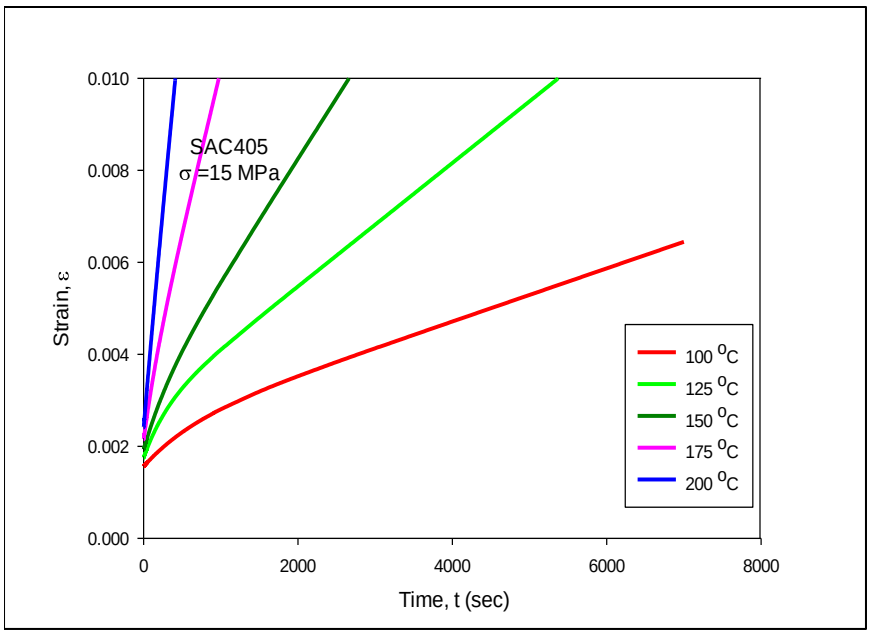

(b)

Figure 4.1 Creep strain vs. Time Curves for SAC405 at Temperatures (100-200 °C)

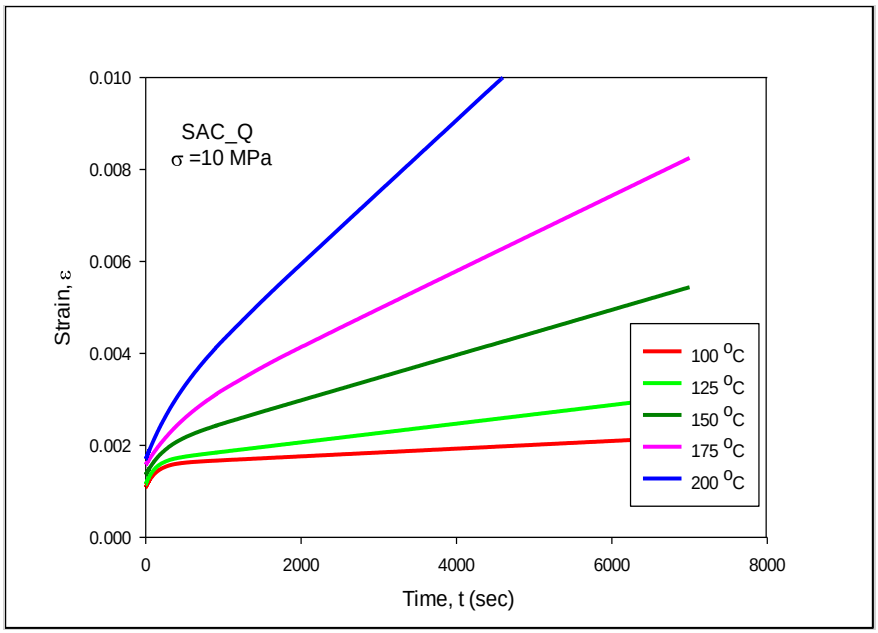

(a)

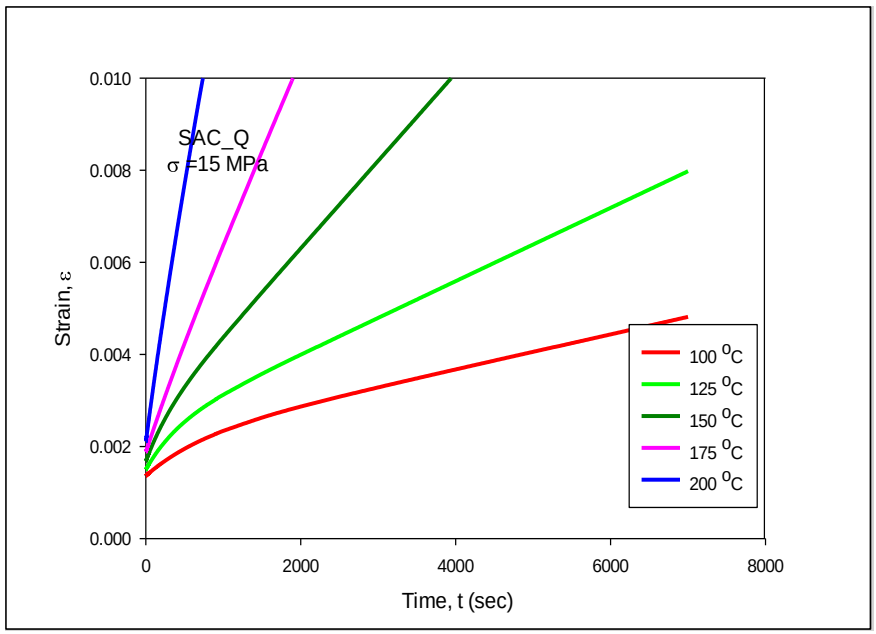

(b)

Figure 4.2 Creep strain vs. Time Curves for SAC_Q at Temperatures (100-200 °C)

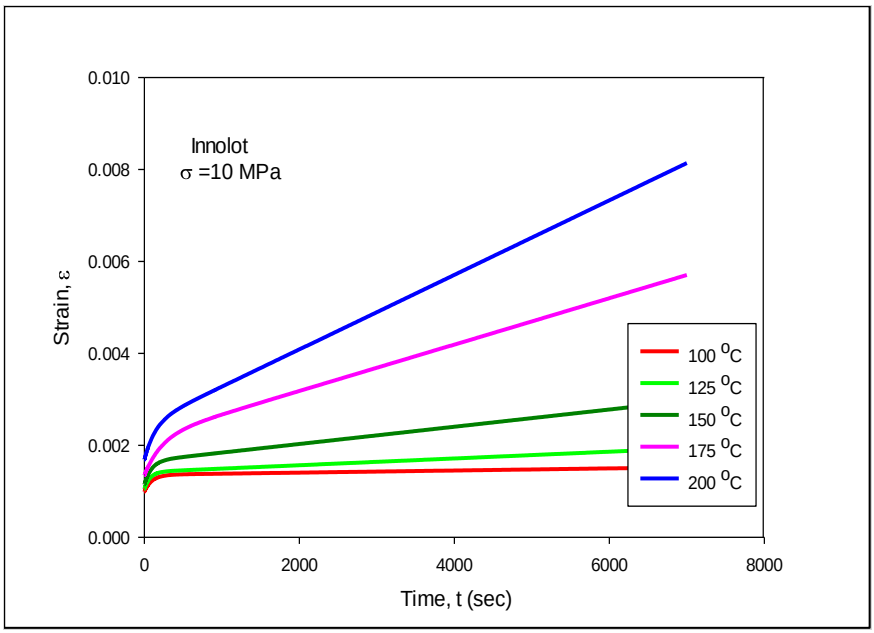

(a)

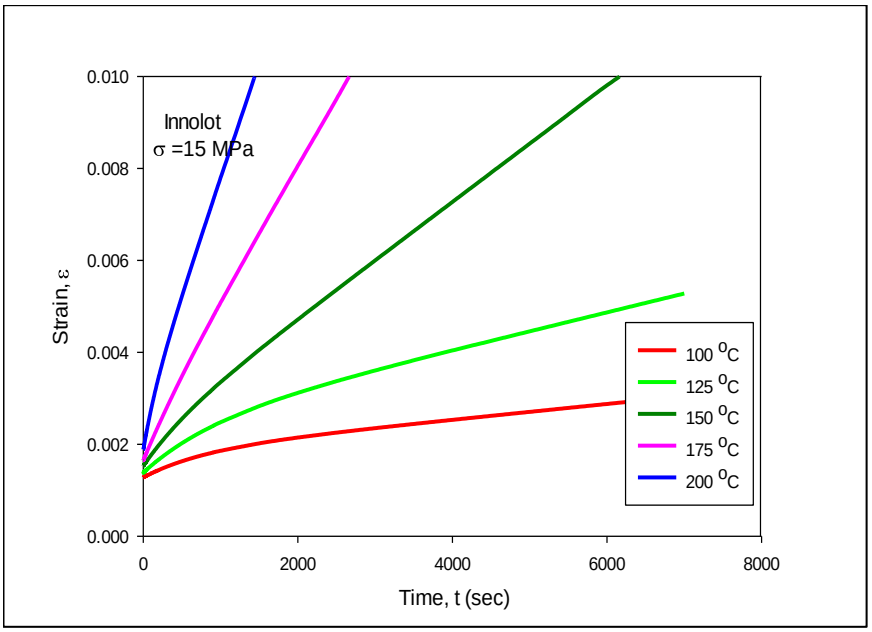

(b)

Figure 4.3 Creep strain vs. Time Curves for Innolot at Temperatures (100-200 °C)

4.4 Comparison of Creep Behavior of Solder Alloys at Various Temperature and Stress level

Comparisons of the uniaxial creep test results for the three solder alloys at different test temperature and stress level are shown in Figures 4.4-4.5. Figure 4.4 represents comparison of creep deformation at 10 MPa stress level. Figures 4.5 correspond to the comparison of similar results obtained at 15 MPa stress level respectively. In each plot, different color curve represents different alloy with red = SAC305, blue = SAC_Q and green = Innolot respectively. It can be easily seen that both the SAC_Q and Innolot alloys strongly outperform SAC305 at 10 MPa stress level at a particular temperature with lower creep deformation. The creep deformation for SAC_Q is lower than SAC305, however, Innolot outperforms SAC_Q and shows the least creep deformation. Similar results were found for all testing temperatures. When the stress level is increased to 15 MPa, creep deformation for all the alloys increased significantly but showed similar trend while compared with three different alloys.

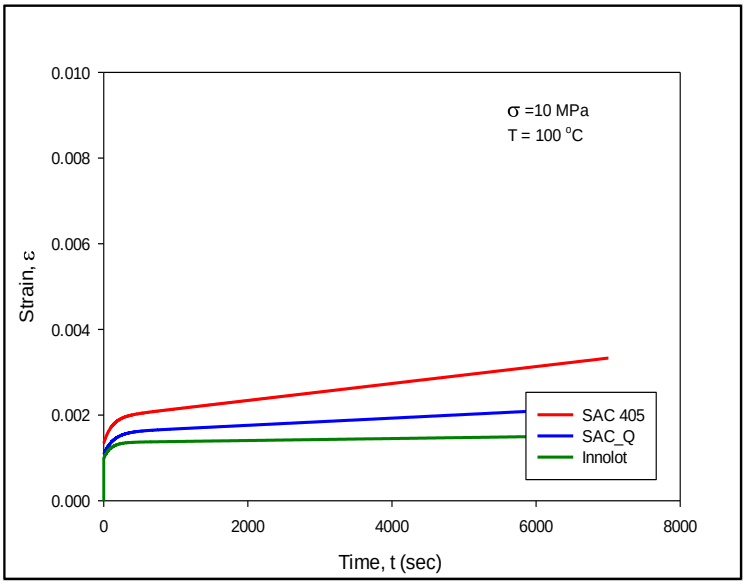

(a)

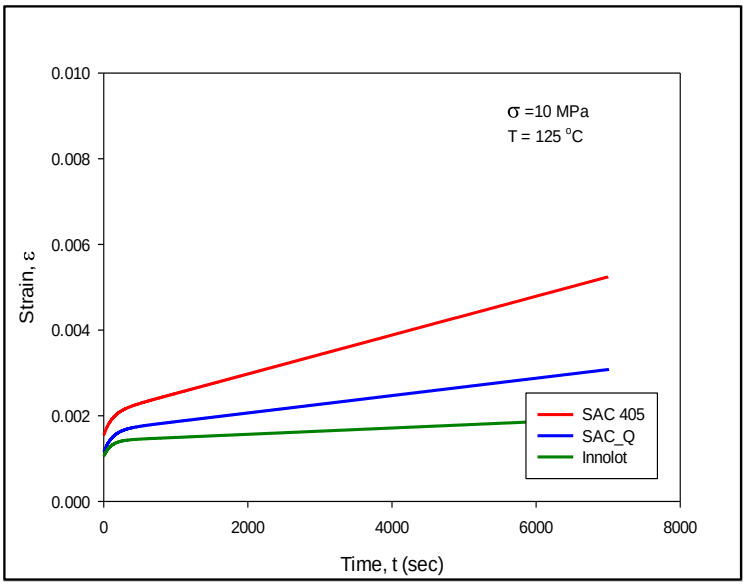
σ =10 MPa
T = 125 °C
Strain, ε
Time, t (sec)
SAC 405
SAC_Q
Innolot
0.010
0.008
0.006
0.004
0.002
0.000
0
2000
4000
6000
8000

(b)

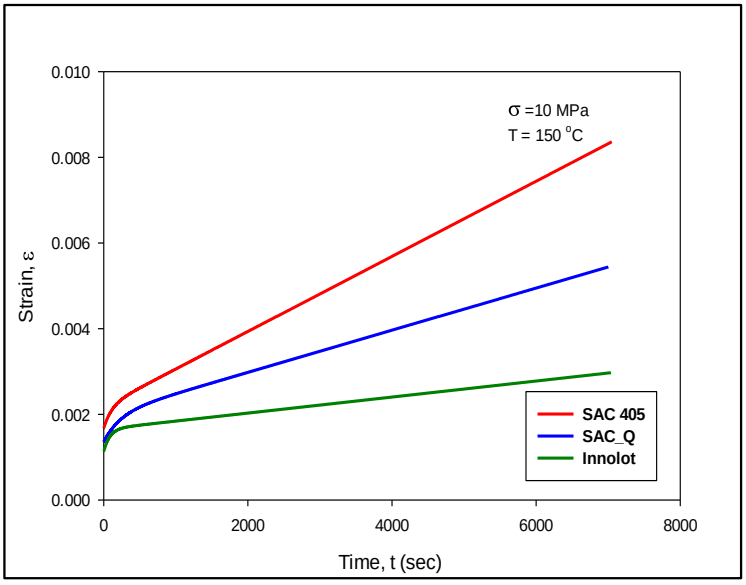
σ =10 MPa
T = 150 °C
Strain, ε
Time, t (sec)
SAC 405
SAC_Q
Innolot
0.010
0.008
0.006
0.004
0.002
0.000
0
2000
4000
6000
8000

(c)

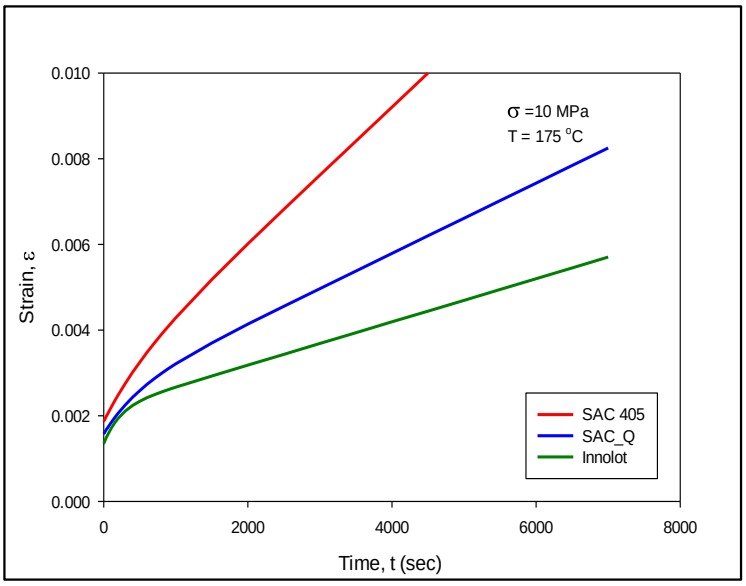

(d)

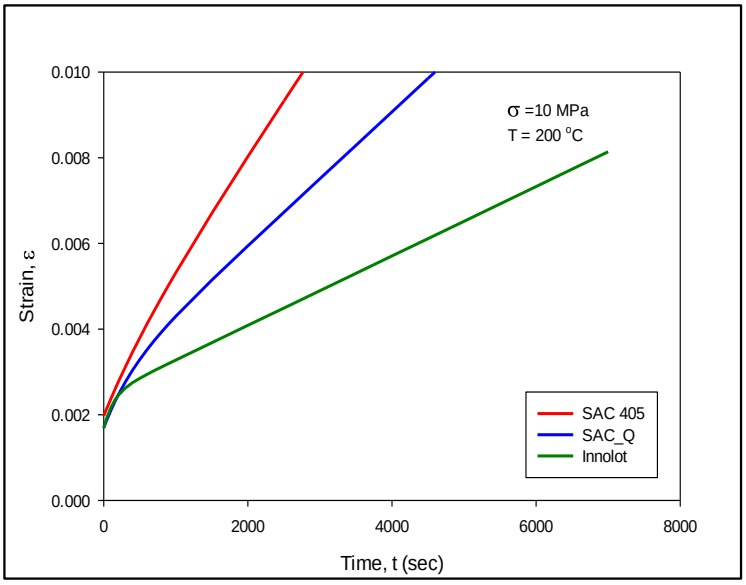

(e)

Figure 4.4 Comparison of Creep Strain vs. Time Curves at σ= 10 MPa for SAC405, SAC_Q and Innolot at Temperatures (100-200 ºC)

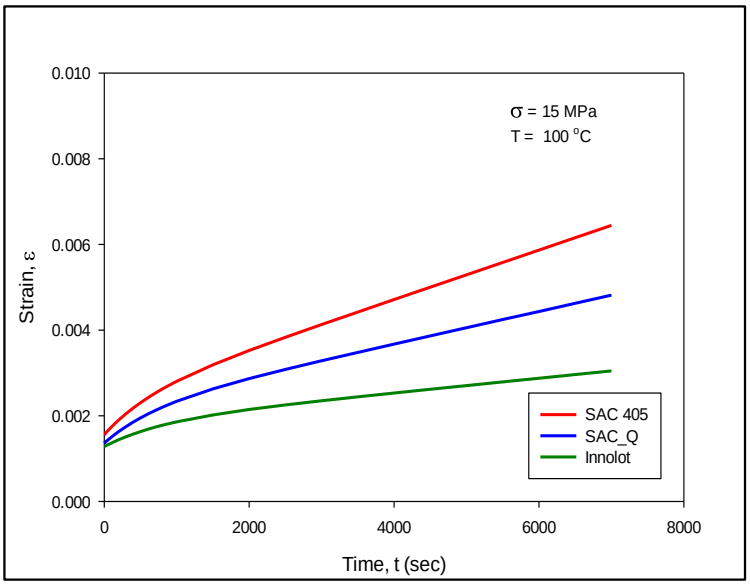
σ = 15 MPa
T = 100 °C
Strain, ε
Time, t (sec)
SAC 405
SAC_Q
Innolot
0.010
0.008
0.006
0.004
0.002
0.000
0
2000
4000
6000
8000

(a)

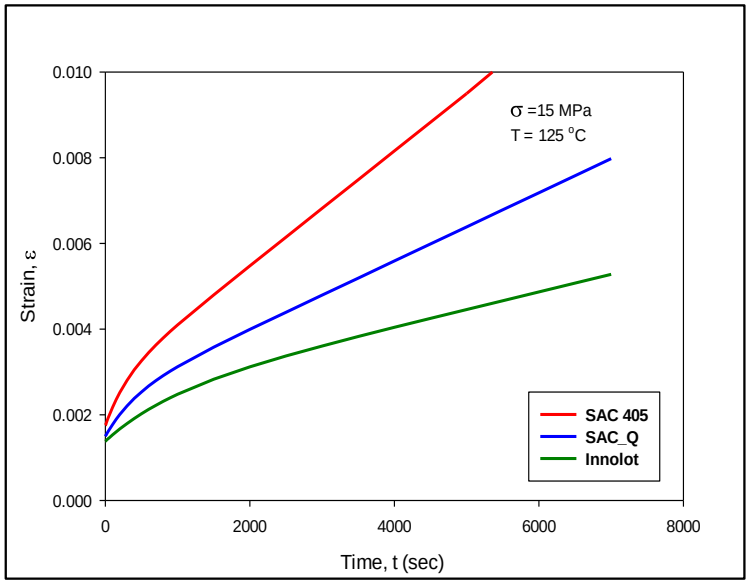
σ =15 MPa
T = 125 °C
Strain, ε
Time, t (sec)
SAC 405
SAC_Q
Innolot
0.010
0.008
0.006
0.004
0.002
0.000
0
2000
4000
6000
8000

(b)

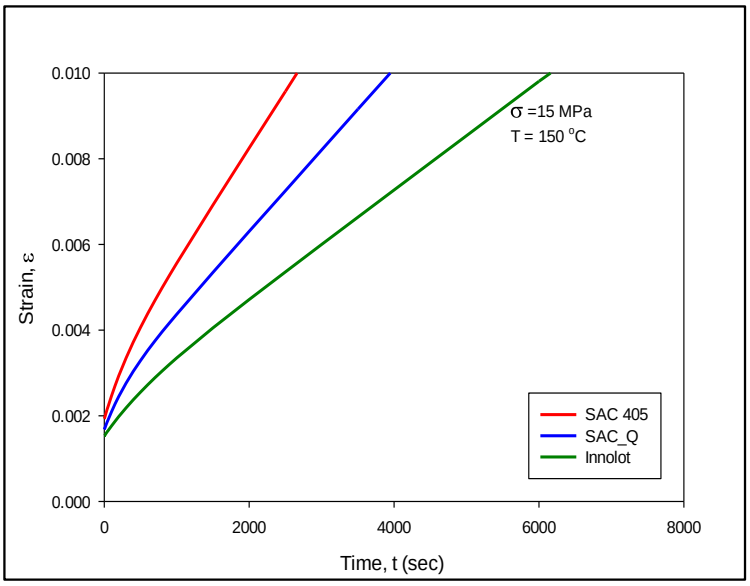
0.010
0.008
0.006
0.004
0.002
0.000
Strain, ε
0
2000
4000
6000
8000
Time, t (sec)
σ =15 MPa
T = 150 °C
SAC 405
SAC_Q
Innolot

(c)

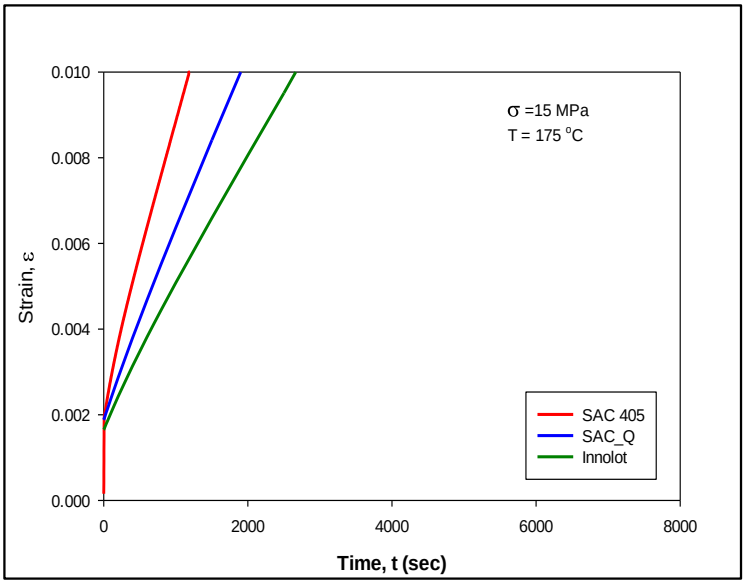
0.010
0.008
0.006
0.004
0.002
0.000
Strain, ε
0
2000
4000
6000
8000
Time, t (sec)
σ =15 MPa
T = 175 °C
SAC 405
SAC_Q
Innolot

(d)

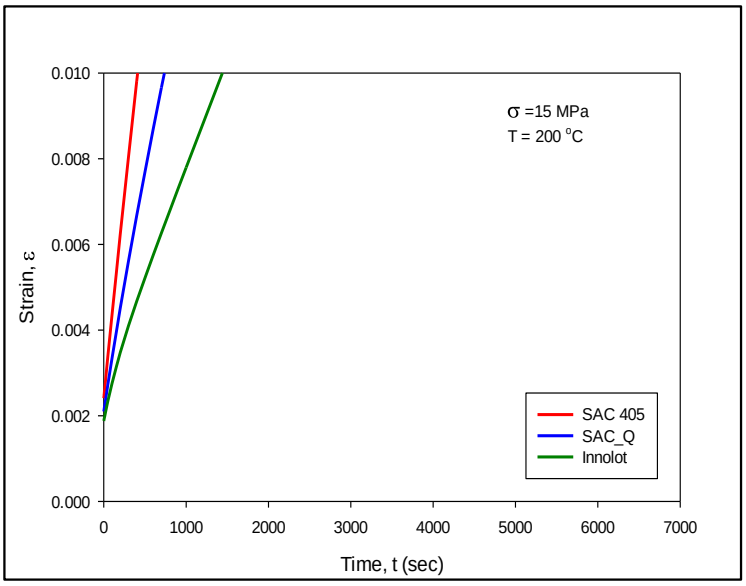

(e)

Figure 4.4 Comparison of Creep Strain vs. Time Curves at σ= 15 MPa for SAC405, SAC_Q and Innolot at Temperatures (100-200 ^{o}C)

4.5 Creep Strain Rate as a Function of Temperature and Stress Level

The creep strain of the three alloys were also extracted from the measured strain vs. time data from the slope of the secondary region. However, our study found that the value of constant C_2 in eqn. 3.4 after fitting the raw data gives very similar results as like lionear fitting in the secondary region. For this study, we used the fitting constant C_2 to calculate the creep strain rate. The values of secondary creep strain rate with this method is tabulated in Tables 4.2. Creep strain rate as a function of temperature at each of the stress level can be seen from the table. Also, figure 4.9 shows the comparison graph of three different alloys as a function of temperature at two different stress level. In each plot, different color curve represents different alloy with and red = SAC305, blue = SAC_Q and green = Innolot. The average extracted secondary creep rates are presented and plotted in Figure.

By visually comparing the analogous curves for the 3 alloys (same stress level and temperature), it can be seen that SAC405 has the highest creep rates (slopes) for all of the considered temperatures and stress levels. In addition, the Innolot alloy has the lowest creep rates (slopes) for all of the considered temperatures and stress levels. The creep rates of SAC_Q are roughly 50% of those for SAC405, while the creep rates of Innolot are roughly 33% of those for SAC405.

Table 4.2 Comparison of Creep Strain Rate

Temperature (°C)	Secondary Strain Rate ($x10^{-8}$ sec^{-1})					
	σ = 10 MPa			σ = 15 MPa		
	Innolot	SAC_Q	SAC 405	Innolot	SAC_Q	SAC 405
100	2.4	8.3	19.7	16.1	33.1	57.7
125	7.3	20.3	45.4	40.9	79.6	154.0
150	18.7	46.2	87.7	102.0	190.0	364.0
175	54.9	82.0	163.9	288.0	394.0	697.0
200	81.0	156.0	234.0	611.0	883.0	1190.0

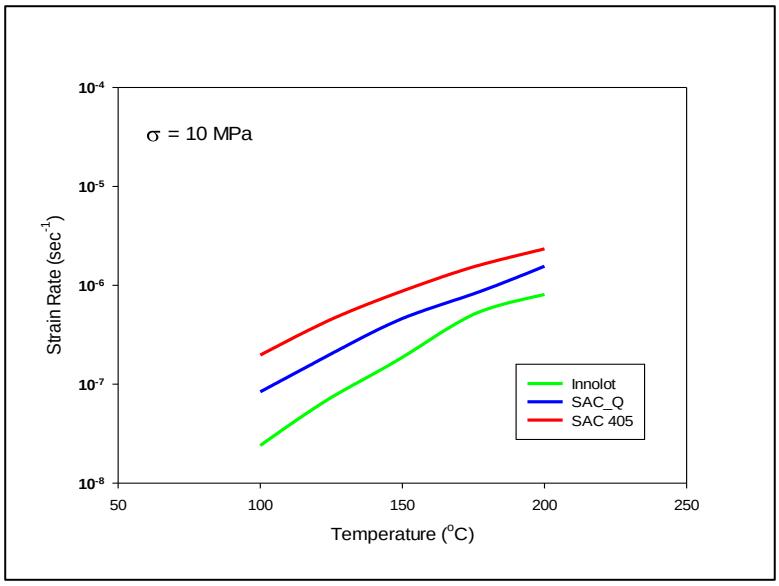

(a)

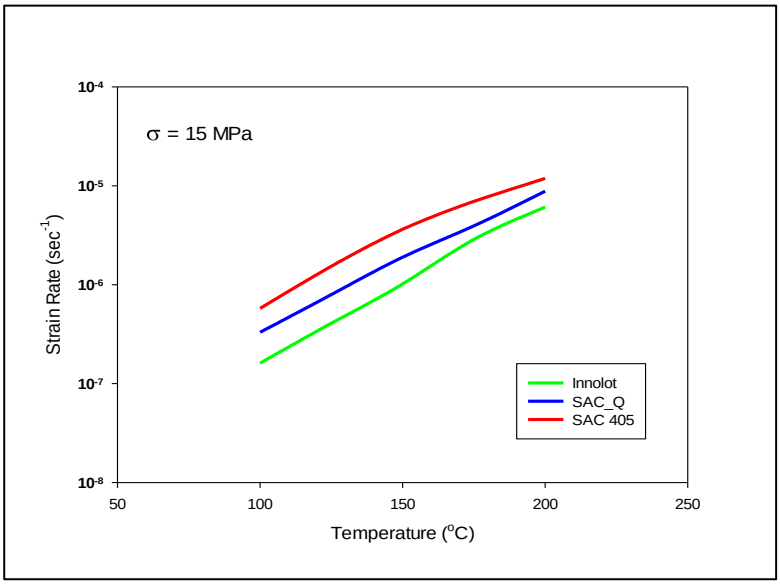

(b)

Figure 4.2 Comparison of secondary creep strain rate as a function of temperature at 10 and 15 MPa for SAC405, SAC_Q and Innolot

4.6 Summary and Discussion

In this work, the creep behavior of several SAC and SAC+X lead free solder alloys at extreme high temperatures up to 200 °C has been investigated. The studied alloys included SAC405 (95.5Sn-4.0Ag-0.5Cu), SAC_Q (92.8Sn-3.4Ag-0.5Cu-3.3Bi), and Innolot (90.95Sn-3.8Ag-0.7Cu-3.0Bi-0.15Ni-1.4Sb). The solder uniaxial test specimens were formed in high precision rectangular cross-section glass tubes using a vacuum suction process. The samples were initially cooled in a water bath. The samples are then aged for 10 days at room temperature to stabilize the microstructures.

For each of 5 elevated temperatures (T = 100, 125, 150, 175, and 200 °C, creep tests were performed at two stress levels (σ= 10 and 15 MPa). For each alloy and testing temperature, the creep deformation and secondary creep strain rate of the solders were measured and compared. As expected, the results have shown significant creep deformation and strain rate of lead-free solders increased at higher temperatures. Also, increasing stress level causes to creep rate goes up significantly at same temperature. However, it was found that the addition of dopants (e.g. Bi, Ni, and Sb) in the SAC+X alloys improved their high temperature properties significantly. Both SAC_Q and Innolot alloys significantly outperformed SAC305 at all temperature levels. However, Innolot showed the least creep deformation among all the alloys. SAC_Q Has Higher Creep Resistance than SAC405. Addition of bi along with Ag and Cu might be the main reason of superior mechanical properties of SAC_Q. Solid solution hardening of Bi leads blocks the dislocation movement which results in higher creep resistance. Innolot shows better creep properties than SAC_Q and much better than SAC 405. Presence of multiple dopants besides Sn, Ag and Cu might be the main reason of superior mechanical properties of this

material [170-172]. Ni has the ability to refine the microstructure. The solid solution hardening effect of Sb also aids to improve creep resistance of Innolot.

CHAPTER 5

INVESTIGATION ON MECHANICAL PROPERTIES OF INTERMETALLIC COMPOUNDS (IMCS) IN SAC SOLDER JOINTS AT ROOM TEMPERATURE AND ELEVATED TEMPERATURES

5.1 Introduction

Isothermal aging of lead-free Sn-Ag-Cu (SAC) solder joints leads to growth of intermetallic (IMC) particles in the solder bulk as well as growth of intermetallic layers at the joint interfaces with copper bond pads. Fracturing near the interfacial IMC layers is often found to be the primary reason for failures caused by drop impacts. The IMCs in SAC joints are primarily Ag_3Sn and Cu_6Sn_5 binary compounds. Cu-Ni-Sn based ternary IMCs can also form at the interface of Ni containing surface finish (i.e. ENIG) and SAC solder [173-174]. The mechanical properties of these IMCs are very different than those of the Sn rich dendrites and Cu pads.

Nanoindentation (NI) techniques are powerful tools to characterize mechanical properties of small particles and thin layers. In this study, the mechanical behaviors of IMC particles and layers in SAC solder joints have been characterized using nanoindentation. SAC BGA solder joints were first aged for 6 months at T = 125 ^{o} C. Test samples were subsequently prepared by cross-sectioning the aged solder joints, and then molding them in epoxy and polishing them to prepare the joint surfaces for microscopy and nanoindentation. Intermetallics formed in the bulk solder region, copper pad and SAC

solder interface, and ENIG plating finish and SAC solder interface were observed and detected using SEM and the energy dispersive x-ray spectroscopy (EDX) technique. The same intermetallics were then indented to measure their room temperature mechanical properties at first phase including the elastic modulus, hardness, and creep strain rate. To ensure the indentation occurred at the desired phase, SPM imaging was done prior and after the indentations. Stress-Strain Data for Various Test Temperatures and Aging Conditions. In the second phase, intermetallics were indented to measure their mechanical properties which includes the elastic modulus and hardness at elevated temperatures (50, 75, 100 and 125 ^{o}C) using a heating stage. Time dependent deformation (creep) behaviors were also evaluated at room temperature and 100 ^{o}C to see the effect of high temperature on the creep rate of IMCs.

5.2 Mechanical and Creep Behavior of Intermetallic Compounds

The microelectronics industry has been facing significant challenges with these IMCs that make increased knowledge and understanding of their mechanical properties desirable. The size of devices and solder joints are continuingly decreasing, and hence, the IMCs comprise a key volume fraction of the entire package. Understanding of the mechanical properties of these individual phases makes predictions of the mechanical behavior of an overall joint more straightforward. In addition, efforts are being made to do reliability analysis from finite-element modeling of solder joints at the microstructural level. These investigations, provided they have the necessary input mechanical property data, have the potential to simulate the influence of microstructure on the strength and reliability of solder joints. However, most previous work on Cu-Sn and Ag-Sn

intermetallics has been carried out on samples prepared from bulk alloys or by forming diffusion reaction couples. These are difficult to prepare and do not reflect accurately the geometries in a real solder joint. Because of intermetallic formations in the small length scale may lead to behavior different from bulk samples, one would like to measure the mechanical properties of the phases of interest in realistic geometries. However, little work has been done to investigate the IMCs formed in the ball grid arrays (BGAs) placed on Cu pads with a reflow profile typical to practical applications. Moreover, time dependent deformations (creep) in solder joints is a primary concern for researchers and understanding the creep behavior is very important during for thermal cycling exposures of electronic packages. During the holding time period for thermal cycling (e.g., high temperature dwells), the joints can have significant creep deformations which can affect the reliability of the whole package. Using the nanoindentation, creep testing can also be performed at small length scales to measure creep properties of IMC particles and layers. During the nanoindentation test, it is very important to make an indent that covers only the desired phase, in order to ensure accurate data. Indents that are much larger compared to the volume being tested may lead to impingement of the elastic/plastic strain field upon surrounding phases and produce erroneous results. In this work, a nanoindentation system with Scanning Probe Microscopy (SPM) capabilities was used to image the individual phases before and after indentation testing to ensure that the desired phases were tested and the indents were placed away from phase boundaries.

5.3 Room Temperature Nanoindentation System and Test Procedures:

The Hysitron TI 950 TriboIndenter system mentioned above was utilized to analyze mechanical properties of intermetallic compounds (IMCs) at room temperature. Nanoindentation testing was carried out by selecting arrays of regularly spaced indentations or by selecting random individual locations for indentation. While performing each indentation experiment, the load versus indentation displacement normal to the cross-sectional surface was measured. Peak load was reached at a loading rate of 600 μN/sec, and then the indenter tip was held at the peak load of 3000 μN for 2 sec for each individual indent. Finally, the indenter was unloaded at the same rate of 600 μN/sec. The elastic modulus on the IMC was obtained using the approach proposed by Oliver and Pharr by calculating the slope of the load-displacement curve in the unloading region of the test. The peak load was kept small in order to ensure that the indent was not big enough to reach to phases other than the desired intermetallic. For creep testing, a longer hold time of 250 sec was applied at the peak load of 3000 μN. Creep data was recorded during this hold time and analyzed. To maintain accuracy of the results, indenter axis calibration followed by hardness and elastic modulus measurement calibrations were performed on standard fused silica and quartz samples. Moreover, every test included a drift measurement and correction prior to the main indent that minimized the effects due to temperature fluctuations. For creep testing, an additional holding segment of 5 sec was applied prior to the creep holding time of 250 sec in order to predict and minimize thermal drift. The minimum drift rate was maintained at 0.05 nm/s.

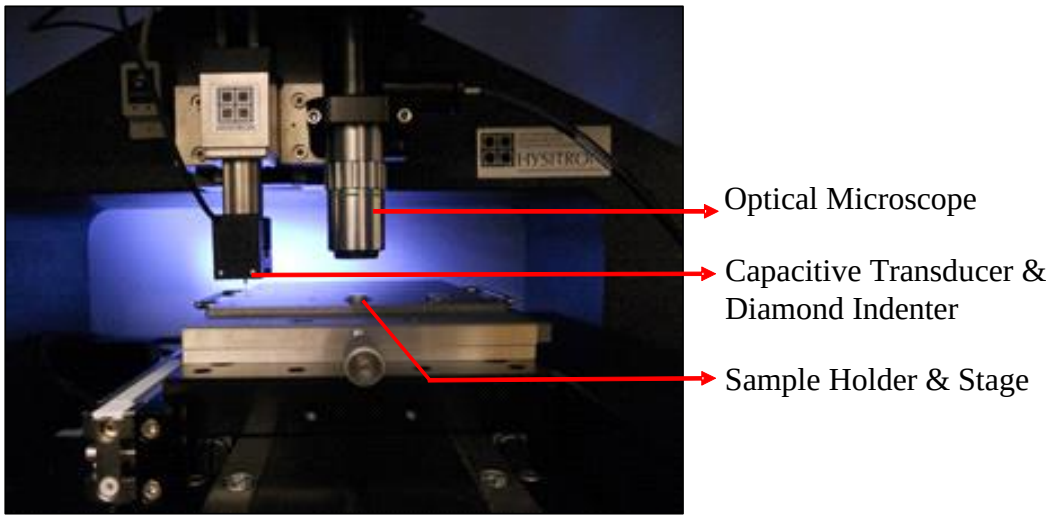

Figure 5.1 Nanoindentation System for Room Temperature testing

5.4 Formation of Intermetallic Compounds

Figure 5.2 (a) shows an SEM image of the cross-sectioned solder joints, and Figure 5.2(b) shows a single solder joint with different IMC layers and IMC particles. The boundaries between the solder bulk and the IMCs within the joint, and between the solder bulk and the IMC interfacial layers at the top and bottom of the joint are clearly visible in Figure 5.2(b). As labeled on the figure, there are three primary intermetallic compounds formed in the solder joint.

5.4.1 Cu_6Sn_5 Intermetallic Layers

The scallop-type IMC layer at the bottom copper pad interface is typically Cu_6Sn_5 (also called Ș-phase). During aging, the Cu_6Sn_5 layer evolved to a thicker and more layer like structure leading to the closure of inter-scallop diffusion channels. Thin Cu_3Sn (β-phase) layers that form between the Cu_6Sn_5 IMC layer and the Cu bond pads were occasionally seen in the backscattered SEM images. Their thicknesses were less than 0.5

μm, so they were a negligible portion of the total IMC layer (total thickness of 15.50 μm as discussed below). They could also not be detected from the SPM examinations. Thus, the IMC layer at the copper pad interface is primarily Cu_6Sn_5. Generally during reflow or aging, a limited diffusion of Sn towards the Cu bond pad through the intermetallic layer leads to formation of Cu_3Sn. This was observed by Laurila, et al. [175], who found a very thin Cu_3Sn layer formed just after reflow via SEM. However, they claimed that the growth of a Cu_3Sn layer was suppressed due to kinetic considerations when a Ni-based plating was used. Similar results were obtained on the suppression of Cu_3Sn in the IMC layer by Ohriner, et al. [176]. They found that Ni-containing solder could not form a Cu_3Sn layer due to the thermodynamic and kinetic effects of the Ni atom. Rizvi et al. [177] also observed in their study that Cu_3Sn layer was completely absent in case of Ni containing Sn0.7Cu solders.

5.4.2 $(Cu_{1-x}Ni_x)_6$-Sn_5 Intermetallic Layers

The IMC layer formed between Ni/Au surface finish (ENIG) of the top copper pad and the solder joint bulk is typically comprised of Ni rich $(Cu1\text{-}xNix)_6Sn_5$ intermetallics. Cu from the SAC solder bulk diffuses into the interface and combines with the Sn and Ni layer to form a ternary phase of $(Cu_{1-x}Ni_x)_6$-Sn_5 IMCs. However, the Ni layer acts as a diffusion barrier that prevents copper from the pad from reacting, and thus it can slow the growth of the IMC layer.

5.4.3 Ag_3Sn Intermetallic Layers

The primary IMCs present in the middle of the joint (solder bulk) are Ag_3Sn particles. Ag_3Sn IMCs can exist as dispersed small particles or some case large ‘branch-like’ needle shaped phases.

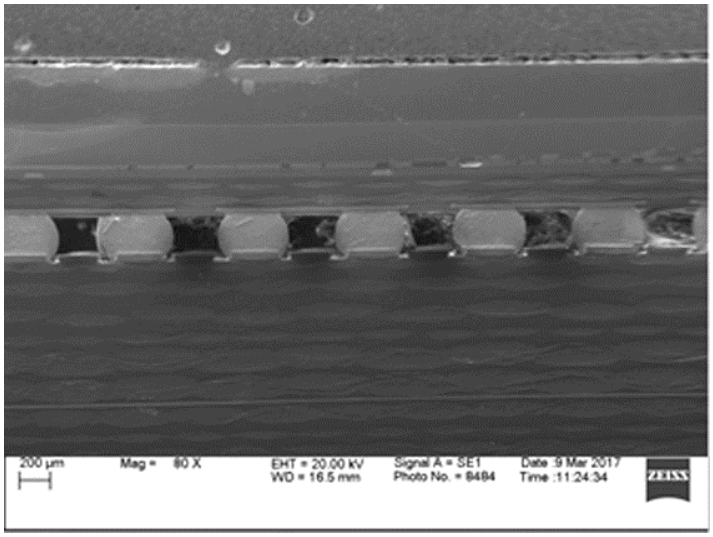

(a)

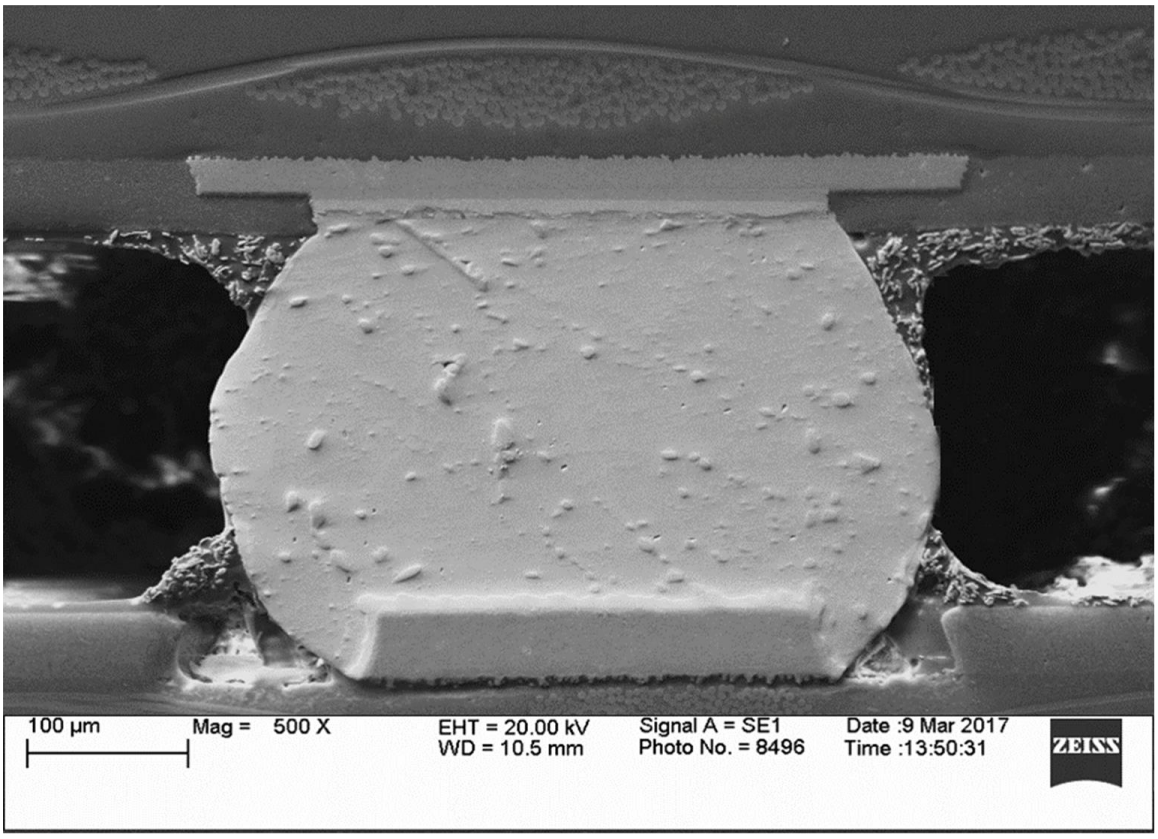

(b)

Figure 5.2 SEM Image of a) Solder Joints b) Single Solder Joint with Different IMC Layers and Particles

5.5 Chemical Composition Analysis

The chemical compositions of the IMC phases were obtained from EDX analysis. Data obtained from EDX was used to calculate the mass percentage of each element present in the selected intermetallic layers and particles. The composition of the layer in between the bottom Cu pad and the solder joint bulk was confirmed to be Cu_6Sn_5 (see Figure 3(a)). Results obtained from EDX for the top pad (ENIG plating) IMC layer confirmed it to be comprised of Ni rich $(Cu_{1-x}Ni_{ix})_6Sn_5$ intermetallics (similar to reference [173]). EDX composition results for $(Cu_{1-x}Ni_x)_6Sn_5$ are shown in Fig. 3(b). The IMC particles that are randomly distributed in the solder joint bulk (middle) were found to be as Ag_3Sn particle (see Figure 5.3).

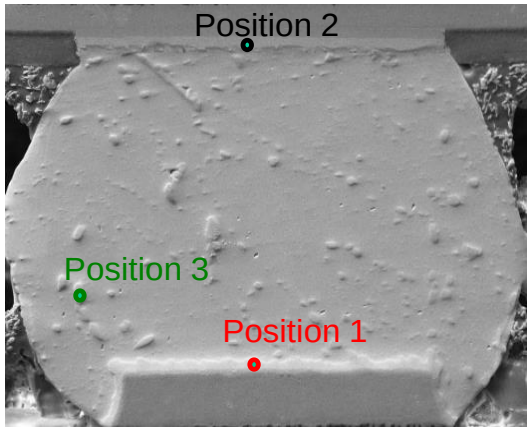

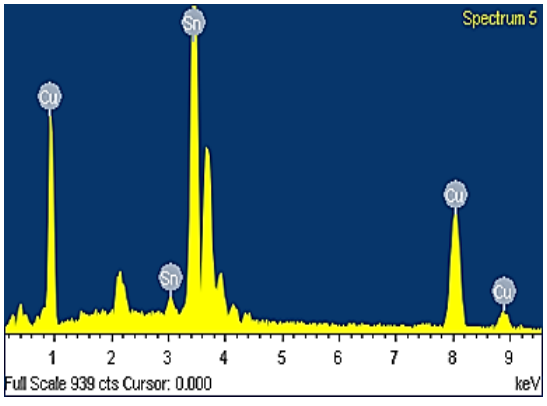

Table 5.1 EDX results of Cu_6Sn_5 IMC Layer (Position 1)

Element	wt.%	at. %
CuK	37.27	52.61
SnL	62.73	47.39
Total	100	100

Table 5.2 EDX results of $(Cu_{1-x}Ni_x)_6Sn_5$ IMC Layer

(Position 2)

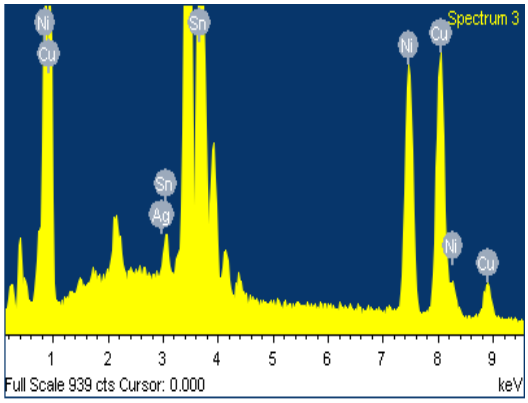

Element	wt.%	at.%
CuK	24.65	32.79
SnL	56.61	40.32
NiK	18.61	26.89
AgL	0.13	0.09

Table 5.3 EDX results of Ag_3Sn IMC Layer

(Position 3)

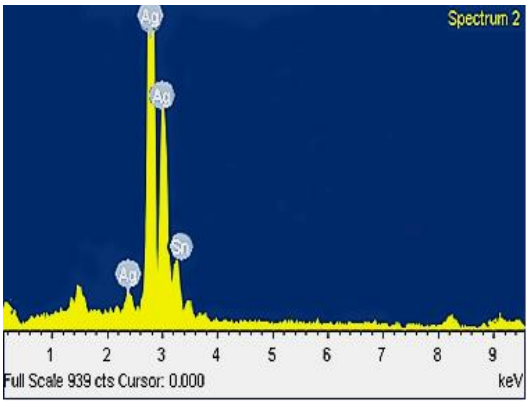

Element	wt.%	at. %
CuK	37.27	52.61
SnL	62.73	47.39
Total	100	100

Figure 5.3 EDX Analysis Results of IMCs

5.6 Nanoindentation Results

5.6.1 Modulus and Hardness Values

The mechanical properties (elastic modulus and hardness) of the IMCs and bulk solder region were measured using nanoindentation testing. During nanoindentation test, load vs. displacement data were recorded continuously. The measured response consists of

three segments: (1) loading at constant loading rate (600 μN/s) to the indentation force reaches its maximum value of 3000 μN; (2) dwell for 2 sec at this maximum load of 3000 μN; and (3) unloading at the same constant loading rate (600 μN/s). The loading curve is a function of loading rate. At maximum load, the slope of the unloading region, S= dP/dh is called the unloading stiffness which can be used to calculate the elastic modulus (E) and hardness, (H) at the point of maximum indentation using the Oliver and Pharr method. Moreover, the procedures to obtain E and H require the values of Pmax, hmax, Poisson's ration of the indented material υ, as well as the geometrical parameters and material constants for the diamond indenter tip. The Poisson's ratios for the three different IMCs were obtained from previous researchers [173-174]. Example load-displacement curves for the three different IMCs are presented in Figure 5.4. Results of at least 6 indents were evaluated for each material, and then the average of those results was obtained. Figure 5.4(a) shows the representative load-displacement behavior during indentation of the Cu_6Sn_5 IMC layer at 25 ^{o}C. For the maximum load of 3000 μN, the maximum indentation displacement after unloading was found to vary between 80- 100 nm. The $(Cu_{1-x}Ni_x)_6Sn_5$ IMC layer showed a maximum indentation displacements between 65-90 nm after unloading. A representative load-displacement graph for the $(Cu_{1-x}Ni_x)_6Sn_5$ intermetallics is shown in Fig. 5.4(b). The Ag_3Sn IMC particles showed higher indentation displacements for same maximum load, which varied between 130-160 nm. Figure 5.4(c) shows a representative load-displacement plot for the Ag_3Sn IMCs. A combined plot showing representative load-displacement curves for the three IMCs, β-Sn matrix, and the bottom Cu pad are shown in Fig. 4.5. It is seen from this graph that variations in the loading and unloading profiles exists among these phases that can provide valuable insight. The loading

profiles demonstrated in Fig. 4.5 can be thought of as an index of the hardness, i.e. a steeper loading slope represents a higher hardness value, and vice versa. Therefore, from left to right, the load-displacement curves for $(Cu_{1-x}Ni_x)_6Sn_5$, Cu_6Sn_5, Ag_3Sn, Cu pad, and β-Sn phase represent a trend of decreasing hardness values. In addition, the slopes of the unloading curves can help visualize the ranking of the elastic modulus. For example, the unloading curves of the β-Sn phase and Cu pad are virtually vertical, which signifies that the deformation within these two entities is mainly plastic. On the other hand, deformation behavior of intermetallic phases was found to be both elastic and plastic.

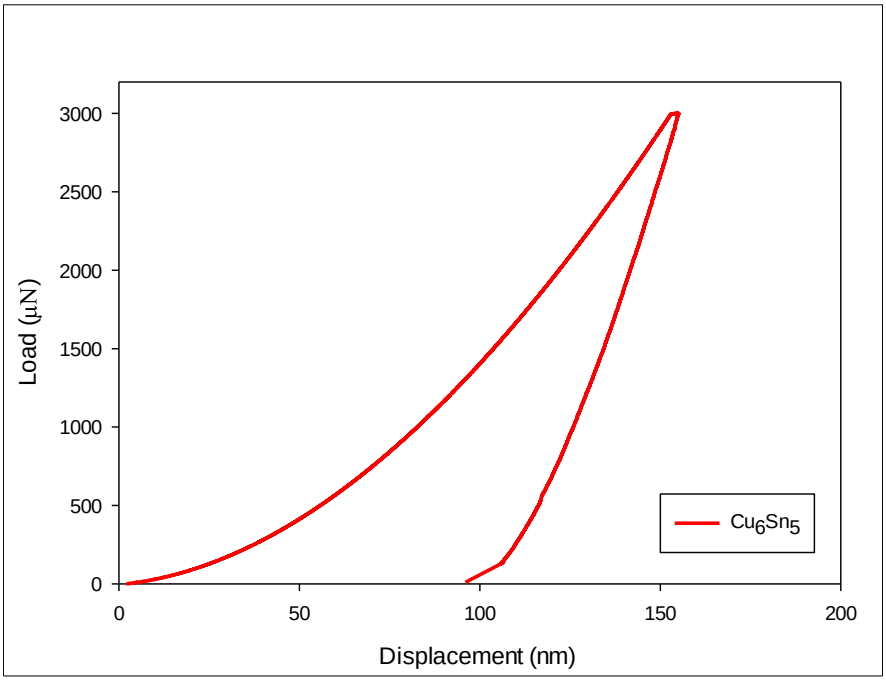

(a)

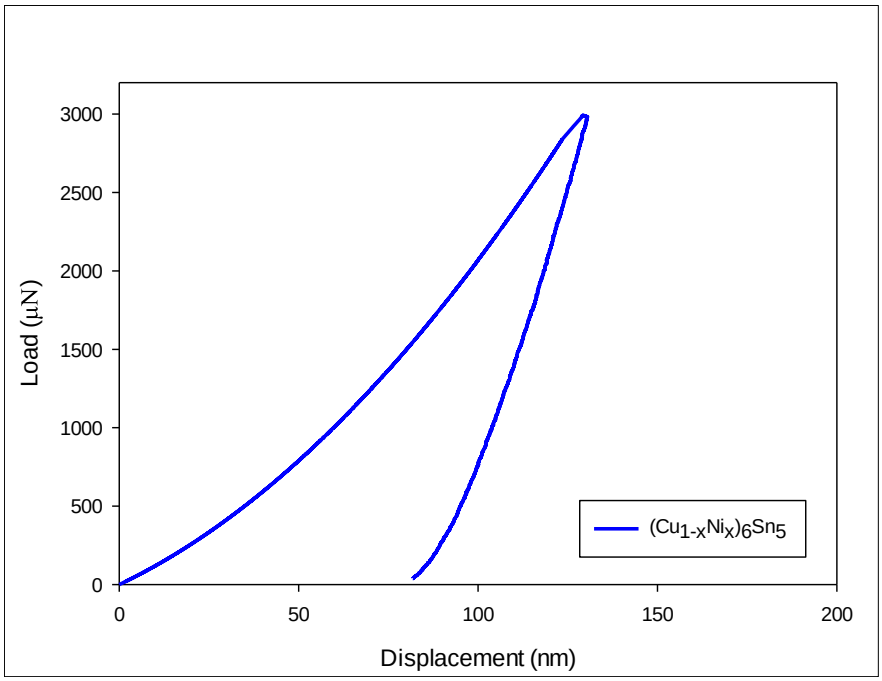
3000
2500
2000
1500
1000
500
0
Load (μN)
0
50
100
150
200
Displacement (nm)
(Cu1-xNix)6Sn5

(b)

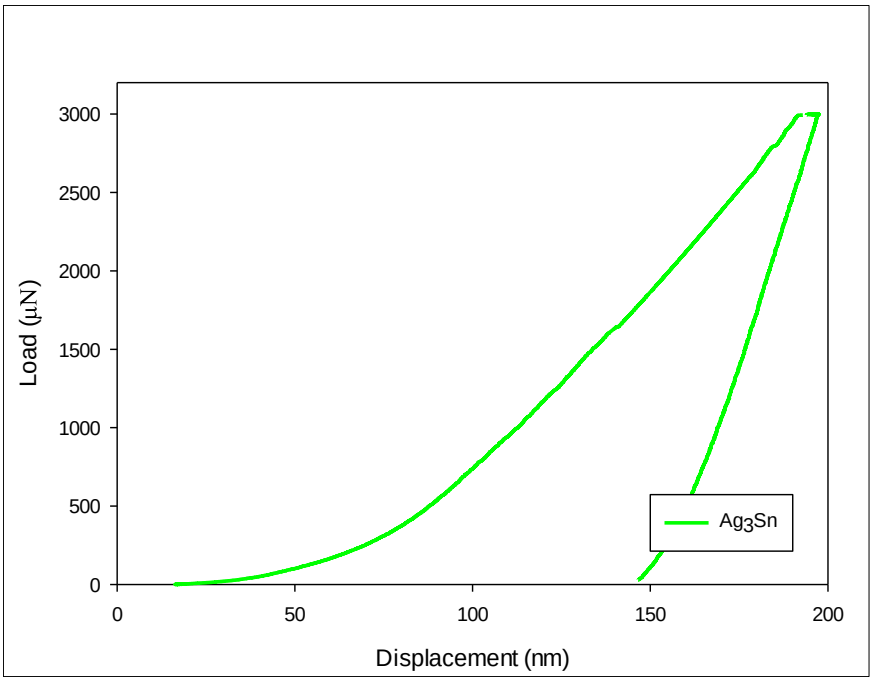
3000
2500
2000
1500
1000
500
0
Load (μN)
0
50
100
150
200
Displacement (nm)
Ag3Sn

(c)

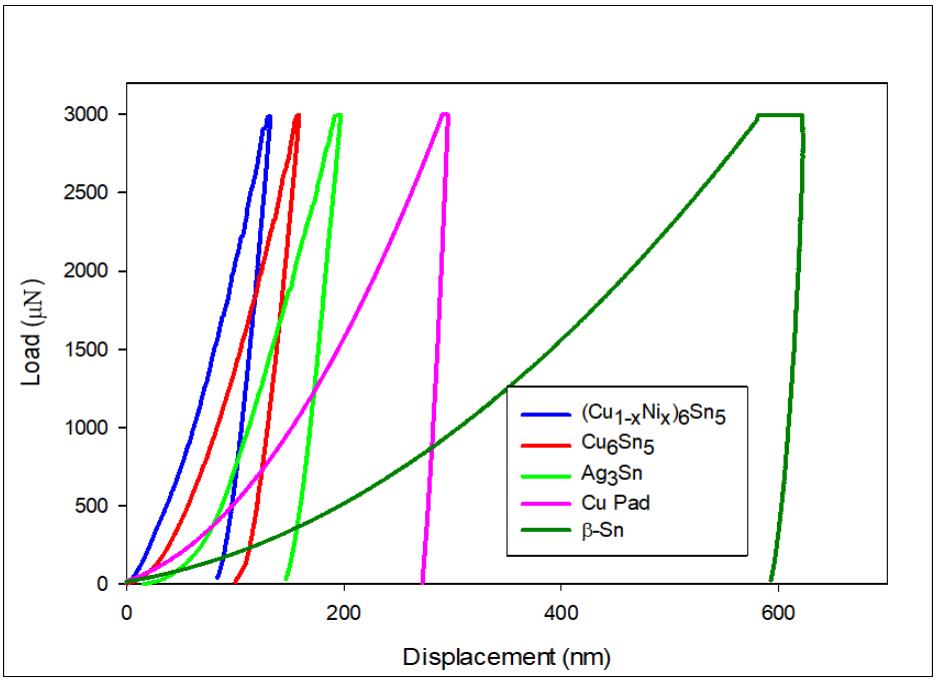

(d)

Figure 5.4 Load-Displacement Curve for a) Cu_6Sn_5 b) $(Cu_{1-x}Ni_x)_6Sn_5$ & c) Ag_3Sn IMCs (d) Combined curve showing all phases

The measured elastic modulus and hardness values were 98.1 ± 6.3 and 5.80 ± 0.70 GPa for the Cu6Sn5 layers at the joint and copper bond pad interfaces, 132.5 ± 4.5 and 8.58 ± 1.13 GPa for the $(Cu_{1-x}Nix)_6Sn_5$ layers at the joint and ENIG plating finish interfaces, and 75.2 ± 4.0 and 3.085 ± 0.50 GPa for the Ag_3Sn IMC particles in the solder joint bulk. These are all much higher than the values of 42.7 ± 2.3 and 0.21 ± 0.12 GPa measured for the β-Sn phase in the solder joint bulk. However, comparisons of the results with the literature revealed that there were differences in the measured values reported by various researchers for a given material. These variations can be attributed to differences in sample preparation and experimental techniques. However, analyzing our current work

and previous work, it can be said that the modulus and hardness of the intermetallics and the solder shows the following trend starting from highest to lowest:

$$(Cu_{1-x}Nix)_6Sn_5 > Cu_6Sn_5 > Ag_3Sn > \beta\text{-Sn}$$

It was also observed that the elastic modulus of Cu6Sn5 IMC was similar to that of pure Cu, while the modulus of $(Cu_{1-x}Nix)_6Sn_5$ was comparatively higher. In addition, the results showed that the Cu-Sn and Cu-Ni-Sn IMCs were found to have hardness values in the range of typical ceramics, while the hardness of the Ag_3Sn particles was similar to the value found for many metals and alloys. This indicates that the Cu-Sn alloys have the potential for crack initiation due to brittle behavior. On the other hand, Ag_3Sn has a lower modulus and hardness, and is thus relatively soft and ductile and would not likely be a source of crack initiation. SEM images of typical indents in the Ag3Sn particles in the bulk of the solder joint are shown in Fig. 5.5

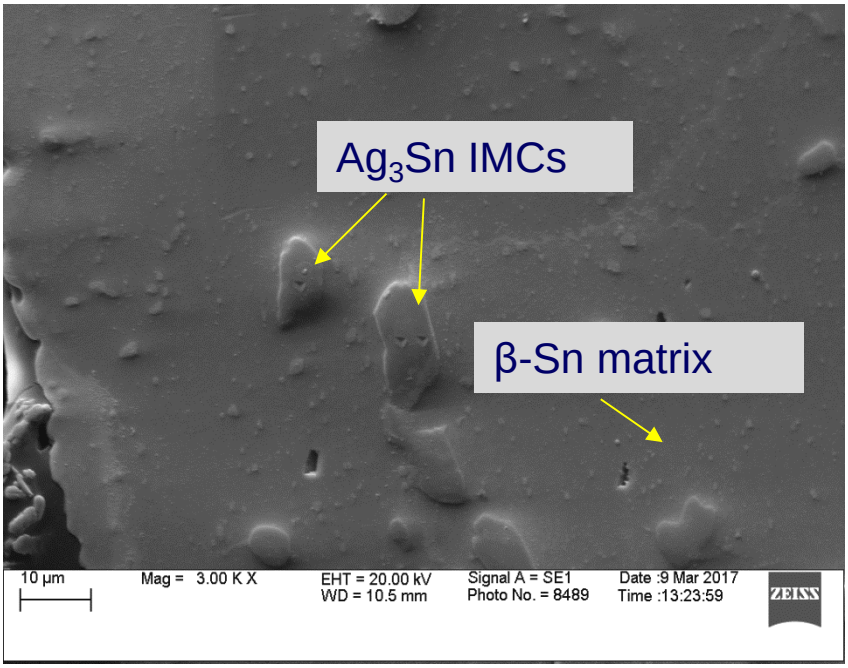

(a)

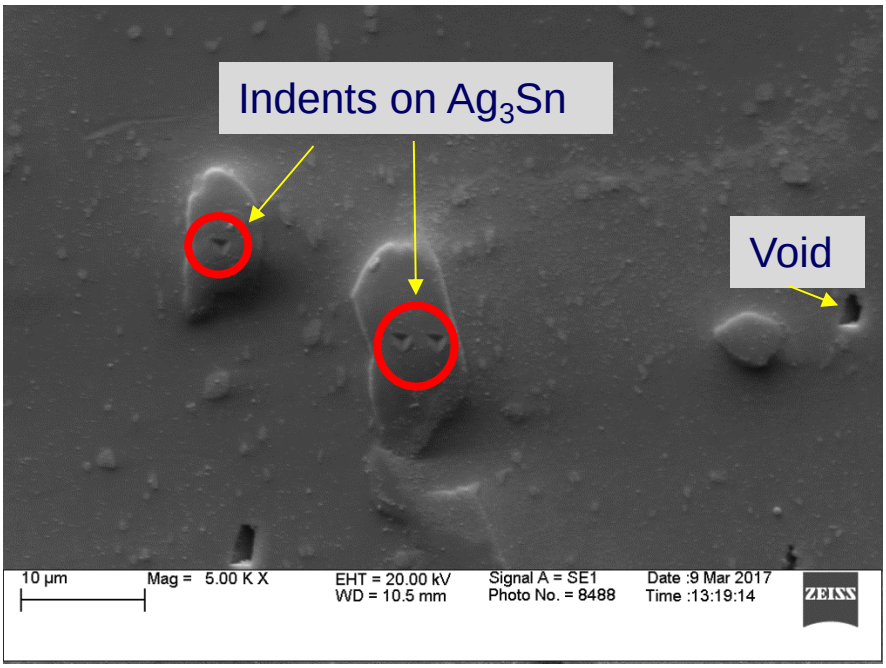

(b)

Figure 5.5 Indents on Ag3Sn Particles (a) 3000X and (b) 5000X

5.6.2 Creep Behavior of Intermetallics

Nanoindentation creep testing was performed on the intermetallics and solder during the hold/dwell at the constant peak load of 3000 µN. As discussed above, a dwell time of 250 sec was considered in this work for the creep tests. The total indentation displacements were measured continuously, from which the creep displacements (change in displacement) during the constant load period were extracted. The creep displacement experimental data can be fit well with various empirical models. Creep data analysis can be found in chapter eqn. 3.11-3.14.

Figure 5.6 illustrates representative creep displacement curves (creep displacement vs. time) for the three IMC materials and the β-Sn phase of solder material for a peak load of 3000 µN at 25 ºC. These curves were obtained by fitting eq. (3.11) to the data for five

indentation creep tests for each material. It was observed that the -Sn had the largest creep displacements, followed by Ag_3Sn. The Cu6Sn5 and $(Cu_{1-x}Ni_x)_6Sn_5$ IMC layers had the smallest creep displacements. For example, at a time of 100 sec, which lies in the secondary creep region, the $(Cu_{1-x}Ni_x)_6Sn_5$ IMC had 6.5 nm of of creep displacement, while Cu_6Sn_5 IMC had a slightly higher value of 8.5 nm. On the other hand, Ag_3Sn particle had 20 nm of creep displacement, which is twice the value of Cu6Sn5 and three times higher than $(Cu_{1-x}Ni_x)_6Sn_5$. The β-Sn phase had a very high displacement value of 100 nm, indicating large plastic deformations during indentation creep. Figure 5.7 (a) shows the representative measured curves of hardness vs. time, while Figure 5.7(b) shows the measured curves for the applied stress vs. time during the nanoindentation creep tests. From the plotted graphs, it is observed that both the hardness and applied stress do not remain constant during the indentation creep tests at constant load. This is because while the load was constant, the projected contact area A of the indentation continued to grow during the creep deformations. However, both the hardness and applied stress values became fairly constant after about 200 sec of creep deformation.

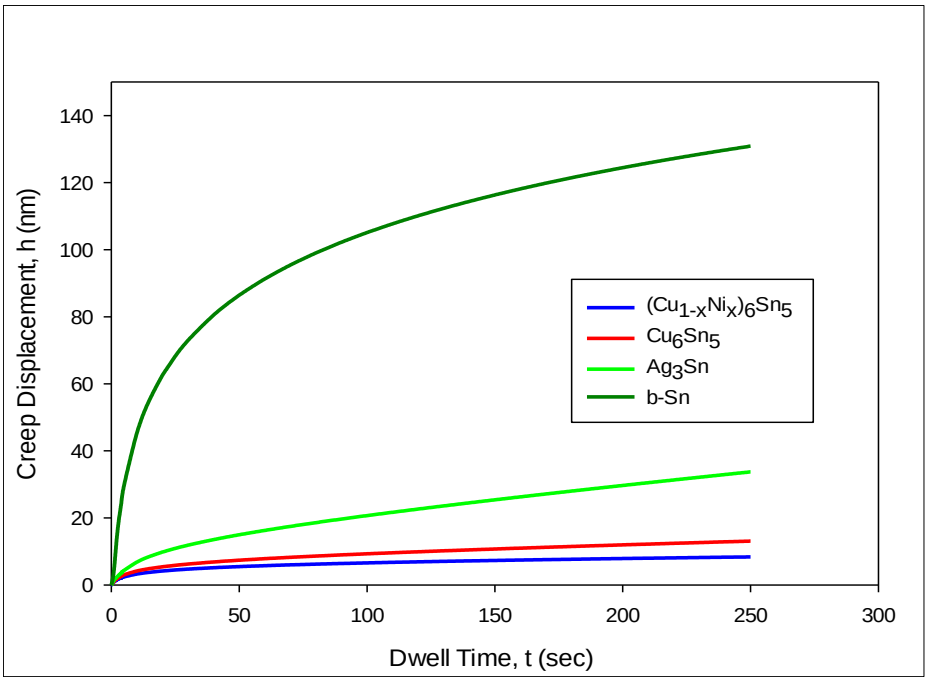

Figure 5.6 Creep Displacement vs. Time Curve of Various Phases

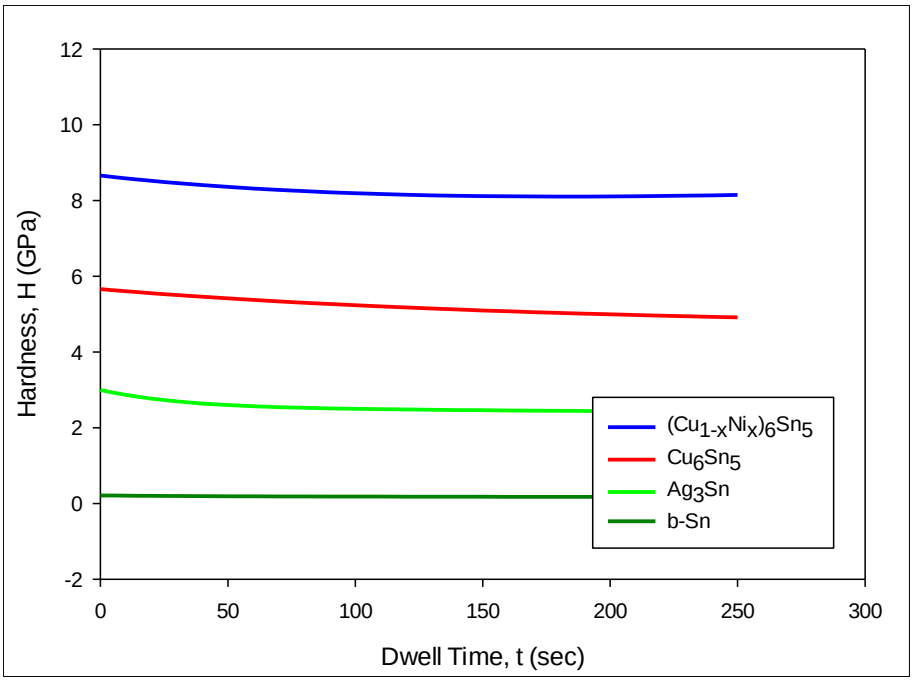

(a)

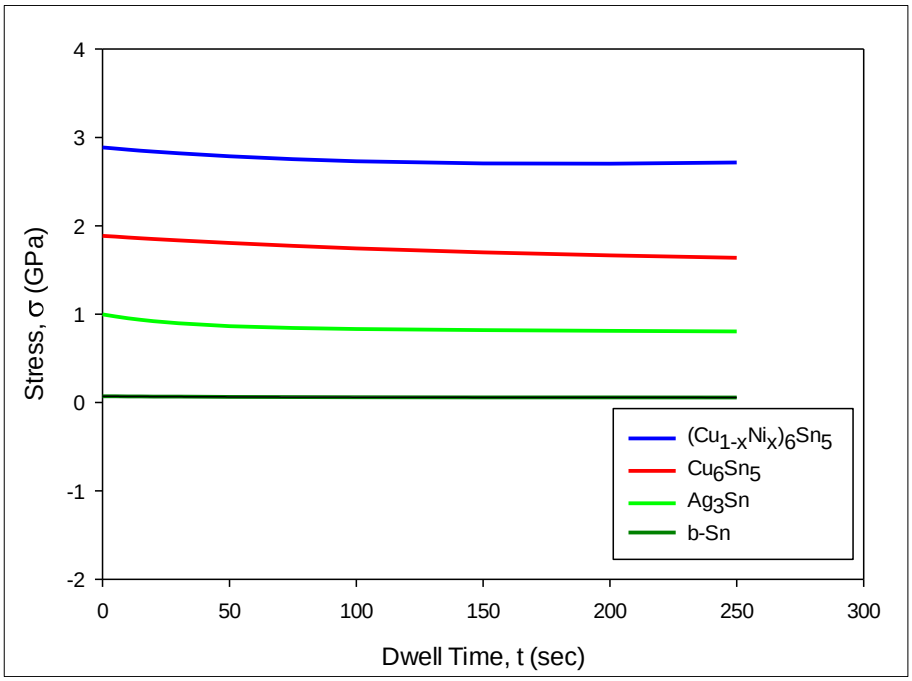

(b)

Figure 5.7 (a) Hardness vs. Time and (b) Stress vs. Time Curve of Various Phases

The values of hardness and stress followed a similar trend as the modulus values found from the Oliver and Pharr method. The $(Cu_{1-x}Ni_x)_6Sn_5$ IMCs had the highest levels of hardness and stress, followed by the Cu6Sn5, Ag_3Sn, and β-Sn phases. The applied compressive stress value varied in between 2.9 and 2.7 GPa, and became constant at σ = 2.7 GPa for the $(Cu_{1-x}Ni_x)_6Sn_5$ IMC layer, whereas for Cu6Sn5, the stress varied between 1.89 and 1.64 GPa, and became constant at σ = 1.64 GPa. The stress variation for Ag_3Sn was between 0.99 GPa and 0.80 GPa, and became constant at H = 0.8 GPa. Finally, for the β-Sn matrix, the stress variation was from 0.070 GPa to 0.057 GPa, and became constant at σ = 0.057 GPa. Figure 5.8 shows the variation of strain rate (calculated from eq. (3.13-3.14)) with stress for four different materials. The value of the constant strain rates for the

three intermetallics were found to be 1.088 x 10-3 sec-1 for $(Cu_{1-x}Ni_x)_6Sn_5$ at σ = 2.7 GPa; 1.66 x 10-3 sec-1 for Cu6Sn5 at σ = 1.64 GPa; and 2.34 x 10-3 sec-1 for Ag_3Sn at σ = 0.8 GPa. While the strain rate vs. stress curves for the four materials did not overlap in stress (cover the same range of stresses), it is clear that the β-Sn matrix has the highest strain rates for a given (fixed) stress value, followed by the Ag_3Sn IMC particles, Cu6Sn5 IMC layer, and then the $(Cu_{1-x}Ni_x)_6Sn_5$ IMC layer with the lowest strain rates.

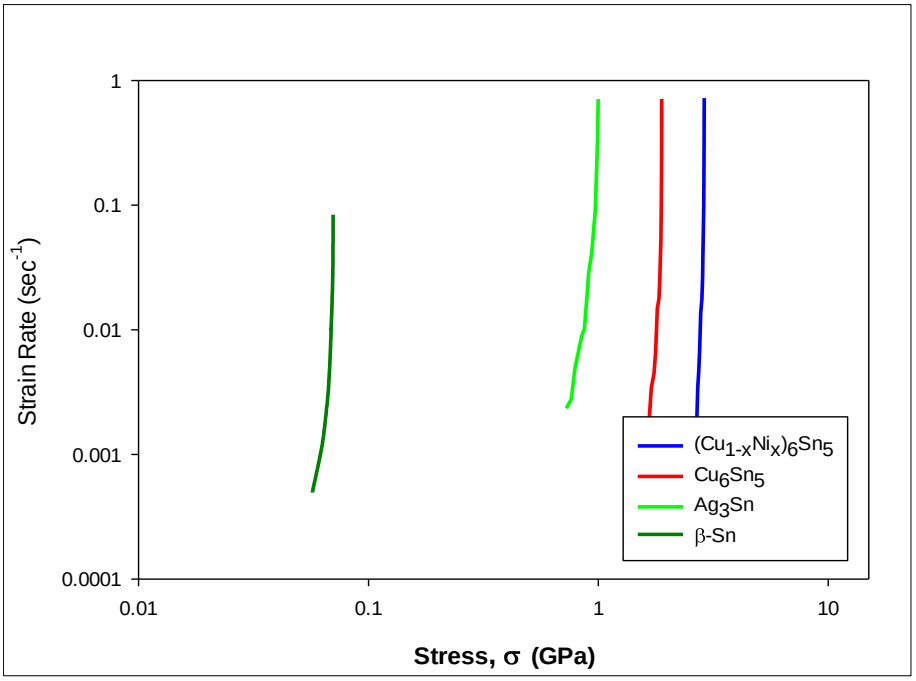

Figure 5.8 Creep Strain Rate vs. Applied Stress Curve of Various Phases

For many materials, the creep stress can be related to the creep strain rate by a power law relationship: eqn. 3.15, where k is a constant, and n is the creep stress exponent. The value of n provides some information about the creep mechanism exhibited by the material. Taking the log of both sides of eq. (3.15), the curve at figure 5.8 is obtained. If eq. (3.15) is valid for a material, a plot of the log (creep strain) vs. log (stress) data should

be nearly linear, with the slope being the creep exponent n. Figure 5.9 shows the log-log plot of strain rate vs. stress data from Figure 5.8. The responses are quite linear, and the slopes of the results for each material have been calculated using a least squares regression fit. At 25 °C, the creep stress exponents of the $(Cu_{1-x}Ni_x)_6Sn_5$, Cu6Sn5, and Ag_3Sn IMCs were found to be 43.9, 33.3, and 13.6, respectively. The β-Sn matrix phase had a much smaller creep exponent value of 8.4.

Images of the indents after creep testing were obtained using the SPM tool in the Nanoindenter. Figure 5.10 shows the SPM micrographs of indents in the Cu_6Sn_5 IMC layer at the interface to the bottom copper pad.

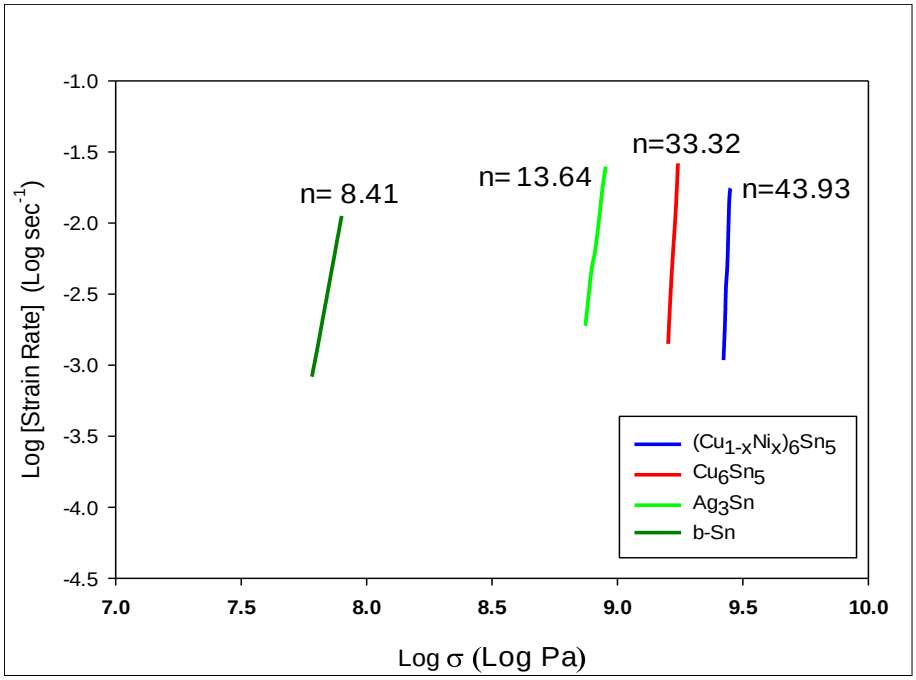

Figure 5.9 Creep Strain Rate vs. Applied Stress Curve of Various Phases

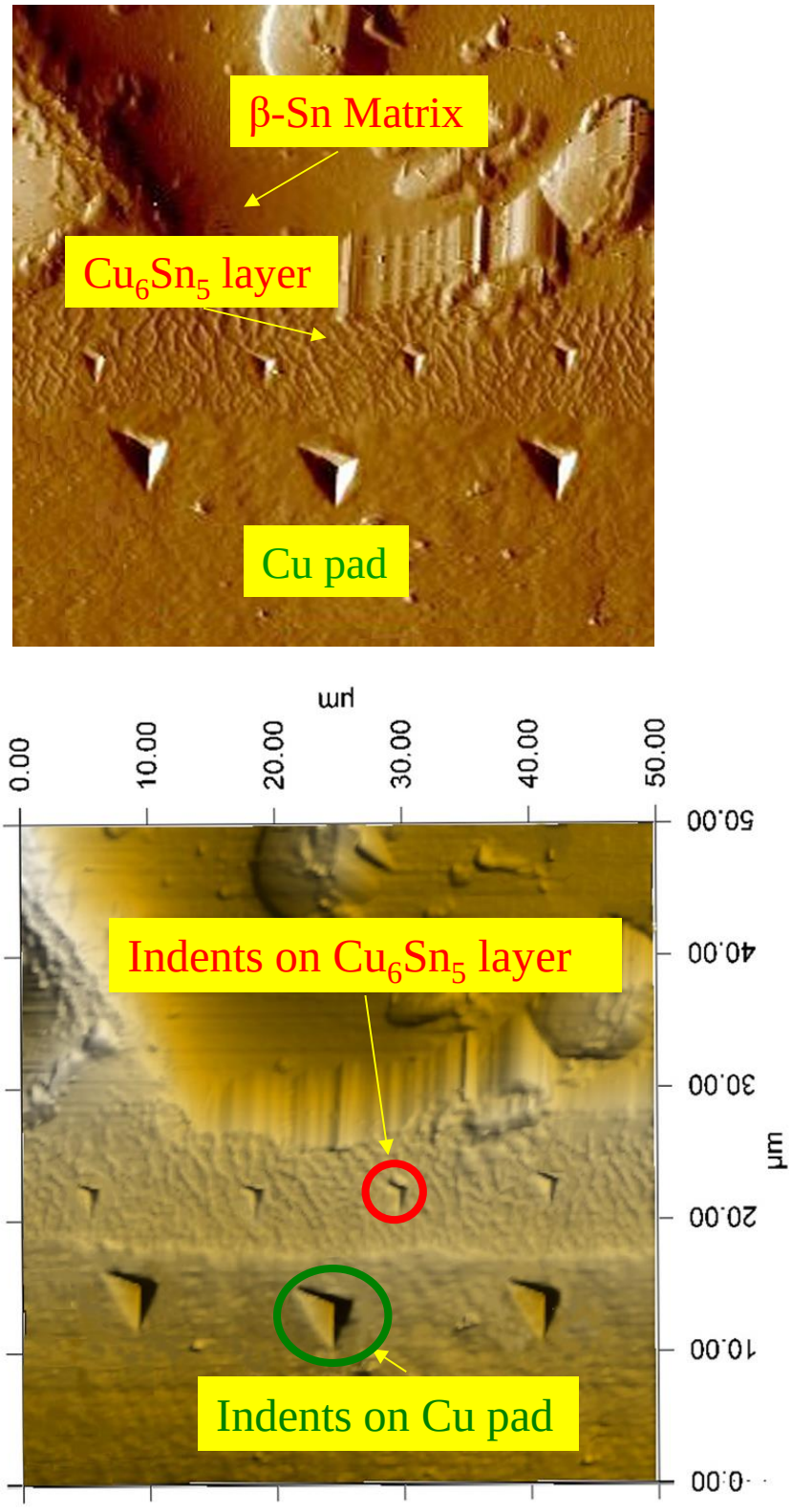

Figure 5.10 SPM Images of Indents after Nanoindentation Test

5.7 High Temperature Nanoindentation Tests of Intermetallics

Understanding the mechanical properties of IMCs and increased knowledge about their behavior in different operating conditions becomes desirable since the microelectronics industry has been facing significant challenges with these IMCs. The size of devices and solder joints are continuously decreasing, and, hence, the IMCs are occupying a key volume fraction of the entire package. Besides, electronic packages are now subjected to harsh operating conditions (i.e. extreme temperature). Understanding of the mechanical properties of these individual phases at various operating conditions makes predictions of the mechanical behavior of an overall joint more straightforward.

5.8 Sample Preparation for High Temperature Nanoindentation

Sample cross-sectioning and polishing procedure outlined in chapter 3, section 3.5 and 3.6 was followed to prepare samples for high temperature nanoindentation experiments.

5.9 High Temperature Nanoindentation System and Test Procedures

Hysitron TI 950 nanoindentation system has been used to perform the nanoindentation tests. A Berkovich indenter tip was chosen in this work. The extreme high temperature tests were performed in a high temperature stage (xSOL 400). During each indentation experiment, load versus indentation displacement response of the solder material in the direction normal to the cross-sectional surface was measured. Figure 5.11 shows the high temperature stage within the nanoindentation system, while Figure 5.12 shows images of a test sample in the high temperature stage.

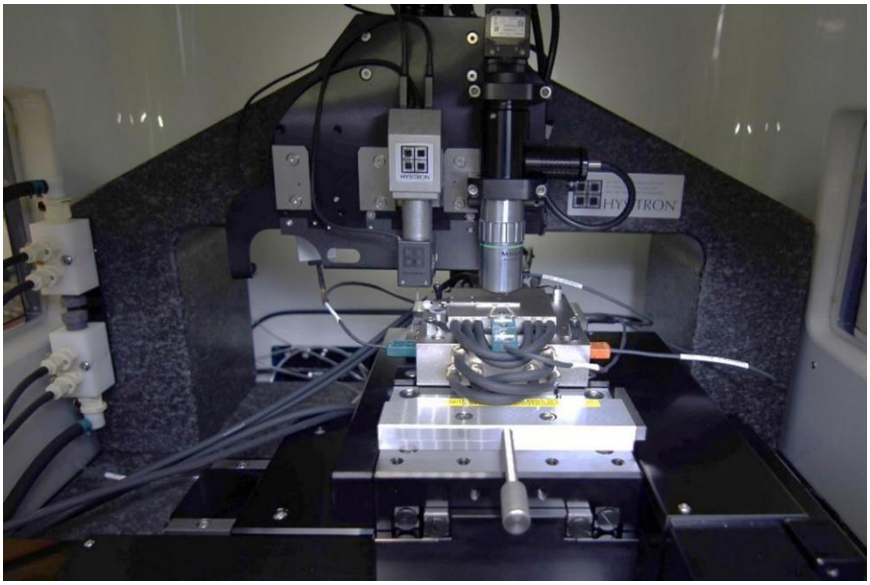

Figure 5.11 High Temperature Nanoindentation System

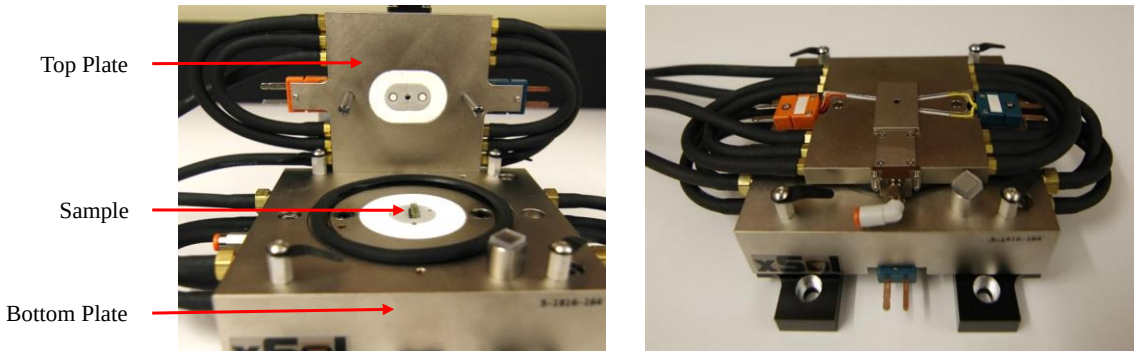

Figure 5.12 Solder Joint Sample in the High Temperature Stage

Nanoindentation testing was carried out by selecting arrays of regularly spaced indentations or by selecting random individual locations for indentation. While performing each indentation experiment, the load versus indentation displacement normal to the cross-sectional surface was measured. Peak load was reached at a loading rate of 600 μN/sec, and then the indenter tip was held at the peak load of 3000 μN for 2 sec for each individual

indent. The indenter was unloaded at the same rate of 600 µN/sec. The elastic modulus on the IMC was obtained using the approach proposed by Oliver and Pharr, by calculating the slope of the load-displacement curve in the unloading region of the test (figure 5.13). The peak load was kept small in order to ensure that the indent was not big enough to reach to phases other than the desired intermetallic.

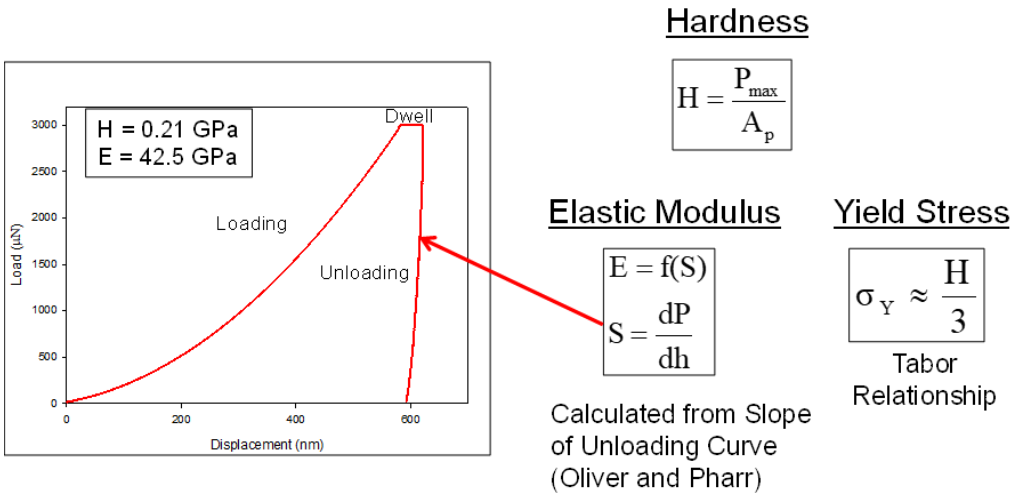

Figure 5.13 Modulus and Hardness Measurement in Nanoindentation

5.10 Measurement of High Temperature Creep Behavior

The displacement during the hold period of 900 second at the maximum load of 10 mN was utilized to obtain creep properties of the solder joint. An example of the measured displacement during the hold period versus time plot, for an array of indents performed on a single grain solder joint under similar test conditions, is presented in Figure 5.14. For creep testing, a longer hold time of 250 sec was applied at the peak load of 3000 µN. Creep data was recorded during this hold time and analyzed. To maintain accuracy of the results, indenter axis calibration followed by hardness and elastic modulus measurement calibrations were performed on standard fused silica and quartz samples. Moreover, every

test included a drift measurement and correction prior to the main indent that minimized the effects due to temperature fluctuations. For creep testing, an additional holding segment of 5 sec was applied prior to the creep holding time of 250 sec in order to predict and minimize thermal drift. The minimum drift rate was maintained at ≤ 0.05 nm/s.

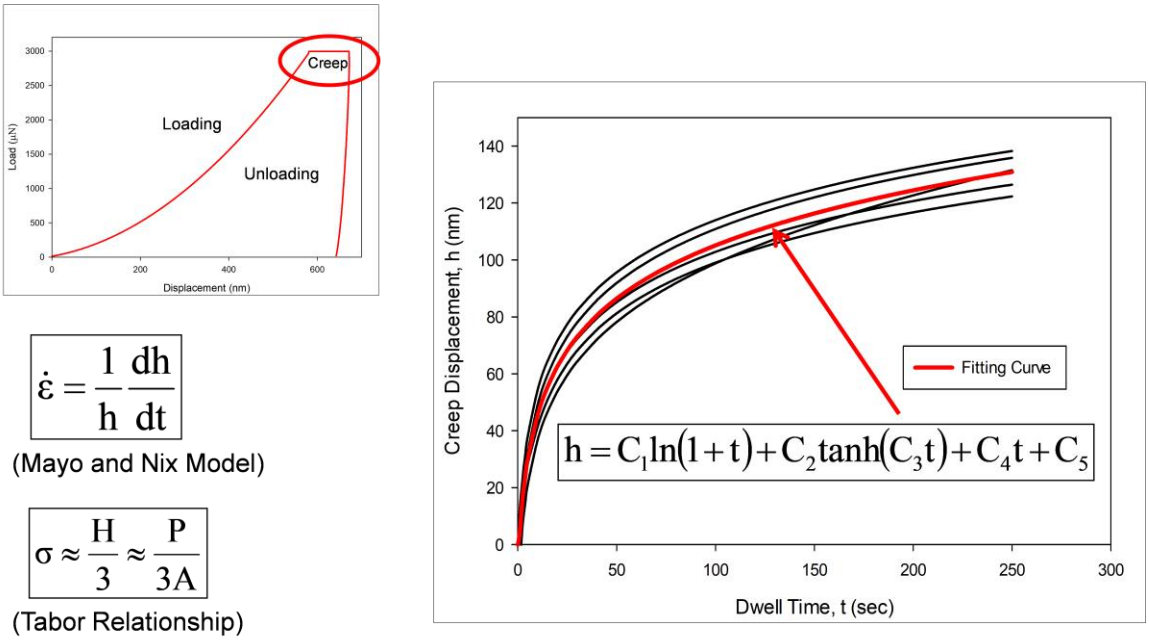

Figure 5.14 Creep Measurement in Nanoindentation

5.11 High Temperature Nanoindentation Test Results (25-125 °C)

5.11.1 Elastic Modulus and Hardness Measurements

Indentation test results of at least 10 indents were evaluated and then the average of those results was obtained. Figure 5.15 (a) shows the representative load –displacement behavior during indentation of Cu_6Sn_5 IMC from 25-125 °C. For the maximum load of 3000 μN, the maximum indentation displacement after unloading was found to vary in between 80-100 nm for Cu_6Sn_5 at 25 °C. At 125 C this value increased to vary between

160-175 nm. $(Cu_{1-x}Ni_x)_6Sn_5$ IMCs showed maximum indentation displacement in between 65-90 nm after unloading which became higher at 125 °C and varied in between 115-125 nm.

Representative load-displacement graph for $(Cu_{1-x}Ni_x)_6Sn_5$ intermetallics at five different temperatures is shown in Fig. 5.15(b). Ag_3Sn IMCs showed higher indentation displacement for the same maximum load which varied in between 130-160 nm at room temperature. With increasing temperature, the indentation depth of Ag_3Sn increased and varied in between 230-250 nm at 125 °C. Figure 5.15(c) showed the representative load-displacement graph for Ag_3Sn IMCs at five different temperatures. The indentation modulus and hardness measured in this work for 3 IMCs, β-Sn and Cu pad are shown in Table 1 & 2. At 25 °C, the Young's moduli and hardness determined from nanoindentation experiments for the three intermetallics are: 101.20±3.35 GPa and 5.80 ± 0.36 GPa for Cu6Sn5 at the joint and copper bond pad interface, 135.50±2.98 GPa and 8.61±0.41GPa for $(Cu_{1-x}Ni_x)_6Sn_5$ layers at the joint and ENIG plating finish interfaces, and 75.10±4.02 GPa and 3.25±0.50 GPa for Ag_3Sn IMC particles in the solder joint bulk. These are all much higher than the values of 42.67±2.3 and 0.21±0.12 GPa measured for β-Sn phase in solder joint bulk.

As the temperature increased, the elastic modulus and hardness value of Cu6Sn5 dropped about 23% and 32% respectively at 125 °C. Whereas the modulus and hardness of $(Cu_{1-x}Ni_x)_6Sn_5$ dropped about 11% and 15% respectively at 125 °C. Ag_3Sn, Cu-Pad and β-Sn showed significant changes in modulus and hardness values all of which are shown in Table 1 and 2. Modulus and hardness of Ag_3Sn decreases to 48.50 ± 3.20 GPa and 1.08

± 0.41 GPa respectively which is about 35% and 66% lower than the room temperature values.

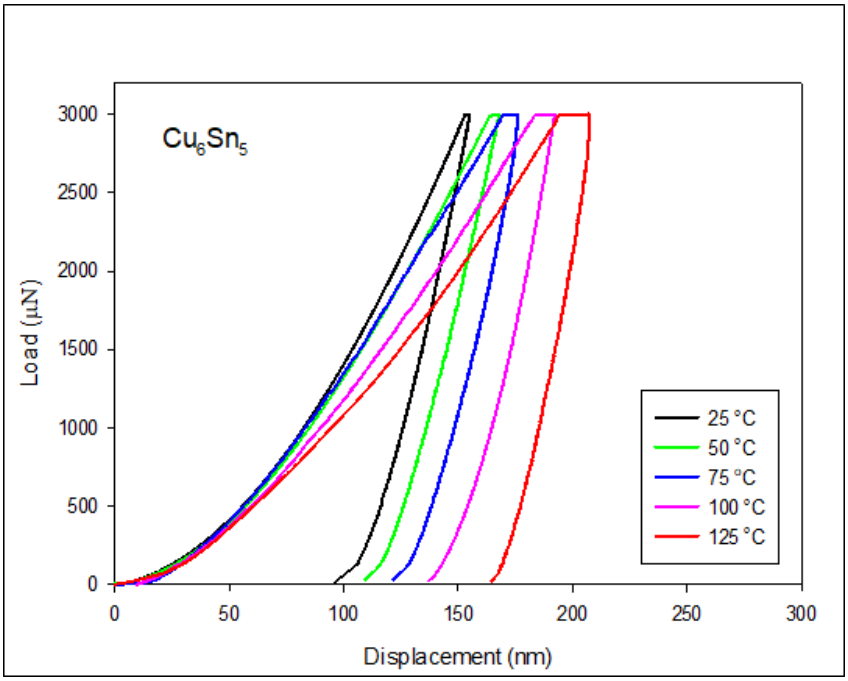

(a)

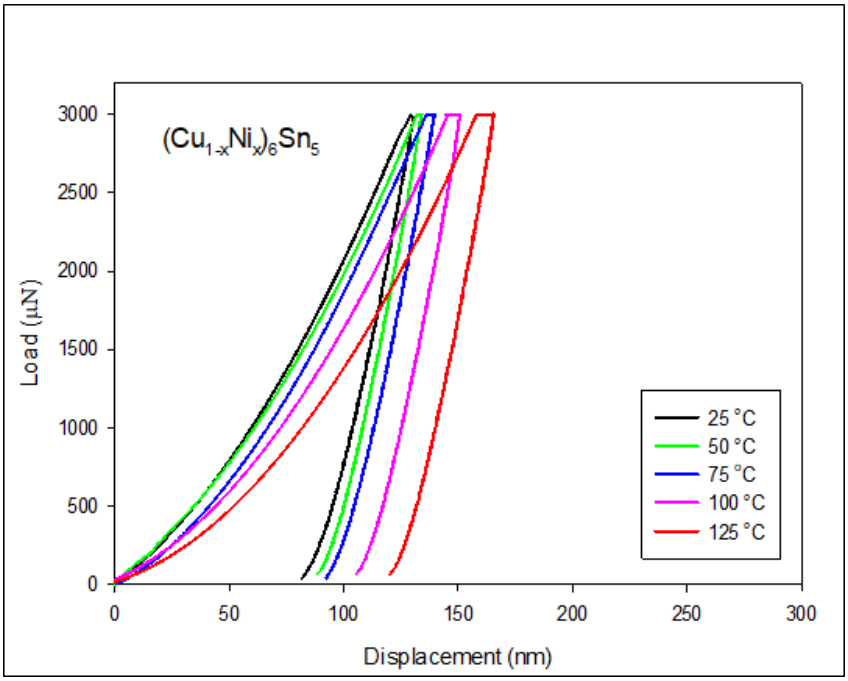

(b)

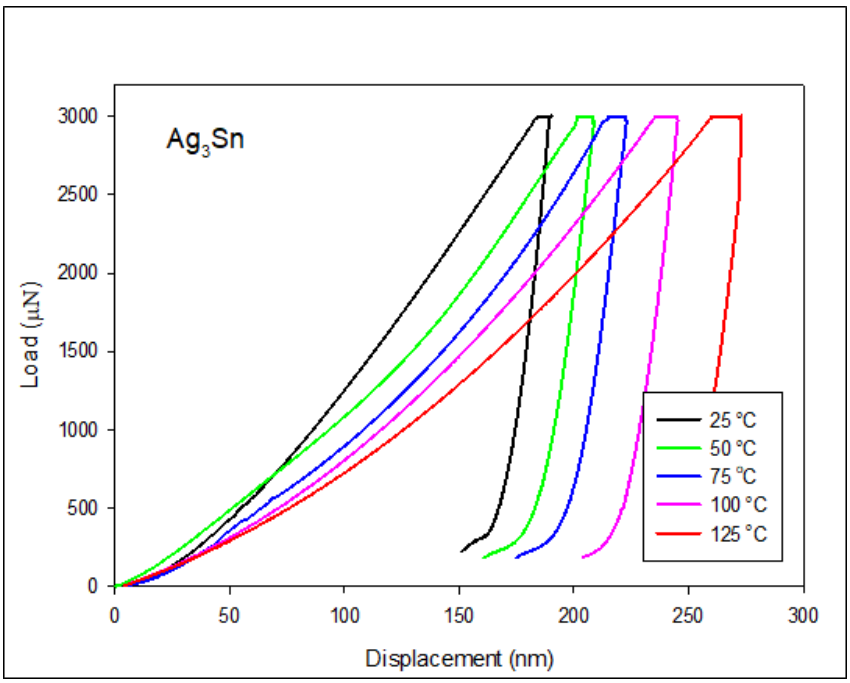

(c)

Figure 5.15 Load- Displacement Curve for (a) Cu_6Sn_5 (b) $(Cu_{1-x}Ni_x)_6Sn_5$ & c) Ag_3Sn IMCs from 25-125 °C

It was also observed that the elastic modulus of Cu_6Sn_5 IMC was similar to that of pure Cu, while the modulus of $(Cu_{1-x}Ni_x)_6Sn_5$ was comparatively higher. In addition, the results showed that the Cu-Sn and Cu-Ni-Sn IMCs were found to have hardness values in the range of typical ceramics, while the hardness of the Ag_3Sn particles was similar to the value found for many metals and alloys. This indicates that the Cu-Sn alloys have the potential for crack initiation due to brittle behavior. On the other hand, Ag_3Sn has a lower modulus and hardness, and is thus relatively soft and ductile and would not likely be a source of crack initiation.

Figure 5.16 shows change of modulus and hardness as function of temperature. It can be seen that modulus drops linearly with temperature whereas hardness changes nonlinearly with temperature form 25-125 °C.

Table 5.4 Modulus of IMCs as a Function of Temperature

Phase	Elastic Modulus, E (GPa)				
	25 ºC	50 ºC	75 ºC	100 ºC	125 ºC
$(Cu_{1-x}Ni_x)_6Sn_5$	135.5± 2.98	132.5± 3.94	128.6± 4.07	123.1± 3.25	118.3± 5.87
Cu_6Sn_5	101.2± 3.35	97.66± 2.58	93.51± 3.36	86.67± 3.97	78.23± 3.36
Ag_3Sn	75.10± 4.02	70.18± 3.67	64.15± 2.87	57.30± 4.37	48.50± 3.20
Cu Pad	106.8± 2.1	100.3± 2.97	95.16± 5.50	89.27± 4.05	82.67± 5.27
`β-Sn	42.67± 2.3	35.85± 1.5	27.67± 2.05	18.67± 1.65	10.07± 2.21

Table 5.5 Hardness of IMCs as a Function of Temperature

Phase	Hardness, H (GPa)				
	25 ºC	50 ºC	75 ºC	100 ºC	125 ºC
$(Cu_{1-x}Ni_x)_6Sn_5$	8.61± 0.41	8.42± 0.35	8.20± 0.47	7.88± 0.26	7.30± 0.44
Cu_6Sn_5	5.80± 0.36	5.52± 0.25	5.24± 0.44	4.75± 0.22	3.94± 0.35
Ag_3Sn	3.25± 0.50	2.86± 0.46	2.34± 0.23	1.75± 0.19	1.08± 0.41
Cu Pad	1.88± 0.023	1.61± 0.252	1.53± 0.146	1.33± 2.05	0.98± 0.23
β-Sn	0.21± 0.012	0.15± 0.002	0.13± 0.017	0.09± 0.018	0.06± 0.015

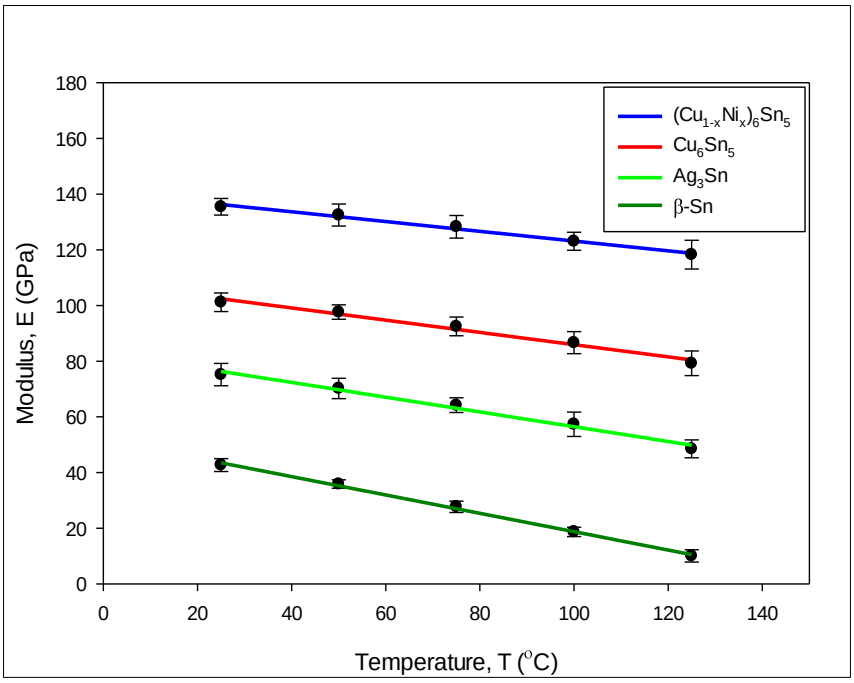

(a)

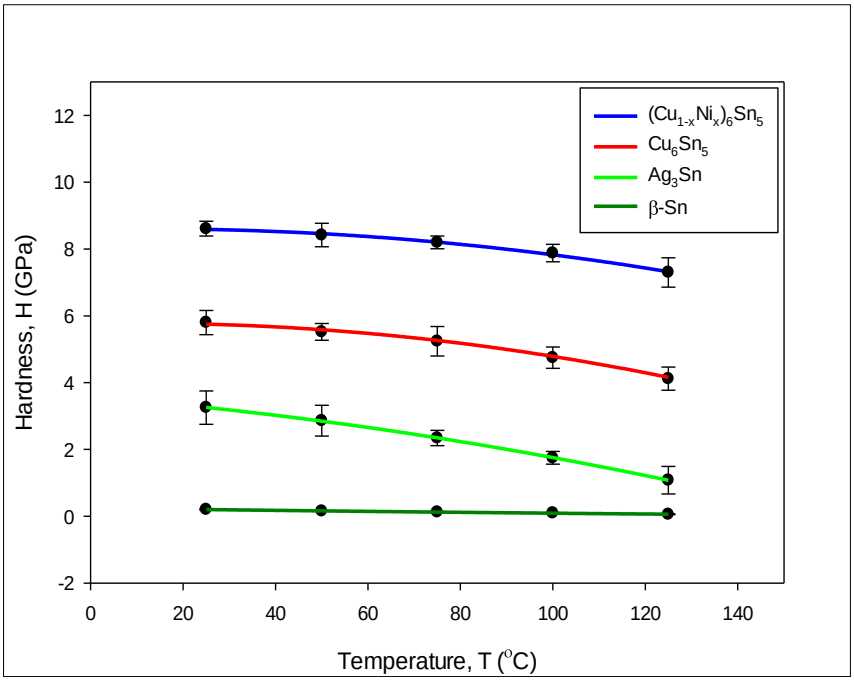

(b)

Figure 5.16 Modulus and Hardness as a Function of Temperature (25-125 °C)

5.11.2 Explore Substrate Effect for Nanoindentation

Since nanoindentaion is performed on IMCs thatare very hard and underneath is the soft solder layer. Hence, during indentation testing soft solder can also deform with IMCs causing additional deformation for indentation and affect the results. This is called the substrate effect. To avoid that, researchers found that if the indentation depth is less than 10% of the total depth of the IMCs, the substrate effect can be avoided. To explore that, FIB analysis was performed to measure depth of IMCs which was evaluated around 7 µm (Fig. 5.17). The highest nanoindentation depth obtained was about .25 µm at 125 ^{o}C, which is about 3.6 % of the depth of IMC (much less than 10% rule [145]. This confirms that the indentation results were not influenced by the substrate affect.

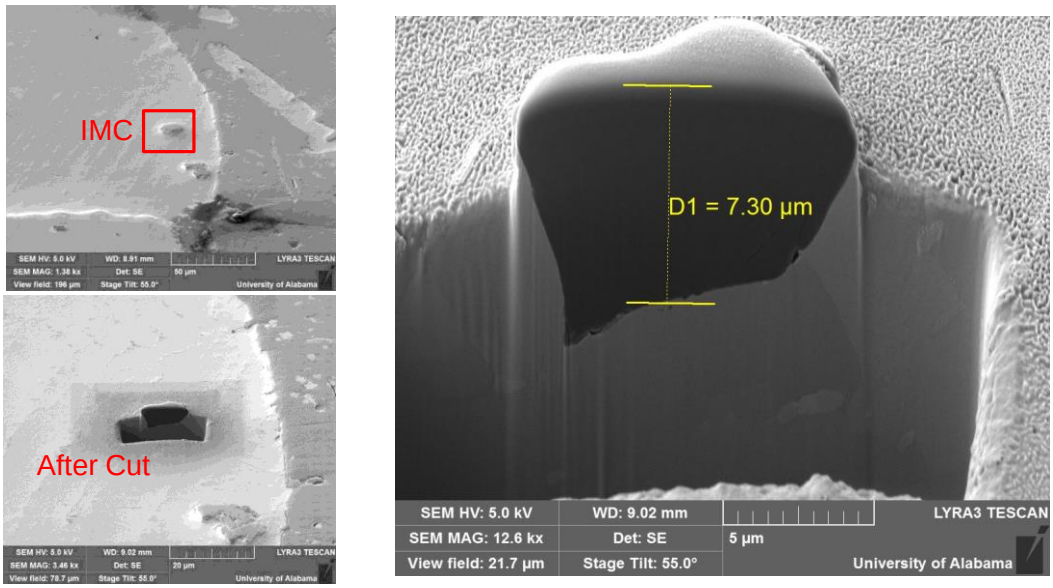

Maximum Indentation Depth is only 3.6% of IMC Thickness.
Recommended: <10% to Avoid Substrate Effect

Figure 5.17 Explore Substrate Effect in IMCs during Nanoindentation

5.11.3 High Temperature Creep Results

Figure 5.18 (a) illustrates representative creep displacement curves (creep displacement vs. time) for the three IMC materials and the β-Sn phase of solder material for a peak load of 3000 μN at 25 and 100 °C. Each of these curves were obtained by fitting eq. (1) to the data for five indentation creep tests for each material at two different temperatures. It was observed that the β-Sn had the largest creep displacements, followed by Ag_3Sn. The Cu_6Sn_5 and $(Cu_{1-x}Ni_x)_6Sn_5$ IMC layers had the smallest creep displacements. For example, at 25 °C for the dwell time of 100 sec, which lies in the secondary creep region, the $(Cu_{1-x}Ni_x)_6Sn_5$ IMC had 6.5 nm of creep displacement, while Cu_6Sn_5 IMC had a slightly higher value of 8.5 nm. On the other hand, Ag_3Sn particle had 20 nm of creep displacement, which is twice the value of Cu6Sn5 and three times higher than $(Cu_{1-x}Ni_x)_6Sn_5$. The β-Sn phase had a very high displacement value of 100 nm, indicating large plastic deformations during indentation creep. While the temperature was increased to 100 °C, the creep deformation on the $(Cu_{1-x}Ni_x)_6Sn_5$, Cu_6Sn_5 and Ag_3Sn IMCs at the same time increased to 14, 27 and 36 nm respectively. Creep deformation at β-Sn phase increased to 142 nm at 100 °C.

Figure 5.18 (b) shows the variation of strain rate with stress for four different materials. While the strain rate vs. stress curves for the four materials did not overlap in stress (cover the same range of stresses), it is clear that the β-Sn matrix has the highest strain rates for a given (fixed) stress value, followed by the Ag_3Sn IMC particles, Cu_6Sn_5 IMC layer, and then the $(Cu_{1-x}Ni_x)_6Sn_5$ IMC layer with the lowest strain rates. As the temperature was increased to 100 °C, all the curves shifted towards left and upward. The

shifting is much prominent in the β-Sn phase and least in $(Cu_{1-x}Ni_x)_6Sn_5$ IMC. This indicated that with increasing temperature higher strain rate is achieved at lower indentation stress. However, it is clear that IMCs showed less increase in strain rate compared to the β-Sn phase. Figure 5.18 (c) shows the log-log plot of strain rate vs. stress data from Figure 5. 18 (b). The responses are quite linear, and the slopes of the results for each material have been calculated using a least squares regression fit. At 25 °C, the creep stress exponents of the $(Cu_{1-x}Nix)_6Sn_5$, Cu_6Sn_5, and Ag_3Sn IMCs were found to be 43.9, 33.3, and 13.6, respectively. The β-Sn matrix phase had a much smaller creep exponent value of 8.4. These creep exponent values went down when the temperature was raised to 100 °C. These results are in reasonable agreement with those from previous nanoindentation creep studies on lead free solders.

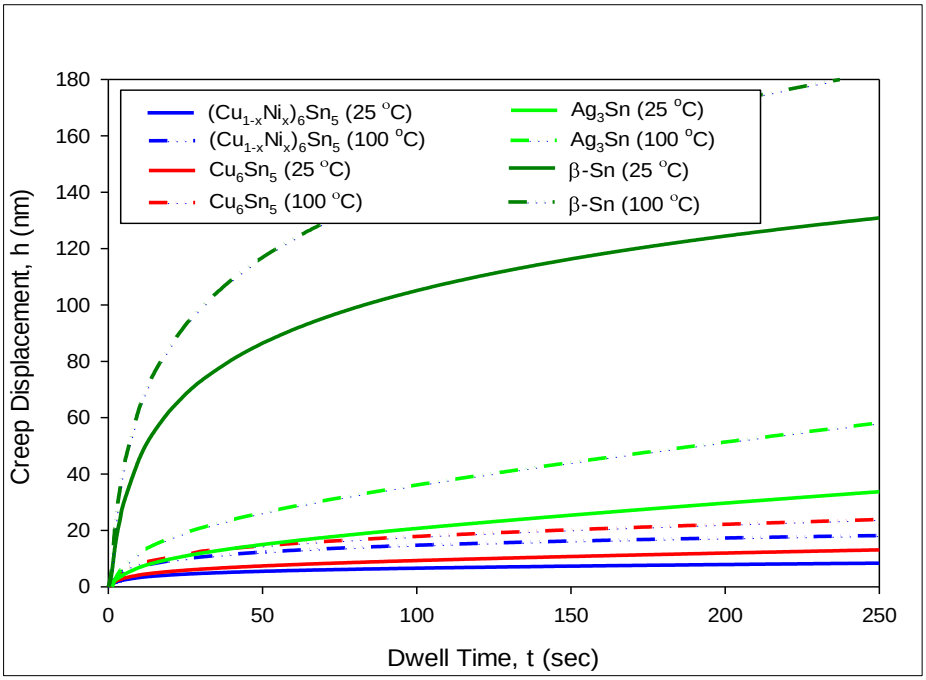

(a)

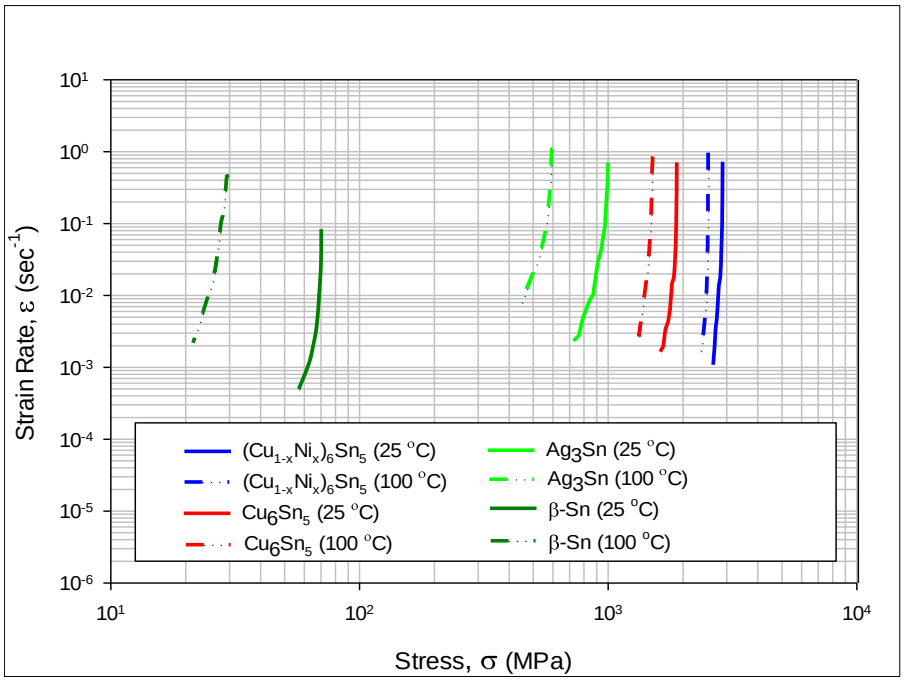

(b)

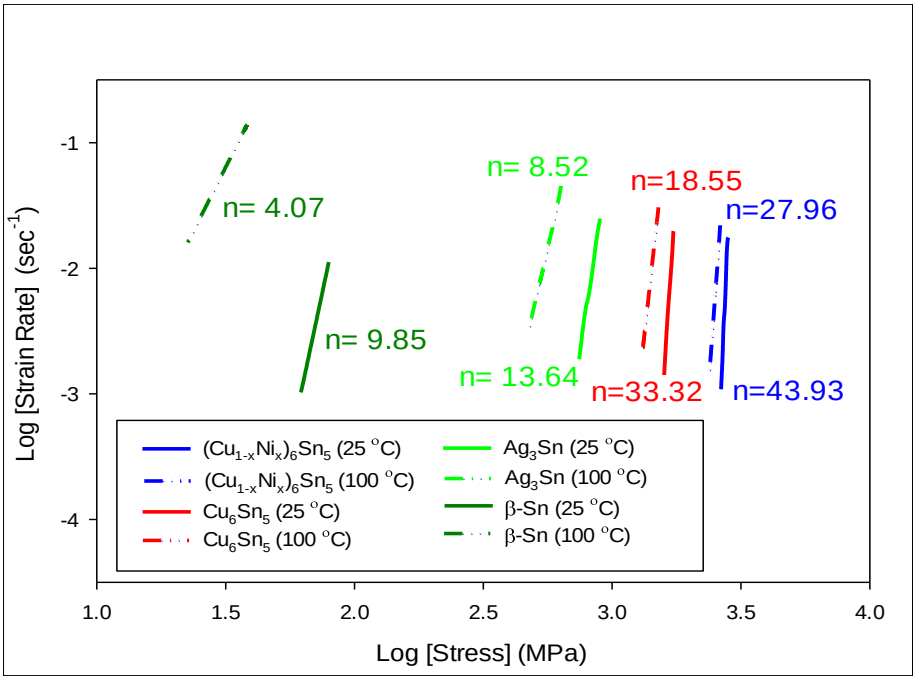

(c)

Figure 5.18 Modulus and Hardness as a Function of Temperature (25-125 °C)

5.12 Summary and Discussion

In this chapter, the mechanical behaviors of IMC particles and layers in SAC solder joints have been characterized using nanoindentation. SAC 205 BGA solder joints were first aged for 6 months at T = 125 ^{o}C. Test samples were subsequently prepared by cross-sectioning the aged solder joints, and then molding them in epoxy and polishing them to prepare the joint surfaces for microscopy and nanoindentation.

Intermetallics formed in the bulk solder region, copper pad and SAC solder interface, and ENIG plating finish and SAC solder interface were observed and detected using SEM and the energy dispersive x-ray spectroscopy (EDX) technique. The same intermetallics were then indented to measure their room temperature mechanical properties including the elastic modulus, hardness, and creep strain rate. To ensure the indentation occurred at the desired phase, SPM imaging was done prior and after the indentations. As expected, the measured properties of the IMCs were significantly higher than the Sn matrix forming the solder joints.

The measured elastic modulus and hardness values were 101.20±3.35 GPa and 5.80 ± 0.36 GPa for Cu_6Sn_5 at the joint and copper bond pad interface, 135.50±2.98 GPa and 8.61±0.41GPa for $(Cu_{1-x}Ni_x)_6Sn_5$ layers at the joint and ENIG plating finish interfaces, and 75.10±4.02 GPa and 3.25±0.50 GPa for Ag_3Sn IMC particles in the solder joint bulk at 25 °C . These are all much higher than the values of 42.7 ± 2.3 and 0.21 ± 0.12 GPa measured for the β-Sn phase in the solder joint bulk. With increasing temperature these values were reduced and became significantly lower at 125 °C. Creep testing performed at 25 °C revealed that the $(Cu_{1-x}Ni_x)_6Sn_5$ IMC layers had the lowest creep deformation, then Cu_6Sn_5 and then Ag_3Sn IMC particles. β-Sn phase showed the highest creep deformation. At 100

°C creep deformation increased which is significantly higher for β-Sn compared to the IMCs.

CHAPTER 6

MECHANICAL CHARACTERIZATION OF INDIVIDUAL PHASES (IMC AND β-SN PHASE) IN PB-FREE SOLDER JOINTS DURING ISOTHERMAL AGING

6.1 Individual Phases of SAC Solder Joint

Electronic devices are subjected to severe conditions during service that exposes solder joints to elevated temperatures. This causes significant change in the performance of SAC solder alloys due to evolution of the microstructure, which consists primarily of β-Sn, eutectic Sn, and Ag–Sn and Cu–Sn intermetallic compounds (IMCs). The entire mechanical properties of the solder joints are dictated by the IMCs, which are generally hard and brittle in nature. Exposure to high temperatures causes thermal coarsening due to which the size of these IMCs grows. Since the mechanical properties of a lead free solder are strongly influenced by its microstructure, hence mechanical response, failure and fatigue behaviors of lead free solder joints in electronic assemblies are affected when subjected to isothermal and/or thermal cycling operating conditions. Moreover, the aging phenomena can further deteriorate the solder joints since the microstructure is constantly evolving (degrading) with time. This alters the structural reliability of the whole assembly and thus become a concern for the researchers for past decades. Many researchers have studied constitutive and failure behaviors of SAC solder alloys due to aging affect extensively. In early investigations, it was seen that, the mechanical properties and creep

behavior of SAC alloys were severely degraded by prior exposure to room temperature (25 ^{o}C) and elevated temperature (50, 75, 100, and 125 ^{o}C) aging conditions. Stress-strain data obtained from these studies demonstrated large reductions in yield stress, stiffness, and ultimate strength during the first 6 months after reflow solidification.

6.2 Aging Effect on Individual Phases of SAC Solder Joint

A Single solder joint consists of various phases i.e. (β-Sn,eutectic phase, IMC particle/layer). However, most of the studies deal with the overall/global property of the solder alloy which were found to decrease with aging [179]. The primary reason was considered as the coarsening of the IMC particles in the bulk solder region. However, very few studies were performed to measure properties of small individual phases (β-Sn, Eutectic phase, IMC particle/layer). Moreover, systematic study to measure properties of these small phases due to isothermal aging were not studied much. In addition, it was not understood whether these phases could possibly degrade with aging and contributes to the overall degradation of the solder joint. Measurement of the mechanical properties of individual phases in a solder joint is now possible using an instrumented indentation technique commonly known as nanoindentation. This nanoindentation technique has now received a great attention to researchers as valuable method for obtaining the mechanical behavior of materials at very small scales by probing, i.e. it has capability to measure the properties of materials in very thin films and coatings. This technique is well suited to investigate mechanical properties of solder joints and IMC particles that exist in bulk solder region. Testing with this tool can be done to probe small volumes by utilizing a diamond indenter tip attached to a sensitive capacitive transducer, which is operated at ultralow load

(e.g., 0.1–10 mN). Throughout the testing load and displacement of the tip are measured which allows the user to determine elastic modulus from the unloading curve. It also gives measurement of hardness by calculating depth at the maximum load point. In this study, we have measured the mechanical properties of individual Sn grain and IMC particles in a solder joint using nanoindentation technique during isothermal aging at 125 ^{o}C. SAC solder joints extracted from Super BGA (SBGA) packages were aged for different time intervals (0, 1, 5, 10 and 30 days). Nanoindentation test samples were prepared by cross sectioning the solder joints, and then molding them in epoxy and polishing them to prepare the joint surfaces for nanoindentation. Several tests were recorded to measure modulus, hardness and creep behavior with aging at 25 ^{o}C and average representations of those results are shown in this work.

6.3 Super BGA Solder Joints

The lead-free solder joints in this study were obtained from Super BGA assemblies with following specifications: 31 x 31 mm, 304 balls, 0.8 mm ball diameter, and 1.27 mm ball pitch. In this work, the solder alloy considered was SAC305 (97.5Sn- 3.0Ag-0.5Cu). The test boards had electroless nickel immersion gold (ENIG) surface finish on package side, and SAC305 solder paste was used in the surface mount assembly process. The assembled PBGA components were cut out from the test boards, and then they were cross-sectioned using an IsoMet precision cutter. Figure 6.1 shows the optical image of a cross-sectioned super BGA solder joint. Fig. 6.1(a) (c) (e) shows the normal view and 6.1(b) (d) (f) shows the polarized view of the joint. From the polarized view it was found that, the joint had different tin grains, which was represented by three different colors. For this

study, we chose to indent on grain 1 and grain 2 of first joint Figure (a) and (b) to obtain properties of β-Sn due to large area available for indentation.

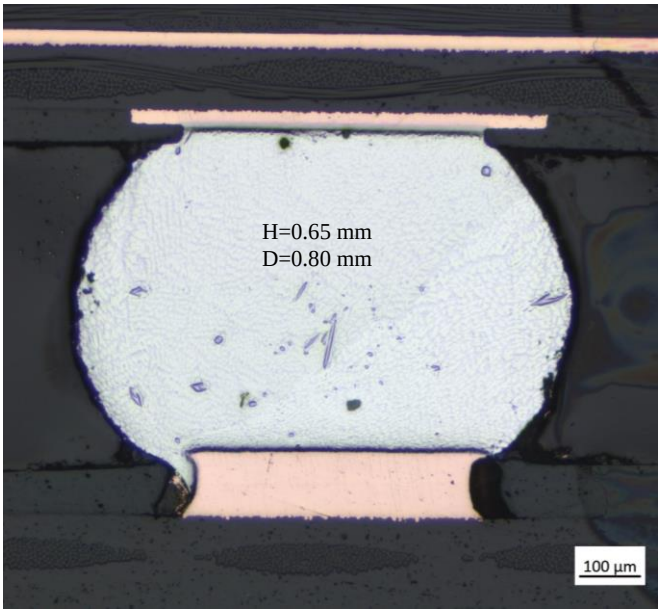

Normal View

(a)

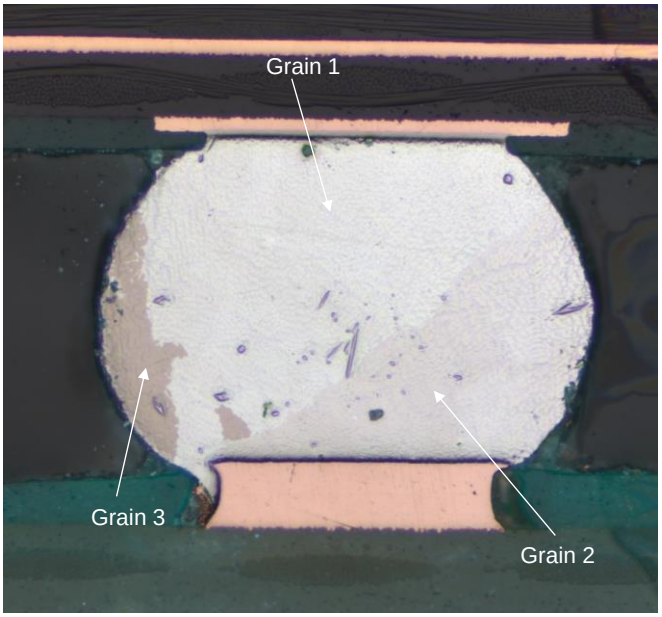

Polarized View

(b)

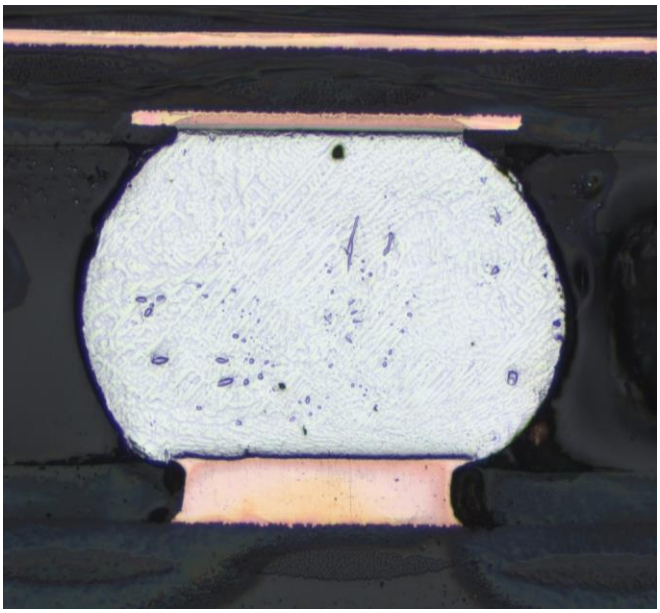

Normal View

(c)

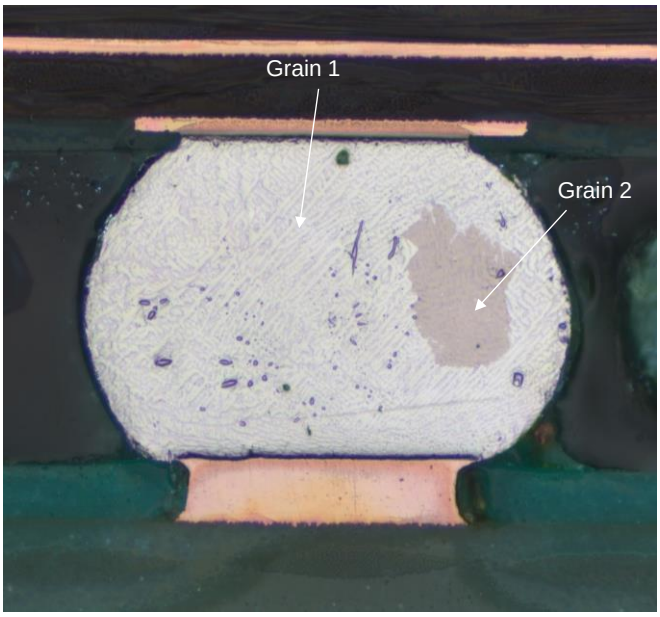

Polarized View

(d)

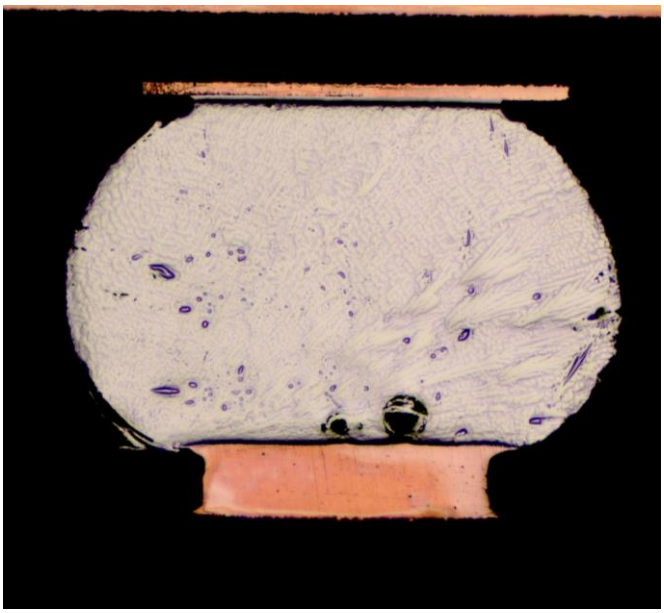

Normal View

(e)

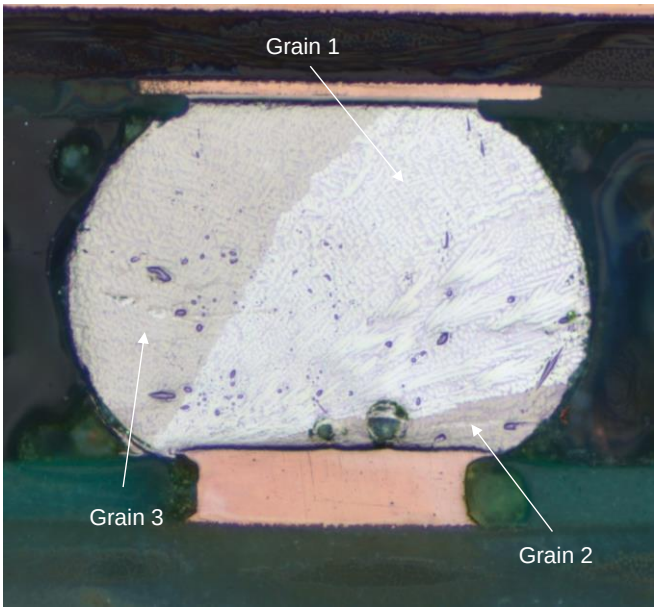

Polarized View

(f)

Figure 6.1 (a) (c) (e) Optical Microscopy and (b) (d) (f) Polarized Microscopy of Super BGA Solder Joints

6.4 Identification of Individual Phases

Figure 6.2 shows different phases present in the super BGA solder joint. The white phases of β-Sn were clearly observed with two different grains. Very small Ag_3Sn IMC particles were observed in the Sn matrix. In addition, bigger size IMC particles were observed in the bulks solder region (primarily (Cu_6Sn_5 and Ag_3Sn). For this study, we only perform nanoindentation on the bigger size particles before and after aging.

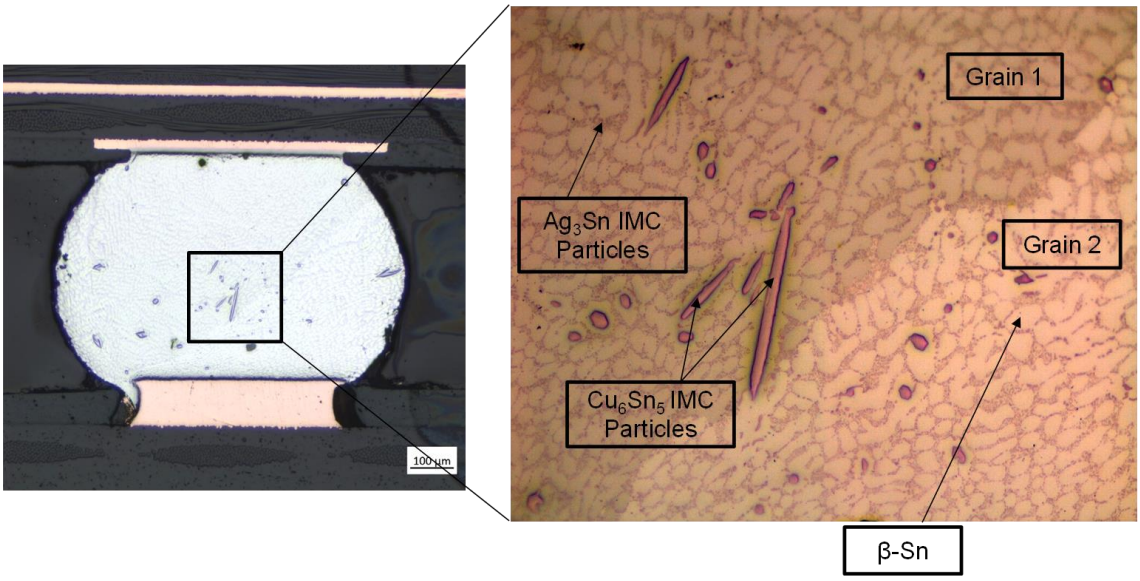

Figure 6.2 Identification of Different Phases in Solder Joints

6.5 Factors Influence in Nanoindentation Test Results

During indentation, two factors affect the nanoindentation test results which need to be considered carefully. First factor is holding time and second factor is surface effect. These two factors need to be established before indenting on individual phases.

6.5.1 Influence of Holding Time on Modulus and Hardness

The SAC solder alloys are soft and shows deformation due to creep. Creep affect influences the initial portion of the nanoindentation-unloading curve by producing bulging affect and thus provide erroneous modulus and hardness value. Figure 6.3(a) and (b) reveals the typical load-displacement curves on standard polycarbonate and β-Sn between without holding between loading and unloading respectively. The bulging out at the initial part of the unloading curve shows the primary creep effect clearly, which indicates that the creep of β-Sn is unavoidable during nanoindentation tests on SAC with no holding time. Apparently if those creep effects were not accounted for, the mechanical properties determined from fitting the unloading curves would be highly unreal and contain errors. However, for the standard quartz and IMCs this creep effect was not that prominent at no holding time (Fig. 6.4(a) and (b)). The IMCs are hard and expected to be resistant to creep.

In order to investigate the creep effect on the mechanical properties (modulus and hardness) of SAC solder alloy measured by nanoindentation, different holding times were tried out in the test to find the optimal holding time to minimize the creep affect. In Fig. 6.5 (a) and (b), one can see that the creep effect became ignorable and gives stable value when the holding time (HT) was longer than 15 sec. Thus, in order to minimize the effect of creep, a 20-second holding time was chosen for the present study. On the other hand, since creep effect is less, holding time for the IMCs were chosen as 2 sec which was found to be sufficient enough to minimize creep effect (if there is any) in IMCs.

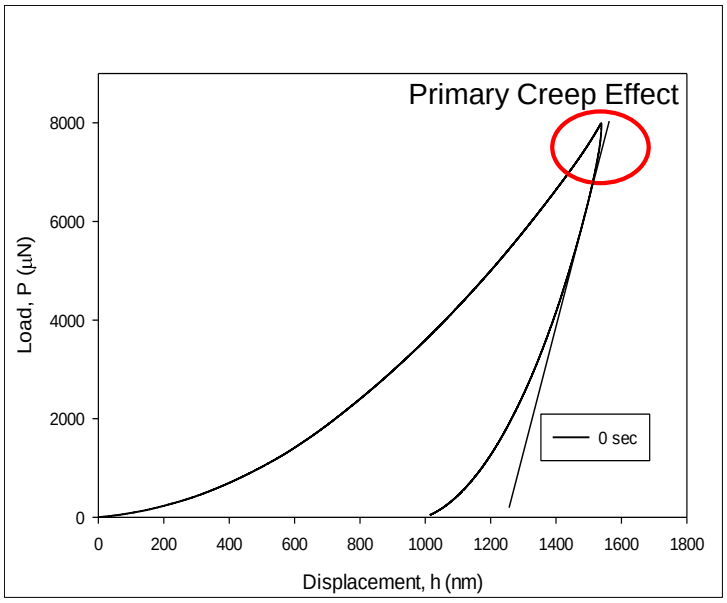

Standard Polycarbonate

(a)

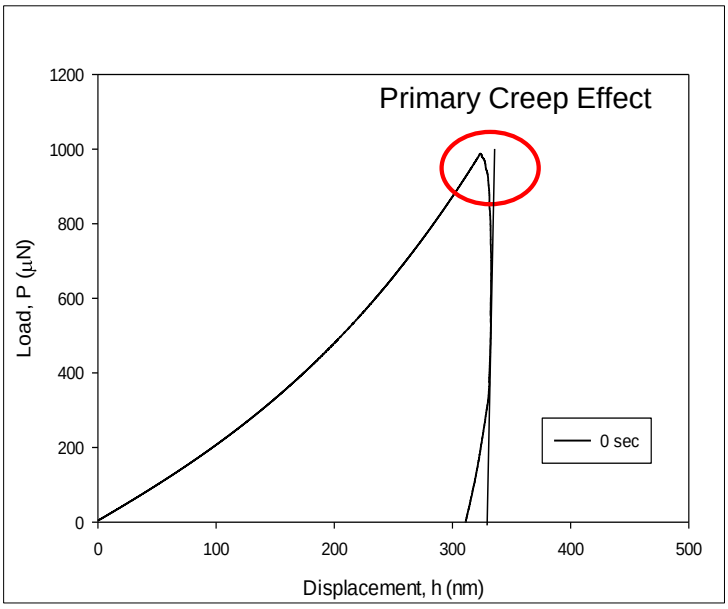

Solder Joint

(b)

Figure 6.3 Load –Displacement Curve (A) Standard Polycarbonate and (B) Solder

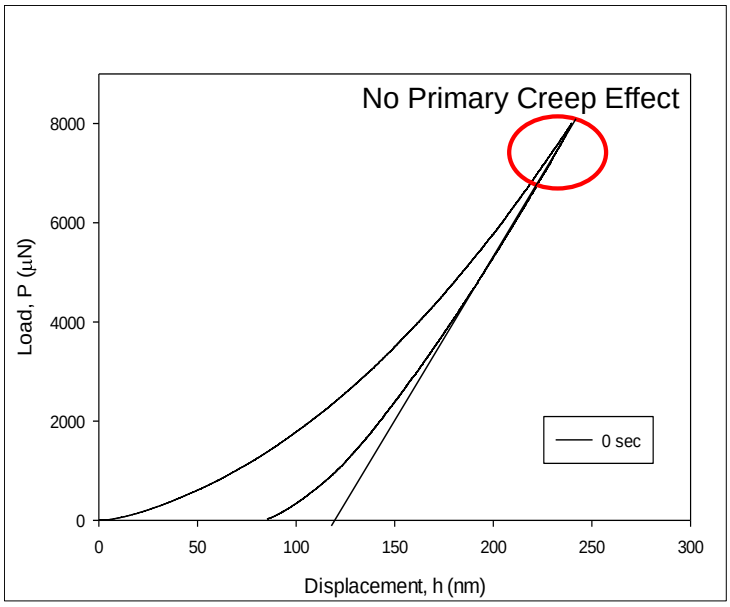

Standard Quartz

(a)

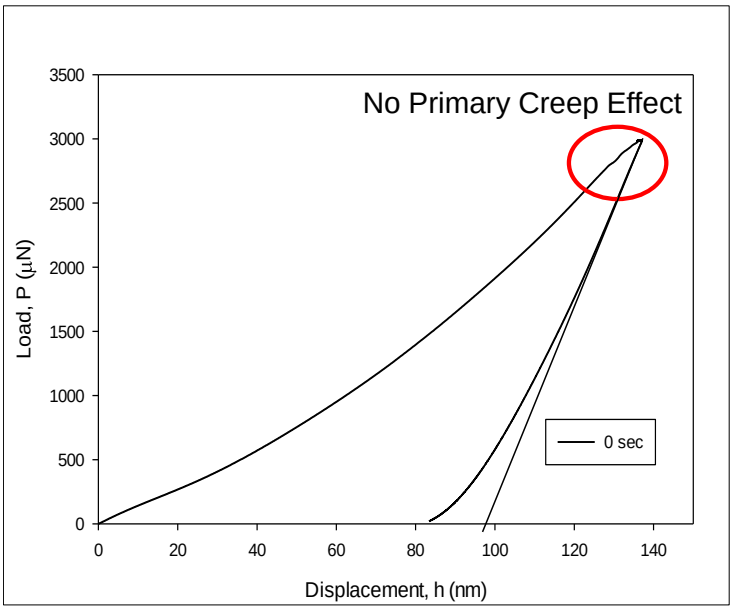

IMC

(b)

Figure 6.4 Load –Displacement Curve (A) Standard Quartz and (B) IMCs

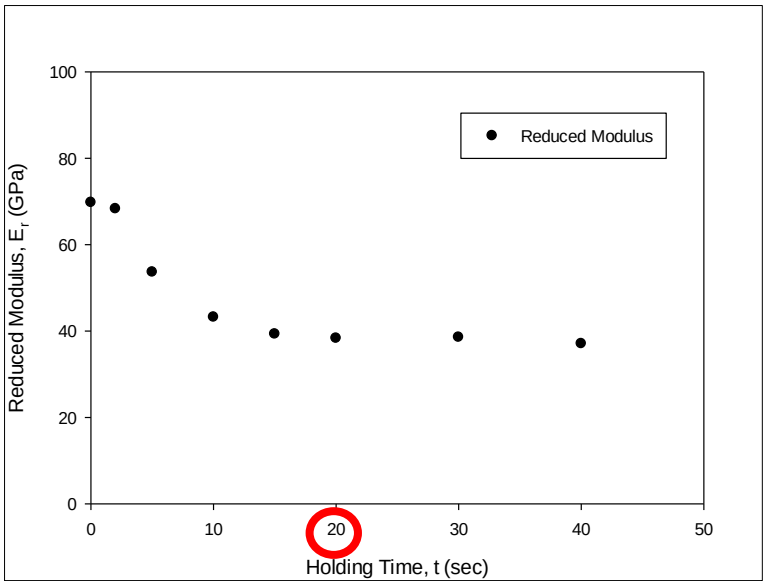

(a)

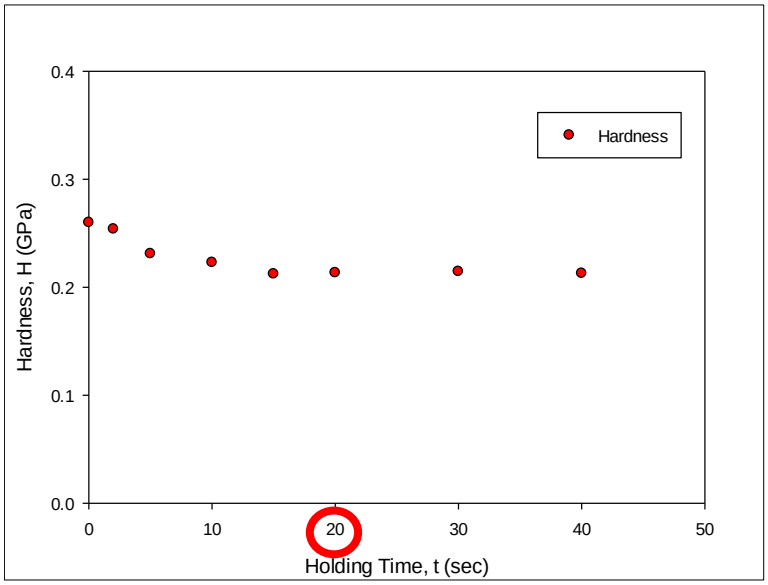

(b)

Figure 6.5 Variation of (A) Modulus and (B) Hardness with Different Holding Time

6.5.2 Influence of Surface Effect on Modulus and Hardness

Another parameter that affects the nanoindentation results is the surface affect. The modulus and hardness value does not show constant value at all indentation depths. The strain hardening effect during sample polishing and/or presence of surface inclusions could provide unstable properties for small indentations. To obtain a stabilized value, the modulus and hardness as a function of indentation depth were characterized. To accomplish this, a multiple load-partial unload testing protocol was performed on the β-Sn and IMC phases where a gradual loading, hold, and then a 50% unloading routine was utilized (Fig. 6.6). Each unload segment was then fitted to calculate the unloading slope and extract the modulus and hardness at a certain depth. Using this procedure multiple times, the modulus and hardness as a function of indentation depth were obtained. Results of this approach are shown in Fig. 6.7 for both β-Sn and the IMC phase. The results were found to stabilize and be independent of depth after approximately 200 nm of indentation depth for β-tin and 60 nm for the IMC phase. Thus, we have determined the E and H values in this work by choosing a load, which gives results at indentation depths higher than the above-mentioned values.

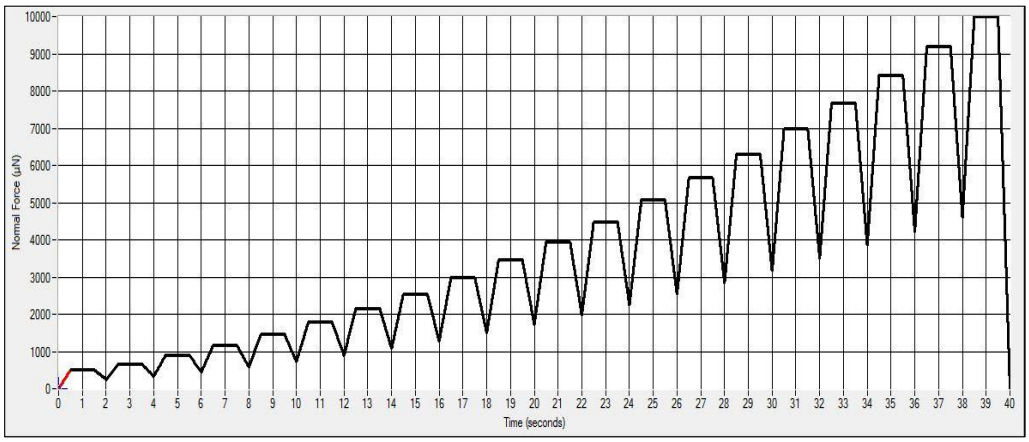

Figure 6.6 Multiple Load-unload Load Function

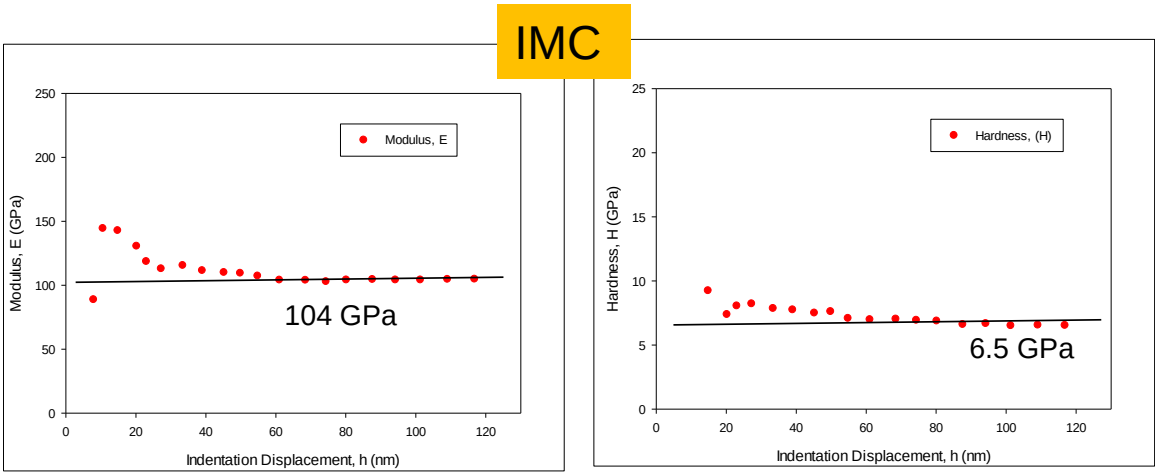

(a)

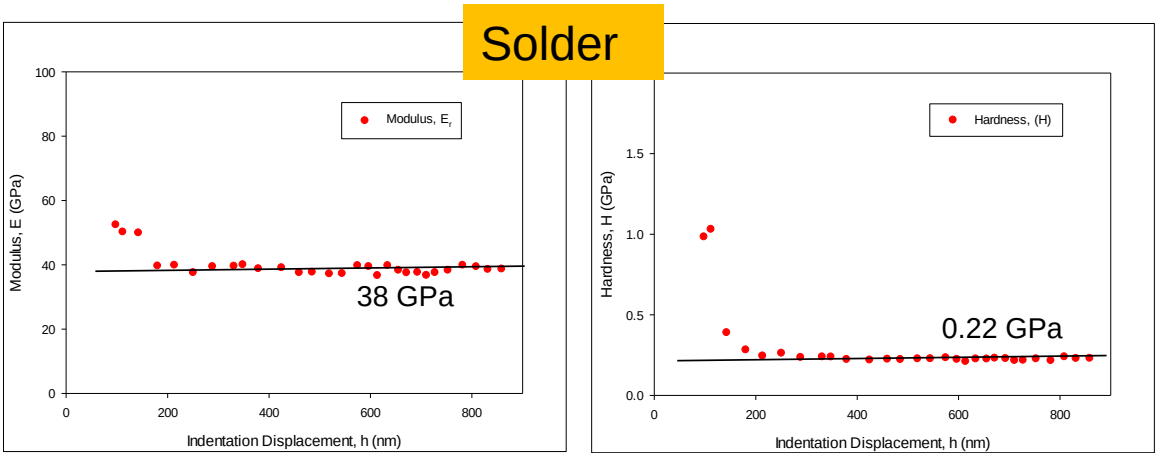

(b)

Figure 6.7 Variation of Modulus and Hardness of (a) IMC and (b) β-Sn

6.6 Modulus and Hardness Measurements on Individual Phases

As mentioned earlier, the modulus and hardness values were obtained using the Oliver and Pharr method and applying maximum load that provides maximum indentation depth at a stable region. Nanoindentation was performed on β-Sn (grain 1 and grain 2) at a load of 1000 μN. About 8-10 indents were performed and their modulus and hardness were measured. Average of those results were calculated which represents the modulus and

hardness of that grain. Figure 6.8(a) shows the representative load-displacement curve for grain 1 at zero days aging of the solder joint. It was seen from the figure that the indentation depth where the slope was calculated was about 350 nm, which lied in the stable depth region. On the other hand for grain 2 (figure 6.9 (a)), slope was calculated at indentation depth of about 370 nm which was also at the stable region. The modulus and hardness value was evaluated and the average representation is also listed below. SPM images of the indents performed is also shown in 6.8 (b) and 6.9 (b).

Nanoindentation was also performed on the IMCs to obtain modulus and hardness. A higher load was applied for the IMCs in order to obtain properties in the stable region. The representative load-displacement curve for the IMCs is shown in Fig. 6.10. The indentation modulus and hardness obtained was much higher than the β-Sn phase at no aging condition of the solder joint. Average value of modulus and hardness is also shown. Indents on the IMC particles are shown in Fig. 6.10 (b). One important factor that can affect the IMC properties is the soft solder below IMCs known as substrate effect. The general rule to avoid substrate affect in IMCs is to indent to a depth that is less than 10% of the thickness of the IMCs. We performed Focused Ion Beam (FIB) milling on IMCs to analyze their thickness. The depth of IMCs was found about 7~8 μm and the maximum indent depth in ours study was about .080~.090 μm which is about 1.2% of the IMC depth. This confirms that the indentation results were influenced very little by the substrate effect.

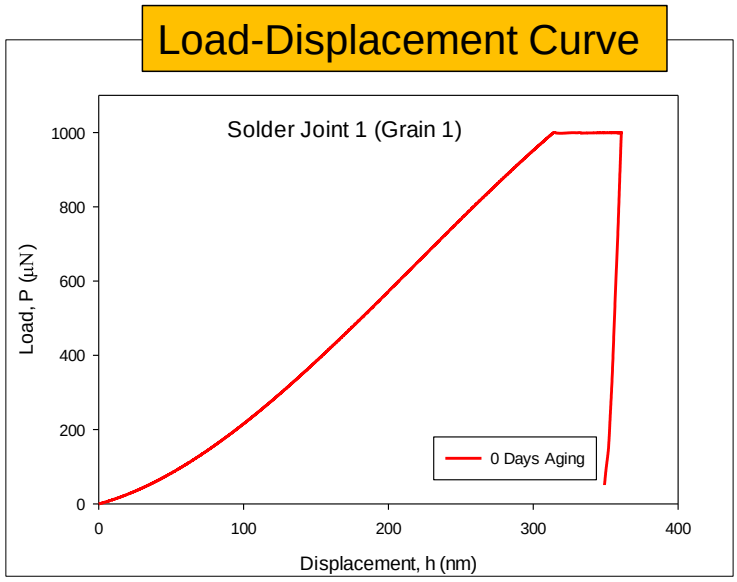

(a)

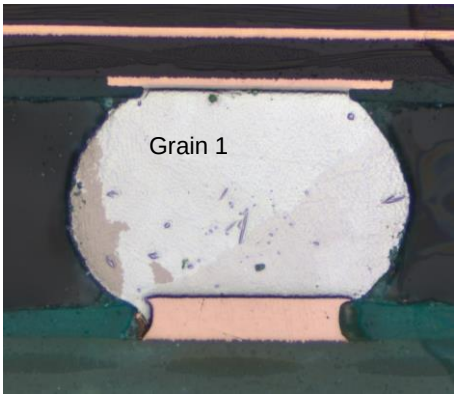

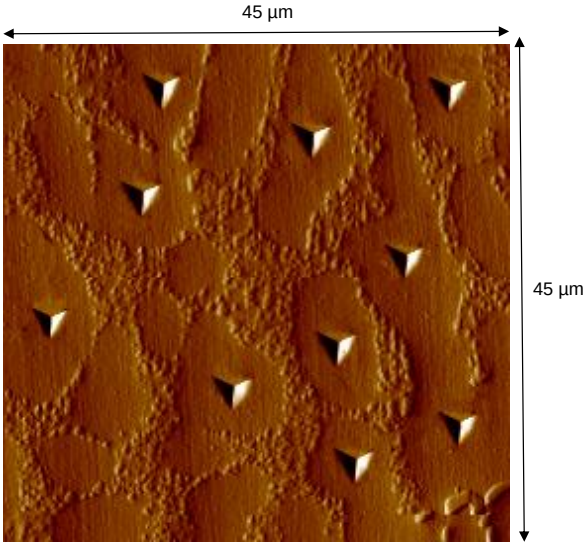

SPM Image of Indents on Grain 1

(b)

Figure 6.8 (a) Nanoindentation load-displacement curve for β-Sn (grain 1); (b) SPM imaging showing indents on grain 1

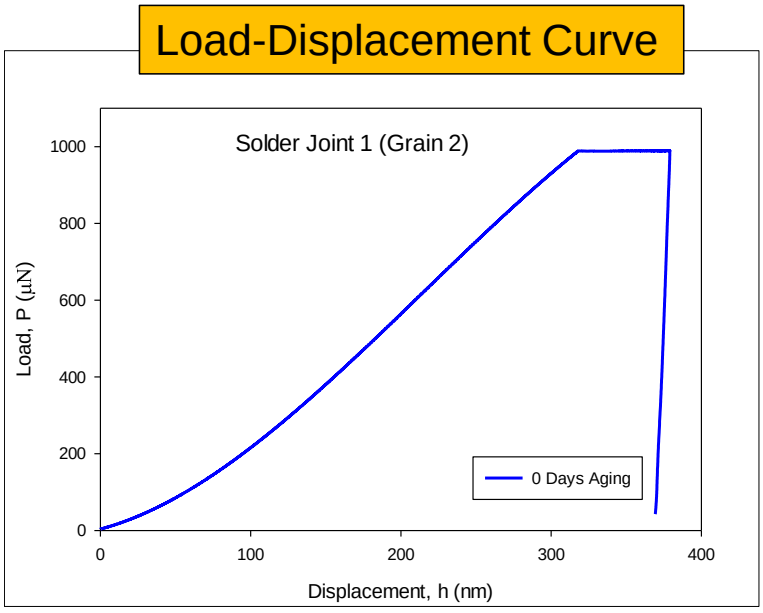

(a)

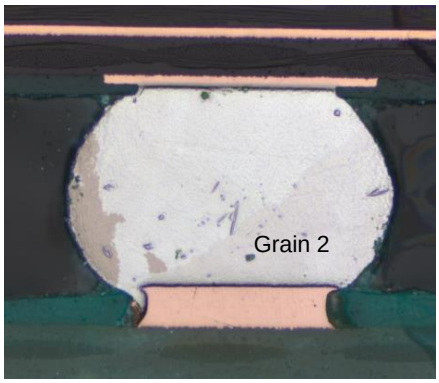

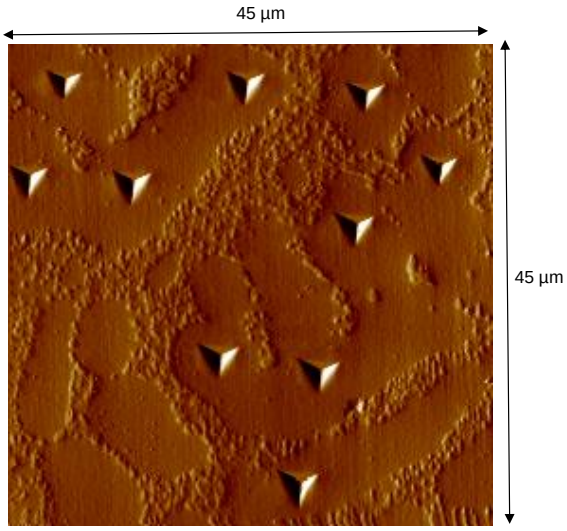

SPM Image of Indents on Grain 2

(b)

Figure 6.9 (a) Nanoindentation load-displacement curve for β-Sn (grain 2); (b) SPM imaging showing indents on grain 2

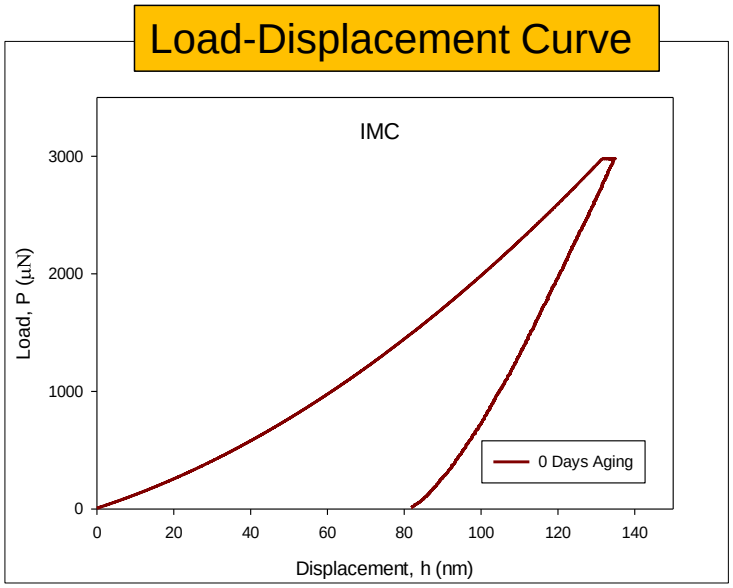

(a)

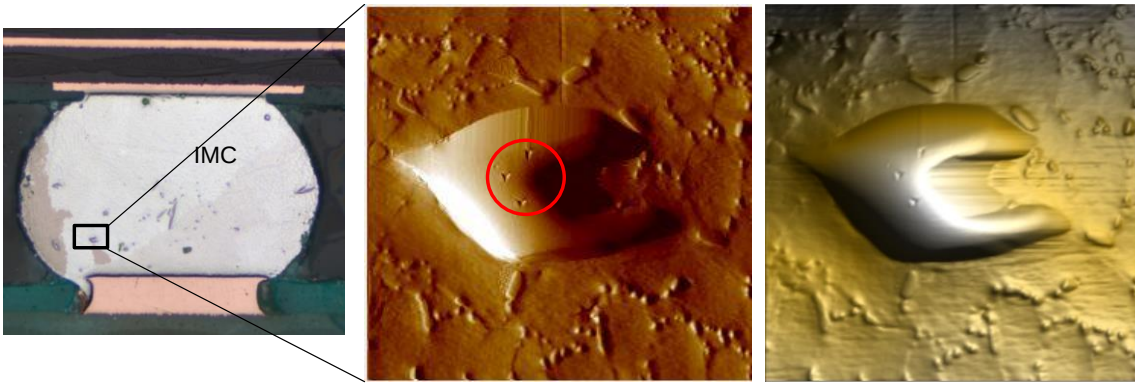

SPM Image of Indents on Cu_6Sn_5 IMC

(b)

Figure 6.10 (a) Nanoindentation load-displacement curve for IMCs; (b) SPM imaging showing indents on IMCs

Table 6.1 Properties of β-Sn and IMC Phase

Phase	Modulus (GPa)	Hardness (GPa)
β-Sn (Grain 1)	38±2.0	0.22±0.2
β-Sn (Grain 2)	33±3.0	0.21±0.1
IMC	105±2.0	6.5±0.3

6.7 Evolution of Mechanical Properties of Individual Phases with Aging

The above-mentioned results were obtained on non-aged solder joint samples. The same solder joint was gradually aged isothermally for different time intervals of 1, 5, 10 and 30 days at 125 ^{o}C using a high temperature oven. For each aging condition, nanoindentation was performed to the same phases to obtain modulus and hardness. Results obtained with aging were then plotted for comparison with the non-aged condition for the same solder joint. Figure 6.11 shows the variation in modulus and hardness with 0-30 days of aging exposure. Aging of 30 days did not show significant changes in the modulus and hardness result of observed in the IMCs showing no significant changes in the modulus and hardness values with 30 days aging. The small changes occurring in the individual phases with aging are starkly different than the large changes observed for the overall properties of the SAC solder joint with aging the β-Sn phase (both grain 1 and grain 2). The values of modulus and hardness were 36 GPa and 0.21 GPa, respectively, for grain 1; and 30.6 GPa and 0.21 GPa, respectively, for grain 2 after 30 days of isothermal aging. The same behaviors were observed in the IMCs showing no significant changes in the modulus and hardness values with 10 days aging. The small changes occurring in the

individual phases with aging are starkly different than the large changes observed for the overall properties of the SAC solder joint with aging.

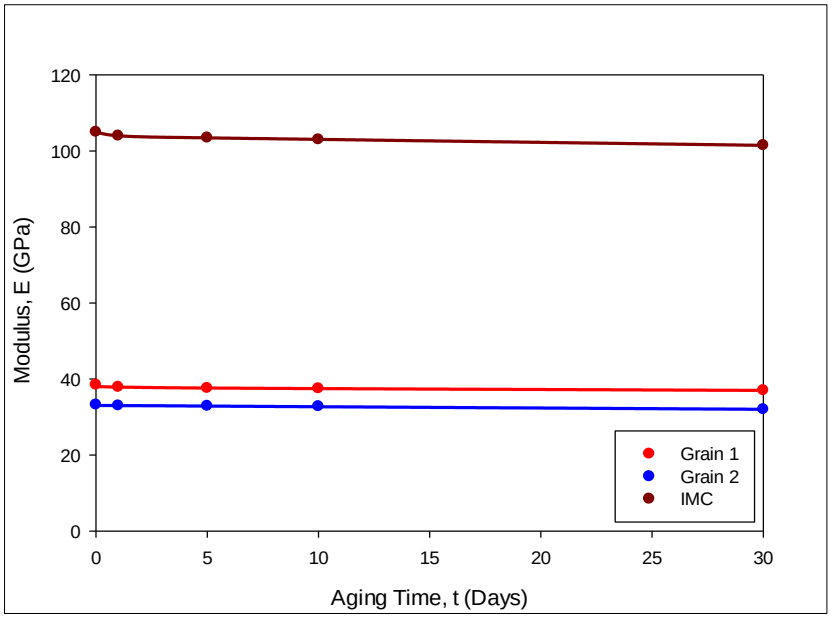

(a)

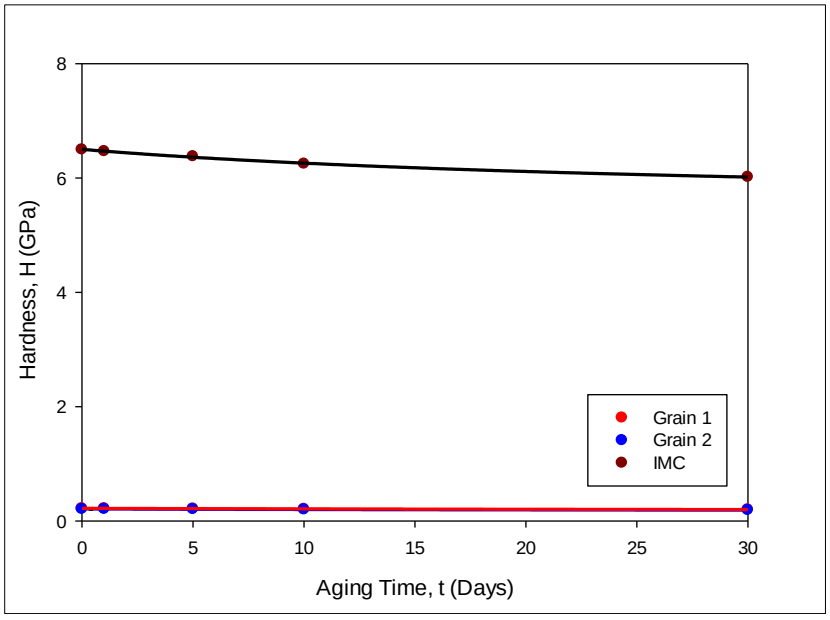

(b)

Figure 6.11 (a) Variations of (a) Modulus and (b) Hardness for β-Sn and IMC during isothermal aging for 0, 1, 5, 10 and 30 days

6.8 Creep Analysis of Individual Phases

Creep testing was performed on two different grains of β- Sn phase and on several IMCs. For creep testing, a longer hold time of 200 sec was applied at the peak load of 1000 and 3000 μN for the β-Sn and IMC phases, respectively. Creep data were recorded during this hold time and then analyzed. Since β-Sn phase showed significant creep effects, the holding time and the maximum load were chosen carefully so that the indent during creep deformation did not reach to the eutectic phase enclosing the β-Sn phase. Whereas the IMC phase showed almost no creep effect.

However, for comparison the same holding time was maintained at a maximum load that gave result in stable region. Figure 6.12 (a) shows the average creep curve (displacement vs. time) for the two different grains of β-Sn phase at no aging condition. It is seen from the graph that grain 1 showed slightly lower creep deformation (65 nm) compared to the grain 2 (74 nm) after 200 sec. This could be related to the variation in hardness of the two different phases. All of these graphs were obtained from an average of 5 good tests and by fitting with a log hyperbolic tangent model.

Creep testing was also performed on the IMCs for the same holding time of 200 sec. Figure 6.12 (b) shows the creep displacement vs. time graph for the IMC at no aging conditions. It was seen from the graph that IMCs showed very low creep deformation (8 nm) at 200 sec. Although for IMCs, a higher maximum load was applied, the creep deformation was much lower compared to the β-Sn grains at the same hold time. This confirms our initial guess of less creep effect in the IMCs.

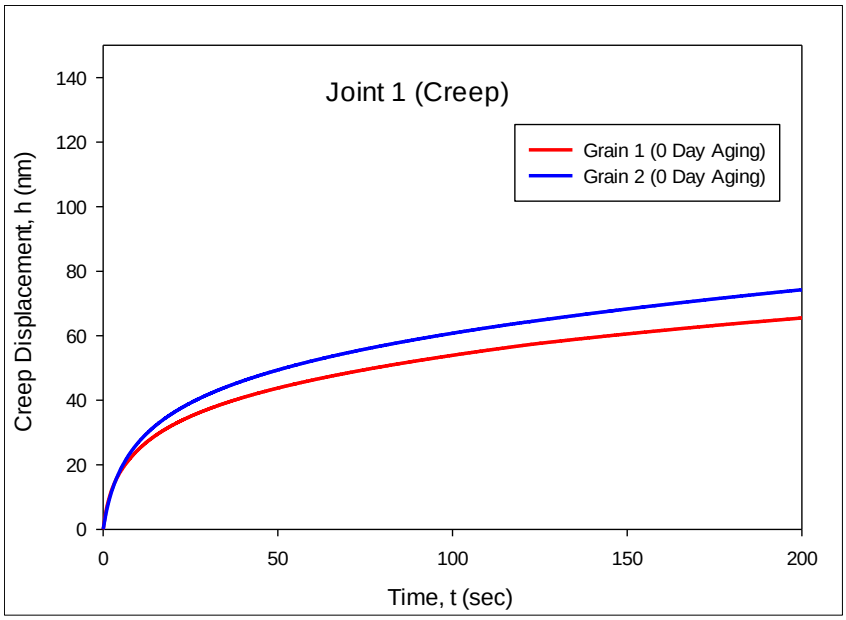

(a)

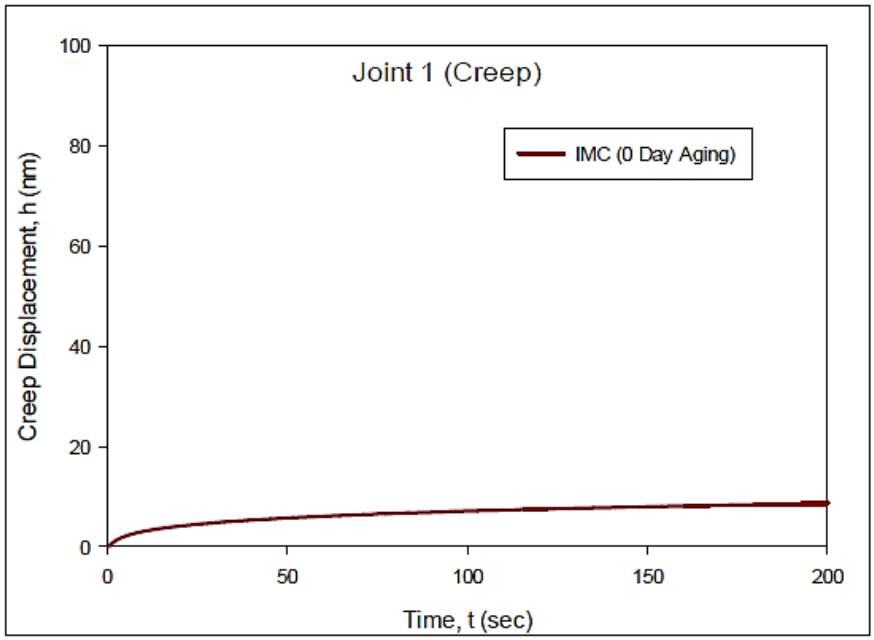

(b)

Figure 6.12 (a) Nanoindentation Creep Displacement vs. Time Curve for (a) β-Sn Phase (Grain 1 and 2) and (b) IMC Phase

6.9 Evolution of Creep Behavior with Aging

Creep testing was performed on solder joints isothermally aged at 125 ^{o}C for 1, 5, 10 and 30 days, and creep displacements were measured for same parameters mentioned above for all conditions. Figure 6.13 shows the creep displacement vs. holding time plots for 0, 1, 5 10 and 30 days of aging for the same maximum load and holding time. Figure 6.13(a) shows the creep curves for β-Sn grain 1. It is seen from the result that after 10 days aging at 125 ^{o}C, there was no significant change in the creep curves. The same phenomenon was also observed for the β-Sn grain 2, which is shown in Fig. 6.13(b). Figure 6.13(c) shows the creep behavior of IMCs for isothermal aging at 125 ^{o}C for 0, 1, 5, 10 and 30 days. It is seen from the results that the creep curves of the IMC material did not show significant changes with aging relative to the non-aged condition. However, significant increases in the creep deformations were observed with aging for the combined β-Sn and IMC composite material making up the SAC solder joint in our previous study. Previous work shows overall joint creep deformation increases about 130~140 nm after 30 days after aging isothermally at 125 ^{o}C.

This study has shown that the individual phase properties do not change significantly with aging. Thus, it can be concluded that the changes occurring in SAC solder joints are due primarily to IMC coarsening and not for property changes of the individual phases during the isothermal aging phenomena. IMC coarsening reduces the surface available to resist the dislocation movement thus causing drop in the mechanical behavior of the SAC solder joint.

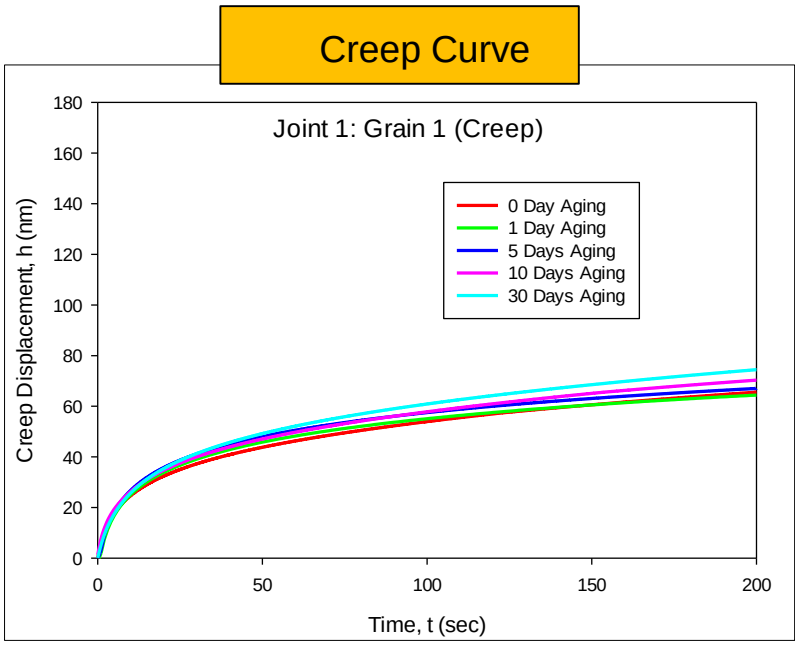
Creep Curve
Joint 1: Grain 1 (Creep)
0 Day Aging
1 Day Aging
5 Days Aging
10 Days Aging
30 Days Aging
Creep Displacement, h (nm)
Time, t (sec)
0
20
40
60
80
100
120
140
160
180
0
50
100
150
200

(a)

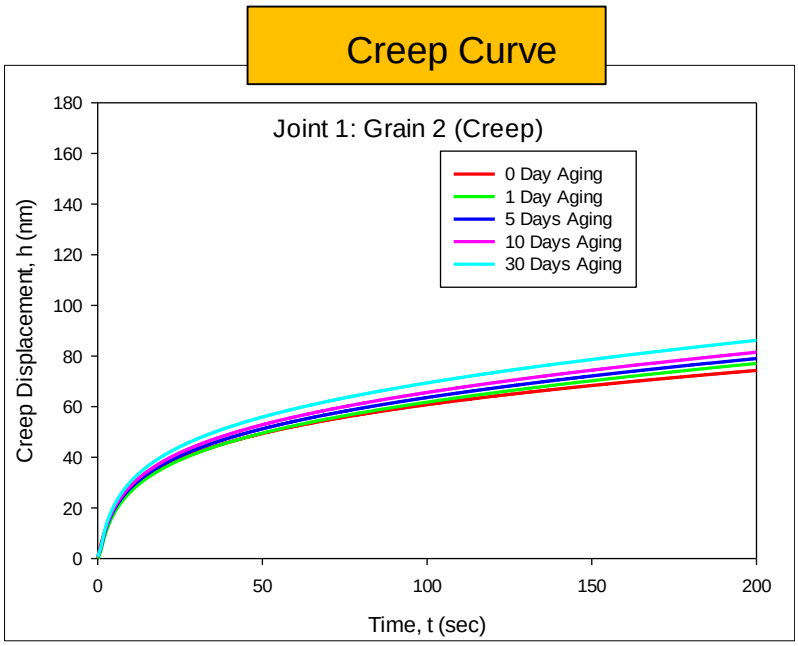
Creep Curve
Joint 1: Grain 2 (Creep)
0 Day Aging
1 Day Aging
5 Days Aging
10 Days Aging
30 Days Aging
Creep Displacement, h (nm)
Time, t (sec)
0
20
40
60
80
100
120
140
160
180
0
50
100
150
200

(b)

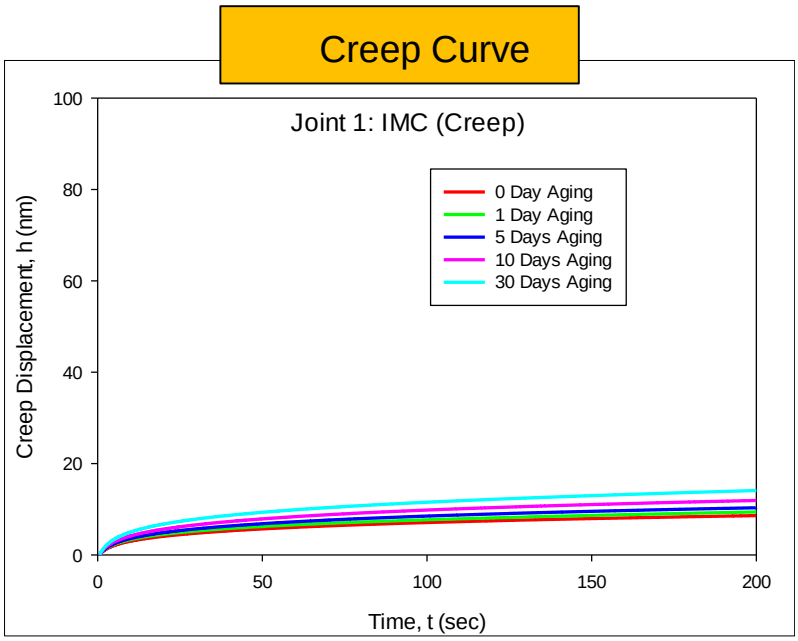

(c)

Figure 6.13 (a) Nanoindentation Creep Displacement vs. Time Curve for (a) β-Sn Phase (Grain 1 and 2) and (b) IMC Phase as a Function of Aging Time (0-30 Days)

6.10 Summary and Discussion

In this chapter, we have performed aging studies on individual phases of SAC solder joints. In particular, aging induced variations of the mechanical properties and creep behavior of the β-Sn phase and of the IMC particles in SAC solder joints have been explored using nanoindentation. SAC solder joints extracted from Super BGA (SBGA) packages were aged for different time intervals (0, 1, 5, 10 and 30 days) at T = 125 ^{o}C. Multiple β-Sn grains were identified in joints using optical polarized microscopy and IMCs were also observed. Individual β-Sn grains and IMC particles were then indented at room temperature to measure their mechanical properties (elastic modulus and hardness) and time dependent creep deformations. Properties measured at different aging time were then

compared to explore aging induced degradations of the individual phases. The properties of the individual phases did not show significant degradation, even though the SAC composite formed by β-Sn and IMC particles is known to experience significant aging induced changes. Thus, IMC coarsening is the primary reason for the degradation of bulk solder joint properties, and changes of the properties of the individual phases making up the lead free solder material are negligible.

CHAPTER 7

MECHANICAL BEHAVIOR OF SAC305 SOLDER JOINTS UNDER THERMAL CYCLING LOADING

7.1 Introduction

Solder joints in electronic packages are frequently exposed to thermal cycling environment. Such exposures can occur in real life application as well as in accelerated thermal cycling tests used for the fatigue behavior characterization. Because of temperature variations and CTE mismatches of the assembly materials, cyclic temperature leads to damage accumulation and material property evolution in the solder joints [180-192]. This eventually results in crack initiation, and subsequent crack growth and failure. However, in all of the prior studies of SAC alloys, the solder joints contained multiple β-Sn grains in their as reflowed microstructure. Moreover, they studied the microstructure and mechanical behavior changes for different thermal cycles in different joints, which does not give a clear idea about the microstructure and mechanical changes happening on the same joint with the same grain orientation. This chapter aims to provide a better understanding of the SAC305 microstructure evolution and changes in mechanical properties occurring during the thermal cycling that is characteristic of thermomechanical fatigue tests. Several single grain solder joints have been studied, and the evolution in mechanical behavior was monitored in each joint. The main ideas were to avoid effects of multiples grains on the overall mechanical behavior of solder joint, and to analyze changes

in the behavior occulting in the same solder joint at multiple times during the cycling. In this study, the nanoindentation technique was used to understand the evolution of mechanical properties (modulus, hardness and creep behavior) of SAC305 BGA solder joints subjected to thermal cycling loading for various durations. In addition, microstructural changes in those joints that occur during thermal cycling were observed using both SEM and optical microscopy. BGA solder joint strip specimens were first prepared by cross sectioning BGA assemblies followed by surface polishing to facilitate SEM imaging and nanoindentation testing. The strip specimens were chosen to contain several single grain solder joints. This enabled large regions of solder material with equivalent mechanical behavior, which could then be indented several times after various durations of cycling. After preparation, the solder joint strip samples were thermally cycled from T = -40 to 125 ^{o}C in an environmental chamber. At various points in the cycling (e.g. after 0, 50, 100, 250, 500, 750 and 1000 cycles), the package was taken out from the chamber, and nanoindentation was performed on each single grain joint to obtain the modulus, hardness, and creep behavior at 25 ^{o}C. This allowed the evolution of the mechanical properties with the duration of thermal cycling to be determined. Moreover, microstructural changes were also observed after various durations of cycling using optical microscopy.

7.2 Sample Preparation for Thermal Cycling Study

The lead-free solder joints in this study were obtained from plastic ball grid array (PBGA) assemblies (Amkor CABGA) with following specifications: 17 x 17 mm, 256 balls, 0.5 mm ball diameter, and 1 mm ball pitch. In this work, the BGA ball alloy

considered to perform thermal cycling study was SAC305 (96.5Sn-3.0Ag-0.5Cu). The test boards had electroless nickel immersion gold (ENIG) surface finish on package side, and SAC305 solder paste was used in the surface mount assembly process. At first, PBGA packages (17 x 17 mm) were cut from the board and only the first row of the solder joints in the package was exposed by grinding and polishing (Figure 1). The remaining of the total package was kept intact. The detail of the grinding and polishing process involves: mechanical grinding with several SiC abrasive papers having different grits (300-1200). Final polishing was done with 1 μm diamond paste followed by colloidal silica suspensions (0.02 μm). This resulted in mirror finish samples suitable for nanoindentation test and SEM microscopy, as shown in Figure 7.1.

7.3 Thermal Cycling Chamber

Thermotron SM series thermal cycling chamber from Thermal Product Solutions (Figure 7.2(a)) was used to perform thermal cycling of the sample in this study. A programmable controller attached to the main chamber was utilized to program the thermal profile. The package obtained after polishing was subjected to a temperature cycle profile with: Temperature excursion: -40 °C to 125 °C Ramp rate: 45 min and Dwell time: 30 min. Before running tests, the chamber was calibrated using a thermal profiler. Also, a dummy sample similar to original sample was placed inside the chamber and was monitored at three different positions to ensure that the original sample follows the same profile during test. Figure 7.2(b) shows the thermal cycling profile seen by the test sample. It can be seen that the 45 min ramp and 30 min dwell periods were well maintained in the profile.

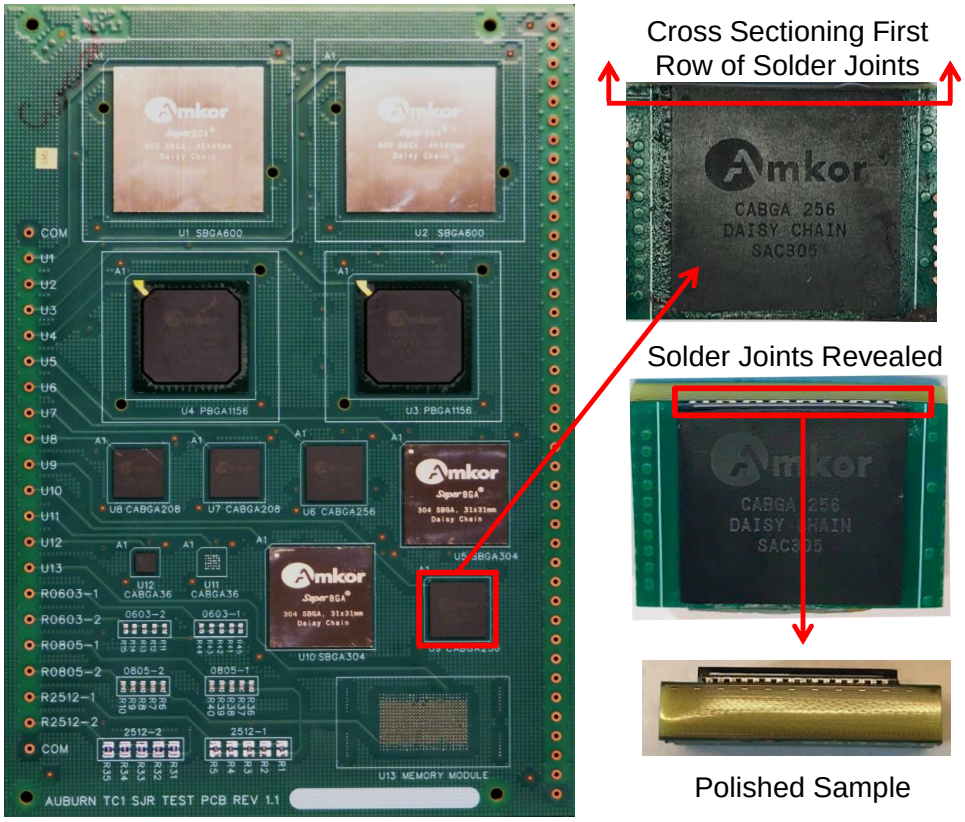

Figure 7.1 Sample preparation of PBGA packages by cross sectioning and polishing

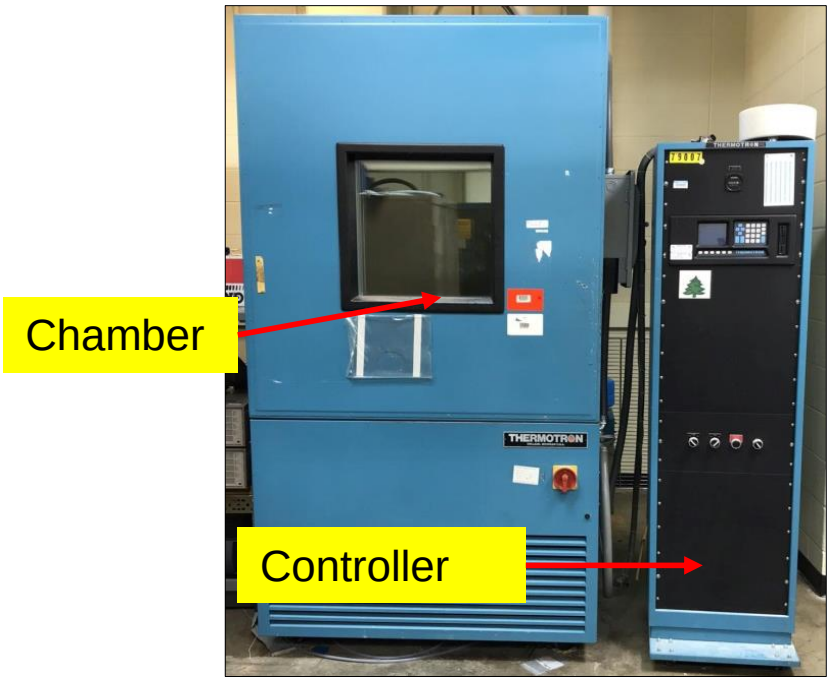

(a)

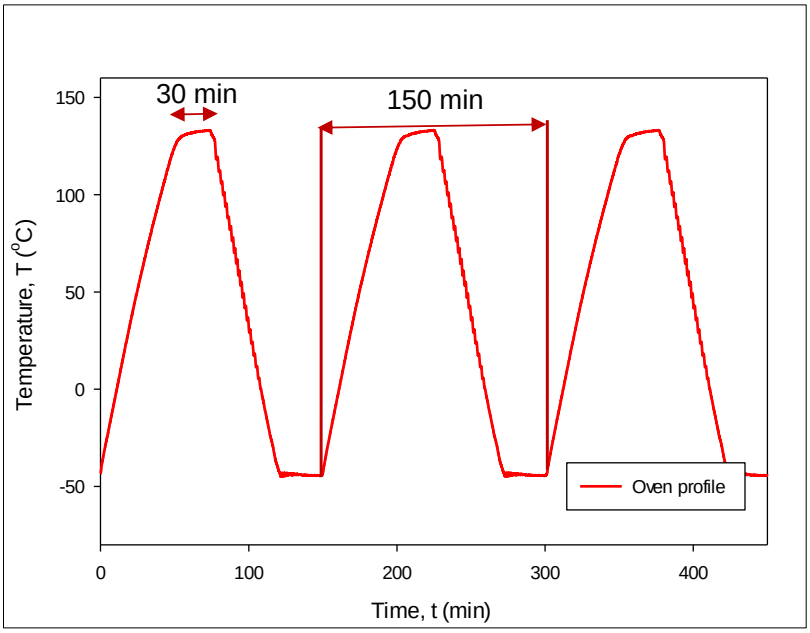

(b)

Figure 7.2 (a) Thermal cycling chamber (b) Thermal cycling profile

Table 7.1 Thermal Cycling Profile

Temperature Range	-40 °C /125 °C
Ramp time	45 mins.
Dwelling time	30 mins.

7.4 Nanoindentation Test Procedure for Thermal Cycling

A Hysitron TI 950 TriboIndenter system was utilized to analyze mechanical properties of solder joints at room temperature using a room temperature stage. Testing was carried out by selecting arrays of regularly spaced indentations on desired solder joints using nanoindentation. During each indentation experiment, the load versus indentation displacement normal to the cross-sectional surface was recorded. A Berkovich pyramidal nanoindenter was used at a loading rate of 3 mN/sec to reach 15 mN during the loading phase.

The load was then kept constant for 30 sec in order to avoid creep effects in the test results. The unloading was also set at a loading rate of 3 mN/sec. The corresponding material properties were obtained using Oliver and Pharr method, using average values from at least 6 indents in order to have consistent results. For creep testing, a longer hold time of 600 sec was applied at the peak load of 15 mN. The creep deformations were recorded during the constant load application and analyzed. Before testing of the solder samples, indenter axis calibration was performed, and then followed by hardness and elastic modulus measurement calibrations on standard fused silica and quartz samples to maintain accuracy of the test results. Moreover, every test included a thermal drift

measurement and correction that minimized the effects due to temperature fluctuations. The minimum drift rate was maintained at less than 0.05 nm/sec.

7.5 Nanoindentation Test Results for Thermal Cycling

7.5.1 Optical Microscopic and SEM Images

The grain identification, microstructure and topographical observations were performed using optical microscopy and SEM imaging. For optical microscopy, a ZEISS Axio Imager.M2m optical microscope was used. The SEM observations were performed using a ZEISS EVO 150 VP microscope with an acceleration voltage of 20 kV.

7.5.1.1 Joints for Modulus and Hardness Measurement

Figure 7.3 (a) shows an optical image of the revealed solder joints in the package after cross-sectioning and Figure 7.3 (b) shows polarized light microscopy of the same joint which shows the presence of only single grain in the solder joint. Figure 7.3 (c) is another single grain solder joint which was confirmed by polarized microscopy showed in Figure 7.3 (d). These two solder joints were labeled as Joint A and Joint B, and were used to evaluate the evolution of the joint modulus and hardness values during thermal cycling by nanoindentation testing. The precise crystallographic orientation of these single grains can be obtained using the EBSD technique. However, we limited our work in this paper to only optical microscopy.

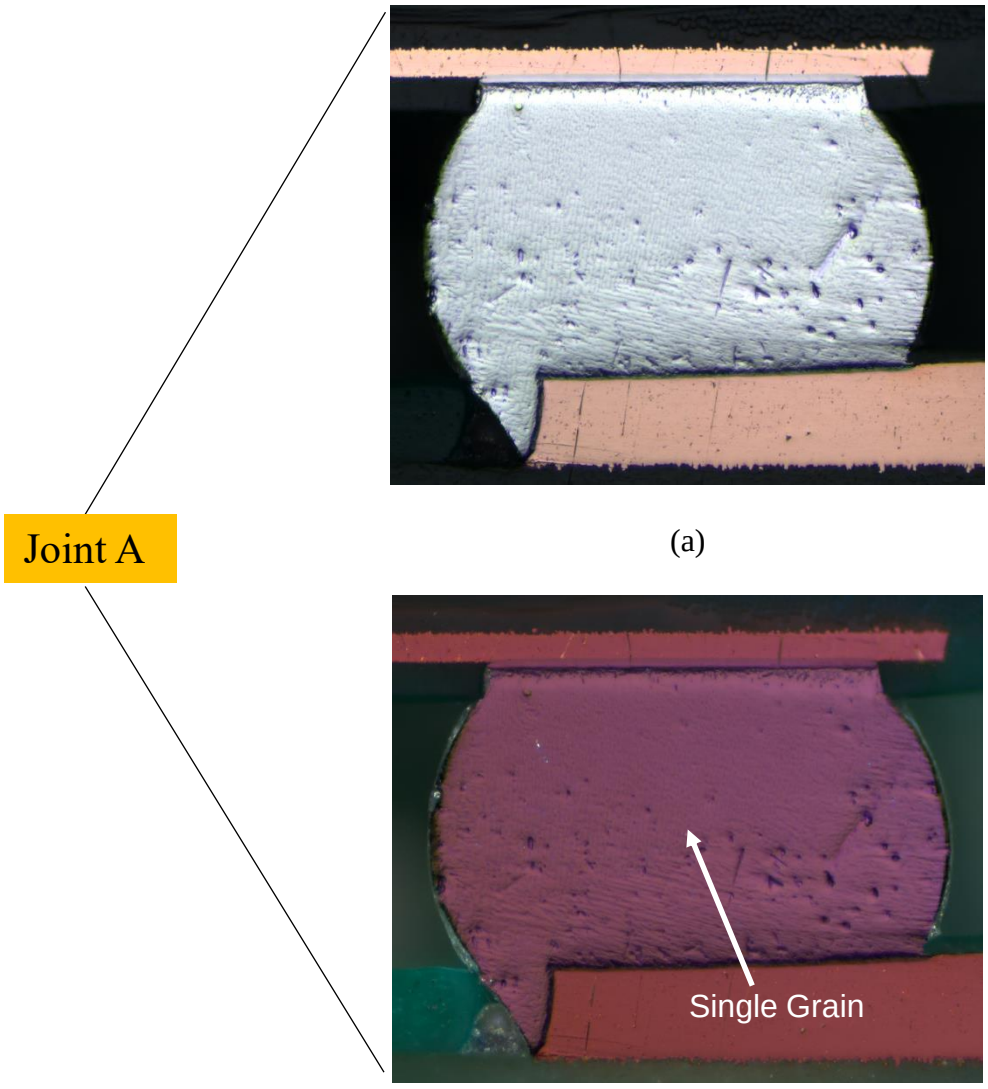

(a)

(b)

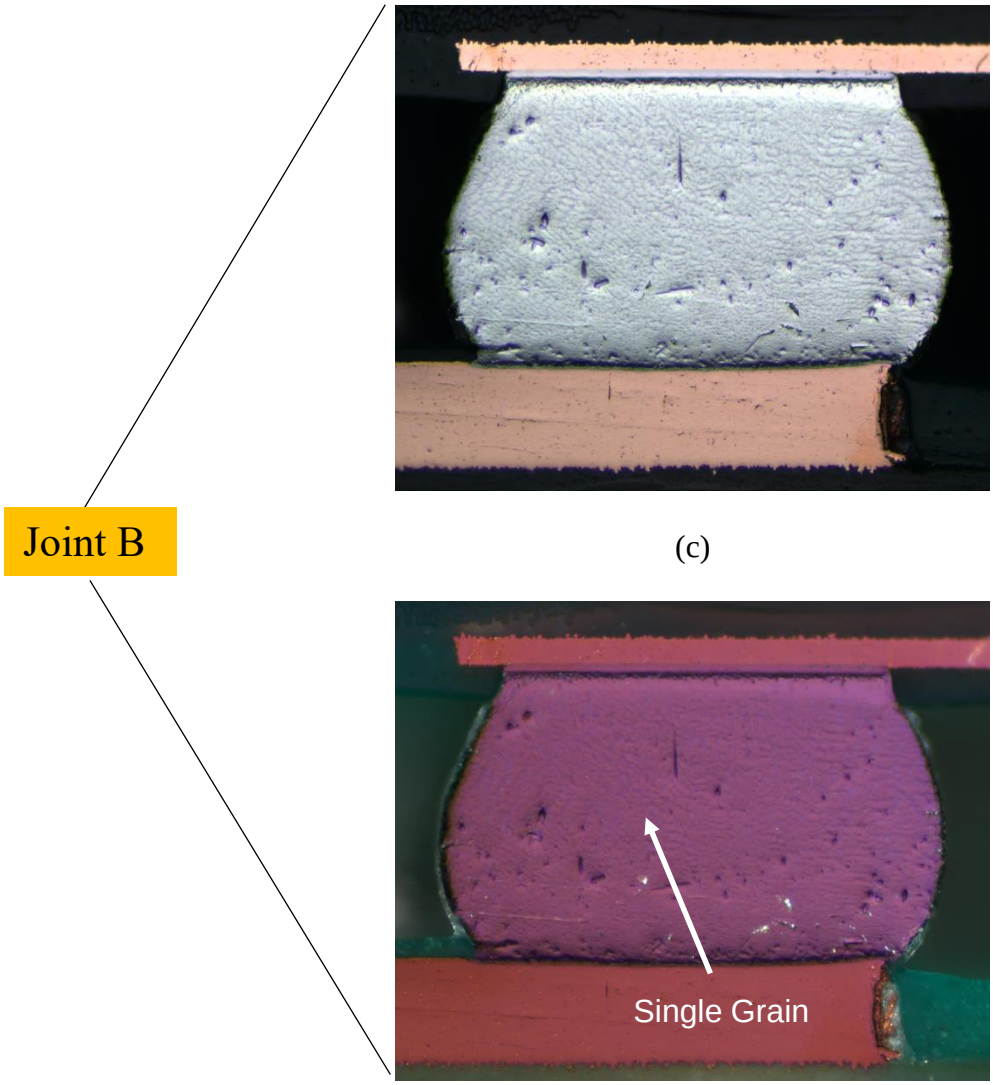

(c)

(d)

Figure 7.3 (a) Optical and (b) polarized microscopy of joint A,

(c) Optical and (d) polarized microscopy of joint B

7.5.1.2 Joints for Measuring Creep Behavior

Other two single grain solder joints (Figures 7.4(a) and 7.4(c)) from the same package were used to observe the change in creep behavior. The single grain natures of these two joints (Joint C and Joint D) are confirmed by polarized microscopy as shown in

Figures 7.4(b) and 7.5(d). These two joints were used to indent and obtain creep behavior of these two single grain solder joints.

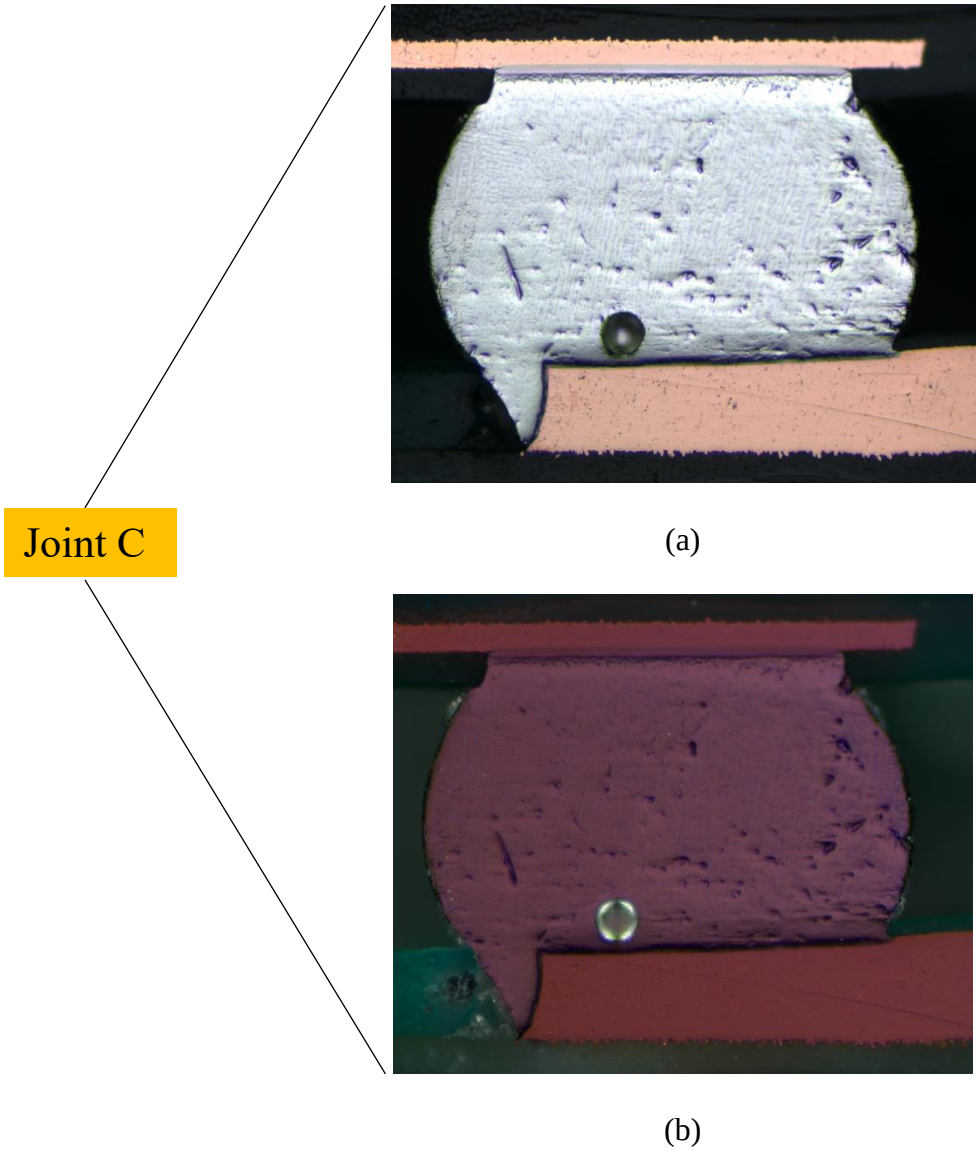

(a)

(b)

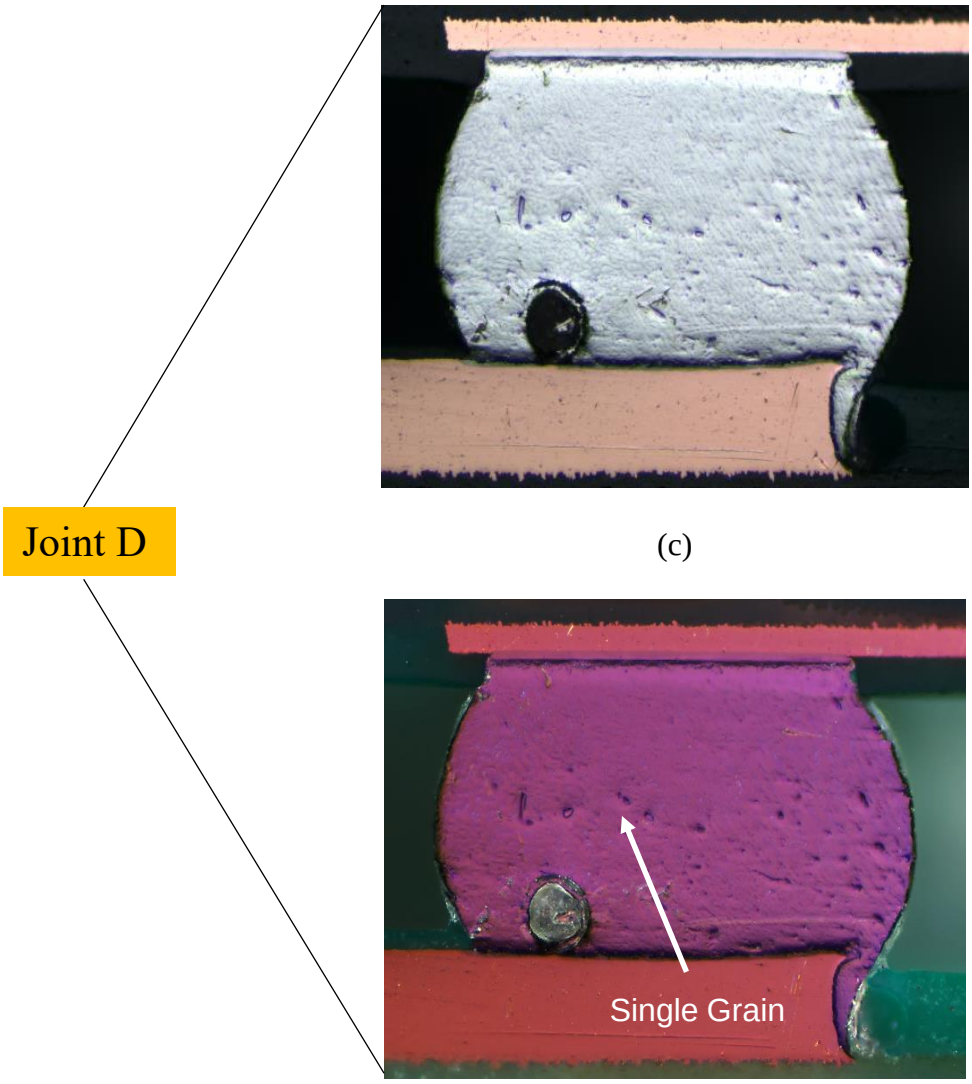

(c)

(d)

Figure 7.4 (a) Optical and (b) polarized microscopy of joint C,

(c) Optical and (d) polarized microscopy of joint D

7.5.2 Microstructure in As-Reflowed Condition

Microstructure in As Reflowed Condition The micro-structure of SAC305 solder interconnects after reflow consists in a network of ù-Sn dendrites surrounded by a β-Sn matrix with secondary nanoscale particles of Ag_3Sn (known as eutectic region). Another

IMC phase can appear depending on the surface finish used. For SAC305 solders assembled on copper pads, Cu_6Sn_5 IMC particles will be formed. Primary IMCs (plate-like shape for Ag_3Sn and rod-like for Cu_6Sn_5 of larger shape can also be formed before the Sn phase during solidification (Figure 7.6).

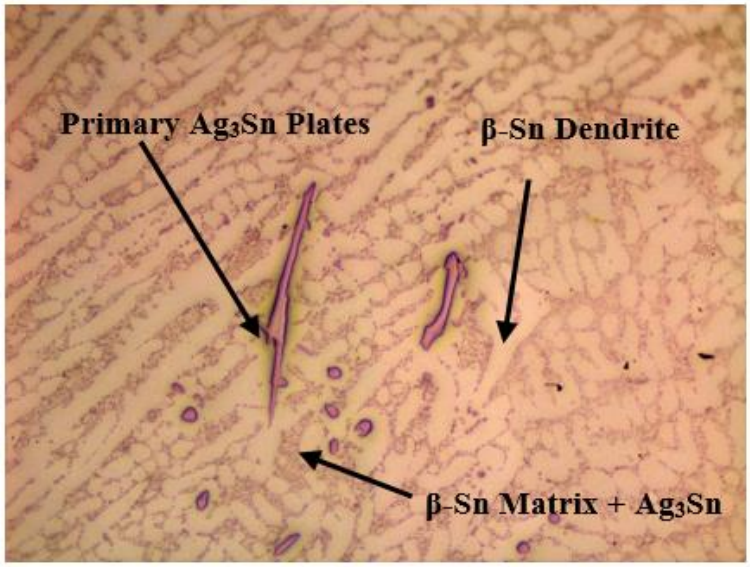

Figure 7.5 SAC305 dendritic microstructure in as-reflowed condition

7.5.3 Modulus and Hardness Measurements

The mechanical properties (elastic modulus and hardness) of the solder joints were measured using nanoindentation testing. During each nanoindentation test, load vs. displacement data was measured and recorded. Modulus was obtained from unloading stiffness and hardness was obtained from maximum load over projected contact area.

7.5.3.1 Indentation Regions

As mentioned earlier, joint A and joint B were used to observe the modulus and hardness variations using nanoindentation for 7 different cycling durations (e.g. after 0, 50,

100, 250, 500, 750 and 1000 cycles). Results for each joint and cycling duration were obtained from the average of 6 indentation tests performed over a 2 x 3 array (Fig. 7.6). SEM image of a single indent is shown in Fig. 7.7

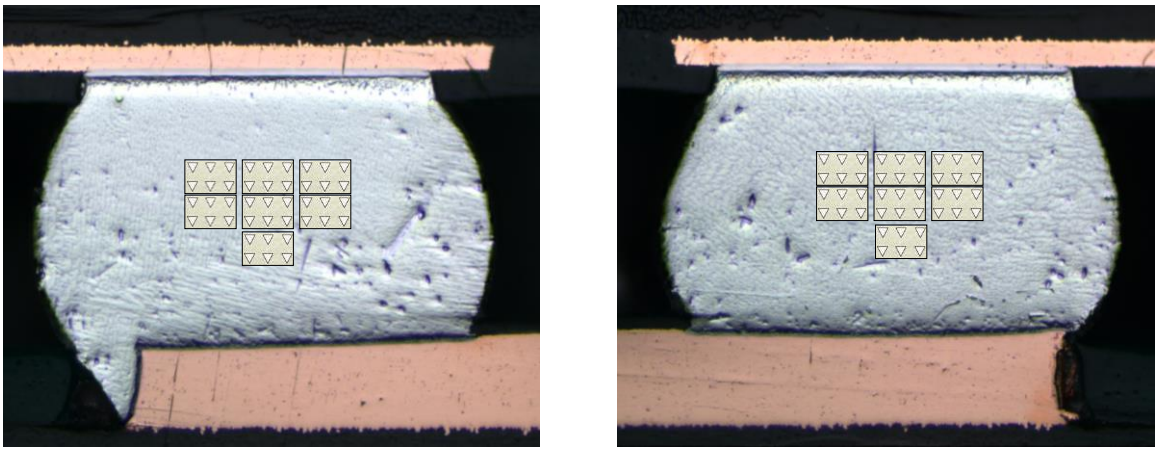

Figure 7.6 Indentation regions (0, 50, 100, 250, 500, 750, 1000 cycles)

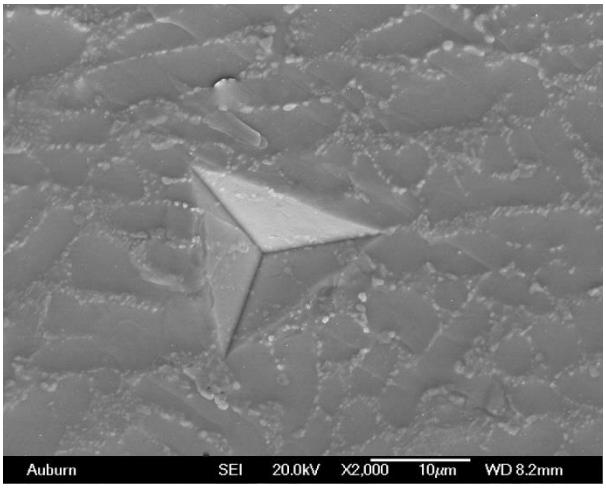

Figure 7.7 Permanent Indentation after Testing

7.5.3.2 Modulus and Hardness in as- Reflowed Condition

Figure 7.8 (a) and 7.8 (b) shows the representative nanoindentation load vs. displacement curves for joints A and B, respectively, before thermal cycling. It can be seen from the graph that, a maximum of 15 mN load was applied on both joints, then load was held and then unloading was performed. It can be also seen that maximum displacement varies from grain 1 to grain 2 under the application of same load. For grain 1 maximum displacement is about 1250 nm whereas for grain 2 maximum displacement is about 1400nm. It can be said that deformation behavior patter is different from grain to grain even though they are from same materials. Using the formulas of Oliver and Pharr mentioned earlier, the modulus and hardness were calculated from unloading stiffness for both the joints in as reflowed condition. The values are tabulated in Table 7.2. Different values were found for the two joints because that had different grain orientations. This variation can be found in literature showing the β-Sn modulus and hardness mapping.

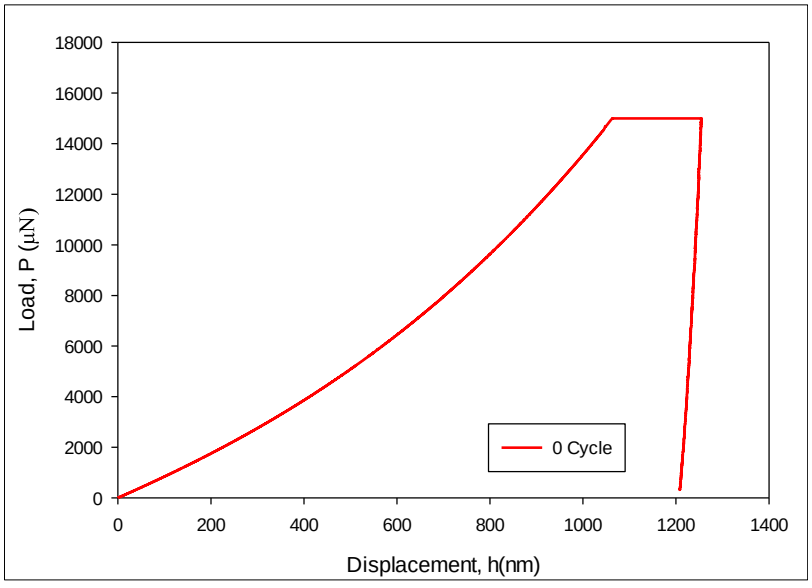

(a)

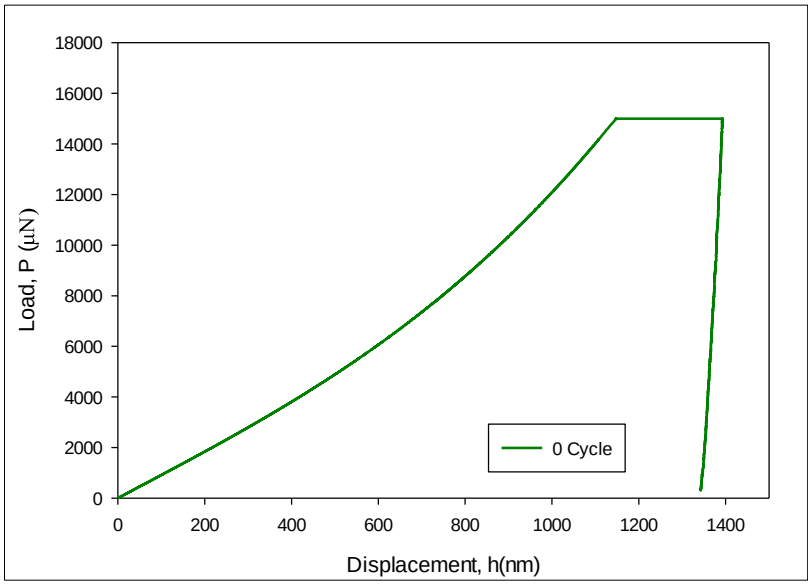

(b)

Figure 7.8 Representative Nanoindentation Load-Displacement Curves (as Reflowed, 0 cycles)

Table 7.2 Mechanical Properties of Joint 1 and Joint 2

Phase	Modulus (GPa)	Hardness (GPa)
Solder Joint A	58.0 ± 1.4	0.36 ± 0.02
Solder Joint B	46.3 ± 1.9	0.34 ± 0.04

7.5.3.3 Evolution of Mechanical Properties with Cycling

After initial measurements, the solder joint samples were thermally cycled for different durations (50, 100, 250, 500, 750 and 1000 Cycles). Variation in mechanical properties (0-1000 cycles) were analyzed and compared. It was found that the modulus and hardness for the SAC305 solder joints dropped significantly during the first 250 cycles. Figure 7.9 (a) shows the variation in modulus with number of thermal cycles for the two. After 250 thermal cycles, it was found that the modulus of joint A dropped about 15% and modulus of joint B dropped about 18% compared to the as reflowed condition (0 cycles). Moreover, the hardness values of the joints dropped about 25% as seen in Figure 7.9 (b). After 1000 cycles, modulus dropped about 28 and 35 % and hardness dropped 31 and 33% for joint A and joint B respectively.

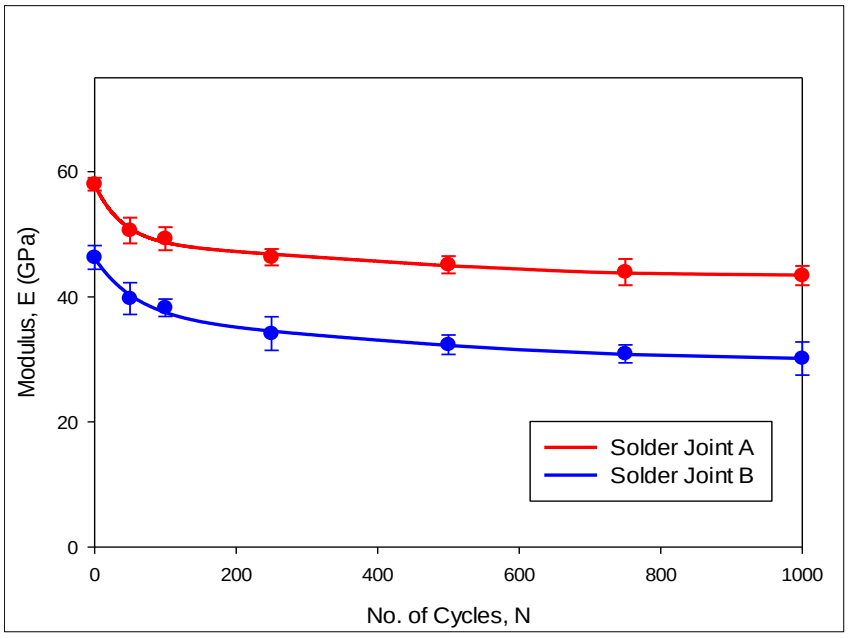

(a)

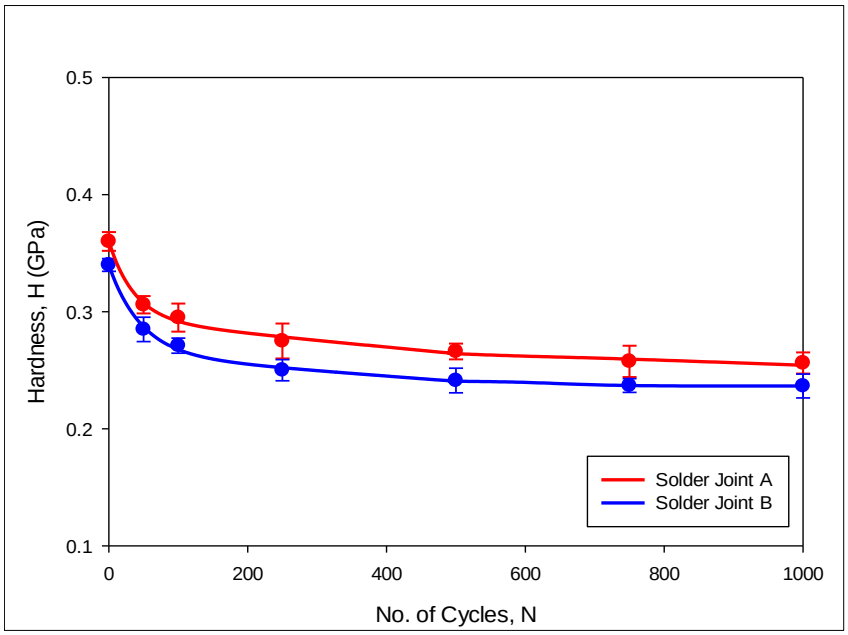

(b)

Figure 7.9 Mechanical Property Variation with Thermal Cycling

7.5.4 Microstructure Evolution during Thermal Cycling

After 250 thermal cycles, the microstructures of the solder joints were observed again using optical microscopy. Figure 7.10 (a) shows a typical SAC305 solder joint microstructure after 250 thermal cycles. Comparing Figs. 7.5 and 7.10(a), it can be seen that the microstructure coarsened significantly after 250 cycles. During the elevated temperatures experienced in thermal cycling, diffusion occurs and smaller IMC particle coalesce to produce larger size particles. This reduces the ability of the particles to block dislocation movements by the pinning effect, so that the effective stiffness and the strength of the material degrade. Figure 10 (b) shows a polarized light microscopy image of joint D after 250 thermal cycles. It is clearly seen that the joint still contains only a single grain. However, this could change with further cycling when recrystallization might occur.

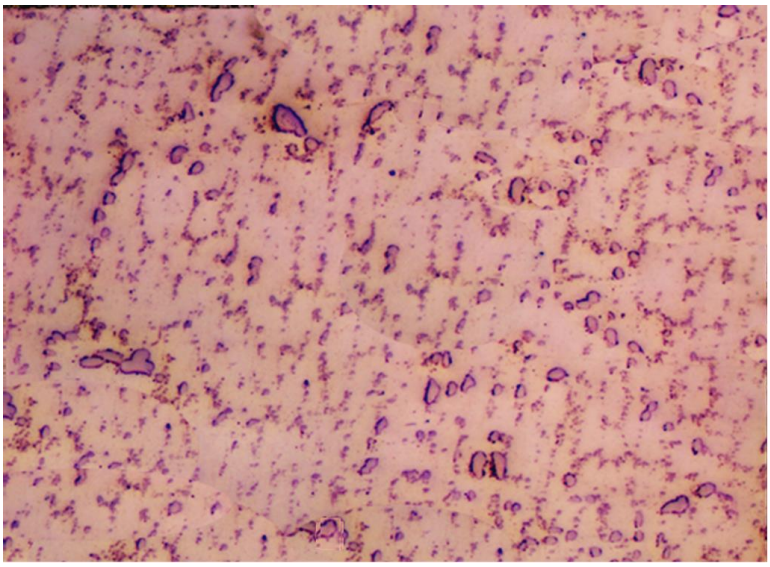

(a)

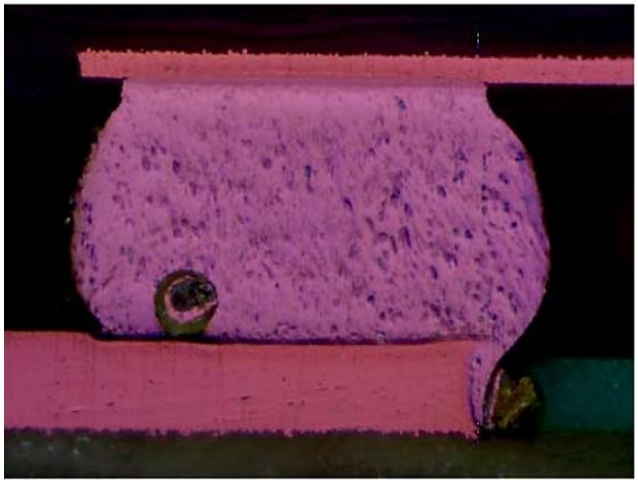

(b)

Figure 7.10 (a) Microstructure and (b) Grain Morphology

of joint D after 250 cycles

7.5.5 Measurement of Creep Behavior

Nanoindentation creep testing was performed on the solder joint C and joint D during the hold/dwell at the constant peak load of 15000 μN. As discussed earlier, a dwell

time of 600 sec was considered in this work for the creep tests. The total indentation displacements were measured continuously, from which the creep displacements during the constant load period were extracted. The recorded creep displacement vs. time experimental data were fit well using the following log hyperbolic tangent model. Creep strain rate was obtained using Mayo and Nix model [167-168]. Stress was calculated using Tabor model described earlier.

7.5.5.1 Indentation Regions for Creep

Nanoindentation creep test was performed on joint C and D shown in Figure 7.11. Creep indentation location for 0-1000 thermal cycles are shown in the figure.

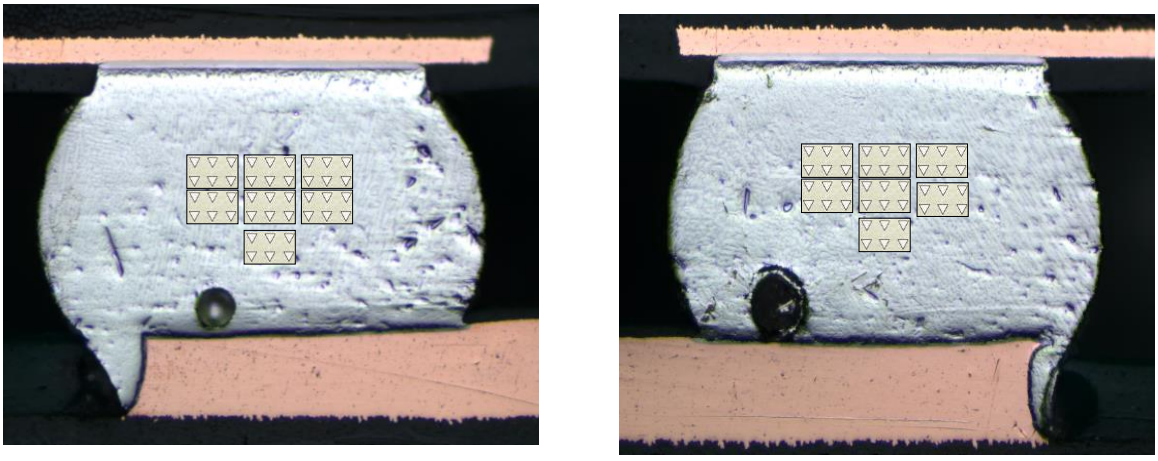

Figure 7.11 Creep Indentation regions (0, 50, 100, 250, 500, 750, 1000 cycles)

7.5.5.2 Creep Test Results for Thermal Cycling

Figure 7.11 illustrates representative creep displacement curves (creep displacement vs. time) for the two joints C and D after different durations of thermal

cycling. Each individual curve shown is the average curve obtained from 6 tests. From the as reflowed (0 cycles) results, it is seen that joint C had 592 nm of creep displacement where joint D had 520 nm of displacement after a loading duration of 600 sec. This indicates that joint C was more prone to creep deformations than joint D. After the first 50 thermal cycles, these values were observed to increase significantly. For example, the creep displacement at 600 sec increased to 720 nm for joint A, and 675 nm for joint B. After 1000 cycles, creep deformations increased even more for both joints. For joint C, the creep deformation was observed to increase to 1180 nm, while it increased to 1230 nm for joint D. Again, the increase in the creep deformations can be attributed to the IMC particle coarsening that occurs during thermal cycling.

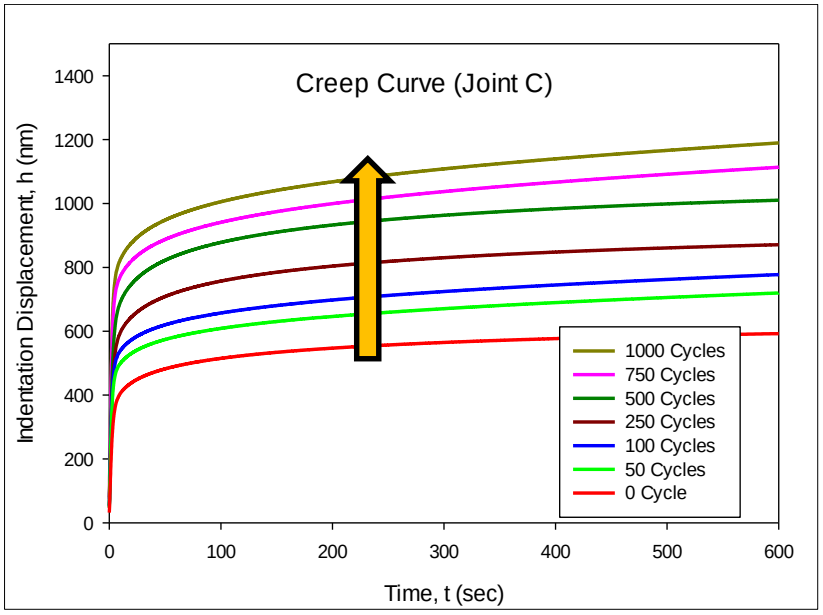

(a)

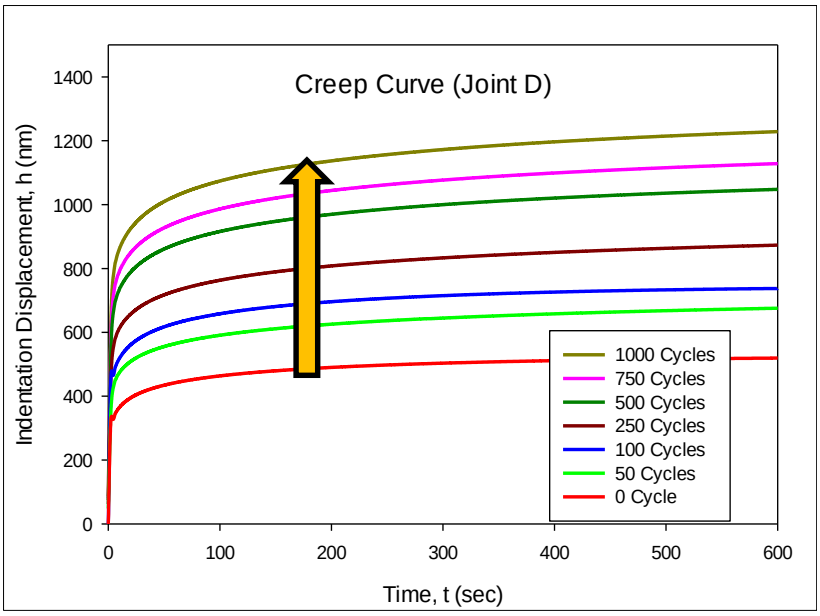

(b)

Figure 7.12 Nanoindentation Creep Displacement on SAC305 Joints

The log hyperbolic tangent creep model has been used to fit and model the recorded indentation depth versus time data during the creep loading.

$$h(t) = C_1 \ln(1+t) + C_2 \tanh(C_3 t) + C_4 t + C_5 \tag{7.2}$$

Where C_1, C_2, C_3, C_4, and C_5 are fitting constants. In addition, the method for calculating the creep strain rate proposed by Mayo and Nix [167,168] has been adopted in this study. According to the method, creep strain rate can be determined from instantaneous creep deformation and deformation rate using the following equation

$$\dot{\varepsilon} = \frac{1}{h}\frac{dh}{dt} \tag{7.3}$$

In order to determine creep strain rate, the derivative of equation 7.2 with respect to time was divided by corresponding instantaneous displacement. Stress can be obtained from Tobor relationship. Strain rate as a function of stress can be plot as shown in fig. 7.13. The stress level attained during the test is typically high whereas the stress level typically used during high temperature tensile creep experiment of SAC305 solder is 10-30 MPa. Since, the stress applied during the nanoindentation test is compressive in nature, the stress level attained during the test is well above the desired range. The exponential model, as shown in Equation 7.4, was used to extrapolate nanoindentation creep results to a lower stress level.

$$\dot{\varepsilon} = C_1 e^{C_2 \sigma} \tag{7.4}$$

Where C_1- C_2 are fitting constants. A log-log plot of strain rate vs. stress for the fitted experimental data (solid red curve) and the extrapolation using the exponential model (dotted curve) is presented in Figure 7.14. Using equations mentioned earlier, the strain rate vs. stress curves for each creep test were determined. Figures 7.14 (a) and 7.14 (b) show the creep strain vs. stress plots for joint C and joint D, respectively. In each graph, results are shown for 0, 50, 100, 250, 500, 750 and 1000 thermal cycles. At constant stress level, the strain rate increased significantly with the duration of thermal cycling. Moreover, the creep strain rate vs. stress responses can be fit with the well-known exponential model and extrapolated to lower stress levels as shown in Figure 13. From these results, the creep rates at a stress level of 15 MPa were seen to increase three to four times during the first

50 thermal cycles. The increases were 16X to 20X after 250 thermal cycles. Thus, the joints became significantly more vulnerable to creep deformations as thermal cycling progressed. After 1000 Cycles, creep rate increased 63X and 87 X respectively for joint C and D.

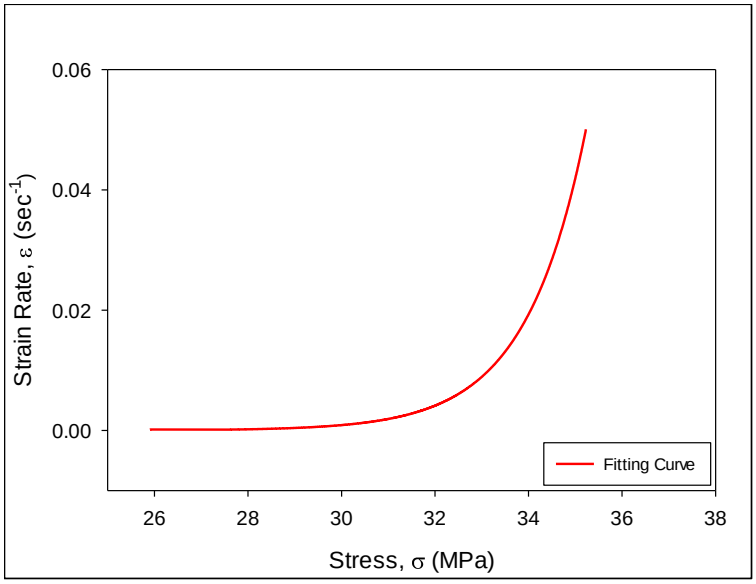

Figure 7.13 Creep Strain Rate vs. Applied Stress Plot

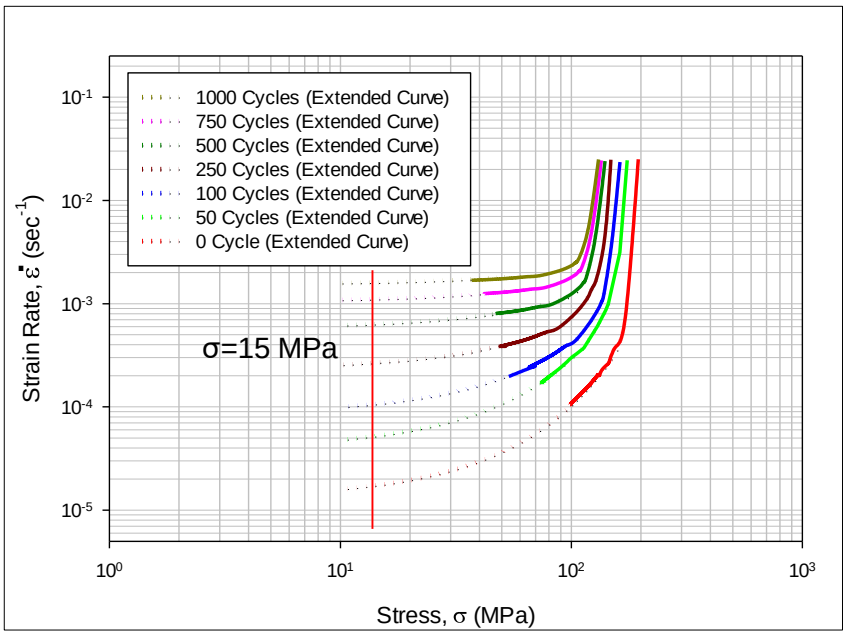

(a)

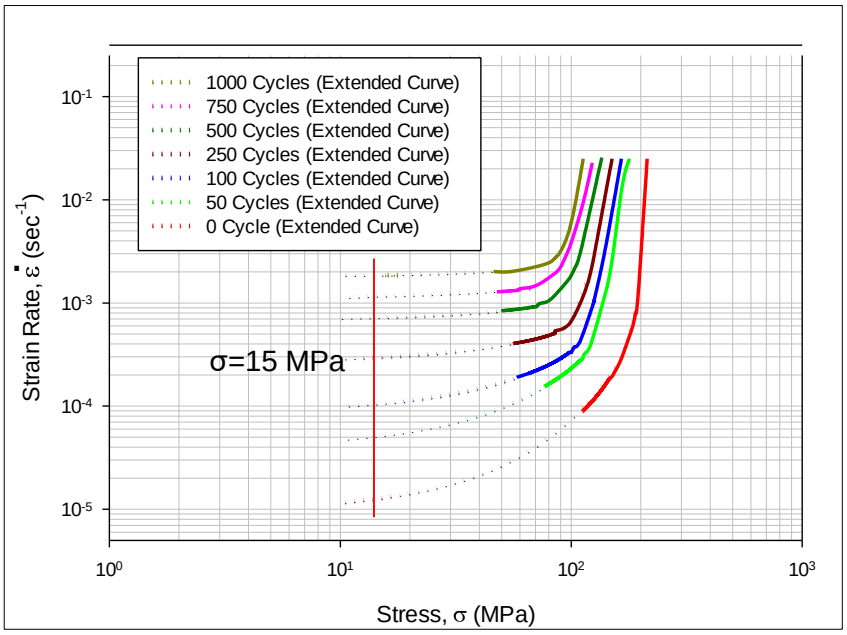

(b)

Figure 7.14 Extended creep strain rate vs. time curves using exponential creep model

7.6 Summary and Discussion

In this chapter, the nanoindentation technique was used to understand the evolution of mechanical properties (modulus, hardness and creep behavior) of SAC305 BGA solder joints subjected to thermal cycling loading for various durations. In addition, microstructural changes in those joints that occur during thermal cycling were observed using both SEM and optical microscopy. Solder joint strip samples were thermally cycled from T = -40 to 125 ^{o}C in an environmental chamber. At various points in the cycling (e.g. after 0, 50, 100, and 250 cycles), the package was taken out from the chamber, and nanoindentation was performed on each single grain joint to obtain the modulus, hardness, and creep behavior at 25 ^{o}C. This allowed the evolution of the mechanical properties with the duration of thermal cycling to be determined. Moreover, microstructural changes were

also observed after various durations of cycling using optical microscopy. From the nanoindentation test results, it was found that the modulus and hardness of the SAC305 solder joints dropped 28-35% and 31-33%, respectively, after 1000 thermal cycles. Moreover, the nanoindentation creep test results showed significant increases of 63X to 87X in the creep strain rate after 1000 thermal cycles.

CHAPTER 8

NANOINDENTATION CHARACTERIZATION OF VARIOUS MATERIALS IN PBGA PACKAGES UNDER THE EXPOSURE OF THERMAL CYCLING LOADING

8.1 Introduction

Electronic packages are frequently exposed to thermal cycling environments in real life applications. Particularly, the plastic ball grid array (PBGA) is one of the most widely used electronic packages, and consists of various component materials, e.g. solder joint, silicon die, die attachment adhesive, mold compound, solder mask, etc. All of these materials play a significant role on the reliability of the overall PBGA assembly. Hence, it is important to study their mechanical property evolution under the thermal cycling environment. Our prior work has shown that cyclic temperature variations cause the solder joints to change their mechanical behavior. However, the other component materials can also change their mechanical properties during cycling. These changes must be evaluated in order to understand and predict their failure behavior in operation. In our previous study, evolution of mechanical properties of SAC305 solder joints in a PBGA package up to 1000 thermal cycles was evaluated using the nanoindentation technique. In this work, the nanoindentation technique was utilized to understand the evolution of mechanical

properties (modulus, hardness, and creep behavior) of the die attachment adhesive, silicon die, and solder mask material for various durations of thermal cycling. Test specimens were first prepared by cross sectioning a PBGA package to reveal the different materials, followed by surface polishing to facilitate SEM imaging and nanoindentation testing. After preparation, the package samples were thermally cycled from T = -40 to 125 ^{o}C in an environmental chamber. At various points in the cycling (e.g. after 0, 50, 100, 250, 500 750 and 1000 cycles), the package was taken out from the chamber, and nanoindentation was performed on above mentioned materials to obtain modulus, hardness, and creep behavior at room temperature (T = 25 ^{o}C).

8.2 PBGA Package Materials

The PBGA packages used for this study were Amkor CABGAs. The package details are as follows: size 17 x 17 mm, no. of balls 256, ball diameter 0.5 mm, and ball pitch 1 mm. The BGA solder ball alloy was SAC305 (96.5Sn-3.0Ag- 0.5Cu). On the package side of the test board, ENIG surface finish was used whereas SAC305 solder paste was used during surface mount assembly process. In the beginning of the specimen preparation, the 17x17 mm package assembly was cut and separated from the original board. Then using a grinder and polisher, the solder joints were revealed and the first row of the solder joints in the package were exposed (Figure 1). The rest of the package body was kept intact. The solder mask, die attach, silicon die, and mold compound were also revealed during this process. The thickness of solder mask layer was 50 μm. The silicon die and die attach layer thicknesses were found to be 270 μm and 70 μm, respectively. During the grinding and polishing process, the following methodology was followed. At

first, mechanical grinding was performed using different grit size (300-1200) SiC abrasive papers. Initial polishing was performed using diamond suspension (1 μm), and final polishing was done using colloidal silica suspensions (0.02 μm). With this, a mirror polished surface was achieved for SEM and nanoindentation. Figure 8.1 (a) shows SEM image of various materials within PBGA packages. Detail view of the materials is shown in Figure 8.1 (b) which is subjected to thermal cycling.

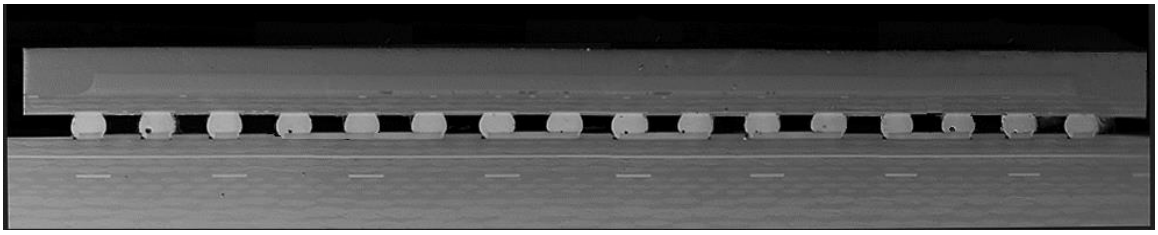

(a)

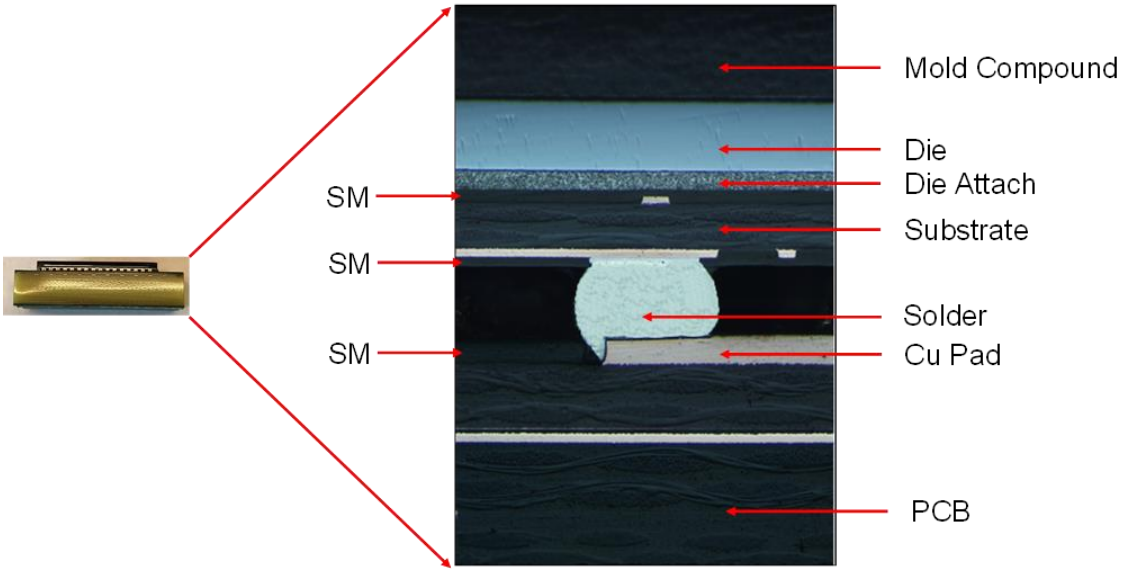

(b)

Figure 8.1 Various Materials within PBGA Packages

The cross-sectioned PBGA package is composed of several materials, which can be seen in Figures 8.1 (a) and 8.1 (b). The silicon die is attached to the substrate with a die attachment adhesive, followed by solder mask material (SM). The top of the package is covered with mold compound. The BGA substrate is connected with the PCB via solder joints connected to Cu pads. Each of these materials has its own functions and influences the reliability of the whole assembly.

A solder mask is typically a thin polymer layer in the package which is often is seen as the green colored outer layer on the printed circuit board. It prevents forming oxidation and helps in resisting solder bridges between copper pads. This solder mask layer covers a significant area, and hence finding the mechanical properties of solder masks is very important for getting high interconnect reliability during operation. Zhu, et al worked on different solder mask materials and showed their mechanical properties and creep response [161]. Chowdhury et al. [162] studied solder mask material mechanical property under different temperatures and various durations of UV exposure. Their study showed elastic modulus and ultimate tensile strength drops with temperature and increases with UV exposure. Die attachment materials are used to attach silicon die to as substrate beneath. Die attach materials have two key functions 1) conducting heat away from the die, and 2) mechanical fixation of the die onto the substrate. Researchers have been studying different die attach materials specially suitable at high temperature applications and sustainable in harsh environments. Siow and Chua [163] studied silver sintered joints as die attach materials, and measured their shear strengths under thermal cycling conditions. They found out that the shear strength of the sintered die attach material drops with the number of thermal cycles. Researchers have also studied die attach and silicon die mechanical

behavior during environmental harsh exposures. Chen and coworkers [164] measured die stress during exposure of a PBGA package to various moisture conditions. They found out that die stress increases with moisture exposure.

8.3 Experimental Procedure

A TI 950 TriboIndenter from Hysitron was used to extract mechanical properties of various materials: solder joints, solder mask, die attach, and silicon die at room temperature with the use of a room temperature stage Nanoindentation testing was performed on different materials in arrays of regularly spaced indentations on desired phases. The total package was placed above a disc and then mounted on the nanoindentation stage (Figure 8.2). A Berkovich pyramidal nano-indenter was used to apply maximum of 15 mN load. A loading rate of 3 mN/sec was chosen during the loading phase, followed by a load hold for 30 s which prevents creep effect in the test results. Finally, unloading was done at the same rate of 3 mN/sec. The load vs. indentation displacement normal to the cross-sectional area was recorded and evaluated. Mechanical properties (modulus and hardness) were obtained using the well-known Oliver and Pharr method. Final values of the properties were obtained by taking the average of at least 6-10 indents providing consistent results. While performing the creep testing, a 600 sec hold was maintained at the peak indentation load of 15 mN. The creep deformations were then recorded during the hold time period and analyzed accordingly. Axis calibration of the nano-indenter was done in order to get accurate test results followed by mechanical property calibrations on standard fused silica and quartz samples. An additional thermal drift measurement was performed, and thermal drift corrections were utilized to minimize

the effects due to temperature fluctuations during indentation experiments. The drift rate was maintained to be less than 0.05 nm/sec for each indentation.

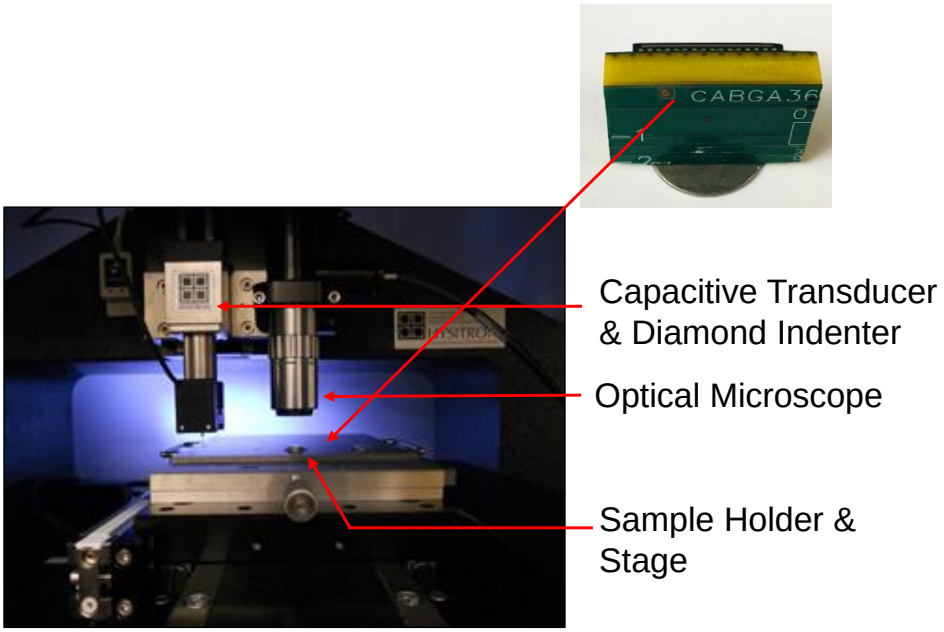

Figure 8.2 Nanoindentation for PBGA Package Materials

8.4 Solder Mask Materials

8.4.1 As Reflowed Condition Mechanical Properties

Nanoindentation testing was performed on the solder mask material in the package located between die attach layer and the BGA substrate. Figure 8.3 (a) shows the indentation marks on the solder mask after nanoindentation testing was performed. A total of 10-12 indentations were performed for each duration of thermal cycling, and the modulus and hardness were calculated from the indentation load displacement curves. Then, average values of modulus and hardness were calculated. Figure 8.3(b) shows a representative load-displacement curve for the solder mask material at the initial no cycle condition. The average modulus and hardness were found to be 7.75 GPa and 0.41 GPa, respectively.

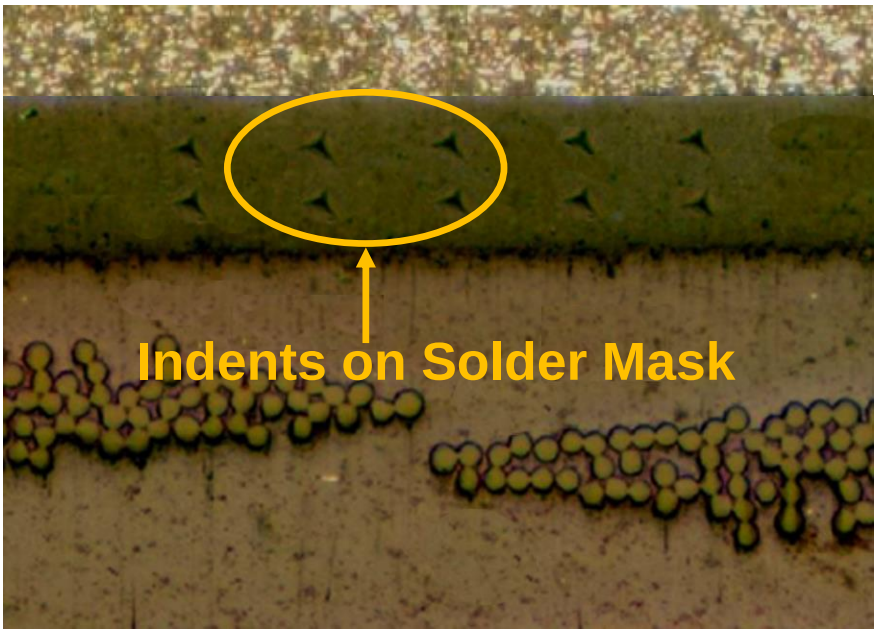

(a)

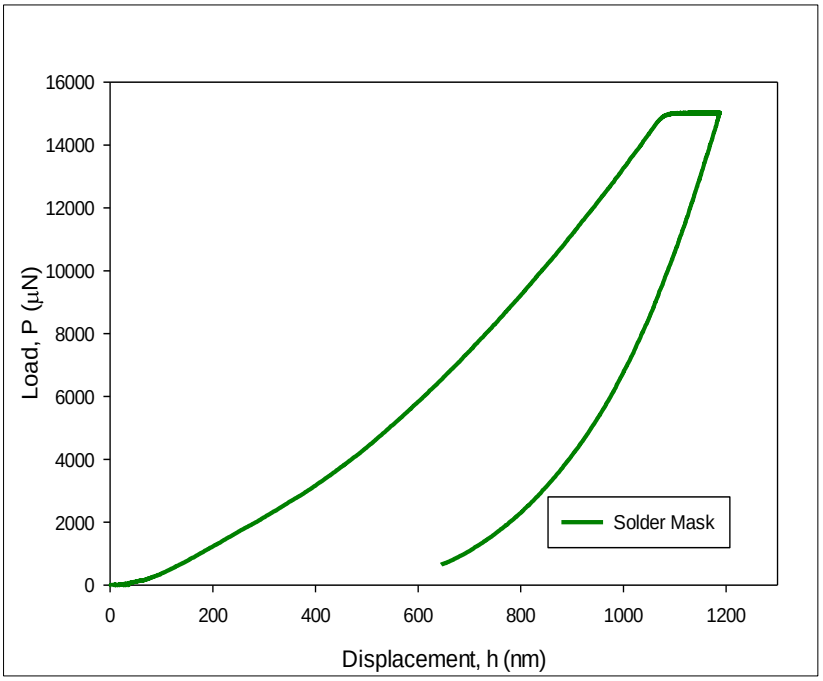

(b)

Figure 8.3 (a) Indentation Marks and on Solder Mask Materials

(b) Representative Load-Displacement Curve

Table 8.1 Modulus and Hardness of Solder Mask Material at No Cycling

Material	Modulus, E	Hardness, H
Solder Mask	7.75 ± 0.23	0.41 ± 0.018

8.4.2 Evolution of Mechanical Behavior with Thermal Cycling

The evolution of the mechanical behavior was observed as a function of the duration of thermal cycling up to 1000 cycles. As the package was cycled and indentations were made in the same solder mask layer, it was found that both modulus and hardness values increased significantly as shown in Figure 8.4. After 250 cycles, the modulus of the solder mask layer increased about 24%. The hardness value also increased about 21% from the no cycling condition. These increases in modulus and hardness could be attributed to additional curing and cross-linking of the polymer chains present in the solder mask when exposed to high temperature during thermal cycling. This phenomenon is very important to know since this change in the mechanical behavior can cause additional stress and CTE changes, which can affect performance of other layers and cause reliability concerns for the BGA package assembly. Between 250 and 500 cycles, both modulus and hardness starts to drop again which could be attributed to the additional thermal degradation during high temperature dwell. Modulus and hardness keep dropping with a lower rate after 750 cycles and then almost stabilizes at 1000 cycles.

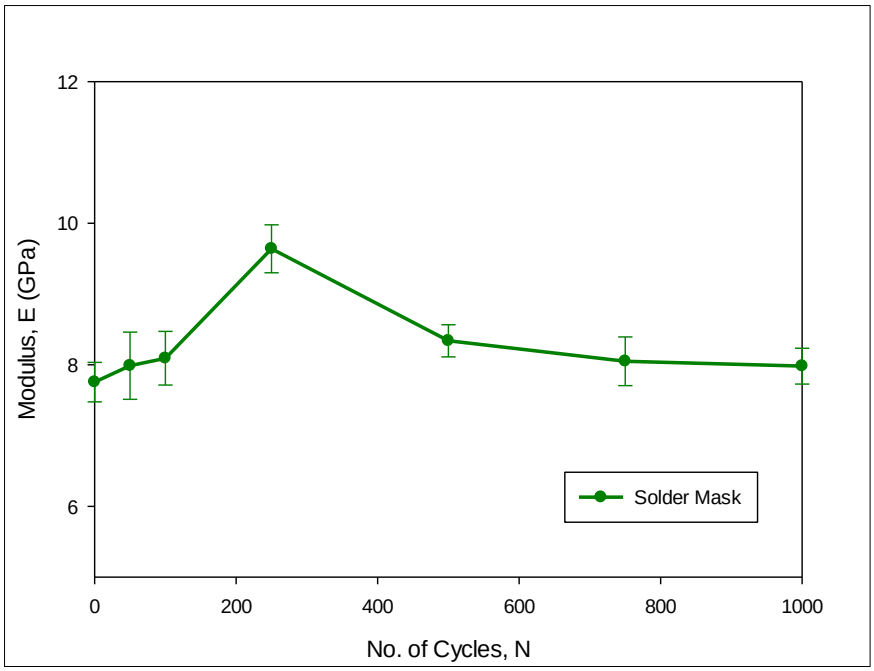

(a)

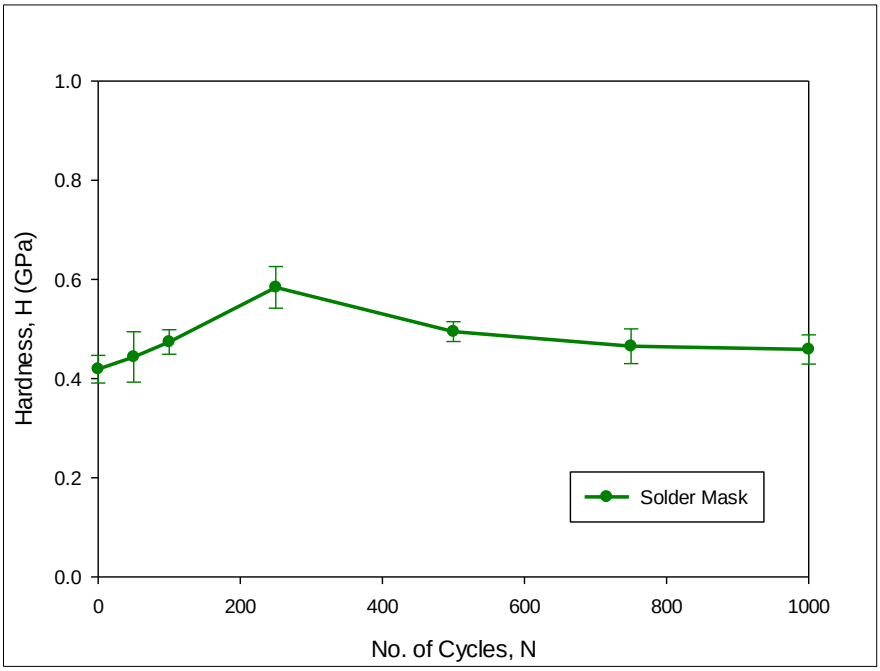

(b)

Figure 8.4 Evolution of (a) Modulus and (b) Hardness of Solder Mask Material as a Function of Thermal Cycling

8.4.3 Evolution of Creep Behavior for Solder Mask Material

Creep study was performed on solder mask material using the same methodology. While observing the creep in solder mask material, opposite behavior was observed compared to solder alloy. Indentation displacement was observed to decrease gradually up to 250 thermal cycles whereas in solder alloy deformation increased with cycling. Indentation displacement vs. time curve for the solder mask material is shown in figure 8.5. At no cycling condition, displacement was found to be about 430 nm which decreased to 400 nm after 50 cycles of thermal cycling. After 250 cycles the indentation displacement of the solder mask layer was found to decrease significantly which is 1.5 times less than the value at no cycling condition. However, after 500 cycles deformation increases about 60 nm from 250 cycles. Figure 11 shows the creep strain rate vs. stress plot of solder mask layer with different durations of thermal cycles. It was found that creep rate decreases about 46X compared to no cycle condition and then increases again at 500 cycles. Crosslinking density of the polymer chain present in the solder mask material increases when exposed to high temperature during cycling which can be described as the main reason for increasing creep rate. Solder mask layer became fully cross-linked in between 250 and 500 cycles and further exposure may cause formation of micro cracks as a fatigue effect or causing thermal degradation of solder mask which increases creep rate at 500 cycles.

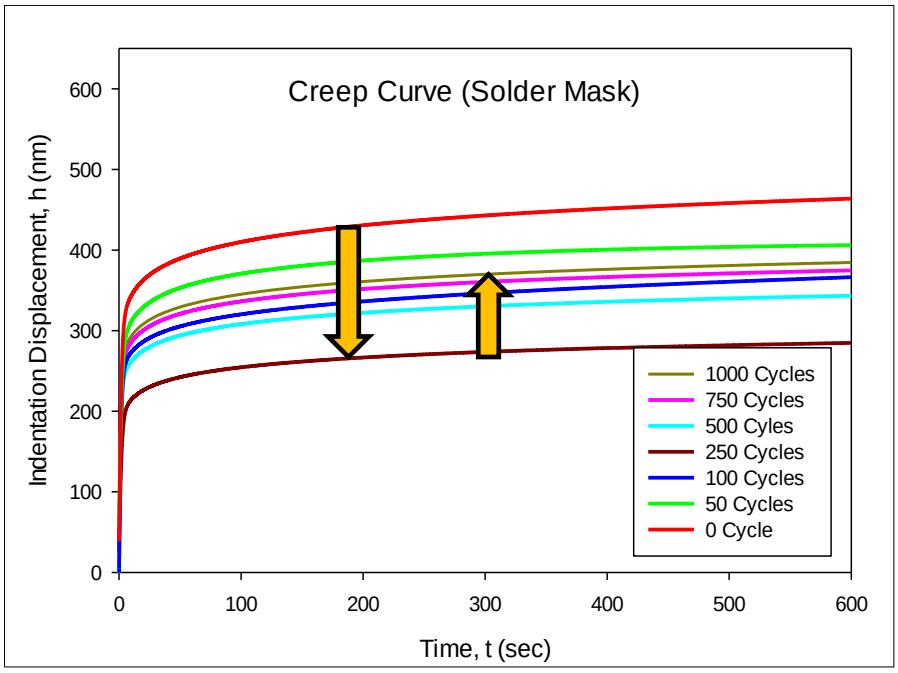

Figure 8.5 Creep Deformation of Solder Mask as a Function of Thermal Cycling

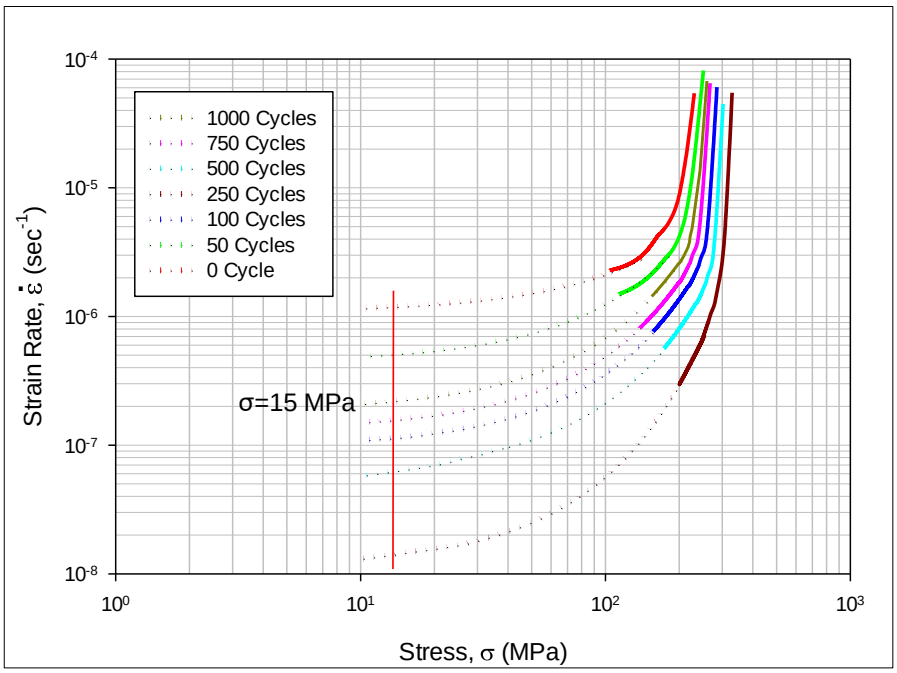

Figure 8.6 Creep Strain Rate vs. Stress of Solder Mask as a Function of Thermal Cycling

8.5 Die Attach Materials

8.5.1 As-Reflowed Condition Mechanical Properties

The die attach material was also studied using nanoindentation to find out its mechanical property changes. Figure 8.7 shows a representative load-displacement curve of the die attach material from a nanoindentation test at the no cycling condition. With the same applied load, the die attach showed a maximum deformation of about 2350 nm. The value of the average modulus and hardness were 3.20 GPa and 0.13 GPa, respectively which is shown in Table 8.2. From the results, if compared with solder mask material the maximum displacement is even higher with die attach and thus have a lower value of modulus and hardness under the application of same load.

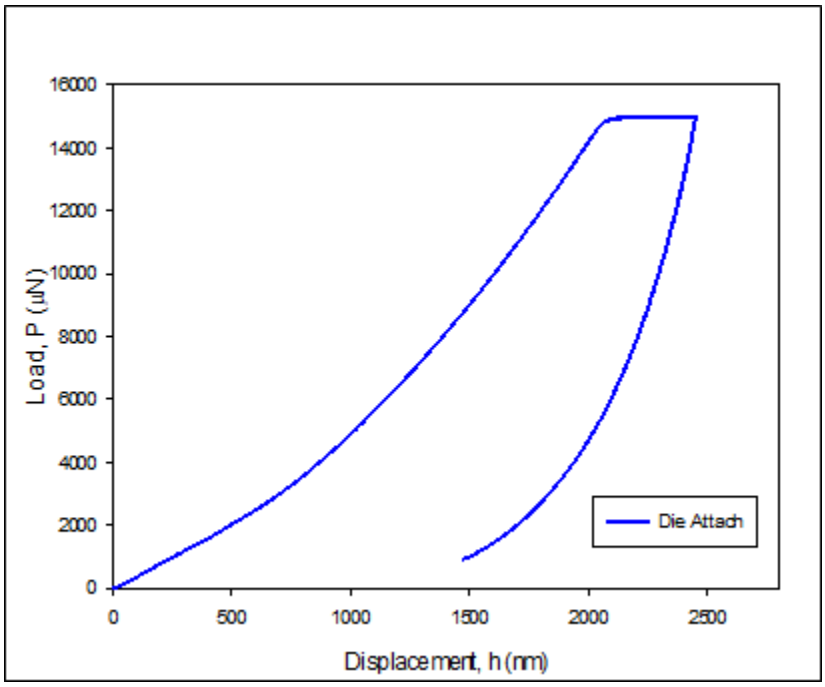

Figure 8.7 Representative Load-Displacement Curve for Die Attach

Table 8.2 Modulus and Hardness of Die Attach Material at No Cycling

Material	Modulus, E	Hardness, H
Die Attach	3.20 ± 0.2	0.13 ± 0.01

8.5.2 Evolution of Mechanical Behavior with Thermal Cycling

As the package was cycled, the properties of the die attach were recorded with different durations of thermal cycling for up to 250 cycles using the same nanoindentation technique. The variations of the modulus and hardness with the number of thermal cycles are shown in Figure 11. The modulus and hardness for the die attach also increased significantly with thermal cycling. The modulus value increased gradually from 3.2 to 7.5 GPa. On the other hand, hardness value increased from 0.13 to 0.285 GPa. The increase in hardness implies an increase in the strength of the die attach. In between 250 and 500 cycles, modulus and hardness started to drop due to additional thermal aging. The value continue to drop up to 1000 cycles but the rate of drop decreased or almost became metastable.

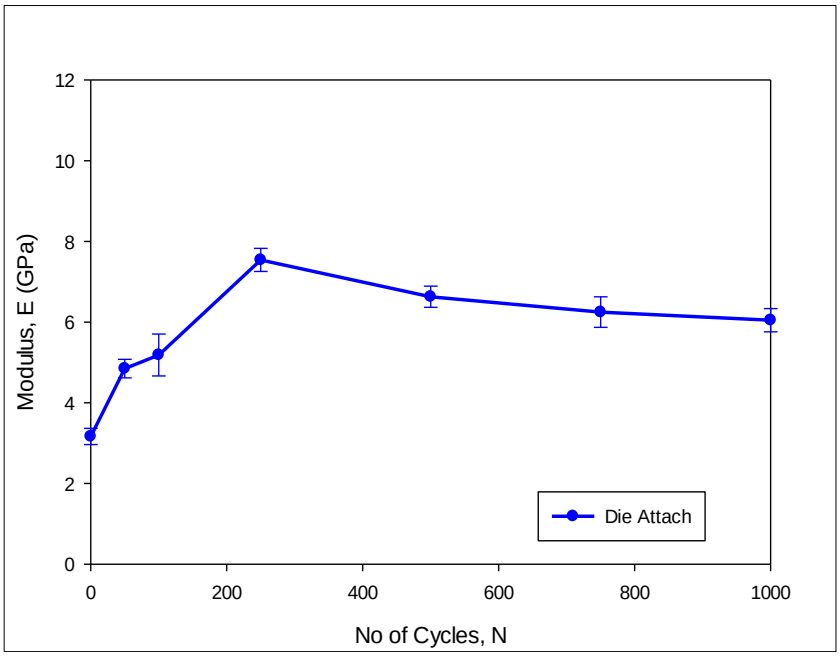

(a)

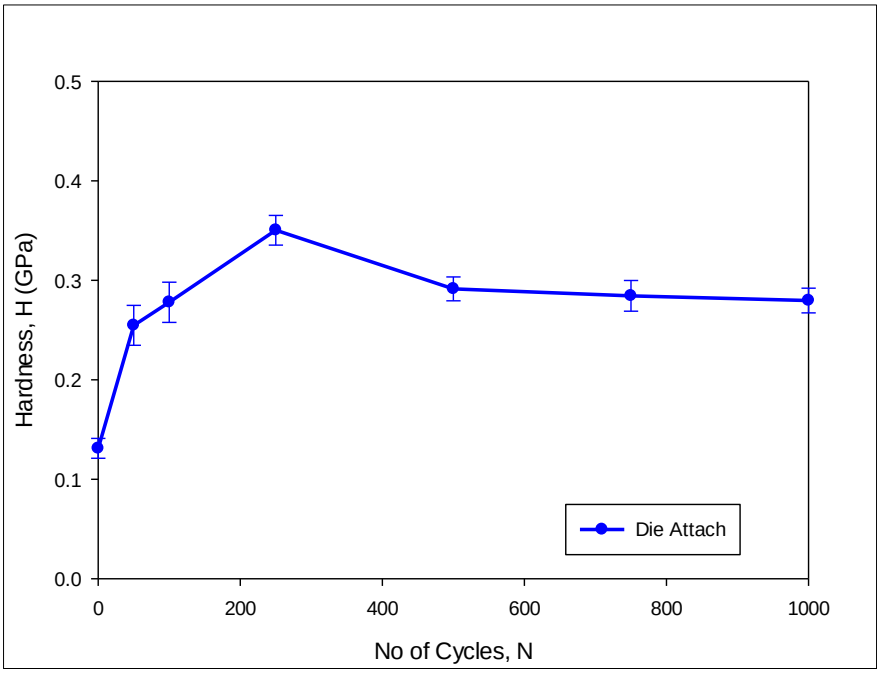

(b)

Figure 8.8 Evolution of (a) Modulus and (b) Hardness of Die Attach Material as a Function of Thermal Cycling

8.5.3 Evolution of Creep Behavior for Die Attach Material

Creep behavior of the die attach material is shown in figure 8.9. Deformation behavior was observed to be very similar with the solder mask. However, the magnitude of the evolution is even higher for the die attach material. Indentation displacement decreases with no. of thermal cycles. At no cycle, die attach showed significant displacement of about 1120 nm. After 50 thermal cycles, displacement dropped to 906 nm. After 100 thermal cycles, it dropped even more and reaches 785 nm. A significant 50% drop in displacement happened after 250 thermal cycles obtaining about 560 nm of displacement. However, after 500 thermal cycles, displacement after 600 s increases to about 650 nm which is higher from the value obtained at 250 cycles. After 1000 cycles, displacement increased to 750 nm approximately.

From the strain rate vs. stress plot in fig. 8.10, it was found that creep rate decreases about 54X at 250 cycles compared to no cycling condition and then again increases at 500 cycles. The reason again could be attributed to the increase in crosslinking sites and getting fully cross-linked between 250 and 500 cycles and then further cycling causes fatigue crack or thermal degrading causing creep rate to increase. After 750 Cycles, the creep strain rate at a fixed stress of 15 MPa again goes up bit not at the rate of after 500 cycles. After 1000 cycles of thermal cycling, creep rate goes up slightly higher compared to 750 cycle results. It can be concluded that the creep rate still going up which means die attach material is still degrading due to thermal exposure. The polymer chain is breaking due to temperature and causing creep rate to go up.

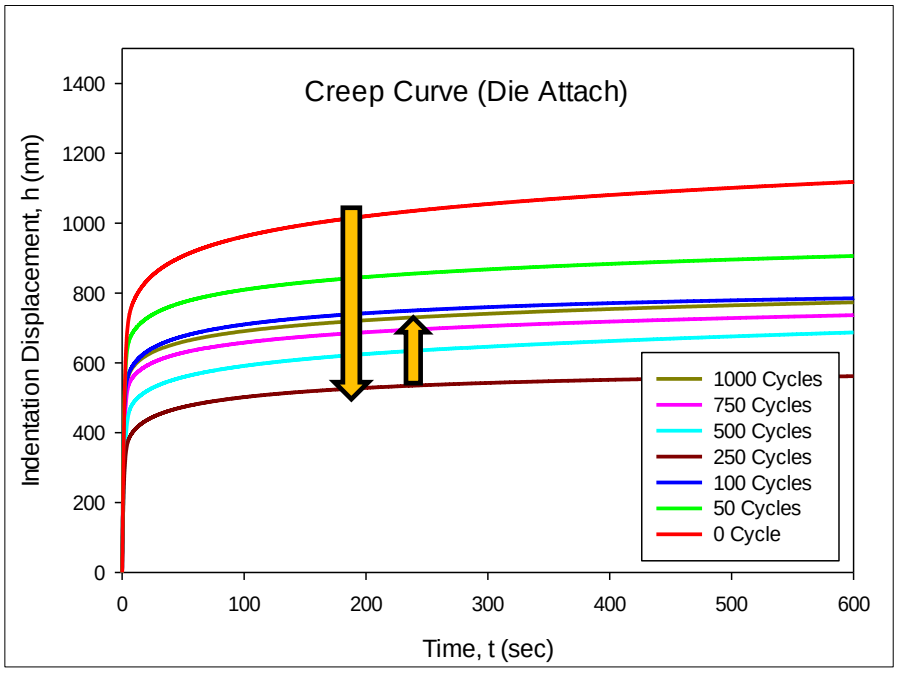

Figure 8.9 Creep Deformation of Die Attach as a Function of Thermal Cycling

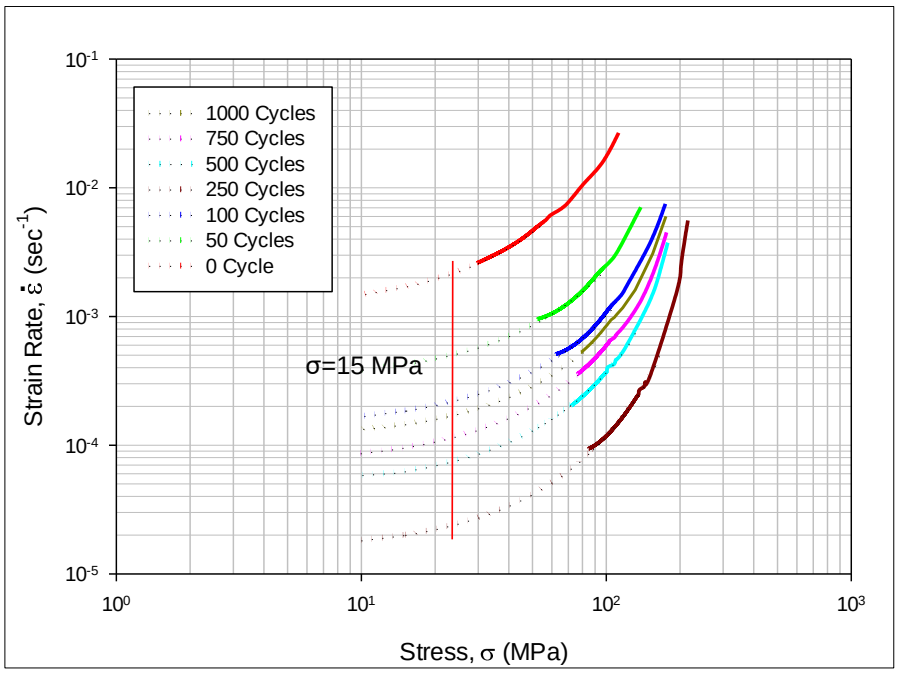

Figure 8.10 Creep Strain Rate vs. Stress of Die Attach as a Function of Thermal Cycling

8.6 Silicon Die Materials

8.6.1 As-Reflowed Condition Mechanical Properties

Nanoindentation was also performed on the silicon die material and the material property evolution was observed. Figure 8.11 shows representative load-displacement curve for Values of the maximum deformation (230 nm) were much lower relative to the other materials at the same applied load. The average modulus and hardness values were 164 GPa and 14 GPa, respectively (Figure 8.11 and Table 8.3). It can be said that, silicon die material is very brittle and has very high stiffness compared to other material in PBGA packages and are very vulnerable to drop or shock load. Crack can propagate through the die material and can cause failure of the whole package easily.

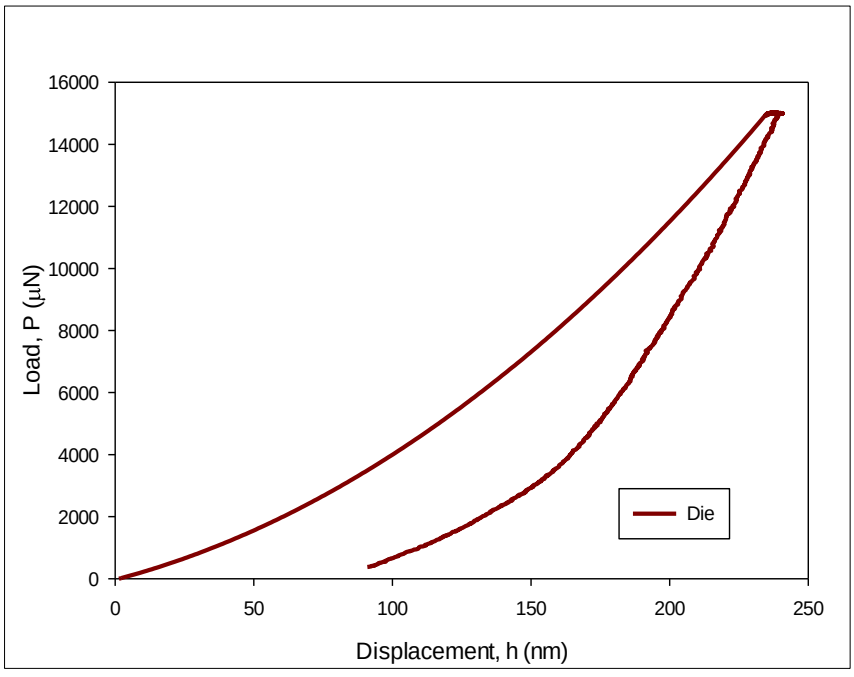

Figure 8.11 Representative Load-Displacement Curve for Die Attach

Table 8.3 Modulus and Hardness of Die at No Cycling

Material	Modulus, E	Hardness, H
Die	164.0 ± 12.0	14 ± 0.84

8.6.2 Evolution of Mechanical Behavior for Die Material

Evolution of modulus and hardness were measure for die material. Since die material is anisotropic in nature, a large variation was observed in the results for each cyclic condition. However, there were no significant changes observed in both the modulus values with thermal cycling which is expected (Figure 8.12). Similar trend was observed for the hardness measurements. It can be said that temperature fluctuations has no effect on Si die material.

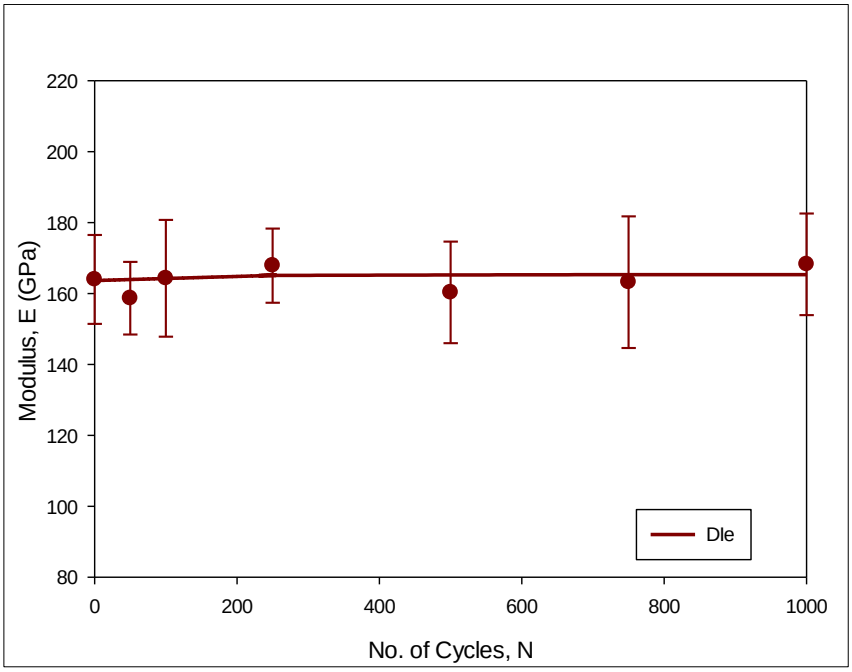

(a)

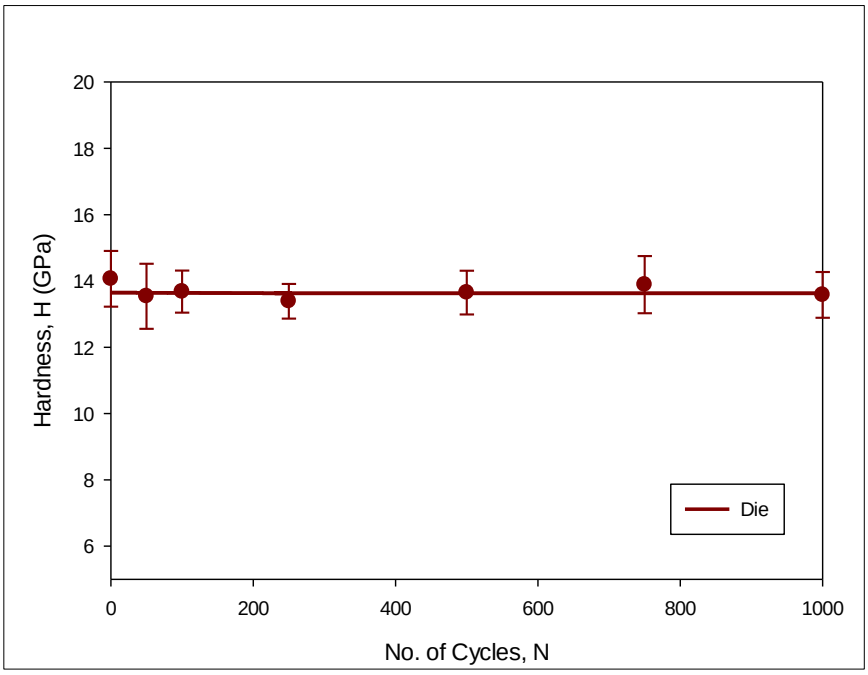

(b)

Figure 8.12 Evolution of (a) Modulus and (b) Hardness of Si Die Material as a Function of Thermal Cycling

8.6.3 Creep Behavior of Die Material

Creep behavior was analyzed on silicon die material and the creep curve is shown in figure 8.13. We can see with the 15 mN applied load, silicon die showed only 20 nm of indentation displacement most of which is the initial jump due to applied load and few nm of displacement due to primary and secondary creep at no cycling. This is expected since Si does not go much under creep deformation. Further cycling was performed and there was not any significant change in the creep behavior of the die. It can be said that creep does now occur in Si die and creep deformation does not change significantly with thermal cycling behavior.

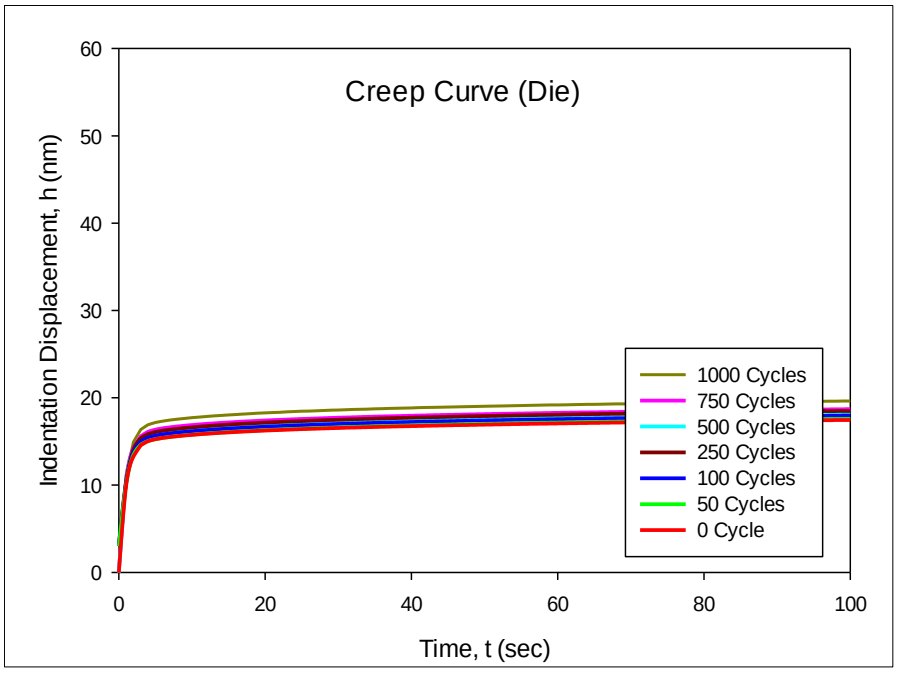

Figure 8.13 Creep Deformation of Die Material as a Function of Thermal Cycling

8.7 Summary

In this chapter, various materials in the PBGA packages were thermal cycled and evolution of mechanical and creep behavior of those materials were studied carefully using nanoindentation technique. Different materials of the PBGA packages studied in this paper were solder mask, die and die attach. Solder interconnects were studied from as reflowed condition to up to 1000 thermal cycles. For the solder mask material, mechanical behavior showed opposite behavior up to 250 thermal cycles. Deformation and creep rate decreases up to 250 cycles and then increased at 500 thermal cycles and then continue to increase upto 1000 cycles with a lower rate. For the die attach material, similar trend as like as the solder mask material was observed but the magnitude of increase in deformation and creep rate is much higher. However, for the die material all these properties did not show any significant variation with thermal cycling.

CHAPTER 9

SUMMARY AND CONCLUSIONS

9.1 Literature Review

The mechanical properties of a solder are strongly influenced by its microstructure, which is controlled by its thermal history including its solidification rate and thermal exposures after solidification. Aging of lead free solders leads to degradations in their constitutive and failure behaviors. For example, research in the literature has shown that aging leads to large reductions in solder material properties including shear strength, elastic modulus, nanoindentation joint modulus and hardness, high strain rate mechanical behavior and creep response. Other studies have shown that aging causes severe degradations in uniaxial cyclic stress-strain curves and fatigue life, shear cyclic stress-strain curves and fatigue life, fracture behavior, drop reliability, and thermal cycling reliability.

Dopants have been found to strongly influence the properties and behaviors of lead free solders. For Example, Bi helps to reduce solidification temperature, increases strength by means of precipitation hardening, helps to reduce IMC (Intermetallic Compound) layer thickness, and also reduce aging induced degradation of mechanical properties in lead free solder materials. Ni helps to improve thermal fatigue life and drop test performance by refining Sn grain size and reducing the IMC layer formation near the Cu pad. The effects

of rear earth (RE) elements and nanoparticle addition on the properties of lead free solder was also discussed in this chapter.

Nanoindentation methods have shown great potential for characterizing solder materials and aging effects at the joint scale. Nanoindentation is mainly used to extract elastic modulus and hardness of solder joints. Many of the prior works have also used nanoindentation technique to characterize the creep properties although most of the nanoindentation experiments, on solder joints, were conducted at room temperature.

The changes in solder mechanical behavior are a result of the evolution of the SAC solder microstructure that occurs during aging. The most well-known and widely observed changes are coarsening of the Ag_3Sn and Cu_6Sn_5 intermetallic compounds (IMCs) present in the eutectic regions between beta-Sn dendrites. Several researchers have proposed empirical models to describe the growth of these secondary phase particles as a function of aging temperature and aging time, and related this growth to mechanical property changes.

9.2 Experimental Procedures

All the experimental procedures and the data processing steps were presented in chapter 3. Micro-scale uniaxial tensile specimens were prepared in a rectangular shaped hollow glass tube using a vacuum suction method. Typical dimension of the uniaxial tensile specimens were 80 (length) X 3 (width) X 0.5 (height) mm. Uniaxial tensile tests were performed using a micro tension torsion testing system. Nanoindentation experiments were conducted on actual solder joints which were typically extracted from 14 x 14 mm PBGA assemblies (0.8 mm ball pitch, 0.46 mm ball diameter). Nanoindentation experiments were performed using Hysitron TI950 TriboIndenter.

9.3 High Temperature Creep Behavior of SAC and Doped Lead Free Solders

In this work, the creep behavior of several SAC and doped lead free solder alloys at extreme high temperatures up to 200 °C has been investigated. The studied alloys included SAC405 (96.5Sn-4.0Ag-0.5Cu), SAC_Q (92.8Sn-3.4Ag-0.5Cu-3.3Bi), and Innolot (90.95Sn-3.8Ag-0.7Cu-3.0Bi-0.15Ni-1.4Sb). The solder uniaxial test specimens were formed in high precision rectangular cross-section glass tubes using a vacuum suction process. The samples were initially cooled in a water bath and were later reflowed. The reflow profile was chosen to closely mimic profiles used for BGA assemblies, so that the obtained microstructures were similar to those found in typical solder joints.

For each of 5 elevated temperatures (T = 100, 125, 150, 175, and 200 °C), uniaxial creep tests were performed at three stress levels (σ =10 and 15 MPa). For each alloy and testing temperature, creep strain with time of the solders were measured and compared. As expected, the results have shown significant degradations of the mechanical properties of lead-free solders at higher temperatures. However, it was found that the addition of dopants (e.g. Bi, Ni, and Sb) in the SAC+X alloys improved their high temperature properties significantly. Both SAC_Q and Innolot alloys significantly outperformed SAC405 at all temperature levels however Innolot performed best among all the alloys.

9.4 Mechanical Behavior of IMC Compounds at Room Temperature

Mechanical behaviors of IMC particles and layers in SAC solder joints have been characterized using nanoindentation. SAC BGA solder joints were first aged for 6 months at T = 125 ^{o} C. Test samples were subsequently prepared by cross-sectioning the aged

solder joints, and then molding them in epoxy and polishing them to prepare the joint surfaces for microscopy and nanoindentation. Intermetallics formed in the bulk solder region, copper pad and SAC solder interface, and ENIG plating finish and SAC solder interface were observed and detected using SEM and the energydispersive x-ray spectroscopy (EDX) technique. The same intermetallics were then indented to measure their room temperature mechanical properties at first phase including the elastic modulus, hardness, and creep strain rate.

9.5 Nanoindentation Characterization of IMCs and β-Sn Phase at High Temperatures

Mechanical properties of IMCs and increased knowledge about their behavior in different operating conditions becomes desirable since the microelectronics industry has been facing significant challenges with these IMCs. The size of devices and solder joints are continuously decreasing, and, hence, the IMCs are occupying a key volume fraction of the entire package. Besides, electronic packages are now subjected to harsh operating conditions (i.e. extreme temperature). Understanding of the mechanical properties of these individual phases at various operating conditions makes predictions of the mechanical behavior of an overall joint more straightforward. In the second phase, intermetallics were indented to measure their mechanical properties which includes the elastic modulus and hardness at elevated temperatures (50, 75, 100 and 125 ^{o}C) using a heating stage. Time dependent deformation (creep) behaviors were also evaluated at room temperature and 100 ^{o}C to see the effect of high temperature on the creep rate of IMCs.

9.6 Mechanical Behavior of Individual Phases of SAC Solder Joints as a Function of Aging Using Nanoindentation

Measurement of the mechanical properties of individual phases in a solder joint is now possible using an instrumented indentation technique commonly known as nanoindentation. This nanoindentation technique has now received a great attention to researchers as valuable method for obtaining the mechanical behavior of materials at very small scales by probing, i.e. it has capability to measure the properties of materials in very thin films and coatings. This technique is well suited to investigate mechanical properties of solder joints and IMC particles that exist in bulk solder region. Testing with this tool can be done to probe small volumes by utilizing a diamond indenter tip attached to a sensitive capacitive transducer, which is operated at ultralow load (e.g., 0.1–10 mN). Throughout the testing load and displacement of the tip are measured which allows the user to determine elastic modulus from the unloading curve. It also gives measurement of hardness by calculating depth at the maximum load point.

In this study, we have measured the mechanical properties of individual Sn grain and IMC particles in a solder joint using nanoindentation technique during isothermal aging at 125 ^{o}C. SAC solder joints extracted from Super BGA (SBGA) packages were aged for different time intervals (0, 1, 5, 10 and 30 days). Nanoindentation test samples were prepared by cross sectioning the solder joints, and then molding them in epoxy and polishing them to prepare the joint surfaces for nanoindentation. Several tests were recorded to measure modulus, hardness and creep behavior with aging at 25 ^{o}C and average representations of those results are shown in this work.

9.7 Mechanical Behavior of SAC Solder Joints under Thermal Cycling Loading

Nanoindentation technique was used to understand the evolution of mechanical properties (modulus, hardness and creep behavior) of SAC305 BGA solder joints subjected to thermal cycling loading for various durations. In addition, microstructural changes in those joints that occur during thermal cycling were observed using both SEM and optical microscopy. Solder joint strip samples were thermally cycled from T = -40 to 125 ^{o}C in an environmental chamber. At various points in the cycling (e.g. after 0, 50, 100, and 250 cycles), the package was taken out from the chamber, and nanoindentation was performed on each single grain joint to obtain the modulus, hardness, and creep behavior at 25 ^{o}C. This allowed the evolution of the mechanical properties with the duration of thermal cycling to be determined. Moreover, microstructural changes were also observed after various durations of cycling using optical microscopy. From the nanoindentation test results, it was found that the modulus and hardness of the SAC305 solder joints dropped 28-35% and 31-33%, respectively, after 1000 thermal cycles. Moreover, the nanoindentation creep test results showed significant increases of 63X to 87X in the creep strain rate after 250 thermal cycles and then drops at 500 cycles.

9.8 Mechanical Behavior of PBGA Package Materials under Thermal Cycling

Various materials in the PBGA packages were thermal cycled and evolution of mechanical and creep behavior of those materials were studied carefully using nanoindentation technique. Different materials of the PBGA packages studied in this paper were solder mask, die and die attach. Solder interconnects were studied from as reflowed condition to up to 1000 thermal cycles. For the solder mask material, mechanical behavior

showed opposite behavior up to 250 thermal cycles. Deformation and creep rate decreases up to 250 cycles and then increased at 500 thermal cycles and then continue to increase upto 1000 cycles with a lower rate. For the die attach material, similar trend as like as the solder mask material was observed but the magnitude of increase in deformation and creep rate is much higher. However, for the die material all these properties did not show any significant variation with thermal cycling.

9.9 Summary

In this Dissertation, several SAC and SAC+X lead free solder alloys have been characterized and the reliability of these alloys in harsh environment applications have been investigated. These alloys were subjected to very high testing temperature up to 200 °C and mechanical properties, such as elastic modulus, ultimate tensile strength, and yield stress were recorded. It was found that mechanical properties of lead free solder alloys degrade significantly at higher temperature. High temperature creep properties of the solder alloys were compared. Comparison of the results for different solders has shown that the addition of dopants (e.g. Bi, Ni, and Sb) in the traditional SAC alloys improved their high temperature properties significantly. Also, this study considered properties of Intermetallic Compounds at room temperatures. Also, mechanical and creep behavior at test temperatures in the range of T = 25-125 °C was also analyzed. Outcome of these results showed IMC particles are much stiffer and harder compared to Sn phase of the joint. Also, properties of the IMC phases drops significantly with increase in test temperature. In another study, mechanical properties and creep behavior of the individual phases of SAC solder joints were characterized as a function of aging time from 0-30 days. The outcome

showed properties of the individual phases does not change significantly with aging time. In another study, mechanical and creep behavior of SAC solder joints were characterized using nanoindentation under thermal cycling loading. Outcome of this work shows significant degradation of the solder material with thermal cycling. However, the larger degradation occurs within the first 250 cycles of thermal cycling. In final work, mechanical and creep behavior of various materials within PBGA packages were evaluated under thermal cycling loading. Outcome of this work shows both solder mask and die attach material shows initial increase in mechanical properties which drops again at 500 cycles due to thermal degradation. The initial increase was due to increase in crosslinking density. However, in case of die material there was no change in mechanical and creep behavior was observed.

9.10 Future Work

Following future work can be performed to extend the findings of this dissertation:

- Extend high temperature creep behavior of different SAC and SAC+X alloys subjected to high temperature aging at various temperatures can be explored at various stress levels (5-20 MPa).
- Understand evolution of mechanical and creep behavior of individual phases of SAC solder joints subjected to thermal cycling loading.
- Study grain orientations of β-Sn using EBSD analysis and develop relation by correlating their theoretical mechanical behavior with nanoindentation test data.
- Microstructure based modelling to understand deformation of solder alloys using the individual phase mechanical behavior.

- Microstructure evolution study of SAC and SAC+X solder alloys can be performed under thermal cycling loading and can be compared with aging induced evolution. A mathematical model can be developed to predict solder joint reliability as a function of thermal cycling time.

REFERENCES

[1] M. Abtew and G. Selvaduray, "Lead-Free Solders in Microelectronics," *Materials Science and Engineering: R: Reports,* vol. 27, no. 5, pp. 95-141, 2000.

[2] P. T. Vianco, "Development of Alternatives to Lead-Bearing Solders," *Proceedings of the Technical Program on Surface Mount Technical Association International Conference,* 1993.

[3] J. S. Hwang, *Implementing Lead-Free Electronics*. McGraw-Hill, New York, 2005.

[4] Q. Zhang, A. Dasgupta, and P. Haswell, "Creep and High-Temperature Isothermal Fatigue of Pb-Free Solders," *Proceedings of ASME InterPACK,* no. 36908a, pp. 955-960, 2003.

[5] NCMS, "Lead-Free Solder Project Final Report," *NCMS Report 0401RE96,* 1997.

[6] N. C. Lee, "Getting Ready for Lead-Free Solders," *Soldering & Surface Mount Technology,* vol. 9, no. 2, pp. 65-69, 1997.

[7] K. S. Kim, S. H. Huh, and K. Suganuma, "Effects of Intermetallic Compounds on Properties of Sn–Ag–Cu Lead-Free Soldered Joints," *Journal of Alloys and Compounds,* vol. 352, no. 1, pp. 226-236, 2003.

[8] J.-W. Yoon, S.-W. Kim, and S.-B. Jung, "IMC Morphology, Interfacial Reaction and Joint Reliability of Pb-Free Sn–Ag–Cu Solder on Electrolytic Ni BGA Substrate," *Journal of Alloys and Compounds,* vol. 392, no. 1, pp. 247-252, 2005.

[9] D. Q. Yu and L. Wang, "The Growth and Roughness Evolution of Intermetallic Compounds of Sn–Ag–Cu/Cu Interface During Soldering Reaction," *Journal of Alloys and Compounds,* vol. 458, no. 1, pp. 542-547, 2008.

[10] C. M. L. Wu, D. Q. Yu, C. M. T. Law, and L. Wang, "Properties of Lead-Free Solder Alloys with Rare Earth Element Additions," *Materials Science and Engineering: R: Reports*, vol. 44, no. 1, pp. 1-44, 2004.

[11] Y. C. Chan and D. Yang, "Failure Mechanisms of Solder Interconnects under Current Stressing in Advanced Electronic Packages," *Progress in Materials Science*, vol. 55, no. 5, pp. 428-475, 2010.

[12] C.-h. Wang and S.-w. Chen, "Sn–0.7wt.%Cu/Ni Interfacial Reactions at 250°C," *Acta Materialia*, vol. 54, no. 1, pp. 247-253, 2006.

[13] G. Zeng, S. D. McDonald, Q. F. Gu, K. Sweatman, and K. Nogita, "Effects of Element Addition on the β→α Transformation in Tin," *Philosophical Magazine Letters*, vol. 94, no. 2, pp. 53-62, 2014.

[14] W. J. Plumbridge, "Tin Pest Issues in Lead-Free Electronic Solders," in *Lead-Free Electronic Solders: A Special Issue of the Journal of Materials Science: Materials in Electronics*, pp. 307-318, 2007.

[15] S. Cheng, C.-M. Huang, and M. Pecht, "A Review of Lead-Free Solders for Electronics Applications," *Microelectronics Reliability*, vol. 75, pp. 77-95, 2017.

[16] M. Hasnine, B. Tolla, and M. Karasawa, "Effect of Ge Addition on Wettability, Copper Dissolution, Microstructural and Mechanical Behavior of SnCu–Ge Solder Alloy," *Journal of Materials Science: Materials in Electronics*, vol. 28, no. 21, pp. 16106-16119, 2017.

[17] Q. B. Tao, L. Benabou, L. Vivet, V. N. Le, and F. B. Ouezdou, "Effect of Ni and Sb Additions and Testing Conditions on the Mechanical Properties and Microstructures of Lead-Free Solder Joints," *Materials Science and Engineering: A*, vol. 669, pp. 403-416, 2016.

[18] J. Glazer, "Metallurgy of Low Temperature Pb-Free Solders for Electronic Assembly," *International Materials Reviews,* vol. 40, no. 2, pp. 65-93, 1995.

[19] M. McCormack, S. Jin, G. W. Kammlott, and H. S. Chen, "New Pb-Free Solder Alloy with Superior Mechanical Properties," *Applied Physics Letters,* vol. 63, no. 1, pp. 15-17 1993.

[20] K. Nogita, "Stabilisation of Cu6Sn5 by Ni in Sn-0.7 Cu-0.05 Ni Lead-Free Solder Alloys," *Intermetallics,* vol. 18, no. 1, pp. 145-149, 2010.

[21] F. X. Che, J. E. Luan, and X. Baraton, "Effect of Silver Content and Nickel Dopant on Mechanical Properties of Sn-Ag-Based Solders," *Proceedings of the 58th IEEE Electronic Components and Technology Conference,* pp. 485-490, 2008.

[22] F. Guo, J. Lee, S. Choi, J. P. Lucas, T. R. Bieler, and K. N. Subramanian, "Processing and Aging Characteristics of Eutectic Sn-3.5 Ag Solder Reinforced with Mechanically Incorporated Ni Particles," *Journal of Electronic Materials,* vol. 30, no. 9, pp. 1073-1082, 2001.

[23] Z. G. Chen, Y. W. Shi, Z. D. Xia, and Y. F. Yan, "Study on the Microstructure of a Novel Lead-Free Solder Alloy SnAgCu-Re and Its Soldered Joints," *Journal of Electronic Materials,* vol. 31, no. 10, pp. 1122-1128, 2002.

[24] F. Gao, S. Mukherjee, Q. Cui, and Z. Gu, "Synthesis, Characterization, and Thermal Properties of Nanoscale Lead-Free Solders on Multisegmented Metal Nanowires," *Journal of Physical Chemistry C,* vol. 113, no. 22, pp. 9546-9552, 2009.

[25] C. M. T. Law and C. M. L. Wu, "Microstructure Evolution and Shear Strength of Sn-3.5 Ag-Re Lead-Free BGA Solder Balls," *Proceedings of the 6th IEEE CPMT Conference on High Density Microsystem Design and Packaging and Component Failure Analysis,* pp. 60-65, 2004.

[26] N.-C. Lee, "Lead-Free Soldering-Where the World Is Going," *Advancing Microelectronics,* vol. 26, no. 5, pp. 29-35, 1999.

[27] A. Pirondi, "Mechanical Failure in Microelectronic Packaging," 2008.

[28] S. Wiese, A. Schubert, H. Walter, R. Dukek, F. Feustel, E. Meusel, and B. Michel, "Constitutive Behaviour of Lead-Free Solders vs. Lead-Containing Solders-Experiments on Bulk Specimens and Flip-Chip Joints," *Proceedings of the 51st IEEE Electronic Components and Technology Conference,* pp. 890-902, 2001.

[29] R. J. McCabe and M. E. Fine, "Athermal and Thermally Activated Plastic Flow in Low Melting Temperature Solders at Small Stresses," *Scripta Materialia,* vol. 39, no. 2, pp. 189-195, 1998.

[30] J. H. Lau, "Solder Joint Reliability of Flip Chip and Plastic Ball Grid Array Assemblies under Thermal, Mechanical, and Vibrational Conditions," *IEEE Transactions on Components, Packaging, and Manufacturing Technology, Part B,* vol. 19, no. 4, pp. 728-735, 1996.

[31] K. M. Ralls, Courtney, T. H., Wulff, J, *Introduction to Materials Science and Engineering*. Wiley & Sons, 1976.

[32] R. W. Hertzberg, R. P. Vinci, and J. L. Hertzberg, *Deformation and Fracture Mechanics of Engineering Materials*. Wiley New York, 1996.

[33] H. Ma and J. C. Suhling, "A Review of Mechanical Properties of Lead-Free Solders for Electronic Packaging," *Journal of Materials Science,* vol. 44, no. 5, pp. 1141-1158, 2009.

[34] J. H. Lau and Y.-H. Pao, *Solder Joint Reliability of* BGA, *CSP, Flip Chip, and Fine Pitch SMT Assemblies,* McGraw-Hill New York, 1997.

[35] R. W. Evans and B. Wilshire, "Creep of Metals and Alloys," 1985.

[36] M. F. Ashby, "A First Report on Deformation-Mechanism Maps," *Acta Metallurgica,* vol. 20, no. 7, pp. 887-897, 1972.

[37] J. Weertman, "Steady-State Creep through Dislocation Climb," *Journal of Applied Physics,* vol. 28, p. 362, 1957.

[38] R. L. Coble, "A Model for Boundary Diffusion Controlled Creep in Polycrystalline Materials," *Journal of Applied Physics,* vol. 34, p. 1679, 1963.

[39] C. Herring, "Diffusional Viscosity of a Polycrystalline Solid," *Journal of Applied Physics,* vol. 21, pp. 437-445, 1950.

[40] A. C. Fischer-Cripps, *Nanoindentation*, Third ed. Springer, 2011.

[41] P. McCluskey, R. Grzybowski, and T. Podlesak, "High Temperature Electronics," CRC Press, 1997.

[42] S. Ganesan and M. Pecht, *Lead-Free Electronics*. John Wiley and Sons, 2006.

[43] R. W. Johnson, J. L. Evans, P. Jacobsen, J. R. Thompson, and M. Christopher, "The Changing Automotive Environment: High-Temperature Electronics," *IEEE Transactions on Electronics Packaging Manufacturing,* vol. 27, no. 3, pp. 164-176, 2004.

[44] M. Hattori, "Needs and Applications of High-Temperature Lsis for Automotive Electronic Systems," *Proceedings of the International Conference on High Temperature Electronics,* pp. 37-43, 1999.

[45] B. Parmentier, O. Vermesan, and L. Beneteau, "Design of High Temperature Electronics for Well Logging Applications," *Proceedings of the International Conference on High Temperature Electronics,* 2003.

[46] H. Ma, J. C. Suhling, P. Lall, and M. J. Bozack, "Reliability of the Aging Lead Free Solder Joint," *Proceeding of the 56th IEEE Electronic Components and Technology Conference,* pp. 849-864, 2006.

[47] H. Ma, J. C. Suhling, Y. Zhang, P. Lall, and M. J. Bozack, "The Influence of Elevated Temperature Aging on Reliability of Lead Free Solder Joints," *Proceeding of the 57th IEEE Electronic Components and Technology Conference,* pp. 653-668, 2007.

[48] Y., Zhang., Z., Cai., J. C. Suhling, P. Lall, and M. J. Bozack, "The Effects of Aging Temperature on SAC Solder Joint Material Behavior and Reliability," *Proceedings of the 58th IEEE Electronic Components and Technology Conference*, pp. 99-112, 2008.

[49] I. E. Anderson and J. L. Harringa, "Elevated Temperature Aging of Solder Joints Based on Sn-Ag-Cu: Effects on Joint Microstructure and Shear Strength," *Journal of Electronic Materials,* vol. 33, no. 12, pp. 1485-1496, 2004.

[50] I. E. Anderson, J. W. Walleser, J. L. Harringa, F. Laabs, and A. Kracher, "Nucleation Control and Thermal Aging Resistanceof near-Eutectic Sn-Ag-Cu-X Solder Jointsby Alloy Design," *Journal of Electronic Materials,* vol. 38, no. 12, pp. 2770-2779, 2009.

[51] Z. Cai, Y. Zhang, J. C. Suhling, P. Lall, R. W. Johnson, and M. J. Bozack, "Reduction of Lead Free Solder Aging Effects Using Doped SAC Alloys," *Proceedings of the 60th IEEE Electronic Components and Technology Conference,* pp. 1493-1511, 2010.

[52] S. Choi, T. R. Bieler, J. P. Lucas, and K. N. Subramanian, "Characterization of the Growth of Intermetallic Interfacial Layers of Sn-Ag and Sn-Pb Eutectic Solders and Their Composite Solders on Cu Substrate During Isothermal Long-Term Aging," *Journal of Electronic Materials,* vol. 28, no. 11, pp. 1209-1215, 1999.

[53] C. M. Chuang, T. S. Lui, and L. H. Chen, "Effect of Aluminum Addition on Tensile Properties of Naturally Aged Sn-9Zn Eutectic Solder," *Journal of Materials Science,* vol. 37, no. 1, pp. 191-195, 2002.

[54] R. Darveaux, "Shear Deformation of Lead Free Solder Joints," *Proceedings of the 55th IEEE Electronic Components and Technology Conference*, pp. 882-893, 2005.

[55] R. Darveaux and K. Banerji, "Fatigue Analysis of Flip Chip Assemblies Using Thermal Stress Simulations and a Coffin-Manson Relation," *Proceedings of the 41st IEEE Electronic Components & Technology Conference*, pp. 797-805, 1991.

[56] Y. Ding, C. Wang, Y. Tian, and M. Li, "Influence of Aging Treatment on Deformation Behavior of 96.5Sn3.5Ag Lead-Free Solder Alloy During in Situ Tensile Tests," *Journal of Alloys and Compounds,* vol. 428, no. 1, pp. 274-285, 2007.

[57] I. Dutta, D. Pan, R. A. Marks, and S. G. Jadhav, "Effect of Thermo-Mechanically Induced Microstructural Coarsening on the Evolution of Creep Response of SnAg-Based Microelectronic Solders," *Materials Science and Engineering: A,* vol. 410-411, pp. 48-52, 2005.

[58] T.-C. Hsuan and K.-L. Lin, "Effects of Aging Treatment on Mechanical Properties and Microstructure of Sn–8.5Zn–0.5Ag–0.01Al–0.1Ga Solder," *Materials Science and Engineering: A,* vol. 456, no. 1, pp. 202-209, 2007.

[59] K.-S. Kim, C.-H. Yu, and J.-M. Yang, "Aging Treatment Characteristics of Solder Bump Joint for High Reliability Optical Module," *Thin Solid Films*, vol. 462-463, pp. 402-407, 2004.

[60] B. Lampe, "Room Temperature Aging Properties of Some Solder Alloys," *Welding Journal*, vol. 55, no. 10, pp. 330-340, 1976.

[61] X. Luhua, J. H. L. Pang, K. H. Prakash, and T. H. Low, "Isothermal and Thermal Cycling Aging on IMC Growth Rate in Lead-Free and Lead-Based Solder Interface," *IEEE Transactions on Components and Packaging Technologies,* vol. 28, no. 3, pp. 408-414, 2005.

[62] A. S. Medvedev, "Aging of Tin-Lead Solders and Joints Soldered by Them," *Metallovedenie I Obrabotka Metallov,* vol. 7, pp. 16-23, 1956.

[63] K. Mysore, D. Chan, D. Bhate, G. Subbarayan, I. Dutta, V. Gupta, J. Zhao, and D. Edwards, "Aging-Informed Behavior of Sn3.8Ag0.7Cu Solder Alloys," *Proceedings of IEEE ITherm,* pp. 870-875, 2008.

[64] J. H. L. Pang, T. H. Low, B. S. Xiong, X. Luhua, and C. C. Neo, "Thermal Cycling Aging Effects on Sn–Ag–Cu Solder Joint Microstructure, IMC and Strength," *Thin Solid Films,* vol. 462-463, pp. 370-375, 2004.

[65] S. Wiese and K. J. Wolter, "Creep of Thermally Aged SnAgCu-Solder Joints," *Microelectronics Reliability,* vol. 47, no. 2, pp. 223-232, 2007.

[66] Q. Xiao, H. J. Bailey, and W. D. Armstrong, "Aging Effects on Microstructure and Tensile Property of Sn3.9Ag0.6Cu Solder Alloy," *Journal of Electronic Packaging,* vol. 126, no. 2, pp. 208-212, 2004.

[67] J.-W. Yoon, C.-B. Lee, and S.-B. Jung, "Growth of an Intermetallic Compound Layer with Sn-3.5Ag-5Bi on Cu and Ni-P/Cu During Aging Treatment," *Journal of Electronic Materials,* vol. 32, no. 11, pp. 1195-1202, 2003.

[68] Y. Zhang, "The Effects of Aging on the Mechanical Behavior of Lead Free and Mixed Formulation Solder Alloys," PhD, Mechanical Engineering, Auburn University, Auburn, AL, 2010.

[69] Y. Zhang, Z. Cai, J. C. Suhling, P. Lall, and M. J. Bozack, "The Effects of SAC Alloy Composition on Aging Resistance and Reliability," *Proceedings of the 59th IEEE Electronic Components and Technology Conference* pp. 370-389, 2009.

[70] S. L. Allen, M. R. Notis, R. R. Chromik, and R. P. Vinci, "Microstructural Evolution in Lead-Free Solder Alloys: Part I. Cast Sn–Ag–Cu Eutectic," *Journal of Materials Research,* vol. 19, no. 5, pp. 1417-1424, 2004.

[71] A. Bansal, T. Lee, K. Liu, and J. Xue, "Effects of Isothermal Aging and in-Situ Current Stress on the Reliability of Lead-Free Solder Joints," *Proceedings of 60th IEEE Electronic Components and Technology Conference,* pp. 1529-1535, 2010.

[72] S. Chavali, Y. Singh, P. Kumar, G. Subbarayan, I. Dutta, and D. R. Edwards, "Aging Aware Constitutive Models for SnAgCu Solder Alloys," *Proceedings of the 61st IEEE Electronic Components and Technology Conference* pp. 701-705, 2011.

[73] W. M. Chen, P. McCloskey, and S. C. O'Mathuna, "Isothermal Aging Effects on the Microstructure and Solder Bump Shear Strength of Eutectic Sn37Pb and Sn3.5Ag Solders," *Microelectronics Reliability,* vol. 46, no. 5, pp. 896-904, 2006.

[74] R. Gagliano, "Shear Testing of Solder Joints: The Effect of Various Parameters on the Maximum Shear Stress of Eutectic Tin-Lead Solder," *Advanced Materials for the 21st Century: Proceedings of the 1999 Julia R. Weertman Symposium,* pp. 107-116, 1999.

[75] M. Hasnine, M. Mustafa, J. C. Suhling, B. C. Prorok, M. J. Bozack, and P. Lall, "Characterization of Aging Effects in Lead Free Solder Joints Using Nanoindentation," *Peoceedings of the 63rd IEEE Electronic Components and Technology Conference,* pp. 166-178, 2013.

[76] S. W. R. Lee, Y.-K. Tsui, X. Hunag, and E. C. C. Yan, "Effects of Room Temperature Storage Time on the Shear Strength of PBGA Solder Balls," *International Mechanical Engineering Congress and Exposition*, pp. 259-262, 2002.

[77] Y. Miyazawa and T. Ariga, "Influences of Aging Treatment on Microstructure and Hardness of Sn-(Ag, Bi, Zn) Eutectic Solder Alloys," *Materials Transactions*, vol. 42, no. 5, pp. 776-782, 2001.

[78] M. Mustafa, Z. Cai, J. C. Suhling, and P. Lall, "The Effects of Aging on the Cyclic Stress-Strain Behavior and Hysteresis Loop Evolution of Lead Free Solders," *Proceedings of the 61st IEEE Electronic Components and Technology Conference*, pp. 927-939, 2011.

[79] J. Wilde, A. R. Fix, and W. Nüchter, "Microstructural Changes of Lead-Free Solder Joints During Long-Term Ageing, Thermal Cycling and Vibration Fatigue," *Soldering & Surface Mount Technology*, vol. 20, no. 1, pp. 13-21, 2008.

[80] M. Motalab, M. Mustafa, J. C. Suhling, J. Zhang, J. Evans, M. J. Bozack, and P. Lall, "Correlation of Reliability Models Including Aging Effects with Thermal Cycling Reliability Data," *Proceedings of the 63rd IEEE Electronic Components and Technology Conference*, pp. 986-1004, 2013.

[81] J. Zhang, Z. Hai, S. Thirugnanasambandam, J. L. Evans, M. Bozack, R. Sesek, Y. Zhang, and J. C. Suhling, "Correlation of Aging Effects on Creep Rate and Reliability in Lead Free Solder Joints," *Journal of SMT*, vol. 25, no. 3, pp. 19-28, 2012.

[82] T. Lee and H. Ma, "Aging Impact on the Accelerated Thermal Cycling Performance of Lead-Free BGA Solder Joints in Various Stress Conditions," *Proceedings of the 62nd IEEE Electronic Components and Technology Conference*, pp. 477-482, 2012.

[83] L. Yin, M. Meilunas, B. Arfaei, L. Wentlent, and P. Borgesen, “Effect of Microstructure Evolution on Pb-Free Solder Joint Reliability in Thermomechanical Fatigue,” *Proceedings of the 62nd IEEE Electronic Components and Technology Conference*, pp. 493-499, 2012.

[84] T. Zhang, J. Evans, C. Mitchell, Z. Z. Li, E. Crandall, a. J. Ridenour, and F. Xie, “Reliability of Lead-Free BGA with SnPb Solder Paste for Harsh Environments,” *Proceedings of SMTA/CAVE Symposium on AIMS Harsh Environment Electronics*, 2009.

[85] B. Çal, “Lead-Free Soldering Risks and Reliability Problems in Space Electronics," 2019 3rd International Symposium on Multidisciplinary Studies and Innovative Technologies (ISMSIT), Ankara, Turkey, 2019, pp. 1-8.

[86] I. Szendiuch, C. Vasko and P. Cejtchaml, "Lead-free Solder Quality Investigation," 2*006 29th International Spring Seminar on Electronics Technology*, St. Marienthal, Germany, pp. 215-218, 2006.

[87] R. J. Coyle, P. P. Solan, A. J. Serafino, and S. A. Gahr, “The Influence of Room Temperature Aging on Ball Shear Strength and Microstructure of Area Array Solder Balls,” *Proceedings of the 50th IEEE Electronic Components and Technology Conference*, pp. 160-169, 2000.

[88] T.-K. Lee, H. Ma, K.-C. Liu, and J. Xue, “Impact of Isothermal Aging on Long-Term Reliability of Fine-Pitch Ball Grid Array Packages with Sn-Ag-Cu Solder Interconnects: Surface Finish Effects,” *Journal of Electronic Materials*, vol. 39, no. 12, pp. 2564-2573, 2010.

[89] M. A. Whitmore, A. C. Chilton, and W. B. Hampshire, “Fatigue Failure in a Model SMD Joint,” *Soldering & Surface Mount Technology*, vol. 1, no. 3, pp. 21-24, 1989.

[90] L. Ming, K. Y. Lee, D. R. Olsen, W. T. Chen, B. T. C. Tan, and S. Mhaisalkar, "Microstructure, Joint Strength and Failure Mechanisms of SnPb and Pb-Free Solders in BGA Packages," *IEEE Transactions on Electronics Packaging Manufacturing*, vol. 25, no. 3, pp. 185-192, 2002.

[91] J.-M. Koo and S.-B. Jung, "Effect of Displacement Rate on Ball Shear Properties for Sn–37Pb and Sn–3.5Ag BGA Solder Joints During Isothermal Aging," *Microelectronics Reliability*, vol. 47, no. 12, pp. 2169-2178, 2007.

[92] R. Darveaux, "Shear Deformation of Lead Free Solder Joints," *Proceedings of the 55th Electronic Components and Technology Conference*, pp. 882-893, 2005.

[93] J. R. Oliver, J. Liu, and Z. Lai, "Effect of Thermal Ageing on the Shear Strength of Lead-Free Solder Joints," *Proceedings of the International Symposium on Advanced Packaging Materials Processes, Properties and Interfaces*, pp. 152-157, 2000.

[94] H. L. J. Pang, K. H. Tan, X. Q. Shi, and Z. P. Wang, "Microstructure and Intermetallic Growth Effects on Shear and Fatigue Strength of Solder Joints Subjected to Thermal Cycling Aging," *Materials Science and Engineering: A*, vol. 307, no. 1, pp. 42-50, 2001.

[95] T. Lee, B. Zhou, and T. R. Bieler, "Impact of Isothermal Aging and Sn Grain Orientation on the Long-Term Reliability of Wafer-Level Chip-Scale Package Sn–Ag–Cu Solder Interconnects," *IEEE Transactions on Components, Packaging and Manufacturing Technology*, vol. 2, no. 3, pp. 496-501, 2012.

[96] R. C. J. Smetana, P. Read, R. Popowich, D. Fleming, and T. Sack, "Variations in Thermal Cycling Response of Pb-Free Solder Due to Isothermal Preconditioning," *Proceedings of SMTA International Conference*, pp. 641-654, 2011.

[97] L. Anand, "Constitutive Equations for Hot-Working of Metals," *International Journal of Plasticity,* vol. 1, no. 3, pp. 213-231, 1985.

[98] S. B. Brown, K. H. Kim, and L. Anand, "An Internal Variable Constitutive Model for Hot Working of Metals," *International Journal of Plasticity,* vol. 5, no. 2, pp. 95-130, 1989.

[99] J.-P. Clech, "An Obstacle-Controlled Creep Model for Sn-Pb and Sn-Based Lead-Free Solders," *Proceedings of SMTA International Conference,* 2004.

[100] Y. Hong, P. Deane, P. Magill, and K. L. Murty, "Creep Deformation of 96.5Sn-3.5Ag Solder Joints in a Flip Chip Package," *Peoceedings of the 46th IEEE Electronic Components and Technology Conference,* pp. 1136-1142, 1996.

[101] X. Q. Shi, Z. P. Wang, Q. J. Yang, and H. L. J. Pang, "Creep Behavior and Deformation Mechanism Map of Sn-Pb Eutectic Solder Alloy," *Journal of Engineering Materials and Technology,* vol. 125, no. 1, pp. 81-88, 2002.

[102] S. Wiese, M. Roellig, and K. Wolter, "Creep of Eutectic SnAgCu in Thermally Treated Solder Joints," *Proceedings of the 55th IEEE Electronic Components and Technology Conference*, vol. 2, pp. 1272-1281, 2005.

[103] Q., Xiao, L., Nguyen, and W. D., Armstrong, "Aging and Creep Behavior of Sn3.9Ag0.6Cu Solder Alloy," Proceedings of the 54th Electronic Components and Technology Conference, pp. 1325-1332, 2004.

[104] J. H. Lau, "Solder Joint Reliability of Flip Chip and Plastic Ball Grid Array Assemblies under Thermal, Mechanical, and Vibrational Conditions," *IEEE Transactions on Components, Packaging, and Manufacturing Technology: Part B,* vol. 19, no. 4, pp. 728-735, 1996.

[105] W. K. Jones, Y. Q. Liu, M. A. Zampino, and G. L. Gonzalez, "The at-Temperature Mechanical Properties of Lead-Tin Based Alloys," in *Microelectronic Interconnections and Assembly*, Springer Netherlands, pp. 53-58, 1998.

[106] Y. L. W. K. Jones, M. A. Zampino, G. Gonzalez, and M. Shah, "Design and Reliability of Solders and Solder Interconnections," *TMS Annual Meeting*, 1997.

[107] X. Q. Shi, W. Zhou, H. L. J. Pang, and Z. P. Wang, "Effect of Temperature and Strain Rate on Mechanical Properties of 63Sn/37Pb Solder Alloy," *Journal of Electronic Packaging*, vol. 121, no. 3, pp. 179-185, 1999.

[108] F. Lang, H. Tanaka, O. Munegata, T. Taguchi, and T. Narita, "The Effect of Strain Rate and Temperature on the Tensile Properties of Sn–3.5Ag Solder," *Materials Characterization*, vol. 54, no. 3, pp. 223-229, 2005.

[109] L. H. Dai and S.-W. R. Lee, "Characterization of Strain Rate-Dependent Behavior of 63sn-37Pb Solder Alloy," *Proceedings of ASME InterPACK*, pp. 307-313, 2001.

[110] H. Nose, M. Sakane, Y. Tsukada, and H. Nishimura, "Temperature and Strain Rate Effects on Tensile Strength and Inelastic Constitutive Relationship of Sn-Pb Solders," *Journal of Electronic Packaging*, vol. 125, no. 1, pp. 59-66, 2003.

[111] W. J. Plumbridge and C. R. Gagg, "Effects of Strain Rate and Temperature on the Stress–Strain Response of Solder Alloys," *Journal of Materials Science: Materials in Electronics*, vol. 10, no. 5, pp. 461-468, 1999.

[112] J. H. L. Pang, B. S. Xiong, and F. X. Che, "Modeling Stress Strain Curves for Lead-Free 95.5Sn-3.8Ag-0.7Cu Solder," *Proceedings of the 5th International Conference on Thermal and Mechanical Simulation and Experiments in Microelectronics and Microsystems*, pp. 449-453, 2004.

[113] J. G. Harper, L. A. Shepard, and J. E. Dorn, "Creep of Aluminum under Extremely Small Stresses," *Acta Metallurgica,* vol. 6, no. 7, pp. 509-518, 1958.

[114] F. Garofalo and D. B. Butrymowicz, "Fundamentals of Creep and Creep-Rupture in Metals," *Physics Today,* vol. 19, no. 5, pp. 100-102, 1966.

[115] L. Anand, "Constitutive Equations for the Rate-Dependent Deformation of Metals at Elevated Temperatures," *Journal of Engineering Materials and Technology,* vol. 104, no. 1, pp. 12-17, 1982.

[116] F. X. Che, H. L. J. Pang, W. H. Zhu, W. Sun, and A. Y. S. Sun, "Modeling Constitutive Model Effect on Reliability of Lead-Free Solder Joints," *Proceedings of the 7th International Conference on Electronic Packaging Technology,* pp. 1-6, 2006.

[117] M. Pei and J. Qu, "Constitutive Modeling of Lead-Free Solders," *Proceedings of International Symposium on Advanced Packaging Materials: Processes, Properties and Interfaces,* pp. 45-49, 2005.

[118] K. Mysore, G. Subbarayan, V. Gupta, and R. Zhang, "Constitutive and Aging Behavior of Sn3.0Ag0.5Cu Solder Alloy," *IEEE Transactions on Electronics Packaging Manufacturing,* vol. 32, no. 4, pp. 221-232, 2009.

[119] M. Motalab, Z. Cai, J. C. Suhling, and P. Lall, "Determination of Anand Constants for SAC Solders Using Stress-Strain or Creep Data," *Proceedings of IEEE ITherm,* pp. 910-922, 2012.

[120] N. Bai, X. Chen, and H. Gao, "Simulation of Uniaxial Tensile Properties for Lead-Free Solders with Modified Anand Model," *Materials & Design,* vol. 30, no. 1, pp. 122-128, 2009.

[121] M. Amagai, M. Watanabe, M. Omiya, K. Kishimoto, and T. Shibuya, "Mechanical Characterization of Sn–Ag-Based Lead-Free Solders," *Microelectronics Reliability,* vol. 42, no. 6, pp. 951-966, 2002.

[122] Y. Kim, H. Noguchi, and M. Amagai, "Vibration Fatigue Reliability of BGA -IC Package with Pb-Free Solder and Pb–Sn Solder," *Microelectronics Reliability,* vol. 46, no. 2, pp. 459-466, 2006.

[123] M. L. Huang and L. Wang, "Effects of Cu, Bi, and in on Microstructure and Tensile Properties of Sn-Ag-X(Cu, Bi, in) Solders," *Metallurgical and Materials Transactions A,* vol. 36, no. 6, pp. 1439-1446, 2005.

[124] M. Matahir, L. Chin, K. Tan, and A. Olofinjana, "Mechanical Strength and Its Variability in Bi-Modified Sn-Ag-Cu Solder Alloy," *Journal of Achievement in Materials and Manufacturing Engineering,* vol. 46, pp. 50-56, 2011.

[125] R. S. Pandher, B. G. Lewis, R. Vangaveti, and B. Singh, "Drop Shock Reliability of Lead-Free Alloys - Effect of Micro-Additives," *Proceedings of the 57th IEEE Electronic Components and Technology Conference*, pp. 669-676, 2007.

[126] Z. Zhenqing, W. Lei, X. Xiaoqiang, W. Qian, and L. Jaisung, "The Influence of Low Level Doping of Ni on the Microstructure and Reliability of SAC Solder Joint," *Proceedings of International Conference on Electronic Packaging Technology & High Density Packaging,* pp. 1-5, 2008.

[127] I. d. Sousa, D. W. Henderson, L. Parry, S. K. Kang, and D. Shih, "The Influence of Low Level Doping on the Thermal Evolution of SAC Alloy Solder Joints with Cu Pad Structures," *Proceedings of the 56th IEEE Electronic Components and Technology Conference*, pp. 1454-1461, 2006.

[128] J. H. Lee, S. Kumar, H. J. Kim, Y. W. Lee, and J. T. Moon, "High Thermo-Mechanical Fatigue and Drop Impact Resistant Ni-Bi Doped Lead Free Solder," *Proceedings of the 64th IEEE Electronic Components and Technology Conference*, pp. 712-716, 2014.

[129] T. Yeung, H. Sze, K. Tan, J. Sandhu, C. Neo, and E. Law, "Material Characterization of a Novel Lead-Free Solder Material — SACQ," *Proceedings of the 64th IEEE Electronic Components and Technology Conference*, pp. 518-522, 2014.

[130] L. Sun and L. Zhang, "Properties and Microstructures of Sn-Ag-Cu-X Lead-Free Solder Joints in Electronic Packaging," *Advances in Materials Science and Engineering*, vol. 2015, no. 639028, 2015.

[131] M. Sadiq, R. Pesci, and M. Cherkaoui, "Impact of Thermal Aging on the Microstructure Evolution and Mechanical Properties of Lanthanum-Doped Tin-Silver-Copper Lead-Free Solders," *Journal of Electronic Materials*, vol. 42, no. 3, pp. 492-501, 2013.

[132] H. Lee, Y. Chen, T. Hong, K. Shih, and C. Hsu, "Microstructural Evolution of Sn-3.5Ag Solder with Lanthanum Addition," *International Conference on Electronic Packaging Technology & High Density Packaging*, pp. 617-622, 2009.

[133] H. Hao, Y. Shi, Z. Xia, Y. Lei, and F. Guo, "Microstructure Evolution of SnAgCu Lead-Free Solders under High Temperature Aging," *Journal of Electronic Materials*, vol. 37, no. 1, pp. 2-8, 2008.

[134] D. Witkin, "Influence of Microstructure on Mechanical Behavior of Bi-Containing Pb-Free Solders," *Proceedings of IPC APEX EXPO Conference and Exhibition*, vol. 1, pp. 540-560, 2013.

[135] A. Delhaise, D. Perovic, and P. Snugovsky, "The Effects of Bi and Aging on the Microstructure and Mechanical Properties of Sn-Rich Alloys," *Proceedings of the International Conference on Soldering and Reliability*, 2015.

[136] R. R. Chromik, R. P. Vinci, S. L. Allen, and M. R. Notis, "Measuring the Mechanical Properties of Pb-Free Solder and Sn-Based Intermetallics by Nanoindentation," *JOM*, vol. 55, no. 6, pp. 66-69, 2003.

[137] X. Deng, N. Chawla, K. K. Chawla, and M. Koopman, "Deformation Behavior of (Cu, Ag)–Sn Intermetallics by Nanoindentation," *Acta Materialia*, vol. 52, no. 14, pp. 4291-4303, 2004.

[138] F. Gao, H. Nishikawa, T. Takemoto, and J. Qu, "Mechanical Properties Versus Temperature Relation of Individual Phases in Sn–3.0Ag–0.5Cu Lead-Free Solder Alloy," *Microelectronics Reliability*, vol. 49, no. 3, pp. 296-302, 2009.

[139] Y. D. Han, H. Y. Jing, S. M. L. Nai, L. Y. Xu, C. M. Tan, and J. Wei, "Temperature Dependence of Creep and Hardness of Sn-Ag-Cu Lead-Free Solder," *Journal of Electronic Materials*, vol. 39, no. 2, pp. 223-229, 2010.

[140] M. Hasnine, J. C. Suhling, B. C. Prorok, M. J. Bozack, and P. Lall, "Exploration of Aging Induced Evolution of Solder Joints Using Nanoindentation and Microdiffraction," *Peoceedings of the 64th IEEE Electronic Components and Technology Conference*, pp. 379-394, 2014.

[141] M. Hasnine, J. C. Suhling, B. C. Prorok, M. J. Bozack, and P. Lall, "Nanomechanical Characterization of SAC Solder Joints - Reduction of Aging Effects Using Microalloy Additions," *Peoceedings of the 65th IEEE Electronic Components and Technology Conference*, pp. 1574-1585, 2015.

[142] M. Hasnine, J. C. Suhling, B. C. Prorok, M. J. Bozack, and P. Lall, "Anisotropic Mechanical Properties of SAC Solder Joints in Microelectronic Packaging and Prediction of Uniaxial Creep Using Nanoindentation Creep," *Experimental Mechanics,* vol. 57, no. 4, pp. 603-614, 2017.

[143] S. Lotfian, J. M. Molina-Aldareguia, K. E. Yazzie, J. Llorca, and N. Chawla, "Mechanical Characterization of Lead-Free Sn-Ag-Cu Solder Joints by High-Temperature Nanoindentation," *Journal of Electronic Materials,* vol. 42, no. 6, pp. 1085-1091, 2013.

[144] V. M. F. Marques, C. Johnston, and P. S. Grant, "Nanomechanical Characterization of Sn–Ag–Cu/Cu Joints—Part 1: Young's Modulus, Hardness and Deformation Mechanisms as a Function of Temperature," *Acta Materialia,* vol. 61, no. 7, pp. 2460-2470, 2013.

[145] V. M. F. Marques, B. Wunderle, C. Johnston, and P. S. Grant, "Nanomechanical Characterization of Sn–Ag–Cu/Cu Joints—Part 2: Nanoindentation Creep and Its Relationship with Uniaxial Creep as a Function of Temperature," *Acta Materialia,* vol. 61, no. 7, pp. 2471-2480, 2013.

[146] H. Rhee, J. P. Lucas, and K. N. Subramanian, "Micromechanical Characterization of Thermomechanically Fatigued Lead-Free Solder Joints," *Journal of Materials Science: Materials in Electronics,* vol. 13, no. 8, pp. 477-484, 2002.

[147] M. Sadiq, J.-S. Lecomte, and M. Cherkaoui, "Individual Phase Mechanical Properties at Different Temperatures of Sn–Ag–Cu Lead-Free Solders Incorporating Special Pileup Effects Using Nanoindentation," *Journal of Electronic Packaging,* vol. 137, no. 3, pp. 031005-031005-5, 2015.

[148] Y. Sun, J. Liang, Z.-H. Xu, G. Wang, and X. Li, "Nanoindentation for Measuring Individual Phase Mechanical Properties of Lead Free Solder Alloy," *Journal of Materials Science: Materials in Electronics*, vol. 19, no. 6, pp. 514-521, 2008.

[149] J. L. Hay and G. M. Pharr, "Instrumented Indentation Testing," *Mechanical Testing and Evaluation*, vol. 8, 2000.

[150] K. O. Kese, Z. C. Li, and B. Bergman, "Method to Account for True Contact Area in Soda-Lime Glass During Nanoindentation with the Berkovich Tip," *Materials Science and Engineering: A*, vol. 404, no. 1, pp. 1-8, 2005.

[151] M. Cabibbo, D. Ciccarelli, and S. Spigarelli, "Nanoindentation Hardness Measurement in Piling up SiO_2 Coating," *Physics Procedia*, vol. 40, pp. 100-112, 2013.

[152] G. J. S. Chou, "Microstructure Evolution of Snpb and SnAg/Cu BGA Solder Joints During Thermal Aging," *Proceedings of the 8th International Advanced Packaging Materials Symposium*, pp. 39-46, 2002.

[153] R. L. J. M. Ubachs, P. J. G. Schreurs, and M. G. D. Geers, "Microstructure Evolution of Tin-Lead Solder," *IEEE Transactions on Components and Packaging Technologies*, vol. 27, no. 4, pp. 635-642, 2004.

[154] U. Sahaym, B. Talebanpour, S. Seekins, I. Dutta, P. Kumar, and P. Borgesen, "Recrystallization and Ag_3Sn Particle Redistribution During Thermomechanical Treatment of Bulk Sn–Ag–Cu Solder Alloys," *IEEE Transactions on Components, Packaging and Manufacturing Technology*, vol. 3, no. 11, pp. 1868-1875, 2013.

[155] M. Maleki, J. Cugnoni, and J. Botsis, "Isothermal Ageing of SnAgCu Solder Alloys: Three-Dimensional Morphometry Analysis of Microstructural Evolution and Its Effects on

Mechanical Response," *Journal of Electronic Materials*, vol. 43, no. 4, pp. 1026-1042, 2014.

[156] A. U. Telang, T. R. Bieler, J. P. Lucas, K. N. Subramanian, L. P. Lehman, Y. Xing, and E. J. Cotts, "Grain-Boundary Character and Grain Growth in Bulk Tin and Bulk Lead-Free Solder Alloys," *Journal of Electronic Materials*, vol. 33, no. 12, pp. 1412-1423, 2004.

[157] P. Kumar, B. Talenbanpour, U. Sahaym, C. H. Wen, and I. Dutta, "Microstructural Evolution and Some Unusual Effects During Thermo-Mechanical Cycling of Sn-Ag-Cu Alloys," *Proceedings of IEEE ITherm*, pp. 880-887, 2012.

[158] P. Chauhan, S. Mukherjee, M. Osterman, A. Dasgupta, and M. Pecht, "Effect of Isothermal Aging on Microstructure and Creep Properties of SAC305 Solder: A Micromechanics Approach," *Proceedings of ASME InterPACK*, pp. V001T07A009, 2013.

[159] W. Yang, R. W. Messler, and L. E. Felton, "Microstructure Evolution of Eutectic Sn-Ag Solder Joints," *Journal of Electronic Materials*, vol. 23, no. 8, pp. 765-772, 1994.

[160] C. Tz-Cheng, Z. Kejun, R. Stierman, D. Edwards, and K. Ano, "Effect of Thermal Aging on Board Level Drop Reliability for Pb-Free BGA Packages," *Proceedings of the 54th IEEE Electronic Components and Technology Conference*, vol. 2, pp. 1256-1262, 2004.

[161] H. Zhu, Y. Guo, W.Y. Li, A.A. Tseng, B. Martin, "Micro-mechanical characterizations of solder mask materials", *Proceedings of the 3rd Electronics Packaging Technology Conference (EPTC 2000)*, pp. 148-153, December 7, 2000.

[162] P. R, Chowdhury, J. C., Suhling, Lall, P., "Mechanical Characterization of Solder Mask Materials," *Proceedings of ITherm 2018*, pp. 1133-1141, San Diego, CA, May 29 – June 1, 2018.

[163] K. S., Siow, S. T., Chua, "Thermal Cycling of Sintered Silver (Ag) Joint as Die-Attach Material," *Journal of Minerals, Metals & Materials Society*, Vol. 71(9), pp. 3066–3075, September 2019..

[164] J. Chen, Q., Nguyen, J. C., Roberts, J. C., Suhling, and R C., Jaeger, "Moisture-Induced Die Stresses in PBGA Packages Exposed to Various Environments," Proceedings of ITherm 2018, pp. 1112-1119, San Diego, CA, May 29 – June 1, 2018.

[165] W. C., Oliver, and G. M., Pharr, "An Improved Technique for Determining Hardness and Elastic Modulus Using Load and Displacement Sensing Indentation Experiments," *Journal of Materials Research*, vol. 7, no. 6, pp. 1564-1583, 1992.

[166] D., Tabor, *The Hardness of Metals*, Oxford University Press, 2000.

[167] M. J, Mayo, W. D., Nix, "A micro-indentation study of superplasticity in Pb, Sn and Sn-38 wt.% Pb," *Acta Materialia*, Vol. 36(8), pp. 2183–2192, 1988

[168] M. J., Mayo, W. D., Nix, "Mechanical properties of nanophase TiO2 as determined by nanoindentation," *Journal of Material Research*, Vol. 5(5), pp.1073–1082, 1990

[169] N., Chawla, "Thermomechanical Behavior of Environmentally Benign Pb-Free Solders," *International Materials Reviews*, Vol. 54(6), pp. 368-384, 2009.

[170]. A., Fahim, S., Ahmed, M. M. R., Chowdhury, J. C., Suhling, P. Lall, , "High Temperature Creep Response of Lead Free Solders," *Proceedings of ITherm 2016*, pp. 1218-1224, Las Vegas, NV, May 31- June 3, 2016

[171] M. M. R., Chowdhury, S., Ahmed, A., Fahim, Suhling, J. C., Lall, P., "Mechanical Characterization of Doped SAC Solder Materials at High Temperature," *Proceedings of ITherm 2016*, pp. 1202 - 1208, Las Vegas, NV, May 30 - June 3, 2016.

[172] M. M. R., Chowdhury, M. A., Hoque, S., Ahmed, J. C., Suhling, S. Hamasha, Lall, P., "Effects of Mechanical Cycling on the Microstructure of SAC305 Lead Free Solder", *Proceedings of ITherm 2018*, pp. 1324-1332, San Diego, CA, May 29 - June 1, 2018.

[173] A., Fahim, S., Ahmed, J. C., Suhling, P., Lall, "Nanomechanical Characterization of IMCs Formed in SAC Solder Joints During Isothermal Aging" *Proceedings of ITherm 2017*, pp. 1398 – 1408, Orlando, FL, May 30 – June 2, 2017.

[174] A., Fahim, S., Ahmed, J. C., Suhling, P., Lall, "Nanomechanical Characterization of Intermetallic Compounds in Lead Free Solder Joints", *68th Proceedings of ECTC*, pp. 2359- 2359, 2018

[175] T., Laurila, V.,Vuorinen, J. K., Kivilahti, "Interfacial Reactions between Lead-Free Solders and Common Base Materials", *Material Science and Engineering*, Vol. 49, pp. 1-60, 2005.

[176] E. K., Ohriner, "Intermetallic Formation in Soldered Copper-Based Alloys at 150° C. to 250° C", *Welding Journal*, pp. 191–202, 1987.

[177] M. J., Rizvi, C., Bailey, Y. C., Chan, M. N., Islam, H., Lu, "Effect of Adding 0.3 wt.% Ni into the Sn-0.7 wt.% Cu Solder Part II. Growth of Intermetallic Layer with Cu During

[178] A., Fahim, S., Ahmed, J. C., Suhling, P., Lall, "Mechanical Characterization of Intermetallic Compounds in SAC Solder Joints at Elevated Temperatures", *Proceedings of ITherm 2018*, pp. 1081 – 1090, San Diego, CA, May 29 – June 1, 2018.

[179] A., Fahim, S., Ahmed, J. C., Suhling, P., Lall, "Nanoindentation Measurements of the Mechanical Properties of Individual Phases within Lead Free Solder Joints Subjected to Isothermal Aging", *Proceedings of ASME InterPACK*, pp. 1-9, San Francisco, California, USA. August 27–30, 2018

[180] M. S., Alam, K M. R., Hassan, A., Fahim, J., Wu, S., Ahmed, J.C., Suhling, P., Lall, "Investigation of the Mechanical Behavior of SAC305 Solder Joints at Extreme High Temperatures Using Nanoindentation," *70th Proceedings of ECTC*, pp. 2175-2184, Orlando, FL, 2020.

.[181] A., Fahim, S. M. K., Hasan, J. C., Suhling, P., Lall, "Investigation on the Mechanical Behavior Evolution Occurring in Lead Free Solder Joints Exposed to Thermal Cycling," *70th Proceedings of ECTC*, pp. 1486-1495, Orlando, FL, Orlando, FL, 2020.

[182] A., Fahim, S. M. K., Hasan, J. C., Suhling, P., Lall, "Evaluation of the Creep Response of Lead Free Solder Materials Subjected to Thermal Cycling," *ASME Proceedings of InterAPCK*, pp. 1-9, Anaheim, CA, October 27–29, 2020.

[183] M. M. R., Chowdhury, M. A., Hoque, A., Fahim, J. C., Suhling, S. Hamasha, Lall, P., "Microstructural Evolution in SAC305 and SAC-Bi Solders Subjected to Mechanical Cycling", *Proceedings of ASME InterPACK 2018*, pp: 1-9, San Fransisco, CA, August 27-30, 2018.

[184] S. M. K., Hasan, A., Fahim, J. C., Suhling, P., Lall, "Effects of Thermal Cycling on the Mechanical and Microstructural Evolution of SAC305 Lead-Free Solder," *Proceedings of ASME InterPACK 2019*, pp: 1-10, Anaheim, CA, October 7–9, 2019.

[185] A., Fahim, S. M. K., Hasan, J. C., Suhling, P., Lall, "Nanoindentation Testing of SAC305 Solder Joints Subjected to Thermal Cycling Loading", *Proceedings of ASME InterPACK 2019*, pp: 1-10, October 7–9, 2019.

[186] S M. K. Hasan, A. Fahim, J. C. Suhling, S. Hamasha, P. Lall, "Mechanical Behavior Evolution of SAC+Bi Lead Free Solder Exposed to Thermal Cycling," *Proceedings of ITherm 2020*, Orlando, FL, pp. 1180-1190, 2020.

[187] M., Al Ahsan, S M. K., Hasan, A., Fahim, J. C., Suhling, P., Lall, "Effect of Different Thermal Cycling Profiles on the Mechanical Behavior of SAC305 Lead Free Solder," *Proceedings of ITherm 2020*, Orlando, FL, pp. 1170-1179, 2020.

[188] A., Fahim, S. M. K., Hasan, J. C., Suhling, P., Lall, "Mechanical Behavior Evolution of SAC305 Lead Free Solder Joints under Thermal Cycling" *Proceedings of ITherm* 2019, pp. 734 – 744, Las Vegas, NV, May 28-31, 2019.

[189] M. A., Hoque, M. M. R., Chowdhury, N., Fu, J. C., Suhling, S., Hamasha, P., Lall, "Evolution of the Cyclic Stress-Strain and Constitutive Behaviors of Doped Lead Free Solder During Fatigue Testing" *Proceedings of ITherm 2018*, pp. 1387-1395, San Diego, CA, May 29 - June 1, 2018.

[190] S. M. K., Hasan, A., Fahim, J. C., Suhling, P., Lall, "Evolution of Mechanical Behavior of Lead Free Solder Joints Exposed to Thermal Cycling" *Proceedings of ITherm 2019*, pp. 1332 – 1341, Las Vegas, NV, May 28-31, 2019.

[191] A., Fahim, S. M. K., Hasan, J. C., Suhling, P., Lall, "Nanomechanical Characterization of Various Materials within PBGA Packages Subjected to Thermal Cycling Loading," *Proceedings of ITherm 2020*, Orlando, FL, pp. 1302-1310, 2020.

[192] A., Fahim, S. M. K., Hasan, J. C., Suhling, P., Lall, "Creep Behavior of Various Materials within PBGA Packages Subjected to Thermal Cycling Loading," *ASME Proceedings of InterPACK*, pp. 1-8, Anaheim, CA, October 27–29, 2020.

[193] D. Mondal, A. Fahim, KM. R. Hassan, , Suhling, JC, & Lall, P. "Deformation Behavior of SAC305 Solder Joints with Multiple Grains, *Proceedings of ASME InterPACK*, pp. 1-8, Anaheim, CA, October 27–29, 2020.

[194] D. Mondal, A. Fahim, J. C. Suhling and P. Lall, “Modeling Deformation Behavior of Multiple Grained SAC305 Solder Joints,” *Proceedings of ITherm 2020*, Orlando, FL, pp. 1221-1228, 2020.